Interactions of regional atmospheric and land surface processes with the West African monsoon system

vorgelegt von

Cornelia Klein

bei der Fakultät für Angewandte Informatik

der Universität Augsburg

zur Erlangung des akademischen Grades

Doktor der Naturwissenschaften

- Dr. rer. nat. -

Augsburg 2016

Contents

Nomenclature

ACM2 .... Asymmetrical Convective Model V.2
ACSWDOWN ... Accumulated incoming shortwave radiation - internal WRF variable
ACT .... Atlantic Cold Tongue
AEJ .... African Easterly Jet
AEW .... African Easterly Wave
ALB .... Albedo
ALBBCK .... 12-monthly albedo climatology - internal WRF variable
ALBEDO12M ... 12-monthly albedo climatology - internal WRF variable
AMMA .... African Monsoon Multidisciplinary Analysis
ARW .... Advanced Research WRF
AVHRR .... Advanced Very High Resolution Radiometer
BMJ .... Betts-Miller-Janjic
CALIPSO .... Cloud-Aerosol Lidar and Infrared Pathfinder Satellite Observation
CAPE .... Convective Available Potential Energy
CLIM .... Climatological surface parameters
CMORPH .... Climate Prediction Center Morphing Technique
CORDEX .... Coordinated Regional Downscaling Experiment
CPC .... Climate Prediction Center
CRU .... Climate Research Unit
CU .... Cumulus
DKRZ .... Deutsches Klimarechenzentrum
DLC .... Regionally optimized land use classification for DYN
DT .... Time step variable in WRF
DYN .... Dynamical surface parameters
EC .... Eddy Covariance
ECMWF .... European Centre for Medium-Range Weather Forecasts
EF .... Evaporative Fraction
ENS .... WRF multi-physics ensemble mean
ERA-I .... ECMWF ERA-Interim reanalysis
FVEG .... Vegetation fraction - internal WRF variable
GCM .... Global Circulation Model
GF .... Grell-Freitas
GHCN .... Global Historical Climatology Network
GLOB .... Global datasets for ALB, LAI, VF from SPOT_VGT

GOCCP .... GCM-Oriented CALIPSO Cloud Product
GPCC .... Global Precipitation Climatology Centre
GREENFRAC .. 12-monthly vegetation fraction climatology - internal WRF variable
HSS .... Heidke Skill Score
IDL .... Interactive Data Language
ITCZ .... Inter-Tropical Convergence Zone
ITF .... Intertropical Front
IVGTYP .... Dominant land use category - internal WRF variable
KF .... Kain-Fritsch
LAI .... Leaf Area Index
LAI12M .... 12-monthly LAI climatology - internal WRF variable
LAM .... Limited Area Model
LANDUSEF ..... Fractional land use category - internal WRF variable
LCL .... Lifted Condensation Level
LH .... Latent Heat
LIN .... Lin Purdue
LRZ .... Leibniz Rechenzentrum
LSM .... Land Surface Model
LU_INDEX ...... Dominant land use category - internal WRF variable
MAD .... Mean Absolute Deviation
MCS .... Mesoscale Convective System
MD .... Mean Deviation
METEOSAT .... Meteorological Satellite
MLC .... MODIS land use classification
MODIS .... Moderate Resolution Imaging Spectroradiometer
MP .... Microphysics
MTE .... Fluxnet Multi-Tree Ensemble
MYJ .... Mellor-Yamada-Janjic
NCAR .... National Center for Atmospheric Research
NCEP .... National Centers for Environmental Prediction
NOAA .... National Oceanic and Atmospheric Administration
PBL .... Planetary Boundary Layer
PCP .... Precipitation
RFE .... African Rainfall Estimate version 2
RRTM .... Rapid Radiative Transfer Model
RRTMG .... Rapid Radiative Transfer Model GCM applications
RSD .... Relative Standard Deviation
SAL .... Saharan Air Layer
SD .... Standard Deviation
SEVIRI .... Spinning Enhanced Visible and Infrared Imager
SH .... Sensible Heat
SHDMAX .... Climatological maximum vegetation fraction - internal WRF variable
SHDMIN .... Climatological minimum vegetation fraction - internal WRF variable
SHL .... Saharan Heat Low

SLP .... Sea Level Pressure
SM .... Soil Moisture
SOILCAT .... Dominant soil category - internal WRF variable
SPOT_VGT ..... Satellite Pour l'Observation de la Terre_Vegetation
SST .... Sea Surface Temperature
SWDOWN ...... Instantaneous incoming shortwave radiation - internal WRF variable
TEJ .... Tropical Easterly Jet
TH .... New Thompson
TRMM .... Tropical Rainfall Measuring Mission
TS .... Surface Temperature
UDEL .... University of Delaware
VEGCAT .... Dominant land use category - internal WRF variable
VEGFRA .... 12-monthly vegetation fraction climatology - internal WRF variable
VF .... Green Vegetation Fraction
WAM .... West African Monsoon
WASCAL .... West African Science Service Center on Climate Change and Adapted Land Use
WPS .... WRF Pre-processing System
WRF .... Weather Research and Forecasting (model)
WS .... Workstation
WSM3 .... WRF Single Moment 3
YSU .... Yonsei University

Abstract

The West African monsoon (WAM) rainfall is characterized by a strong temporal and spatial variability. The interplay of various large- and small-scale drivers generates frequent weather extremes such as droughts or floods, making West Africa one of the most vulnerable parts of the world in terms of food security. While it is known that teleconnections to sea surface temperatures determine the overall WAM regime, it is still uncertain by which margin and at which scales regional atmospheric and land surface processes may modify it.

In this data scarce region, atmospheric models are indispensable tools allowing physically consistent interaction experiments on different components of the monsoon system. This thesis uses the Weather Research and Forecasting model (WRF) driven by reanalysis data to investigate the relevance of regional moist processes, convection and vegetation patterns for the WAM regime and presents the abilities and limits of the model to properly capture the involved processes. Furthermore, the possibility to improve WRF by adjusting it to regional characteristics is analysed. This includes the choice of a favourable model set-up based on a region-specific parameterization classification, the explicit treatment of convection and the implementation of satellite-derived land surface parameters.

A mixed-physics ensemble with 27 parameterization combinations is used to evaluate the effect of regional moisture distribution on the WAM for the rainy season 1999. Although all ensemble members use the same boundary forcing, the ensemble spread covers the whole range of dry to wet monsoon regimes observed in the Sahel between 1979 and 2010. The most rigorous shift from wet to dry monsoon conditions was found to be related to an increase of low- and mid-level clouds weakening the incoming solar radiation and hence the sea-land pressure gradient. In particular, significant large-scale changes in precipitation are always linked to a change in the intensity of the pressure gradient and thus of the moist Hadley-type meridional circulation that connects the monsoon winds to the Tropical easterly jet. This shows that regional moist processes may indeed alter the monsoon dynamics.

A closer look at the convective processes reveals that explicit instead of parameterized convection considerably improves both the precipitation characteristics as well as the incoming shortwave radiation associated with the modelled cloud cover. This confirms convection as a key process for the monsoon circulation since it affects the water and energy balance not only in the atmosphere but also at the surface.

In turn, the partitioning of surface energy and moisture fluxes may affect the location and frequency of convective systems. Land cover and vegetation play a crucial role in this partitioning. To investigate the effect of observed interannual vegetation changes between 2009 and 2010 on the WAM precipitation, novel high-resolution satellite-derived dynamical datasets for vegetation fraction, albedo and leaf area index are implemented into WRF. The two years exhibit opposing vegetation anomalies. In comparison to a climatological land surface, the vegetation changes exhibit the strongest effect on latent heat fluxes and associated surface temperatures. Moisture divergence (convergence) and a decrease (increase) of rainy hours is found over regions with higher (lower) vegetation fraction during the day and the opposite during the night. These effects cancel out when averaged over larger regions, leading to negligible changes in total precipitation amounts. An improvement of modelled rainfall through the integration of observed dynamical surface information with respect to observations was only detectable in the Sahel region.

These findings suggest that both regional atmospheric and land surface processes may trigger significant changes in precipitation amounts or shifts of the monsoon rainband when they affect the large-scale temperature gradient over land, which is always connected to a change of the large-scale pressure gradient driving the WAM. Accordingly, temperature changes at smaller scales rather affect local moisture convergence or divergence and therefore the rainfall distribution instead of total amounts.

The results presented in this thesis contribute to further improve our picture of factors for WAM variability, which forms the basis for any practical measures that could improve the resilience of the West African population whose livelihood still depends on rainfed agriculture.

Sissili river, Ghana. Photo by C.K., May 2013.

Zusammenfassung

Die Niederschläge des westafrikanischen Monsuns (WAM) sind durch eine starke räumliche und zeitliche Variabilität charakterisiert. In Hinblick auf Nahrungsmittelsicherheit ist West Afrika eine der gefährdetsten Regionen der Welt, da das Zusammenspiel verschiedener groß- und kleinskaliger Wetterfaktoren regelmäßig zu Wetterextremen wie Dürren oder Überflutungen führt. Es ist bekannt, dass das übergeordnete Monsunregime von Telekonnektionen mit Meeresoberflächentemperaturen dominiert wird. Unsicher ist allerdings, in wie weit und auf welchen Größenskalen regionale Atmosphären- und Landoberflächenprozesse den WAM beeinflussen können.

Atmosphärische Modelle sind unerlässliche Werkzeuge in dieser datenarmen Region. Sie erlauben physikalisch konsistente Interaktionsexperimente für verschiedene Komponenten des Monsunsystems. In dieser Studie wird das Weather Research and Forecasting (WRF) Modell verwendet, um die Relevanz von regionalen Feuchteprozessen, Konvektion und Vegetationsmustern für das Monsunregime zu untersuchen. Weiterhin wird WRF auf seine Fähigkeit den WAM und seine beteiligten Prozesse korrekt zu simulieren geprüft und mögliche Limitierungen aufgezeigt. Dabei werden Möglichkeiten der Modellverbesserung durch eine Anpassung an regionale Charakteristika diskutiert. Diese Anpassung beinhaltet die Auswahl der Modellkonfiguration, basierend auf einer regionsspezifischen Klassifikation der Parametrisierungen, dem Anwenden einer expliziten Konvektionsbeschreibung und die Implementierung satellitengestützter Oberflächenparameter.

Es wird ein Modellphysik-Ensemble mit 27 Parameterisierungskombinationen verwendet, um den Effekt von regionaler Feuchteverteilung auf den WAM 1999 zu untersuchen. Obwohl alle Ensemble-Mitglieder die selben Randbedingungen als Antrieb verwenden, spannt das Ensemble die gesamte Bandbreite von feuchten zu trockenen Monsunregimen auf, die in der Sahelzone von 1979 bis 2010 beobachtet wurden. Die drastischste Verschiebung von trockenem zu feuchtem Regime wurde dabei in Zusammenhang mit einem Anstieg der Wolkenbedeckung in der niederen bis mittleren Troposphäre festgestellt. Diese schwächt die Sonneneinstrahlung und somit den Meer-Land-Druckgradienten. Generell konnten alle signifikanten, großskaligen Niederschlagsänderungen auf eine Veränderung der Intensität dieses Druckgradienten, und damit auf eine Veränderung der feuchten meridionalen Monsunzirkulation die den Monsunwind mit dem Tropical Easterly Jet verbindet, zurückgeführt werden. Dies zeigt, dass regionale feuchte Prozesse tatsächlich die Monsundynamik modifizieren können.

Ein genauerer Blick auf die konvektiven Prozesse zeigt, dass eine explizite anstatt einer parametrisierten Konvektionsbeschreibung nicht nur die Niederschlagscharakteristiken, sondern auch die modellierte Wolkenbedeckung und die damit zusammenhängende einfallende kurzwellige Strahlung verbessert. Das verdeutlicht, dass Konvektion ein Schlüsselprozess für die Monsunzirkulation darstellt, da sie den Wasser- und Energiehaushalt sowohl in der Atmosphäre als auch an der Landoberfläche beeinflusst.

Umgekehrt kann die Partitionierung dieser Energie in latente und sensible Wärmeflüsse an der Landoberfläche wiederum den Ort und die Häufigkeit der Entstehung von konvektiven Systemen beeinflussen. Landbedeckung und Vegetation spielen für diese Partitionierung eine ausschlaggebende Rolle. Um den Effekt beobachteter interannueller Vegetationsänderungen zwischen den Jahren 2009 und 2010 auf den Monsunniederschlag zu untersuchen, werden neue, satellitengestützte dynamische Datensätze für die Vegetationsfraktion, die Albedo und den Blattflächenindex in das WRF Modell implementiert. Die beiden Jahre weisen entgegensetzte Vegetationsanomalien auf. Im Vergleich zu einer klimatologischen Landoberfläche zeigen die Vegetationsänderungen den stärksten Effekt für latente Wärmeflüsse und die daran gekoppelten Landoberflächentemperaturen. Tagsüber werden Feuchtekonvergenz (-divergenz) und weniger (mehr) Regenstunden über Regionen mit höherer (geringerer) Vegetationsfraktion verzeichnet. Nachts verhält es sich genau umgekehrt. Diese Effekte scheinen sich, gemittelt über eine größere Region, gegenseitig aufzuheben, was zu vernachlässigbaren Veränderungen der absoluten Niederschlagsmenge führt. Eine Verbesserung des modellierten Niederschlags durch die Integration der satellitengestützten Oberflächeninformation im Vergleich zu Beobachtungsdaten war nur in der Sahelzone feststellbar.

Die präsentierten Ergebnisse legen nahe, dass regionale Prozesse in der Atmosphäre und an der Landoberfläche signifikante Veränderungen in Niederschlagsmengen oder Verschiebungen des Monsunregenbandes hervorrufen können, wenn sie den großskaligen Gradienten der Landoberflächentemperatur modifizieren. Dies ist automatisch verbunden mit einer Veränderung des großskaligen Druckgradienten, der den WAM antreibt. Gleichermaßen beeinflussen Temperaturveränderungen auf kleineren Skalen die lokale Feuchtekonvergenz und -divergenz, was sich eher auf die Niederschlagsverteilung als auf absolute Niederschlagsmengen auswirkt.
Diese Arbeit trägt dazu bei das Verständnis über Faktoren, die die Variabilität des WAM beeinflussen, weiter zu verbessern. Dieses Verständnis bildet die Grundlage für alle praktischen Maßnahmen, die die Widerstandsfähigkeit der von regengestützter Landwirtschaft abhängigen westafrikanischen Bevölkerung verbessern könnten.

Introduction

1.1 Background

The West African monsoon (WAM) is probably the most prominent feature of the West African climate. Seasonal rains occur from May to October over the subcontinent where they travel northward from the Guinean coast to the Sahel, and back again. Accounting for the majority of the annual precipitation, the WAM is of paramount importance for the West African population that primarily relies on rain-fed agriculture for food and income. With yearly precipitation rates ranging from semi-arid to humid conditions, wide areas of West Africa are considered to be potential breadbaskets (e.g. Morris et al., 2012; Bharati et al., 2008). However, food security remains an unachieved goal since people frequently suffer from sudden droughts or floods and the lack of appropriate measures for mitigation and adaptation. West Africa was identified as one of the worldwide most vulnerable regions to climate change because of the combination of endemic poverty, complex governance, insufficient infrastructure and technology, strong population growth and finally, an extreme variability of the WAM (IPCC, 2014).

The WAM system is driven by a complex and not yet fully understood interplay of several dynamical features and multi-scale factors influencing the precipitation intensity and continental coverage (e.g. Sultan and Janicot, 2003; Nicholson, 2008). It is characterized by a large variability at both intra-annual and interannual time scales, especially in the Sahel region (Barbe et al., 2002; Grist and Nicholson, 2001), which may culminate in severe droughts as in the 1970s and 1980s (Fig. 1.1). A potential rainfall recovery since the 1990s is still under debate since, although dry years became less extreme with interspersed positive anomalies, the trend is not yet significant (L'Hôte et al., 2002; Ozer et al., 2003).
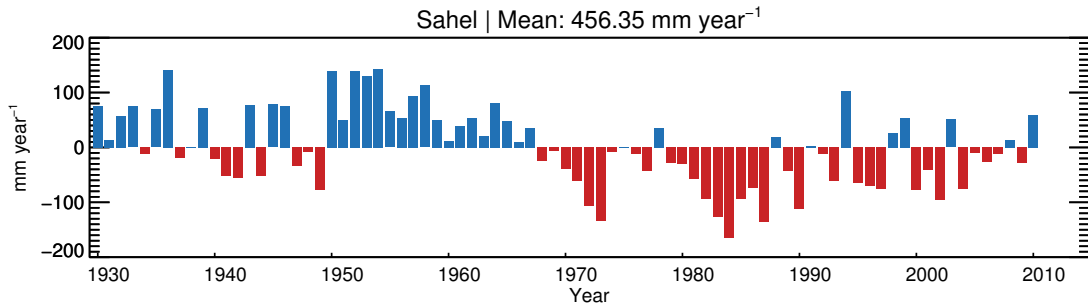
Figure 1.1: Rainfall anomaly (mm year^{-1}) between 10°E-10°W with respect to the average of 1930-2010 in the Sahel (12-18°N) from the gridded Global Precipitation Climatology Centre dataset.

Over the south-north gradient, about 30-80% of the rainfall during the WAM arises from mesoscale convective systems (MCSs) (Fink and Reiner, 2003). Although MCSs extend over an area of 4000 km^2 or more, these organized thunderstorm complexes emerge from formerly isolated small-scale showers. The mechanisms by which MCSs are initiated and maintained are manifold and range from atmospheric disturbances in the monsoon dynamics to very small-scale surface conditions. In the atmosphere, the strength of the low-level monsoon wind that transports moisture from the Atlantic ocean over land plays a crucial role for wet or dry WAM conditions. In addition, other dynamical ingredients like the Tropical easterly jet or the African easterly jet influence the strength of the monsoon. These large-scale factors were found to be mainly governed by teleconnections to sea surface temperatures (SSTs) that affect the Northern Hemisphere and therefore impose the overall WAM regime (e.g. Hertig et al., 2015; Nicholson, 2013).

Nevertheless, during recent decades, the investigation of land-atmosphere interactions also evolved into a focal point of research on WAM variability. By now, a number of studies explored by which processes, under which conditions and by what magnitude the land surface might impact WAM rainfall. The picture emerged that soil moisture and particularly its heterogeneities (Taylor et al., 2011a) may affect the initiation and maintenance of convective systems. Atmospheric models suggest that large-scale vegetation changes might even have a direct effect on the monsoon dynamics (Zheng and Eltahir, 1998; Lauwaet et al., 2009). In conclusion, while the large scales dominate the particular monsoon regime, the land surface may modify, strengthen or buffer its state (Li et al., 2007). Furthermore, land surface conditions are prone to anthropogenic changes making their impact on the WAM a sensitive factor for land use planning and future climate.

For a better understanding of how regional large- to small-scale factors affect WAM variability, limited area models (LAMs) are useful tools in this data sparse region (cf. Fig. 1.2). They provide gap-free atmospheric fields at high spatio-temporal resolution. LAMs allow to conduct physically consistent experiments on different components of the WAM system, which would not be possible with observational data or statistical models alone. Depending on their configuration, potential applications of LAMs reach from dynamical downscaling of past and present climate to weather prediction and finally to climate projections.
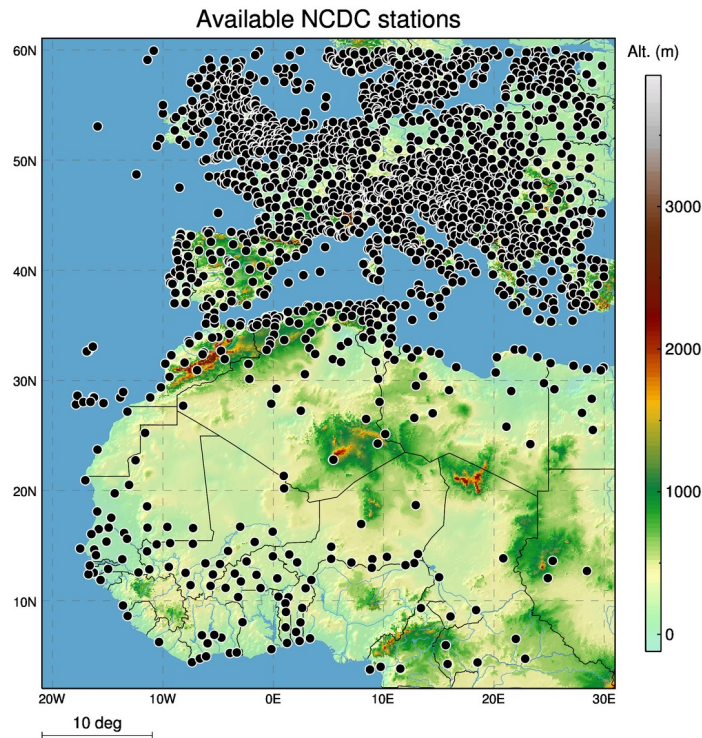
Figure 1.2: Distribution of all weather stations listed by the National Climatic Data Center measuring air temperature for Europe and West Africa between 2000 and 2015. Only stations with at least one year of data are shown.

Recent studies demonstrate the ability of state-of-the-art LAMs to represent the WAM for the past and present: Nikulin et al. (2012) confirm that LAMs can considerably enhance the representation of WAM precipitation in comparison to coarser reanalyses datasets or global circulation models (GCMs). They relate this enhancement to an improved representation of regional and local processes. Sylla et al. (2013) likewise state that LAMs are suitable for the investigation of the dynamical features and associated precipitation patterns of the WAM. However, they also emphasize considerable differences in the simulation results for different LAMs in spite of the same boundary forcing and relate the largest uncertainty to physical parameterizations. First attempts of regional climate projections for West Africa likewise revealed a large spread and even diverging rainfall trends in the results for different models and configurations (e.g. Jung and Kunstmann, 2007; Linden and Mitchell, 2009). This lead Paeth et al. (2011) to the conclusion that important systematic errors still persist in present-day LAMs over West Africa. They point out that a regional adjustment of model parameterizations and parameters in comparison to observations might considerably improve the model performance and provide new insights on process interactions.

There is an urgent need for weather and climate information in West Africa. A reliable regional climate modelling system that properly captures the processes that are influenced by regional particularities could, for example, help to improve the forecasts of extreme events, to narrow

down the critical time period providing suitable conditions for crop planting (e.g. Laux et al., 2010; Waongo et al., 2014), to ensure the transfer of water from wet to dry periods or to develop strategies for sustainable farming systems under climate change. (e.g. Salack et al., 2015). This would ultimately improve the resilience of the West African population.

Therefore, programs like WASCAL (West African Science Service Center on Climate Change and Adapted Land Use), in which this thesis is embedded, aim at establishing a regional climate modelling system that can be used for process and impact studies in West Africa by various disciplines. Within this highly interdisciplinary framework, this thesis intends to broaden our understanding of the sensitivity of WAM rainfall to regional atmospheric processes and land surface states by dynamically downscaling the WAM with the Weather Research and Forecasting (WRF) model. The thesis furthermore contributes to the evaluation of the uncertainties in simulating the WAM with WRF and assesses potential performance improvements by a regional model adjustment.

1.1.1 Motivation

The WAM is thought to be mainly governed by large scale teleconnections. It is known that these large scale factors drive regional processes that ultimately create a certain monsoon regime. However, it is still unclear which regional processes are most important for determining WAM characteristics such as inland movement, extent or rainfall patterns. It is also an open question to which degree regional processes might in turn modify the large scales. In the following, our current state of knowledge regarding two main actors potentially determining the WAM characteristics is discussed: atmospheric moist processes including convection and land surface conditions with associated land-atmosphere interaction processes.

Moist processes are of crucial importance for the maintenance of the WAM. Without the latent heat of condensation, the driving atmospheric pressure gradient between ocean and land would quickly drop after monsoon onset due to surface cooling by other moist processes: the generation of cloud cover and rainfall (Levermann et al., 2009). Regional moist processes therefore play a critical role for the monsoon regime.

Most notably, convection deserves attention because it is the key element for vertical transport and rainfall production during the WAM. Several LAM studies suggest that it interacts with the AEJ that is weakened when convective activity is weak or missing (e.g. Sylla et al., 2011; Cornforth et al., 2009). However, it is not yet clear whether moist processes also modify other dynamical features like the TEJ. If yes, it remains the question whether changes of different dynamical features like the monsoon wind, the AEJ and the TEJ are necessarily interlinked and how these changes translate into rainfall characteristics.

Besides atmospheric processes, land surface conditions such as soil moisture and vegetation were found to potentially affect monsoon precipitation and even its dynamics (e.g. Lauwaet et al., 2009; Li et al., 2007). However, a limiting factor of these studies is that many rely on LAMs where surface changes are set arbitrarily or where modelled land use scenarios are used. Although recent satellite-based observational studies (Taylor et al., 2011a, 2012) indeed find a statistical relationship between surface conditions and local rainfall probabilities, they lack a process-based analysis of these findings. Therefore, there is a need for studies that combine the application of a LAM with satellite-based observations of surface changes to profit from both: the ability to analyse land-atmosphere interaction processes while prescribing more realistic surface changes. In particular, the potential effect of natural year-to-year variability of vegetation on WAM rainfall received no attention so far.

To address the above mentioned research gaps, feedback studies are necessary. For this, LAMs are especially helpful since they allow to artificially separate cause and effect by turning a variable into a fixed forcing which is why WRF is used in this thesis. However, a factor hampering a robust evaluation of the effect of moist processes or of land surface changes on the WAM system is their crude representation in most state-of-the-art LAMs. Microphysical processes or turbulence that vertically transports water vapour have to be parameterized since they are too small-scale to be physically resolved. Since the parameterization choice considerably affects the model results, it

is a common approach to test physics schemes by try and error to receive a favourably behaving model set-up (e.g. Flaounas et al., 2011a; Noble et al., 2014). This favourable set-up is usually neither well-behaving for all variables nor necessarily transferable to other applications (e.g. Fersch and Kunstmann, 2013), calling for a methodology that provides generalizable informations on parameterization performances. In addition, the uncertainty in model results related to a certain parameterization choice is often neglected.

In the case of convection, most LAM studies over West Africa use a parameterization although this could be avoided if the horizontal resolution of the LAM allows a physically explicit representation. However, very high model resolutions (<4 km, Weisman, 1997) are considered necessary to explicitly represent convection, which is computationally expensive and thus limits the models applicability in space and time. So far, only a few studies, all relying on the same model and dataset, discuss the positive effects of explicit convection on the representation of the modelled WAM (Marsham et al., 2013; Birch et al., 2014). Therefore, the advantages of an explicit treatment of convection, its importance for a correct representation of the WAM and the upper scale limit for its applicability are not well established.

Regarding the land surface conditions, LAM standard applications often use satellite-derived climatologies or even table values for surface parameters like albedo or vegetation cover (e.g. Pohl et al., 2014; Hagos et al., 2014). Other approaches apply more sophisticated land surface models (LSMs) that treat these parameters dynamically but suffer from model inherent uncertainties (e.g. Notaro et al., 2011; Brovkin et al., 2013). Both surface treatments obviously do not allow to evaluate the effect of observed interannual changes of the land surface. Satellite-derived surface information could be used to provide an 'observed' lower boundary condition to the LAM reducing the uncertainty of the surface state, which could ultimately improve the model results.

Nevertheless, in line with Box and Draper (1987) who stated that "essentially, all models are wrong, but some are useful", it should be emphasized that an erroneous representation of the 'real world' in a model does not only tell us that the model needs improvement. It also tells us that the erroneous part of the model is essential for the functioning of the investigated system in reality. Accordingly, any failure of the WRF model to correctly simulate the WAM that can be traced back to a simplified or 'false' implementation of one of the discussed processes gives a hint on the governing process chains that drive the real WAM system.

Experiments where the representation of a certain process is changed in the model while all other parameters are kept constant are therefore helpful to potentially improve the representation of this process *and* to better understand process interactions within the system. Since LAMs permit to keep the 'external' drivers (large-scale boundary conditions) constant while changing 'internal' drivers (e.g. regional moist processes or vegetation), such experiments also allow to separate the former from the latter. With this approach, interaction experiments for atmospheric moist processes and interannual vegetation changes are conducted with WRF to evaluate their effect on different components of the WAM system, building the content of this thesis.

1.2 Objectives

This thesis addresses two complementary questions concerning WAM process interactions and WRF model development:

(i) By which mechanisms and to which extent may moist processes, convection and interannual vegetation changes modify precipitation characteristics during the WAM in spite of the dominating role of the large-scale forcing?

(ii) Does a regional adjustment of these processes in the WRF model improve our ability to correctly model WAM characteristics?

Both questions are separately examined for moist processes, convection and interannual vegetation changes in different chapters of the thesis. The specific aims for the three corresponding experiments are:

Interactions of moist processes with the monsoon system

- Evaluating the interactions of regional moist processes with the monsoon dynamics

- Quantifying the uncertainty in the representation of moist processes in the WRF model and classifying their process-based impact on the WAM regime in order to extract transferable guidelines to set up the model in West Africa.

The relevance of a physically explicit convection description

- Assessing the deficiencies of parameterized convection as compared to physically explicit convection and arising consequences for the simulated WAM and rainfall characteristics

- Testing the validity of simulation results with explicit convection in the convective grey scales above 4 km resolution.

The effect of vegetation-atmosphere feedbacks

- Identifying the processes by which interannual vegetation changes have an effect (if any) on the atmosphere during the WAM

- Investigating whether the implementation of satellite-derived surface parameters improves the representation of surface variables and rainfall in WRF.

1.2.1 Innovation

This thesis uses new methods in order to tackle the open questions and aims defined in Section 1.2:

Different from other ensemble studies, the spread of a mixed-physics WRF ensemble is not only interpreted as the uncertainty range of the representation of moist processes in the model. It is also used as an analysis strategy to evaluate to which degree a change in the moist processes is able to provoke changes in the monsoon dynamics and related precipitation. Although already hypothesized by observational studies, the linear co-variability between different dynamical features of the WAM presented here was not systematically shown before. Moreover, parameterization schemes are classified with respect to their effect on different components of the WAM system instead of following a 'try and error' approach for model set-up.

This thesis also presents one of the first convection-allowing subcontinental-scale LAM simulations highlighting the importance of explicit convection for the modelled WAM. Previous studies focussed on the diurnal cycle of convection, which is extended to intense precipitation events and MCS propagation. Different from common assumptions, it is shown that explicit convection can give reasonable results in the convective grey scales and outperforms a parameterization. Regarding parameterization deficiencies, most studies concentrate on rainfall. Here, the often neglected importance of cloud cover for the modelled WAM regime is emphasized.

In addition, it is relatively new to implement satellite-derived surface information into a LAM due to a lack of satellite data at sufficient spatio-temporal resolution and quality in the past. To my knowledge, the potential of such high-resolution satellite-derived information for a LAM improvement was not tested before in West Africa. With this approach, the effect of realistic, natural interannual changes of vegetation on the WAM characteristics could be investigated. This is not possible with the land surface treatment in standard LAM applications. The adjusted WRF allowed to trace land-atmosphere interactions even in the Sudanian zone, which is something observational studies failed to do due to the strong dynamical forcing in this region.

This thesis incorporates two peer-reviewed papers:

Klein, C., Heinzeller, D., Bliefernicht, J., Kunstmann, H.: Variability of West African monsoon patterns generated by a WRF multi-physics ensemble, Clim Dyn, 45(9), 2733-2755, 2015

Klein, C., Bliefernicht, J., Heinzeller, D., Gessner, U., Klein, I., Kunstmann, H.: Feedback of observed interannual vegetation change: A regional climate model analysis for the West African monsoon, Clim Dyn, doi:10.1007/s00382-016-3237-x, 2016

In both publications, I was responsible for the experimental design, the numerical simulations, data pre- and post-processing, the analysis, all figures and the writing. The co-authors contributed by helping to define research gaps, by proposing methodological approaches and by discussing the study results. They were also responsible for corrections and proofreading. For the second paper, U. Gessner and I. Klein provided pre-processed satellite-based surface data and took part in writing Section 6.2.1.

1.2.2 Structure of the thesis

After a general introduction into the study region and the WAM system in Chapter 2, Chapter 3 gives some background on dynamical downscaling with a focus on the WRF model and shortly presents sensitivity studies that were performed in order to define a first WRF baseline configuration that was used for following studies.

The scientific core of this thesis, consisting of Chapter 4, Chapter 5 and Chapter 6, presents the three main experiments. The experiments required further adjustment of the model set-up and of the analysis strategies, some of which directly arose from preceding analyses. Therefore, each of these chapters starts with an introduction on the particular background followed by a description of the experimental WRF set-up and reference datasets and ends with an individual conclusion.

Finally, the identified interactions of the WAM system with regional atmospheric and surface processes are discussed and the potential for further analyses and regional adjustments of the WRF model are outlined in the concluding Chapter 7.

The West African monsoon

West Africa denotes the westernmost region of the African continent between 15°E-16°W and 4-28°N, which is north of the Gulf of Guinea and reaches up into the central Sahara. It consists of 16 countries with Mauritania, Mali and Niger constituting the northern boundary. From the Guinea coast to the Sahara desert, West Africa is characterized by east-west oriented climate zones. These climatic zones can be divided into four main regions: the tropical Guinea coast (4-8°N), the sub-humid Sudano-Sahel (8-14°N), the semi-arid Sahel (14-18°N) and the Saharan desert in the North (Fig. 4.1, Meynadier et al., 2010).

When referring to the West African summer monsoon, people usually think of its most obvious perceptible feature: rainfall. The monsoon rainfall that occurs during the boreal summer constitutes the only significant atmospheric water source for regions situated above approximately 10°N. Most parts of West Africa exhibit a distinct dry and rainy season, resulting from the interaction of two migrating air masses: the dry and dusty Harmattan wind from the Northeast and the moist monsoon wind from the Southwest. The confluence of these two air masses is known as the intertropical front (ITF, black dashed line in Fig. 2.1, Nicholson, 2013).

The Harmattan is part of the trade wind system and is mainly composed of dry desert air from the Sahara. From November to February, it sweeps over the whole West African subcontinent, sometimes reaching the Guinea coast (Cornforth, 2013, Fig. 2.1a).

However, during summer from July to September, the belt of maximum net solar radiation and related maximum surface temperatures move northward in response to the solar zenith angle. This results in the migration of the region of maximum moisture convergence, convection and rainfall termed here the inter-tropical convergence zone (ITCZ):

Differential heating of the ocean and land surface acts to initiate and maintain a moist low-level southwesterly monsoon flow (Fig. 2.1c). This characteristic seasonal change of the large-scale wind systems is comparable to a large sea breeze, where the land-sea pressure gradient leads to the advection of relatively cool moist air from the Gulf of Guinea onto the hot dry continent (Sultan and Janicot, 2003; Janicot et al., 2008). The resulting rainband travels from the Guinea Coast to the Sahel and back again.

There is no characteristic climatological wind pattern during the transition time in May, when wind directions just start to change (Fig. 2.1b). During this time, SSTs decrease in the southern parts of the Gulf of Guinea establishing the Atlantic cold tongue (ACT) that is visible in Fig. 2.2(a) as a phase of increased sea level pressure reaching up to the Guinea coast. At the same time, the Saharan heat low (SHL), a large low-pressure region of dry convection that forms due to surface heating, strengthens and moves northward to a position close to 20°N (Fig. 2.1c) where it resides throughout the summer (Fig. 2.2a).

It is not until the end of June that this pressure gradient between ocean and land reaches a threshold that causes an abrupt shift of the ITCZ from ∼ 5°N to 10°N, referred to as the 'monsoon jump', which marks the onset of the rainy season in the Sahel (Fig. 2.2 b, dashed line). In the Sahel, the rainy season is shortest with a concentration of rainfall in August. The duration of the rainy season gradually increases equatorward with finally humid conditions at the Guinea coast. Rainfall amounts exhibit a peak in August in the Sahel and a bimodal distribution with the so-called 'little dry season' in August at the Guinea coast (cf. Fig. 2.1 c), which is related to the inland movement and subsequent retreat of the monsoon rainband.
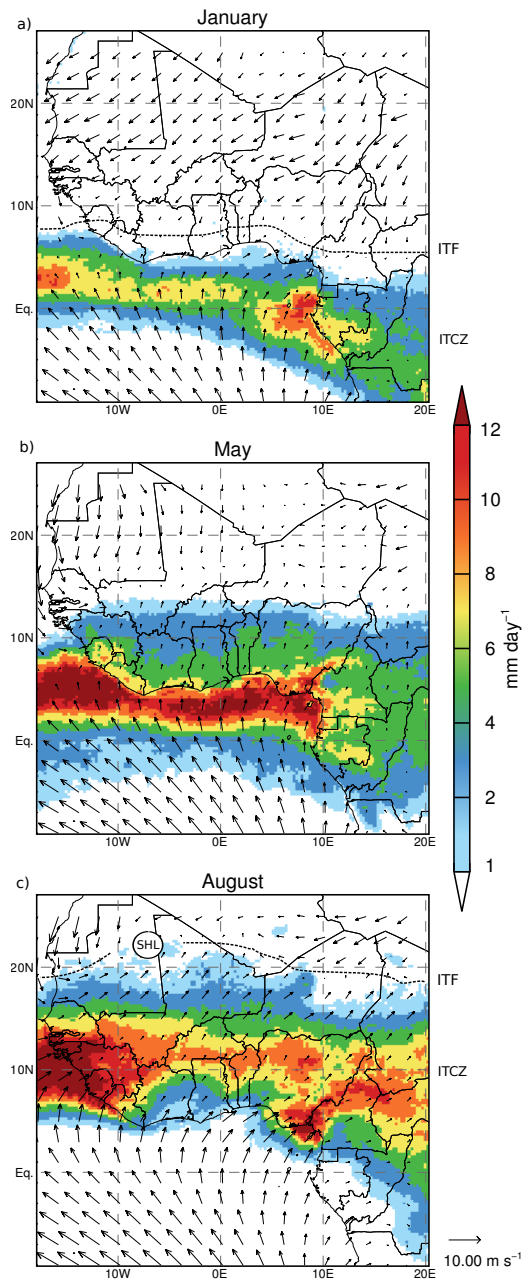
Figure 2.1: 1998-2013 climatology of ERA-Interim reanalysis 10 m wind vectors (m s^{-1}) and Tropical Rainfall Measuring Mission (TRMM) precipitation (mm day^{-1}) for January, May and August. Dashed lines indicate the position of the inter tropical front (ITF) and the circle marks the center of the Saharan Heat Low (SHL). The rainband represents the intertropical convergence zone (ITCZ).
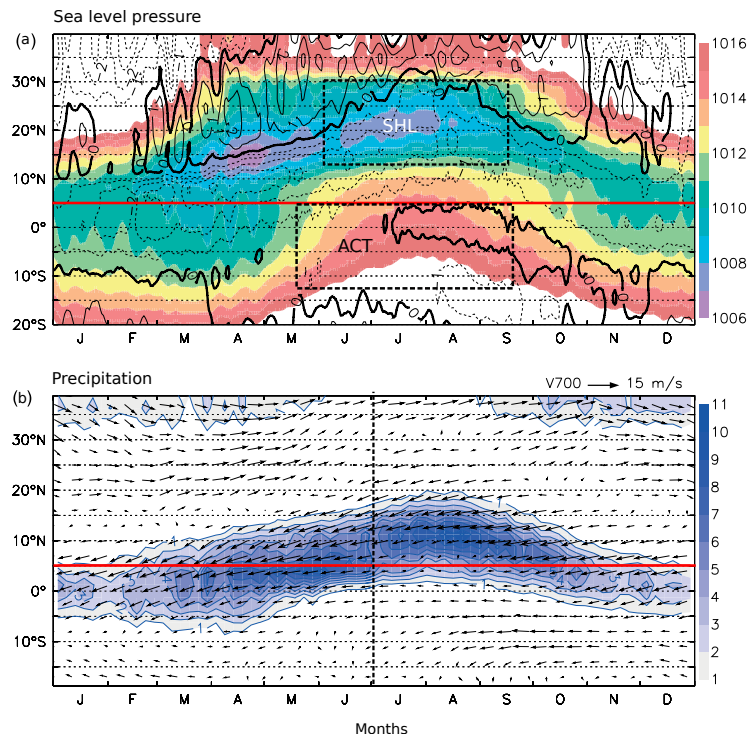
Figure 2.2: Hovmöller diagrams for 1989-2009 ERA-I (10°W-10°E) zonal mean **(a)** sea level pressure (hPa) and **(b)** precipitation of the Global Precipitation Climatology Project (mm day^{-1}) and 700 hPa wind (m s^{-1}). The dashed black line depicts the monsoon jump. The red line marks the West African coast. Adapted from Thorncroft et al. (2011).

Different from the classical picture of converging trade winds directly causing the tropical rainband, the ITF and the ITCZ do not coincide during the WAM. Instead, the ITCZ resides about 1000 km south of the ITF (Fig. 2.1c), indicating the complexity of mechanisms governing the WAM circulation. This revised picture of the WAM was extensively discussed by Nicholson (2013), who emphasized the diminished importance of the ITF compared to other atmospheric features like the SHL, the African easterly jet (AEJ), the tropical easterly jet (TEJ) and the predominance of organized convection that is fostered by strong wind shear in the region.

2.1 Atmospheric features

The atmospheric circulation maintaining the WAM resembles a moist Hadley-type meridional overturning as is depicted in Fig. 2.3 (blue arrows). During the pre-monsoon phase (Fig. 2.3, top), maximum precipitation amounts are located over the coastal region where warm SSTs and frictional uplift foster convection (Nicholson, 2008). Atmospheric features that become driving factors during the peak monsoon phase are already visible but less pronounced (Thorncroft et al., 2011). The SHL is still weak and resides further south. Figure 2.1 illustrates that it is part of the ITF with the Harmattan passing at its northwestern flank and the monsoon winds joining at

the southeastern side. On basis of rain gauge and reanalysis data, Sultan and Janicot (2003) found the position and strength of the SHL affecting the timing and extent of the monsoon jump since it represents the pressure minimum of the pressure gradient driving the monsoon.

When the monsoon sets in, the meridional circulation and its atmospheric features shift polewards (Fig. 2.3, bottom). Precipitation is now strongly controlled by dynamical features such as the two strengthened jet streams that frame the region of maximum rainfall:

The TEJ is a high-level jet ($\sim$ 200 hPa) and emerges from the Asian monsoon region (Flaounas et al., 2011a). It shows high interannual variability in wind velocities. By inducing upper-level divergence, it fosters moisture convergence at the surface and therefore deep convection.

The AEJ is a mid-tropospheric jet at $\sim$ 600 hPa that exhibits strong interannual variability in position. The AEJ forms to adjust for the thermal wind balance between the approximately moist-adiabatic monsoon air mass and the dry-adiabatic Saharan air mass that create a baroclinic zone. The latitudinal position of the AEJ therefore coincides with the largest surface temperature gradient, as illustrated in Fig. 2.4. The core of the AEJ develops at the altitude where the temperature gradient between the two air masses reverses and near-surface southwesterly winds change to northeasterly winds, creating strong vertical shear. The reversal of the temperature gradient occurs due to latent heating in the zone of moist convection and marks the point where moist adiabatic and dry adiabatic lapse rates cross (Parker et al., 2005a). The AEJ is a source of African Easterly Waves (AEWs), which are an important factor for the initiation and maintenance of organized convection (Fink and Reiner, 2003). AEWs are atmospheric disturbances with wave-lengths of 3000-5000 km and periods of 3-5 days that often develop over regions of complex topography to the East, such as the Jos Plateau, the Darfur region or the Ethiopian highlands (Noble et al., 2014). The waves propagate westward where they interact with deep convection and provide a favourable dynamical forcing for intense and/or long-lived MCSs over land and for tropical cyclones over the Atlantic (Mohr and Thorncroft, 2006).

As shown in Fig. 2.4 (right), the westerly monsoon wind layer reaches far inland but is thickest between 5-10°N where most of its moisture is rained out. The ocean-land pressure gradient considerably influences how far it may penetrate. From the North, the monsoon layer is overrun by the Harmattan forming the Saharan Air Layer (SAL). The extent of the warm and dust-laden SAL is influenced by the SHL-driven shallow convection depicted in red in Fig. 2.3. The SAL is capping the cooler, moist monsoon layer and thus imposes convective inhibition, which is why the WAM shows a pronounced diurnal cycle: during the day, surface warming creates thermals that may break through the convective inhibition. Resulting convection then drives a strong vertical transport. In turn, convection ceases during the night, which allows a strengthening of meridional circulations and horizontal moisture advection (Parker et al., 2005b).

Figure 2.5 summarizes the main dynamical features that affect the strength of the WAM. It also illustrates why the Sahel is especially prone to large rainfall variability: depending on the inland expansion of the WAM system, the Sahel is either situated in the region of deep convection or it is affected by large-scale subsidence of dry air belonging to the circulation of the ITF.
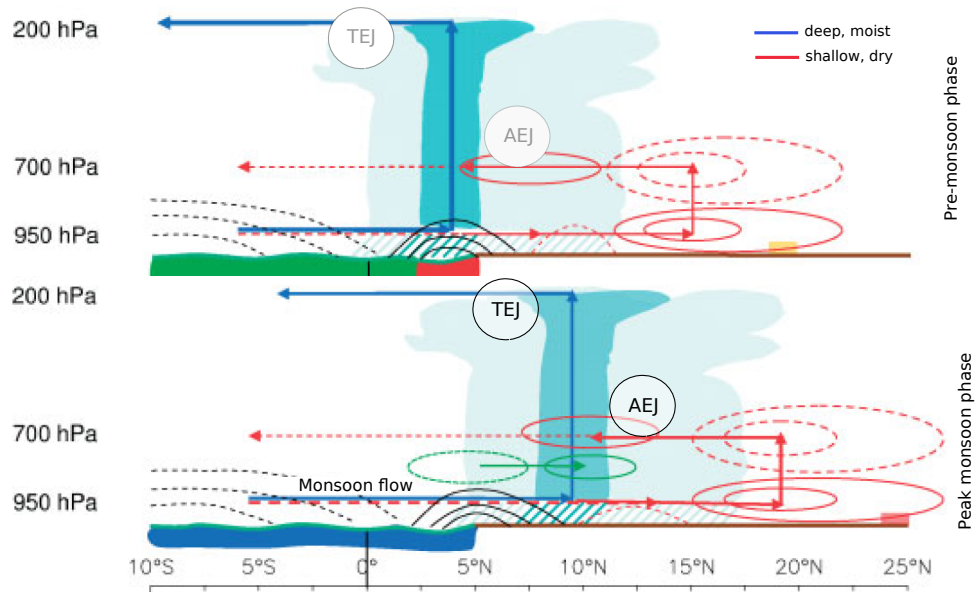
Figure 2.3: Schematic cross section of the WAM with position of atmospheric features during the pre-monsoon phase (April-June) and the peak monsoon phase (July-September) with the TEJ and the AEJ with the grey color indicating less pronounced jet streams. The yellow (weaker) and red (stronger) bar in the North indicates the SHL. Warmer (green to red) and cooler (blue) sea surface temperatures are also depicted. Solid lines mark convergence zones while dashed lines mean divergence. Adapted from Thorncroft et al. (2011), their Fig. 12.
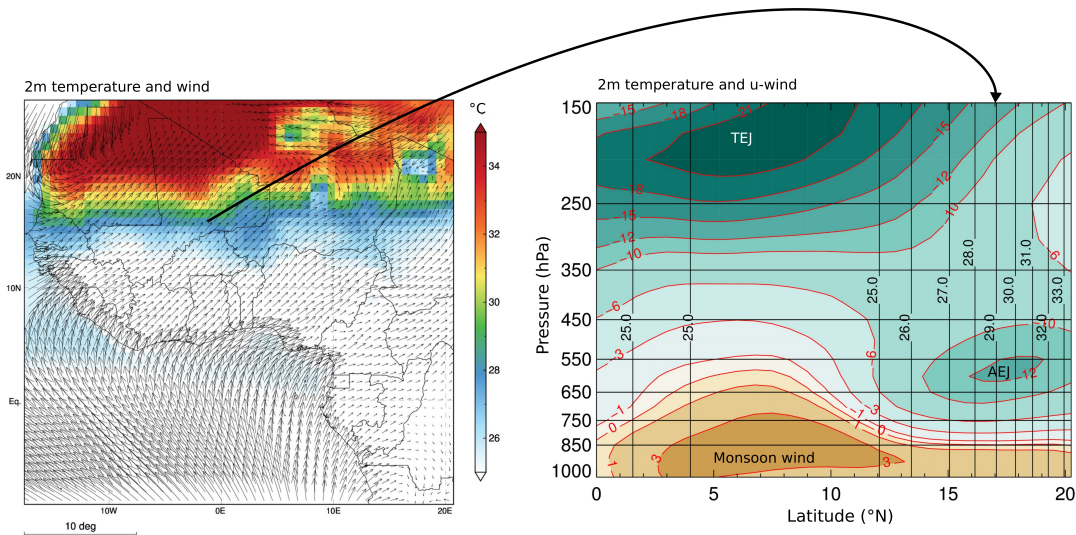
Figure 2.4: Example of August 1999 2m temperature (Global Historical Climatology Network) with ERA-Interim reanalysis wind $(\mathrm{m\,s}^{-1})$ (*left*) and the crossection of latitudinal averages ($10°$W-$10°$E) of the u-wind component $(\mathrm{m\,s}^{-1})$. Vertical black lines indicate the latitudinal position of the 2m temperature in steps of $1°$C (*right*). The arrow depicts the position of the largest temperature gradient.

2.2 Teleconnections

The main modes of WAM precipitation variability are known to be closely linked to teleconnections with SSTs (e.g. Giannini et al., 2005; Douville et al., 2007; Paeth and Friederichs, 2004). However, the exact contribution of any particular ocean and related atmospheric oscillations is often difficult to ascertain due to the large number of competing physical mechanisms and drivers acting on different time scales (Nicholson, 2013).

There is a well documented non-stationary interannual relationship between anomalies of tropical SSTs and WAM precipitation: from 1900 until the 1970s, the correlation of WAM rainfall and tropical Pacific SSTs was found to be slightly negative but insignificant (e.g. Camberlin et al., 2001; Janicot et al., 2001). For the same time period, warm

Figure 2.5: Schematic cross section of the revised picture of the WAM during the peak season (August) with all governing atmospheric features after Nicholson (2013).

anomalies of the tropical Atlantic (also called the Atlantic Equatorial Mode or the Atlantic Niño, Lutz et al., 2015) were identified to cause a significant southward shift of the WAM precipitation, leading to wetter conditions (positive correlation) at the Guinea Coast and drier conditions (negative correlation) in the Sahel ('dipole situation') (Losada et al., 2010).

Until then, Atlantic SSTs seemed to have a stronger relationship with WAM precipitation than Pacific SSTs. Since the 1970s however, the correlation of Sahel rainfall with Atlantic SST became extremely weak while it grew stronger with Pacific SSTs, significantly relating negative (positive) precipitation anomalies to El Niño (La Niña) events. GCM experiments revealed that this is caused by the interference of the effect of the two tropical basins combined with the frequent co-occurence of Atlantic Niños and Pacific La Niñas since the 1970s. By imposing anomalies on only one tropical basin at a time, Losada et al. (2012) were able to reproduce the known dipole situation for warm Atlantic SSTs and the increase of WAM precipitation for cold Pacific SSTs. They found the sum of these independently produced rainfall anomalies closely corresponding to a third simulation with prescribed anomalies in both basins. They concluded a primarily linear response of WAM precipitation to tropical SST anomalies that is relatively stationary over time for each *single* basin, which was also suggested in other studies (e.g. Joly et al., 2007; Mohino et al., 2011; Rodríguez-Fonseca et al., 2011).

A further factor for interannual variability is the Mediterranean sea, showing positive correlations between SSTs and Sahel rainfall (Rowell, 2003). However, Camberlin et al. (2001) point out that the interannual relationships are further complicated by slow decadal SST changes, either globally or of single basins.

For example, the Atlantic Multidecadal Oscillation (the average temperature of the North Atlantic) shows a positive correlation with low-frequency Sahel rainfall variations on a temporal scale of 30-50 years (Rodríguez-Fonseca et al., 2011). In the Pacific, the Pacific Decadal Oscillation describes a phenomenon where the extratropical Pacific Ocean remains in an El Niño-like state over decades, imposing drier conditions over the Sahel, which was the case in the last two decades of the 20th century (Mantua and Hare, 2002; Rodríguez-Fonseca et al., 2011).

Proposed mechanisms by which SSTs ultimately affect WAM rainfall are for example the weakening of the inter-hemispheric temperature gradient (Atlantic Niño) favouring a southward shifted ITF (Hoerling et al., 2006), an increased moistening of the Harmattans favouring moisture convergence and rainfall over the Sahel (warm Mediterranean sea) or an anomalous Walker-type equatorial circulation over the Atlantic leading to less moisture advection and large-scale subsidence over West Africa (El Niño) (Janicot et al., 2001).
The current state of knowledge on the impact of SSTs on WAM rainfall at different time scales was recently summarized by Rodríguez-Fonseca et al. (2015).

2.3 The role of the surface

The land surface is the link between the incoming solar radiation and the transfer of this energy back into the atmosphere, which is described by the surface energy balance

$$R_{net} = SW_{in}(1 - ALB) + LW_{in} - \epsilon\sigma \, TS^4 = LH + SH + G, \tag{2.1}$$

where SW_{in} and LW_{in} are the incoming shortwave (Wm^{-2}) and longwave radiation (Wm^{-2}) and ϵ, σ and TS are the surface emissivity, the Stefan-Boltzmann constant and the surface temperature (K), respectively. The left-hand side of this equation represents the budget of incoming and outgoing solar radiation and gives the available net radiation R_{net} (Wm^{-2}) at the ground. The net radiation is balanced by outgoing fluxes of latent heat (LH, Wm^{-2}), sensible heat (SH, Wm^{-2}) and the ground heat flux (G, Wm^{-2}).

Both sides of this equation are directly affected by the surface: surface conditions determine the albedo (e.g. bare light soil vs. dark vegetation), surface temperatures (e.g. wind speed adjustment due to surface roughness, evaporation) and the partitioning between latent, sensible and ground heat flux (e.g. vegetation, wet/dry soil, soil type). Therefore, the surface can considerably modify the energy budget of the overlying atmosphere and in which form, as sensible or latent heat, this energy actually enters the atmosphere. The partitioning of the turbulent fluxes of heat and moisture foster convection in different ways: The SH flux increases planetary boundary layer

(PBL) temperatures and leads to PBL growth while the LH flux provides moisture to the PBL and helps to lower the lifted condensation level where clouds start to form (Findell and Eltahir, 2003). Furthermore, while the SH flux directly warms the lower troposphere, LH is released in the mid and high levels making it the dominant source of energy for tropical deep convection (Goosse, 2015).

Interactions between the land surface and the atmosphere take place on a wide range of spatio-temporal scales. Surface features may vary over scales of a few metres up to continental scales and may affect the evolution of the atmosphere on a temporal scale of days to decades (Zheng and Eltahir, 1998). However, generally, land-atmosphere interactions were found to play a minor role under strong synoptic forcing (strong advection) (Eltahir, 1998; Ferguson and Wood, 2011) or for soils that are saturated/at the wilting point (Seneviratne et al., 2010), rising the question which conditions actually favour the interaction.

Koster et al. (2004) identified regions of the world where strong gradients of soil moisture, vegetation and surface temperature prevail as especially prone to surface-atmosphere feedbacks. West Africa, and especially the semi-arid Sahel, is such a transition zone between wet and dry regimes, where surface anomalies have the potential to affect precipitation distributions. Several studies propose different governing process chains that link surface heterogeneities to precipitation depending on the spatio-temporal scale that is looked at (e.g. Taylor et al., 2011b, their Table 1). For example, mesoscale horizontal circulations induced by differential heating between wet and dry patches can generate moist updrafts that trigger deep convection (Anthes, 1984; Wang and Eltahir, 2000; Emori, 1998). On local scales, the surface specific partitioning of net radiation into latent and sensible heat fluxes contributes to spatial variations in PBL growth and moistening, which sets the conditions for potential convection (Kohler et al., 2010).

However, favourable surface and atmospheric conditions first have to coincide in order to actually produce a feedback. Therefore, the persistence of surface heterogeneities is an important factor for the probability that the atmosphere actually reaches a state that is sensitive for surface conditions within the time that the surface anomaly prevails (Dirmeyer, 2006). If either atmospheric or surface conditions are not favourable, no feedback can occur.

Framework for the dynamical downscaling experiments

In this thesis, a LAM is used to investigate the interaction of regional processes with the West African monsoon system. LAMs are used to simulate only portions of the Earth (e.g. the West African subcontinent) by *dynamically downscaling* information from global datasets: At its boundaries, a LAM is usually driven by atmospheric forcing data of coarser scale, either derived from a GCM or from reanalysis data (Section 3.1), which is often referred to as the LAM being *nested* into the coarser-scale surroundings. This has the advantage that for the same computational expense, LAMs can be run at higher horizontal resolutions over the region of interest ($\sim$1-50 km) as compared to GCMs whose resolution often ranges between 100 to 300 km.

In this context, the *horizontal resolution* refers to the grid size of the model: The partial differential equations that describe the continuous field of the atmospheric flow need to be discretized to be numerically solvable. One possible approach is to 'put the atmosphere in boxes' (cf. Fig. 3.1) between which the equations can be approximated by finite differences (Mesinger and Arakawa, 1976). The model solves the equations at specific locations of a regular Cartesian grid that are separated by a spatial step Δx (Goosse, 2015). Therefore, it is only able to explicitly resolve atmospheric phenomena that are of considerably larger size than Δx (Thunis and Bornstein, 1996), which explains the frequent application of high-resolution LAMs.

However, the LAM performance is known to be sensitive to potential biases in the forcing data (Rockel et al., 2008). The ultimately added value of a LAM simulation, in spite of such biases, therefore depends on its ability to produce higher resolved, physically-based spatial details of the observed atmospheric patterns compared to the coarser forcing datasets, i.e. to dynamically downscale atmospheric features (Paeth et al., 2011).

This improvement is on one hand related to a higher resolution of surface characteristics in the model such as topography, coastlines, vegetation, soil moisture, rivers and lakes. On the other hand, it emerges from the LAM's ability to better capture mesoscale atmospheric phenomenons (e.g. MCSs and thunderstorms, fronts, low-level jets and land/sea breezes) and related processes (e.g. turbulence, convection), which are either crudely simulated or have to be parameterized in GCMs.

The added value by utilizing LAMs is largest over complex terrain, where an increased detail in the representation of mountain ranges and valleys results in a more realistic simulation due to strong

Figure 3.1: Schematic of a nested LAM with information from the larger scales depicted as arrows. Adapted from (Stensrud, 2009).

orographic forcing (Feser et al., 2011). The resolution advantage might be less obvious over relatively flat terrain like in West Africa.

However, most convective phenomena also fall into the mesoscale from 2-200km (e.g. Thunis and Bornstein, 1996). Since convection is the dominating process for the generation of precipitation during the WAM, the correct representation of convective processes and of surface characteristics that could foster convection are important small-scale factors, which are therefore evaluated in detail in Chapter 5 and 6, respectively.

3.1 Boundary conditions

In this thesis, the LAM is purely used for a *'refinement of the past'* at seasonal to interannual scales meaning that no predictions or projections are conducted. Instead, the LAM is continuously provided with available information on the past state of the atmosphere from a *global reanalysis dataset* at its lateral and surface boundaries. This allows to conduct LAM experiments on the WAM system with a 'perfect' external driver, as opposed to a GCM. Another advantage is that the model results can actually be compared to observational data for validation.

The *reanalysis* procedure merges all available observations of the past (e.g. radiosoundings, weather stations, radar, satellites) with a short-range GCM forecast from a previous *analysis* time to produce a superior state estimate of the atmosphere in space and time (Saha et al., 2010). The results are spatio-temporally coherent, gridded fields of variables: some of which were directly constrained by observations (e.g. temperature, wind) and others that were mostly unknown because no observations exist and are therefore pure model products (e.g. soil moisture, evaporation). The main difference between atmospheric analyses and reanalyses is that the former were created to serve as initial condition for subsequent real-time forecasting.

Only fast available observations are used in the analysis data assimilation system and methods

or model are changed if this promises any improvement in the forecasts. Reanalyses on the other hand are revisited analyses from the past with assimilated non-realtime observations and, more importantly, with a temporally uniform analysis strategy that should prevent e.g. artificial trends (Trenberth et al., 2008; Bengtsson, 2004). Reanalyses usually span several decades and are therefore a precious data archive for any kind of climate research of the past.

Nevertheless, it should be noted that regionally, there can be large differences between different reanalysis products (Decker et al., 2012; Lorenz and Kunstmann, 2012; Cook and Vizy, 2015; Siam et al., 2013) and temporal inconsistencies can still emerge from changes in the observation systems or from model biases (Rienecker et al., 2011; Trenberth et al., 2001). Therefore, although reanalyses might represent 'the best known state of the atmosphere', they should not be blindly trusted.

3.2 Internal model variability

Although the results of atmospheric models are based on deterministic equations, they exhibit a sensitive dependence on initial conditions due to the non-linear chaotic nature of the climate system. This death sentence for any long-term weather forecasting was first discovered by the pioneer of chaos theory, Edward Lorenz (1963), who demonstrated that any deterministic nonperiodic (turbulent) flow is unstable with respect to modifications, even of small amplitude. This means that a parts per thousand difference in the initial conditions or during subsequent calculations (e.g. due to numerical uncertainties; Freitas, 2002) between two otherwise identical model simulations perturbs all following model solutions and leads to a considerable divergence of the model results after some integration time steps, which is called the internal model variability.

Nevertheless, the statistics of different model simulations can remain similar because of existing boundary conditions (e.g. SST) imposed on the model (Shukla, 1998). Boundary conditions prescribe the internal model variability to a certain range of possible states, which is why climate projections with imposed increasing CO_2 concentrations allow the detection of increasing global mean surface temperature (a reproducible, forced variability) in spite of intrinsically unpredictable temperature fluctuations on small time scales (an unreproducible, internal variability) (Knutti and Hegerl, 2008; Goosse, 2015). Similarly, a LAM cannot completely diverge from its boundary forcing, but it can generate its own weather that exhibits internal variability. This is especially critical for regional analyses at high temporal resolutions, since the day-to-day model solution is strongly influenced by this variability with a strong effect on e.g. the spatio-temporal occurrence of heavy precipitation events (Giorgi and Bi, 2000).

Consequently, when utilizing a LAM or any other kind of atmospheric model, the experimental modelling set-up and/or the analysis strategy should always consider the internal model variability in order to avoid a misinterpretation of the internal variability as a response to a forcing.

3.3 Ensemble approaches

Ensembles consist of a suite of simulations either produced with several models (GCM/LAM) and/or by using ensembles of perturbed initial conditions or model parameterizations. Ensemble approaches help to quantify uncertainties in the model results (the modelled response to a forcing) through the ensemble spread (e.g. Knutti and Hegerl, 2008). They are also useful to attribute uncertainty to different model components and to natural or internal model variability (Tebaldi and Knutti, 2007; Teutschbein and Seibert, 2010; Murphy et al., 2004).

With respect to the applicability of LAMs over West Africa, ensemble approaches can help to reduce uncertainties in the simulation of WAM characteristics and variability (Sylla et al., 2013). Research initiatives like the Coordinated Regional Downscaling Experiment (CORDEX, Giorgi et al., 2009) Africa aim at satisfying the demand for standardized LAM simulations over the West African region with diverse models, which facilitates a joint analysis of model performance and uncertainties.

Here, parameterization (Chapter 4) and perturbed initial condition (Chapter 6) ensembles are used to evaluate the uncertainty in the representation of the WAM introduced by moist physics and to ensure that an identified land-atmosphere interaction signal is larger than internal model variability, respectively.

3.4 Regional adjustment

LAMs are used to simulate only specific parts of the world, which allows them to take into account regional peculiarities as opposed to GCMs. For example, parameterizations usually do not work similarly well for every region on Earth since they were often adapted to reproduce an observed process in a specific region (Stensrud, 2009). While for a GCM, a 'global compromise' has to be found, a LAM can be regionally optimized.

In this thesis, the adjustment includes for example the evaluation of parameterization combinations that produce reasonable results in the study region (Chapter 4), to take into account increased aerosol concentrations (Section 3.5.5), to use model resolutions that allow the explicit treatment of convection (Chapter 5) or to adjust land surface parameters to better match the actual surface conditions in West Africa (Section 3.5.6, Chapter 6).

3.5 The Weather Research and Forecasting model

The WRF model is a non-hydrostatic LAM that was originally designed for numerical weather prediction but was gradually extended to fulfil the needs of regional climate research alike. Its development is an open source project with a large and active community but is mainly coordinated between the National Center for Atmospheric Research (NCAR), the National Center for Environmental Prediction (NCEP), the Forecast Systems Laboratory, the Air Force Weather Agency and the Oklahoma University.

Certain WRF systems and extensions are also suitable for data assimilation, for atmospheric chemistry or hydrological research, which however will not be discussed here. The WRF model is free to download[1].

3.5.1 Technical background

The WRF software package has grown extremely large and consists on one hand of the dynamical solver, in this case the Advanced Research WRF, and on the other hand of various model physics that come in more or less independent modules. The WRF code is entirely written in parallelized Fortran90/95.

The schematic in Fig. 3.2 illustrates how the different parts of WRF intertwine. Details on the following descriptions of the dynamical core and different model physics can be found in (Skamarock et al., 2008) and references therein. Detailed information on exact software requirements, installation and the manifold WRF options is given in the WRF user guide (NCAR, 2015).

Dynamical core
Here, the heart of the WRF model is the ARW dynamical core[2] where the Euler equations with the integration of moisture are solved (Skamarock et al., 2008). This set of equations approximates the atmospheric motion by describing the spatio-temporal evolution of the zonal, meridional and vertical wind velocities (u,v,w), pressure, temperature, specific humidity and density and constitutes of:
(i) the continuity equation representing the conservation of mass (and moisture)
(ii) the conservation of momentum for each velocity component u,v,w
(iii) the conservation of energy
(vi) the ideal gas law, giving the relationship of pressure, density and temperature
(see e.g. Goosse, 2015, pp. 85 for details)
The dynamic solver also handles diffusion[3] and the spatial and temporal discretization.

---

[1] http://www.mmm.ucar.edu/wrf/users
[2] *WRFV3/dyn_em/module_big_step_utilities_em.F*
[3] *WRFV3/dyn_em/module_diffusion_em.F*
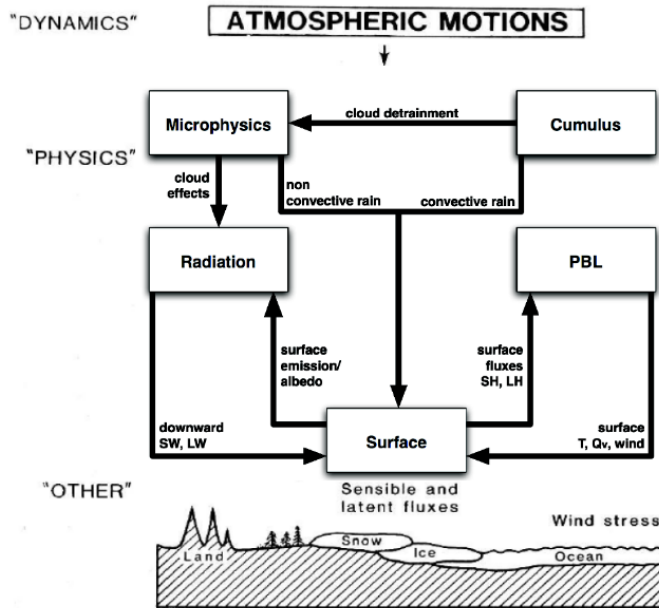
Figure 3.2: Schematic of the main WRF components and their interconnections. Adapted from (NCAR, 2015).

Discretization

The spatial discretization takes place on an Arakawa-C staggered horizontal grid with the velocity vectors u,v,w being calculated at the centres of the left/right, front/back, bottom/top grid cell faces, respectively. These vectors are positive for westerly, southerly and upward winds.

All other variables are calculated at the mass points at the center of each grid cell box (Skamarock et al., 2008).

On this grid, the vertical coordinate (η) is terrain-following and uses the hydrostatic pressure to define a horizontal model layer that coincides with the grid cell mass points:

$$\eta = \frac{P_h - P_h(top)}{P_h(bottom) - P_h(top)},\tag{3.1}$$

where P_h is the hydrostatic pressure at an arbitrary elevation, $P_h(top)$ denotes the value at the model top (can be chosen and is fixed) and $P_h(bottom)$ is the hydrostatic pressure surface value. Therefore, η ranges from 0 (top) to 1 (bottom) (Skamarock et al., 2008).

For temporal discretization, the 3rd order Runge-Kutta integration scheme[1] is used.

---

[1] *WRFV3/dyn_em/solve_em.F* and the related time-stepping routines

Parameterizations

WRF is only able to explicitly resolve atmospheric phenomena that are larger than its grid resolution. Even at a horizontal resolution of 1 km, there are processes that have an effect on the atmosphere, but cannot be 'seen' by the model, e.g. small cumulus clouds or turbulence. For example, turbulence could be explicitly resolved only when applying WRF in a large eddy simulation set-up at < 200 m (e.g. Moeng et al., 2007).

In this context, a parameterization is a translation of the effect of an 'unseen' sub-grid process to the scale that is resolved by the model. Another reason why parameterizations are necessary is the fact that not all physical processes are yet sufficiently understood to be implemented by exact physical laws (e.g. cloud microphysics) but can be described by empirical laws. A further argument for a parameterization is the pure simplification of otherwise extremely complex processes, rendering their explicit implementation computationally too expensive.

The most recent WRF version 3.7.1 allows a total of about 78 different parameterization schemes to include the effects of

- Cloud microphysics: water phase changes, resolved cloud and precipitation processes

- Short- and longwave radiation: external solar forcing including absorption, reflection and scattering in the atmosphere and the surface; infrared and thermal radiation absorbed and emitted by gases and surfaces

- Convection (cumulus parameterization): sub-grid scale effects of clouds and shallow and deep convection (vertical transport of heat and moisture)

- Surface physics (the LSM): calculates the turbulent surface fluxes of sensible and latent heat with respect to the given radiative forcing and precipitation

- Surface layer: interface between LSM and atmosphere, where friction velocities and exchange coefficients are calculated

- Turbulence (planetary boundary layer) scheme: vertical fluxes due to eddy transport

Figure 3.2 gives an overview on the links between the different parameterizations[1] in WRF and in which direction information is passed on (NCAR, 2015). Several parameterization schemes provide detailed options[2] that have to be chosen for each simulation in the *namelist.input*[3] configuration file.

---

[1] *WRFV3/phys*
[2] *WRFV3/run/README.namelist*
[3] *WRFV3/run/namelist.input*

Nesting strategies

The technique of *nesting* a high-resolution grid into a coarser grid is not only a common technique for implementing a LAM into a global dataset but it can also be used within the same LAM. This is necessary if the resolution of the global dataset is too coarse to be directly downscaled to the target model resolution (Chapter 5). According to Denis et al. (2003), the resolution jump should not exceed a factor of 12 to ensure a realistic relaxation of the finer to the coarser grid.

Generally, two nesting strategies are available with WRF: one- and two-way nesting. Driving WRF with a global dataset inevitably represents a one-way nesting, meaning that information of the coarse grid enters the WRF domain, but WRF cannot give a feedback to the global scales. The same approach may be used when a higher resolution WRF domain (also called the *child*) is nested into a coarser resolution WRF domain (also called the *parent*): the parent feeds the child domain, but does not get back any information from the child.

Between two WRF domains, two-way nesting would be an alternative, which refers to an information exchange in both directions. It is in principle more realistic than one-way nesting since it accounts for the possibility that small-scale perturbations lead to changes at the larger scales. This is especially important for global scale impact studies with GCMs. However, when using reanalysis data, which is supposed to represent the large scales as realistic as possible (already including potential effects of the small scales), the sense of two-way nesting is debatable since it might lead to a larger divergence of WRF from the 'perfect' forcing data (Lorenz and Jacob, 2005). Furthermore, two-way nesting creates artefacts in the parent domain where the boundaries of the child are located, rendering the parent simulation unusable. Therefore, only one-way nesting is used here.

3.5.2 Baseline set-up

For all experiments in this thesis, WRF is driven by the European Center for Medium range Weather Forecasting (ECMWF) Re-Analysis-Interim (ERA-I) data (Dee et al., 2011) at its lateral boundaries (temperature, u/v wind, geopotential height, relative humidity, pressure). ERA-I also provides data for the lower boundaries in form of SST and estimates for soil moisture and temperature. All boundary conditions are provided every 6 hours at a resolution of 0.75°.

Previous experiments with the Climate Forecast System Reanalysis (Saha et al., 2010) at 0.5° worsened the simulation of WAM rainband characteristics. In addition, Siegmund et al. (2015) reported deficiencies of WRF to capture the rainband movement when driven with the Climate Forecast System real-time forecast version 2. Other reanalysis products were excluded due to considerably coarser resolutions (e.g. NCEP Reanalysis 2 at 2.5°). By now, the Modern Era Restrospective-Analysis for Research and Applications (MERRA, Rienecker et al., 2011) product at 0.5° would be another interesting alternative to ERA-I, but was relatively new and not thoroughly tested when the presented experiments were conducted.

As a baseline set-up, WRF version 3.5.1 is used in an 'out of the box' state for climate simulations given in the WRF user guide (NCAR, 2015). This includes the Noah LSM (Chen and Dudhia, 2001) with the 21-category Moderate Resolution Imaging Spectroradiometer (MODIS) land-use classification (cf. Appendix A), the Kain-Fritsch cumulus scheme (Kain, 2004), the Yonsei University PBL scheme (Hong and Lim, 2006) and the WRF Single Moment 6 microphysics scheme (Hong et al., 2004). The only difference is that the shortwave radiation scheme by Dudhia (1989) and the Rapid Radiative Transfer Model longwave radiation scheme (Mlawer et al., 1997) are used instead of the Community Atmosphere Model radiation scheme options. The latter provided extremely dry conditions in the WAM region during test simulations.

Surface information for broadband black-sky albedo, leaf area index and vegetation fraction are taken from climatological values available for the region from the WRF pre-processing system (Section 3.5.3, see Table 6.1 for references). Static classification maps for land use (dominant vegetation type) and dominant soil types are used to read the corresponding values for e.g. soil moisture capacity, root depth or surface roughness length from fixed tables[1] provided by WRF. These maps also identify the location of lakes, whose temperature is interpolated from SST per default. Here, the average of surrounding surface temperatures is used for lake surface temperatures instead, as described in the WRF user guide (NCAR, 2015), to avoid extremely cold inland lake temperatures. All static terrestrial lower-boundary conditions, including topography, are part of the pre-processing package.

3.5.3 Data processing and visualization

WRF pre-processing system
The WRF software comes with a whole data pre-processing system (WPS) consisting of different programs that facilitate the conversion of lateral and surface boundary data into a format that WRF is able to read. In Fig. 3.3, the WPS work flow is illustrated consisting of the programs:

- ungrib.exe: extracts global input data from gridded binary files to be readable by *metgrid*.

- geogrid.exe: Defines the domain position and extent, horizontal model resolution and interpolates static terrestrial information onto the WRF grid for all nests such as land use and soil maps, topography, albedo, vegetation fraction etc.

- metgrid.exe: Horizontally interpolates the global data extracted by *ungrib* onto the WRF grid and combines it with the terrestrial data.

The result of WPS are *metgrid* files in the temporal resolution of the global input data (here: 6-hourly). Finally, *real.exe* is the WRF-ARW data pre-processor and reads the WPS *metgrid* files to vertically interpolate the information onto all vertical WRF levels. It provides files for the initial state and the (6-hourly) surface and lateral boundary conditions for WRF.

---

[1] *WRFV3/run/*: SOILPARM.TBL, LANDUSE.TBL, VEGPARM.TBL
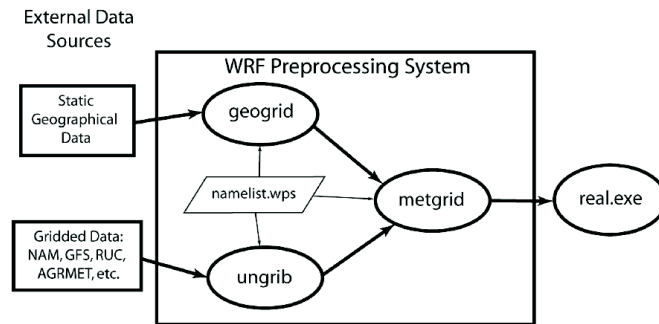
Figure 3.3: Data flow between the programs of the WRF pre-processing system (NCAR, 2015).
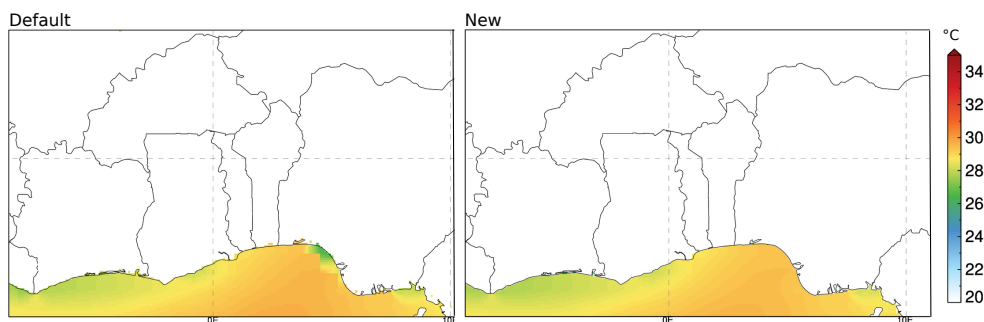
Figure 3.4: Metgrid interpolated ERA-I SST for 15-03-1999 for the default and new interpolation (see text) to a horizontal resolution of 10 km.

Interpolation at coastlines

There are various options for the horizontal interpolation of variables in the *metgrid* configuration table that can make an important difference, especially for the interpolation of SST close to coastlines.

Senatore et al. (2014) found for WRF simulations conducted in the Mediterranean that certain interpolation approaches might produce artefacts in the SST field that considerably affect rainfall patterns close to the coast. The interpolation technique along the coastline has to be able to cope with masked values and therefore to cope with a reduced number of available values surrounding the point to be interpolated since land pixels have to be excluded.

By default, WRF uses a sixteen points parabolic (*sixteen_pt*) or four point bi-linear (*four_pt*) interpolation method that do not handle masked points (NCAR, 2015). In case of the ERA-I data, these approaches indeed lead to artefacts at the coast in the north-eastern part of the Gulf of Guinea (cf. Fig. 3.4, left). Several performed tests gave a smoothly interpolated coastline (Fig. 3.4, right) with the following entry for SST interpolation in the *metgrid* configuration table substituting the old entry below:

WRFV3/WPS/metgrid/METGRID.TBL, line 531 and following
# New
name=SST
interp_option=sixteen_pt+four_pt+wt_average_4pt
interp_mask=LANDSEA(1)
masked=land
missing_value=-1.E30
fill_missing=0.
flag_in_output=FLAG_SST

Default
name=SST
interp_option=sixteen_pt+four_pt
fill_missing=0.
missing_value=-1.E30
flag_in_output=FLAG_SST

The list of interpolation options (*interp_option*) is tested for applicability one after another. Since with the new entry, the land-sea mask from ERA-I is defined as interpolation mask (*interp_mask*) with the land masked out, *metgrid* will use the last interpolation method (*wt_average_4pt*) that can handle masked values when they are encountered along the coast. This third interpolation method creates a weighted average of all *valid* points surrounding the point to be interpolated.

Generally, it is advisable to always check the *metgrid* interpolation results in the WRF lower boundary file[1] before starting a WRF simulation.

Data post-processing and visualization
WRF output is usually spread over several files to avoid too large single files. For convenient data analysis, each single variable in the WRF files is extracted and merged temporally to obtain one single file over the analysis period for each variable, which is realized with netCDF operators implemented in Linux bash scripts.

Here, the interpolation of 3D-variables from η to pressure levels (1000, 975, 925, 900, 850, 800, 750, 700, 650, 600, 550, 500, 450, 400, 350, 300, 250, 200, 150, 100, 75 hPa) is directly performed by WRF by using the pressure level diagnostics (*p_lev_diags*) option in the *namelist.input*.

The 3-hourly to hourly single-variable files are additionally aggregated to daily and monthly files. This aggregation step and all visualizations in this thesis are performed with the Interactive Data Language (IDL) with the latter based on the Coyote Graphics library by David Fanning[2].

---

[1] *wrflowinp**
[2] http://www.idlcoyote.com/documents/programs.php

3.5.4 Computing environment

Since WRF simulations are computationally expensive and computing time on any high performance computing system is usually limited, the question may arise whether model simulations can be spread over different computing systems. The computing systems in question are most likely not identical but differ in hardware components, number of threads (the number of simultaneously executed processes) or the installed compilers, among other. This can lead to numerical differences (e.g. round-off errors) in the WRF simulations.

Experimental set-up
To test the margin of the uncertainty in simulated rainfall amounts that is induced by numerical errors, an identical case-study is conducted on four different computing systems with the WRF configuration described in Chapter 3.5.2 for April 1999 with one month of spin-up time. The domain extent is shown in Fig. 3.5 and encompasses the whole WAM region at a resolution of 24 km. In addition, the margin of numerical errors within the Volta basin ($\sim$400,000 km^2) is analysed as a test case for the impact at a large catchment scale.

Tested system differences
Besides for different computing systems, the reproducibility of the WRF simulation is also tested for varying numbers of threads (nb_threads) and different compiling optimizations[1] (opt) on the same system as well as with or without adaptive time stepping[2] (ats).
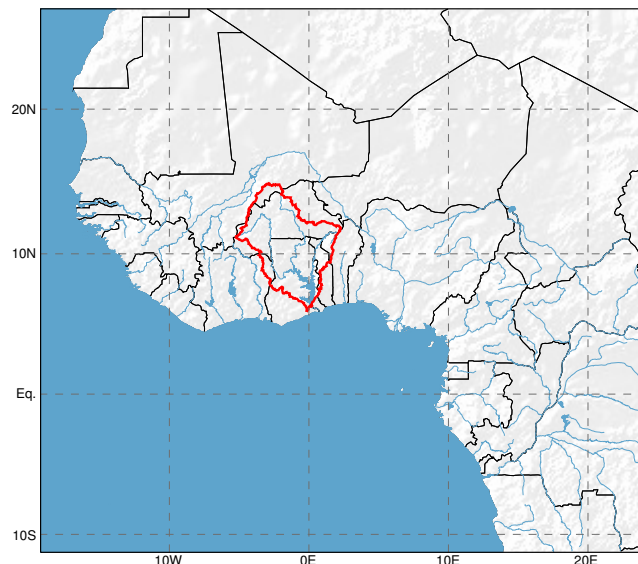
Figure 3.5: Extent of the WRF domain and the Volta basin (red)

---

[1]Optional, compiler specific optimizations for the interpretation of the WRF source code that can ultimately speed up the model and therefore shorten the simulation time

[2]Instead of being fixed, the model time step is variable allowing longer time steps (less computations) if stability criteria are not violated, which speeds up the simulation (Hutchinson, 2007)

Three high performance computing systems and one workstation are used for the experiment:

- "Linux Cluster" of the Leibniz Computing Centre (Leibniz Rechenzentrum, **LRZ**), Munich: MPP Cluster, Intel compiler, 178 nodes, 64 threads per node

- "Blizzard" of the German Climate Computing Centre (Deutsches Klimarechenzentrum, **DKRZ**), Hamburg: IBM Power6 , IBM (AIX) compiler, 264 nodes, 64 threads per node

- "Kea" (**KEA**) of the Institute of Meteorology and Climate Research, Karlsruhe Institute of Technology, Garmisch-Partenkirchen: Intel Sandy Bridge (Intel Xeon Processor E5-2643), Intel compiler, 10 nodes, 16 threads per node

- Linux workstation (**WS**) of the Institute of Meteorology and Climate Research, Karlsruhe Institute of Technology, Garmisch-Partenkirchen: Intel i7-3630QM (quad-core), gfortran compiler, 1 node, 8 threads per node

The conducted experiments are summarized in Table 3.1. The set-ups for the experiment *same* constitute the baseline set-ups for each system. The last column *identical* indicates whether the two simulations compared in the experiment provide exactly identical results (*yes*) or not (*no*). In the case of experiment *comp_sys*, four simulations (DKRZ, KEA, LRZ, WS) are compared.

Table 3.1: Conducted comparison experiments on the same computing system with: identical configurations (same), a different number of threads (nb_threads), with or without compilation optimization (opt), with or without adaptive time stepping (opt). In addition, the reproducibility between completely different computing systems (comp_sys) is tested. A *yes* for *identical* means that the simulation was reproduced for the compared experiments. Overall, six simulations were conducted on each computing system. For details on the computing systems, see text.

Test case	System	ats_1	opt_1	nb_threads1	ats_2	opt_2	nb_threads2	identical
same								
	DKRZ	yes	yes	128	yes	yes	128	yes
	KEA	yes	yes	12	yes	yes	12	yes
	LRZ	yes	yes	128	yes	yes	128	yes
	WS	yes	yes	8	yes	yes	8	yes
nb_threads								
	DKRZ	yes	yes	**128**	yes	yes	**64**	yes
	KEA	yes	yes	**12**	yes	yes	**24**	**no**
	KEA	yes	**no**	**12**	yes	**no**	**24**	yes
	LRZ	yes	yes	**128**	yes	yes	**64**	**no**
	LRZ	yes	**no**	**128**	yes	**no**	**64**	yes
	WS	yes	yes	**8**	yes	yes	**4**	yes
opt								
	DKRZ	yes	**yes**	128	yes	**no**	128	**no**
	KEA	yes	**yes**	12	yes	**no**	12	**no**
	LRZ	yes	**yes**	128	yes	**no**	128	**no**
	WS	yes	**yes**	8	yes	**no**	8	**no**
ats								
	DKRZ	**yes**	no	128	**no**	no	128	**no**
	KEA	**yes**	no	12	**no**	no	12	**no**
	LRZ	**yes**	no	128	**no**	no	128	**no**
	WS	**yes**	no	8	**no**	no	8	**no**
comp_sys								
	ALL	no	no	8-128	-	-	-	**no**

Simulation differences

Overall, the experiments in Table 3.1 reveal that the WRF simulations are not reproducible on different computing systems, even if no compiling optimization or adaptive timestepping is used (*comp_sys*). However, the simulations are always identical when just repeating a simulation (identical configuration) on the same system (*same*).

The picture is more complicated when a different number of threads is used on the same computing system (*nb_threads*), where DKRZ and WS never show a change in simulation results, but KEA and LRZ show differences if a compiling optimization is used. This could be specifically related to the Intel compiler, which is used on both systems. Only when no optimization is used, KEA and LRZ are able to reproduce the simulation with any number of threads. The experiments for compiling optimization (*opt*) and adaptive time stepping (*ats*) finally show that a change in these options always leads to different simulation results on the same computing system.

Figure 3.6 illustrates that for non-identical simulations, the difference of monthly average rainfall shows spatially random patterns for all the test cases and frequently reaches over ± 100 mm month^{-1} per grid cell.
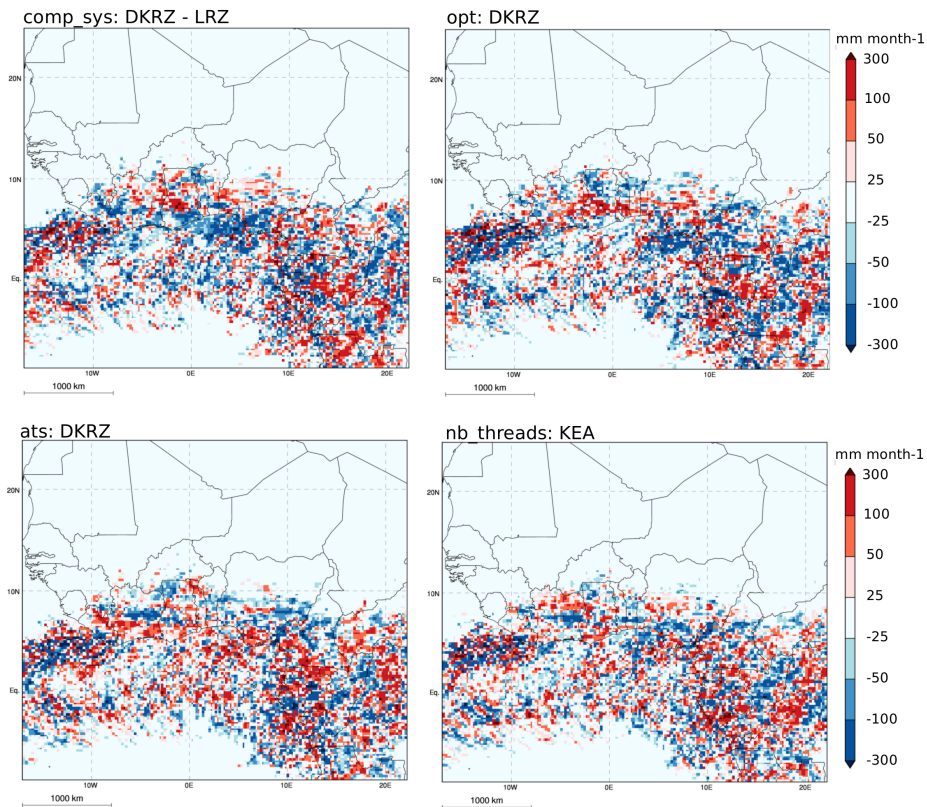
Figure 3.6: Examples of April 1999 rainfall differences for: DKRZ and LRZ (comp_sys), compilation optimization on/ off for DKRZ (opt), adaptive time stepping on/ off for DKRZ (ats) and a different number of threads with opt on for KEA (nb_threads).

Table 3.2 summarizes the monthly precipitation averages of the different simulations for the whole WRF domain and for the Volta basin: While for the domain average, the maximum difference in precipitation amounts remains small ($\sim$3 mm month^{-1}), it reaches about 19 mm month^{-1} in the Volta basin, which corresponds to a standard deviation (SD) of $\pm$ 6 mm month^{-1} or to a relative SD (RSD) of $\pm$ 6 % with respect to the average modelled rainfall of 96 mm month^{-1} during April. The relative SD remains comparable even if only the DKRZ machine is considered, indicating that the numerical error introduced on one machine by compiler or computational options (*opt/ats*) is about the same as the numerical error between different machines. The maximum rainfall difference for the Volta basin average on a specific day for DKRZ is 15 mm day^{-1}, basically reflecting the effect of a displaced convective event.

Table 3.2: Overview of April 1999 average rainfall (Mean, mm month^{-1}) and its range (maximum-minimum, mm month^{-1}), standard deviation (SD, mm month^{-1}) and relative SD (RSD, %) over the whole WRF domain and over the Volta basin (cf. Fig. 3.5). To separate the effect of a completely different computing system, *all* includes all conducted simulations while *DKRZ only* includes only test simulations that were run on the DKRZ machine. Only simulations that are different from each other are considered.

	Number	Mean	Range	SD	RSD
Domain					
all	14	93.01	3.07	0.94	1.01
DKRZ only	4	92.73	1.27	0.71	0.76
Volta basin					
all	14	96.12	18.88	5.98	6.22
DKRZ only	4	99.40	12.50	6.32	6.36

Reproducibility of model results

Generally, the WRF output is not reproducible on different computing systems. Neither is it reproducible on the same system when changing the compilation optimization or the adaptive timestep option in WRF. If compilation optimization is used, even a change in the number of computing nodes might perturb the simulation on some systems, as shown for KEA and LRZ.

The variations between the simulations in this experiment represent the error margin inherent to numerical modelling that ultimately emerges from a combination of rounding errors and discretization errors i.e. the approximation of a continuous system by a finite length. Hong et al. (2013) found the system dependency of simulations to be comparable to the internal model variability induced by minimal perturbations / different initial conditions (cf. Section 3.2). They point out that simulations from different systems can adequately be used to increase the number of members for ensemble approaches working with perturbed initial conditions.

Usually, numerical errors are regarded as negligible since the induced differences are much smaller than other uncertainties, for example from model parameterizations (Freitas, 2002). Nevertheless, the above findings have critical implications for the experimental set-up of analyses that rely on pointwize comparisons, for example with weather station data but also for catchment-scale hydrological studies. The uncertainty however decreases when averaging larger spatio-temporal scales as shown in Table 3.2 when comparing the results for the Volta basin (RSD$\approx$6%) with the domain average (RSD$\approx$1%).

For practical reasons, all following experiments in this thesis were computed on the DKRZ machine Blizzard with compiling optimization and adaptive time stepping turned on. While this assigns the same numerical error to all following simulations and makes virtually similar simulations indeed identical, it does not mean that internal model variability can be ignored when using the same computing system and model set-up. On contrary, the model response to a forcing can only be trustworthy if the extracted signal is significantly larger than the model variability induced by small perturbations. Therefore, ensemble approaches are used in this thesis to ensure a robust signal detection (Chapter 4 and 6).

3.5.5 Cumulative radiation and atmospheric scattering

By WRF default settings, long- and shortwave radiation of the Dudhia radiation scheme as well as latent, sensible and ground heat fluxes are provided as instantaneous values only. This leads to an error in the temporal averages of the continuous variables and in the identification of extreme values, especially if model output is written at 3-hourly intervals only, as is done in Chapter 4 and Chapter 5. Therefore, all radiation and surface flux variables were redefined to be cumulative variables for the Noah LSM in the LSM driver. The exemplary formulation in Fortran for accumulated incoming shortwave radiation reads

WRFV3/phys/module_surface_driver.F, subroutine: surface_driver, line 2624 and following

```
DO j=j_start(ij),j_end(ij)
DO i=i_start(ij),i_end(ij)
  IF (PRESENT(ACSWDOWN))ACSWDOWN(I,J)=ACSWDOWN(I,J)+SWDOWN(I,J)*DT
ENDDO
ENDDO
```

where SWDOWN is the array of instantaneous values (W m^{-2}) and DT is the model time step (seconds). SWDOWN is accumulated in ACSWDOWN (J m^{-2}) for every model time step and every i,j coordinate in the model domain.

The effect of this formulation for incoming shortwave radiation with *hourly* model output in August 2013 at 24 km horizontal resolution is shown in Fig. 3.8. The instantaneous approach (WRF_def) shows higher values until 13h with the maximum one hour too early at noon when compared to the cumulative approach (WRF_cum). The latter is in phase with the diurnal cycle obtained from three WASCAL Eddy Covariance (EC) stations (Appendix B) situated at the border of Ghana and Burkina Faso (Fig 3.7). This confirms a more realistic representation of the incoming shortwave radiation.

In conclusion, the advantage of cumulative instead of instantaneous radiation and flux variables is the general independence of model output intervals to derive exact temporal averages, which better matches the high-frequency flux and radiation measurements of EC stations.
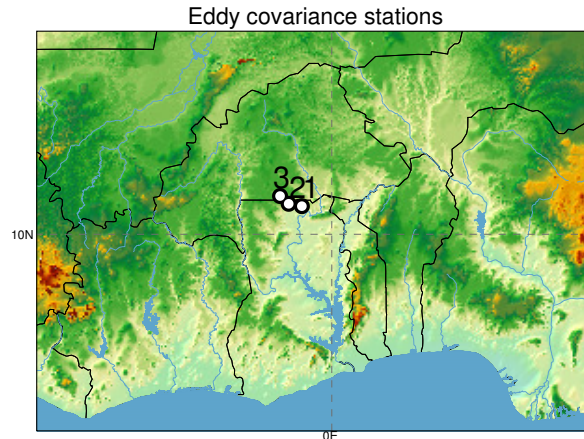
Figure 3.7: Positions of the WASCAL EC stations in **(1)** Sumbrungu (Ghana), **(2)** Kayoro (Ghana) and **(3)** Nazinga (Burkina Faso).

The same should be kept in mind for other WRF variables that are instantaneously provided, such as temperature, humidity or wind speed. To be able to compare WRF output with frequently measuring weather stations, it should either be written at an hourly basis or the WRF *output_diagnostics* option in the *namelist.input* should be used. This option automatically provides averages and minimum/maximum values for various variables over a defined time period, e.g. daily, which was used here.

Adjustment of the atmospheric scattering

The comparison between the EC stations and WRF_cum in Fig. 3.8 shows an overestimation of incoming solar radiation by WRF with the baseline set-up (Section 3.5.2). This bias is especially problematic because the incoming shortwave radiation is the external forcing, the 'engine', for our modelled system. The overestimation of incoming solar radiation leads to an exaggeration of available energy in the climate system subsequently affecting all other processes.

Indeed, first experiments with WRF in the framework of this thesis involved testing its behaviour with different parameterizations for shortwave radiation revealing a much larger model sensitivity to this choice than to any other parameterization tested later on. This is in line with other WRF studies over West Africa (Li et al., 2014) and East Africa (Pohl et al., 2011), where the largest uncertainty in model results is attributed to the radiation physics.

Large differences exist in how the radiation parameterizations treat clouds (resolved and unresolved), which probably has some part in this uncertainty. In addition, only certain WRF parameterization combinations (e.g. Thompson microphysics, RRTMG shortwave scheme, NCAR, 2015) take aerosols into account, which are not used here. Therefore, the lacking representation of the dusty SAL could be one reason for the positive radiation bias in Fig. 3.8.
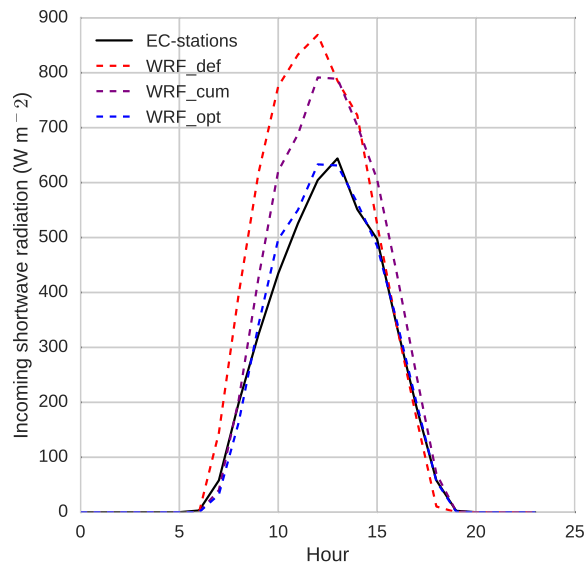
Figure 3.8: Average diurnal cycle of incoming shortwave radiation at hourly resolution during August 2013 for the EC station mean (EC-stations) and WRF for the default approach with instantaneous radiation (WRF_def), the cumulative approach (WRF_cum) and the optimized solar radiation with adjusted optical depth (WRF_opt). For comparability, only the 24x24 km WRF grid cells that enclose the three EC station positions are chosen and averaged.

Other WRF compartments could be tuned to cancel out this bias but this would mean to optimize the model to work with an originally faulty energy source. Therefore, it makes sense to first of all adjust the incoming shortwave radiation to make sure that it is, on average, in an acceptable range.

The Dudhia scheme allows an adjustment with a scattering tuning parameter[1] that can be set at runtime in the *namelist.input*. Figure 3.8 illustrates the result of this tuning: by default, the parameter is set to 1 (WRF_cum, 10% scattered) and was raised to 3 (WRF_opt, 30% scattered) after different experiments. This implicitly takes into account the increased effect of aerosols in this region and leads to a better correspondence to the EC measurements. However, the parameter changes scattering homogeneously and is not able to represent a meridional gradient in dust concentrations, leaving a positive bias over the Sahara (cf. Fig. 5.10).

---

[1] *swrad_scat*

3.5.6 Implementation of remote-sensing data

In this thesis, new satellite-derived surface variables are implemented into WRF (see Chapter 6 for details on these datasets). For this, the static climatological surface variables for albedo, leaf area index (LAI) and vegetation fraction as well as the existing land use map from *geogrid* need to be substituted. For implementation, the *metgrid* files are rewritten with an IDL routine to include the updated variables.

Surface variable overview

There are various WPS and WRF surface variables, some of which need to be externally updated for the implementation of new surface information. Table 3.3 summarizes the affected variables with their names in the *metgrid* (WRF input[1]) files. Most surface information in the *metgrid* files originally stems from the terrestrial information provided by *geogrid* except for VEGCAT, which is provided from the global forcing dataset, if available (extracted by *ungrib*).

Table 3.3: Overview of WPS/WRF variables that play a role for implementing new albedo, vegetation fraction, LAI and land use information. The names corresponding to a certain variable in *metgrid* and in the WRF input files is given. The *source* indicates the program that creates the variable. The variables are only taken into account by WRF if the corresponding *namelist.input option* is set to the value given here.

Metgrid	WRF input	Source	Namelist.input option	Description
ALBEDO12M	ALBBCK	geogrid	usemonalb= .true.	Monthly albedo climatology (12 months)
GREENFRAC	VEGFRA	geogrid	sst_update=1	Monthly vegetation fraction climatology (12 months)
LAI12M	LAI	geogrid	rdlai2d=.true.	Monthly leaf area index climatology (12 months)
LU_INDEX	LU_INDEX	geogrid	surface_input_source=3	Dominant land use category
VEGCAT	VEGCAT	ungrib	surface_input_source=2	Dominant land use category
LANDUSEF	LANDUSEF	geogrid	surface_input_source=1	Fractional land use category
-	SHDMAX	real	-	Maximum climatological vegetation fraction
-	SHDMIN	real	-	Minimum climatological vegetation fraction
-	IVGTYP	real	-	Dominant land use category

---

[1] *wrflowinp*, wrfbdy*, wrfinput**

Substitution of the land use classification map

To include the new land use classification map, the functions of the *surface_input_source* option in the *namelist.input* is used: WRF contains three different variables for the dominant land use category (cf. Table 3.3) and handles an additional variable for fractional land use (percentage of land use class per grid cell). The *surface_input_source* option determines which of these variables are read by WRF by distinguishing between three cases[1] :

- surface_input_source=1: the *fractional* land use information (LANDUSEF) from geogrid is used. The dominant land use category is recomputed by the *real* program[2] (IVGTYP). All other existing dominant land use variables (LU_INDEX, VEGCAT) are overwritten by IVGTYP.

- surface_input_source=2: the global driving dataset provides a dominant land use map that was read by *ungrib*. If such a variable was available from the global dataset, and only then, the VEGCAT variable exists in the *metgrid* files. In this case, VEGCAT overwrites LU_INDEX and IVGTYP.

- surface_input_source=3: the *dominant* land use information (LU_INDEX) from *geogrid* is used and is *not* recomputed by the *real* program. In this case, LU_INDEX overwrites VEGCAT and IVGTYP.

By default, WRF uses option 1. With this option, a new land use map will be overwritten if it is only implemented as LU_INDEX or IVGTYP (or both). The *real* program changes both variables to the default land use map using LANDUSEF.

Therefore, the way to externally define a dominant land use map and to prevent it from being overwritten is to declare it as 'LU_INDEX' in the *metgrid* files and to set 'surface_input_source=3'.

Here, the *real* program is used for computing the dominant land use map in order to apply the same procedure for defining a dominant class with both, the default and the new land use map. Therefore, fractional land classes of the new land use map (native resolution of 250 m) are externally computed at WRF resolution to form an array of the dimensions *[X x Y x 21]*. In this case, X and Y are the dimensions of the WRF domain and 21 represents the number of MODIS land use classifications (see Annex A), which is used throughout this thesis and for which corresponding surface parameters can be found in WRF tables[3].

---

[1] */WRFV3/dyn_em/module_initialize_real.F*

[2] */WRFV3/share/module_soil_pre.F* ; SUBROUTINE process_percent_cat_new

[3] */WRFV3/run/LANDUSE.TBL* and */WRFV3/run/VEGPARM.TBL*: the LSM reads the LANDUSE.TBL first, but any value is overwritten afterwards by VEGPARM.TBL if there is an overlap in variables.

Substitution of climatological surface parameters

To implement new fields for albedo, vegetation fraction and LAI, they have to be mapped to the WRF grid and can then substitute the existing variable arrays in the *metgrid* files. However, the variables are expected to be of *[X x Y x time]* dimension, where *time* has twelve entries for the default annual climatologies. The subsequently called *real* program uses these climatologies to:

- compute the climatological maximum (SHDMAX) and minimum (SHDMIN) vegetation fraction for each grid point. This information is later used by the LSM to e.g. approximate the surface emissivity.

- linearly interpolate the monthly values to the chosen time step in which the boundary information is updated (here: 6-hourly).

The *real* routine for the temporal interpolation of the surface variables only handles monthly data. Therefore, this interpolation has to be done externally for new surface datasets of higher temporal resolution. Here, an IDL routine is used to interpolate 10-daily values to the targeted 6-hourly values. To bypass the interpolation of the *real* program, the interpolated 6-hourly value field is written twelve times into the corresponding *metgrid* file to form the expected *[X x Y x 12 months]* array. Like that, the interpolation from *real* takes place but has no effect. Furthermore, SHDMAX and SHDMIN are also externally derived from climatological monthly means for the available time period (2007-2012, cf. Chapter 6) and each grid cell. A step further would be to make these variables interannually dynamic.

To avoid the necessity of defining new variables in various WPS routines, SHDMAX and SHDMIN are introduced via the already existing variable names SOILCAT and VEGCAT as 'vehicles'. The computation of the monthly climatological min/max values by the *real* program (*monthly_min_max*) is changed to be called only if the configuration flag in the *namelist.input* (config_flag) is set to *surface_input_source=1*:

WRFV3/dyn_em/module_initialize_real.F, line 1128 and following

```
IF ( config_flags%surface_input_source .EQ. 1 ) THEN
        CALL monthly_min_max ( ... )
ELSE
        DO j = jts , MIN(jte ,jde −1)
          DO i = its , MIN(ite ,ide −1)
              grid%shdmax(i,j) = grid%vegcat(i,j)
              grid%shdmin(i,j) = grid%soilcat(i,j)
              grid%vegcat(i,j) = 0
              grid%soilcat(i,j) = 0
END DO
END DO
ENDIF
```

Else, SHDMAX and SHDMIN are read from the 'vehicle variables' VEGCAT and SOILCAT. *surface_input_source=3* was adjusted to act exactly like *surface_input_source=1*, except that the computation of SHDMAX and SHDMIN by the *real* program is omitted due to the formulation above. The adjusted WRF therefore allows the implementation of new surface variables with *surface_input_source=3* and can still be used with the default climatological datasets with *surface_input_source=1*.

Definition of barren land surfaces

In the Noah LSM, barren land surfaces are defined very strictly with a formulation in

WRFV3/phys/module_sf_noahmplsm.F, line 868

IF (VEGTYP == ISURBAN .**OR**. VEGTYP == ISBARREN) FVEG = 0.0

and *line 1100*

IF (VEGTYP == ISBARREN) .**or**. (VEGTYP == ISURBAN)) **THEN**
    LAI = 0.
ENDIF

meaning that any grid cell classified as 'barren' (VEGTYP == ISBARREN) is defined to have a vegetation fraction (FVEG) and LAI of zero. The marker 'ISBARREN' is set in the VEGPARM.TBL and reads 'BARE 16' in case of the MODIS land use classification used here. This means that the land use classification map overwrites any information from the satellite-derived vegetation fraction/LAI if the particular grid cell is classified as barren.

While this might be acceptable when the vegetation fraction/LAI dataset and land classification map correspond perfectly (which is usually not the case when using datasets from different sources) and indeed match the 'barren' land class description (cf. Appendix A, MODIS: not more than 10% vegetated cover during any time of the year), this is definitely not the case any more after an upscaling. Therefore, the 'barren' class should not force the vegetation fraction/LAI to zero. It also leads to an unrealistically abrupt change between vegetated and less vegetated areas.
The behaviour can be removed, either by changing the VEGPARM.TBL or by recompiling WRF with the formulation above commented out.

Interactions of moist processes with the monsoon system

In the WRF model, many processes affecting how moisture is distributed in the atmosphere have to be parameterized when they are too small-scale to be physically resolved at grid-scale. Different from many other LAMs, WRF incorporates a vast number of physical parameterizations for microphysical processes, for turbulence that vertically transports water vapour or for convection, making it highly adaptable. At the same time, it is challenging to set up the model since such parameterizations are usually a key source of uncertainty, which limits the ability to make robust statements on moist process interactions (Flaounas et al., 2011b). The different formulations in the parameterization schemes change their sensitivity to resolved drivers, potentially leading to process interactions of different intensity. It is well-known that the results of a model can change considerably with the choice of the model physics. With its large number of available parameterizations, the WRF model is ideal to assess this introduced uncertainty.

So far, only a small number of studies applied WRF in the West African region. These studies demonstrate the skill of the WRF model and its predecessor, the Mesoscale Meteorology Model 5 (Grell et al., 1994) in representing specific features of the West African climate (e.g. Vizy and Cook, 2002; Bliefernicht et al., 2013; Hagos and Cook, 2007; Sijikumar et al., 2006), for LAM-based climate projections (Jung and Kunstmann, 2007; Vigaud et al., 2011), for the investigation of tropical storms triggered over the region (Vizy and Cook, 2009; Druyan et al., 2009; Chiao and Jenkins, 2010) and for evaporation tagging (Knoche and Kunstmann, 2013). These studies either simply mention which model parameterizations were employed, or include a pragmatic testing of model physics to minimize the bias against observations. However, they rarely discuss uncertainties introduced by their choice of parameterizations for moist processes.

Flaounas et al. (2011b) conducted a first comprehensive study of the sensitivity of WRF for three convective and two turbulence parameterizations during the WAM 2006. They investigate the behaviour of the tested schemes by analysing their capability in representing surface variables and some dynamical monsoon features. While they indeed identify large differences between model results, they do not evaluate what is causing the differences. Noble et al. (2014) compared AEW occurrences of 64 WRF configurations with those of two reanalysis datasets and radiosonde observations for 12-days time slices over ten years. They give valuable insights into the development of these atmospheric disturbances and reveal deficiencies of the model in reproducing them but likewise do not explain the process interactions that govern the change in model performance.

Accordingly, the goal of this experiment is to use a multi-physics ensemble approach for an uncertainty assessment but also as an analysis strategy to investigate the interaction of moist processes with the WAM system. The different parameterization descriptions are perturbations that allow to investigate to which degree a change in the moist processes is able to provoke changes in the monsoon dynamics and related precipitation. In addition, the multi-physics ensemble will be used to generalize the process-based impact of individual parameterization schemes in the WRF model.

The members of the multi-physics ensemble represent all possible combinations of three schemes per parameterization of cumulus convection (CU), microphysical cloud processes (MP) and planetary boundary layer turbulence (PBL), totalling 27 different CU_MP_PBL combinations. These parameterizations modulate the atmospheric moist processes and thus can be used to indirectly assess the impact of changing moisture distribution on the WAM dynamics, while the large-scale forcing at the domain boundaries remains the same for all simulations (ERA-I). Analysing all possible combinations of parameterizations rather than taking an iterative approach allows to identify the impact of each scheme, since it reveals robust tendencies for changing parameterization partners. This experiment therefore gives insights into the feedback of the WAM system to local and regional moist processes, as represented by the model physics schemes. It can further help to trace back bad model behaviour to a certain process, and suggest which parameterization scheme to change in order to improve the WAM representation in the WRF model.

4.1 Experimental set-up and reference datasets

4.1.1 Model configuration and analysis strategy

The simulations in this experiment are conducted with WRF version 3.5.1. The selected physics schemes should (i) directly be linked to moisture transport and moisture redistribution in the atmosphere, and (ii) differ in complexity or methodology to represent a particular process.

The investigated CU, MP and PBL schemes (see Table 4.1) include the effects of latent heat release through deep and shallow convection, microphysical cloud and precipitation processes, and vertical turbulent mixing due to eddy transports, respectively. The PBL scheme is determining the flux profiles of temperature and moisture within the whole atmospheric column, hence generating tendencies that serve as input for the CU and MP scheme at every model time step. The CU scheme is responsible for releasing instabilities in the atmospheric sounding, preventing the MP scheme from generating potentially unrealistic grid-scale convection. As a side-effect of the redistribution of temperature and moisture towards a stable profile, the CU scheme produces convective precipitation. In a last step, the MP scheme removes excess atmospheric moisture in case the air is still saturated, which will be referred to as non-convective precipitation.

For the CU, MP, and PBL groups, parameterization schemes that follow different approaches to represent the same physical effects are combined. The CU group includes a mass-flux type cloud model (KF), a sounding-adjustment type model (BMJ) and a mass-flux type model based on a stochastic approach, providing an ensemble mean (GF). For the KF scheme, the alternative trigger function (option 2) based on moisture advection was used instead of the default option because of reduced precipitation overestimations in preceding experiments.

The MP schemes used here differ in their classification of hydro-meteors. The WSM3 differentiates between three classes: cloud water/ice, rain/snow and vapour, depending on the temperatures being above or below freezing. LIN and TH take into account all six classes of hydro-meteors: cloud water, cloud ice, rain, snow, vapor and graupel. The more sophisticated TH scheme additionally predicts number concentrations for rain and ice species.

Table 4.1: Cumulus, microphysics and planetary boundary layer schemes used for the ensemble members.

	Abbreviation	References
Cumulus schemes	**CU**	
Betts-Miller-Janjic	BMJ	Janjic (1994), Janjic (2000)
Grell-Freitas	GF	Grell and Freitas (2014)
Kain-Fritsch, convection trigger 2	KF	Kain (2004), Ma and Tan (2009)
Microphysics schemes	**MP**	
Lin Purdue	LIN	Lin et al. (1983)
New Thompson	TH	Thompson et al. (2008)
WRF Single Moment 3	WSM3	Hong et al. (2004)
Planetary boundary layer schemes	**PBL**	
Asymmetrical Convective Model V.2	ACM2	Pleim (2007)
Mellor-Yamada-Janjic	MYJ	Janjic (1994)
Yonsei University	YSU	Hong and Lim (2006)

The PBL schemes can be divided into 1.5th order closure schemes based on prognostic turbulent kinetic energy (MYJ), and schemes which treat the turbulent mixing by a first order closure (YSU, ACM2). While the MYJ only considers local mixing into vertically adjacent grid cells, the YSU and ACM2 schemes consider non-local mixing through large convective eddies. In YSU, this is expressed by adding a counter-gradient term to non-local gradients of heat and momentum. ACM2 changes smoothly from local eddy diffusion in stable environments to combined local (downward fluxes) and non-local (upward fluxes) transport for heat, momentum and moisture components in unstable conditions. Further details about these schemes can be found in the literature listed in Table 4.1 and in Skamarock et al. (2008). All possible combinations of the schemes are included in the multi-physics ensemble, resulting in a total of 27 members. Analyses of the ensemble or sub-ensembles always refer to the mean value.

The model domain as shown in Fig. 4.1 encompasses the entire WAM system and its important features. If not specified otherwise, analyses are carried out for the study region depicted by the black box and for the three sub-regions with the sea masked out. To avoid problems with the convective grey zone ($\sim$4-20 km, Molinari and Dudek, 1992), the model is operated at a medium horizontal resolution of 24 km, with 36 vertical levels and a model top of 50 hPa. The integration time step is 120 s and model results are stored every three hours. The rest of the model set-up corresponds to the baseline configuration in Section 3.5.2.
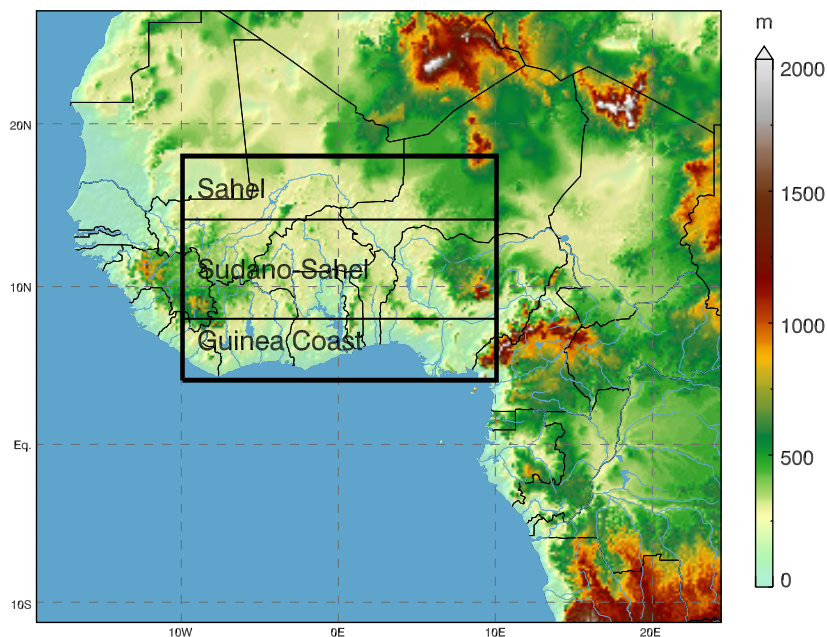
Figure 4.1: WRF model domain and elevation (m) at 24 km horizontal resolution. The study region (10°W–10°E, 4°N–18°N) is depicted by the black box. Sub-regions indicate the humid Guinea Coast (4°N–8°N), the Sudano-Sahel (8°N–14°N) and the semi-arid Sahel (14°N–18°N).
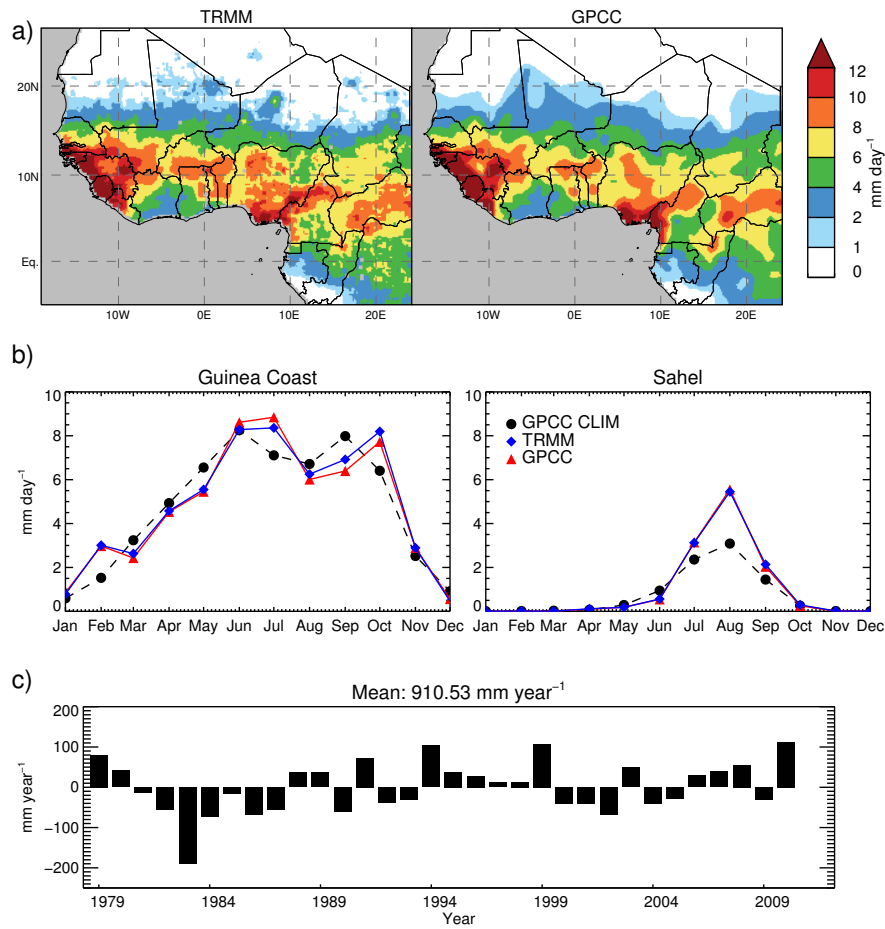
Figure 4.2: **(a)** JAS 1999 average precipitation (mm day^{-1}) for TRMM (left) and GPCC (right) **(b)** Annual cycle of 1999 monthly average precipitation for TRMM and GPCC. In addition, the GPCC climatological mean (GPCC CLIM) for 1979-2010 is given. **(c)** Annual precipitation amounts for the study region with respect to the climatological mean for 1979-2010 from GPCC

Simulation period

The rainy season of the wet year 1999 is simulated from March to September, including one month of spin-up time. This time span covers the two monsoonal phases as described by Thorncroft et al. (2011): the coastal phase from April to June (AMJ), and the continental phase from July to September (JAS). A wet year is chosen to investigate the ensemble spread under a boundary forcing that favours moist conditions to ensure that the monsoon regime simulated by the LAM is not constrained by low incoming moisture fluxes and remote effects that dictate a weak WAM.

The year 1999 is characterized by an extraordinarily wide monsoon rainband with an extended zone of maximum precipitation (Fig. 4.2a). At the same time, an above-average northward transition of the monsoon rainband leads to very wet conditions in the Sahel and the Guinea Coast, as can be seen from Fig. 4.2(b). The year is among the three wettest years in the reference period since 1979 (Fig. 4.2c), for which the ERA-I dataset is available.

4.1.2 Reference Datasets

The model simulations are compared to satellite and observational data in order to evaluate the skills and physical plausibilities of the different model configurations.

Precipitation   For precipitation, the Global Precipitation Climatology Centre (GPCC) 0.5° gridded full data reanalysis product (Schneider et al., 2011) and the NASA Tropical Rainfall Measuring Mission (TRMM) 0.25° resolution 3B42V7 (3-hourly, daily) and 3B43V7 (monthly) rainfall estimates (Huffman et al., 1995, 1997) are used. The GPCC product provides interpolated precipitation fields over the land surface based on a total of ∼64,400 rain gauges globally for the period 1901-2010. TRMM on the other hand is a blended product based on satellite and GPCC gauge reanalysis information for 1998-2015: The 3B42V7 product merges multiple independent precipitation estimates from microwave and infrared sensors of the TRMM satellite. The monthly averages of 3B42V7 are weighted against GPCC to form a monthly best-estimate precipitation rate (3B43V7). The 3-hourly 3B42V7 product is then scaled to match the monthly sums of the 3B43V7 product. The implementation of GPCC into TRMM results in a good agreement of the two dataset in capturing the wet regime at the Guinea Coast and over the Sahel with respect to the climatological mean from 1979-2010 (Fig. 4.2a, b). Thus, the two datasets are not independent but their combination makes the TRMM product more robust: Nicholson et al. (2003a,b) conducted a validation study for the GPCC and TRMM products as well as for non-blended satellite products against a large set of independent gauge data for different years over West Africa. They find largest systematic errors in the satellite-only analyses but also considerable limitations in the gauge-based GPCC product due to the insufficient spatial coverage of considered rain gauges. The 3B43V7 TRMM gauge-merged analysis product on the other hand shows very good agreement with the independent gauge data on monthly to seasonal time scales and averaged over 1° latitude/longitude boxes. This gives some confidence in the performance of TRMM to capture precipitation amounts and patterns of the WAM.

Surface temperatures   Surface temperatures are compared to the Merged Land-Ocean Surface Temperature Analysis product by the National Oceanic and Atmospheric Administration (NOAA). This 5° monthly gridded temperature product is based on the Global Historical Climatology Network (GHCN) Version 3 with about 7,000 locations worldwide (Lawrimore et al., 2011) and will be termed GHCN here. Although this dataset shows consistent results with other datasets for global analyses, the regional validity can strongly vary since it relies on station information only (Vose et al., 2012). The lack of stations renders the interpolated temperature estimates and their patterns very uncertain (cf. Fig. 1.2). Therefore, GHCN is in the first place used to obtain large-scale temperature gradients in this experiment.

Atmospheric dynamics   To address the question to which degree regional processes modify the large-scale patterns, the ERA-I forcing data is taken as reference for the atmospheric dynamics and surface fluxes. Since the surface fluxes of ERA-I are a pure model product, they are not used for validation but merely for a model intercomparison with WRF.

4.2 Precipitation

Seasonality of precipitation

WRF captures the seasonal cycle, as can be seen from the Hovmöller diagrams (Fig. 4.3) for the WRF ensemble mean (ENS) in comparison to TRMM. For both, the area of maximum precipitation from April to June is situated at the coast at about 5°N.

According to Hagos and Cook (2007), the SHL reaches its maximum by the end of June when it is positioned around 20°N, and when the ACT in the Gulf of Guinea is established, which induces a pressure gradient strong enough to trigger the monsoon jump. Here, the date of the monsoon jump is defined as the first occurrence of two consecutive days with rainfall amounts within the 0.9 percentile for the period May-July between 9 -11°N. For TRMM, the monsoon jump takes place on 1st of July, as can be seen in Fig. 4.3 from the extension and subsequent relocation of the precipitation maximum from the coast to $\sim$ 12°N. ENS is also capturing the monsoon jump, although three days earlier. Most ensemble members are able to capture the monsoon jump close to the observed date with a mean absolute deviation (MAD) of 4.3 days and a maximum shift of 16-20 days for three of the members.
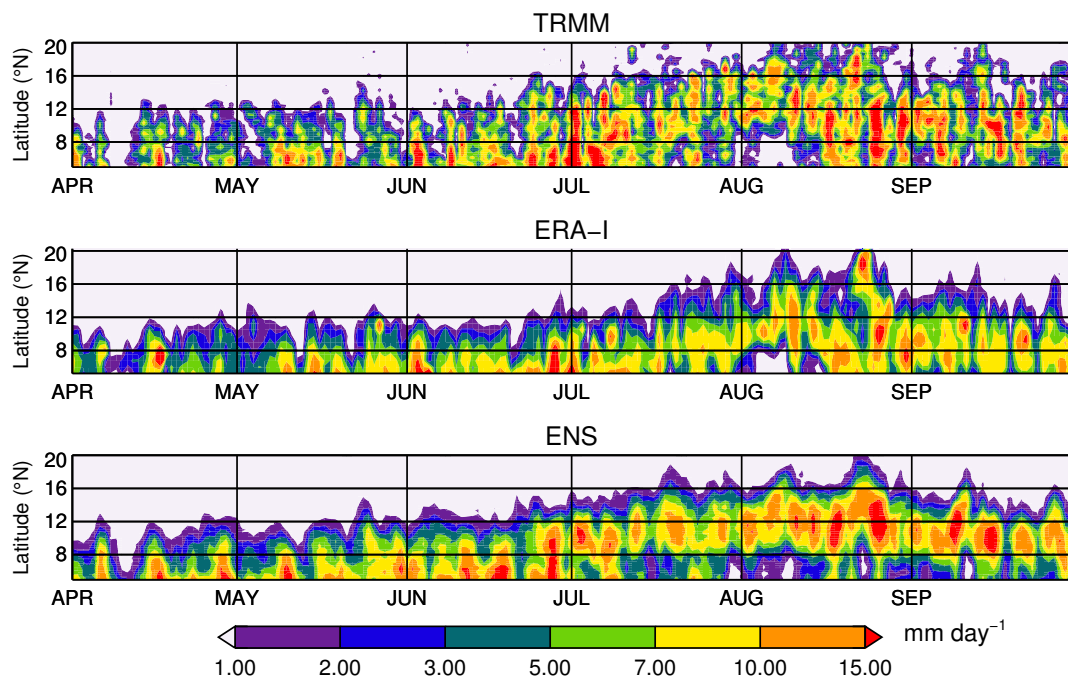
Figure 4.3: Time-latitude Hovmöller diagrams of 1999 daily precipitation for TRMM (*top*), ERA-I (*middle*) and the WRF ensemble mean (ENS, *bottom*)

Intense precipitation events are better represented in ENS than in ERA-I, because of the higher horizontal resolution of WRF. The rainband is slightly shifted to the south over the whole rainy season in comparison to TRMM, but less than for ERA-I. The shift is especially pronounced in August, when the monsoonal rainfall is at its peak and TRMM shows precipitation throughout the whole month in the northern Sahel between 16-20°N, while ERA-I and ENS are not able to capture all of these events. This also applies to all individual ensemble members. The retreat of the rainband to the Guinea Coast sets in by mid-August for TRMM and ERA-I. This movement is delayed in ENS, which results in a too dry coast in the late summer. On the other hand, the observed dry period at the coast during August, i.e., before the retreat of the rainbelt, is not very well represented in ENS, since for some members the rainband remains too far south for the whole period. All ensemble members show a seasonal relocation of the rainband, but strongly differ in the extent, intensity and width, which will be discussed in the following sections.

4.2.1 Spatial distribution of precipitation

In order to reveal the differences in precipitation with respect to certain physics influences, Fig. 4.4 (c) shows the bias against the ensemble mean of the spatial average of JAS precipitation for each of the nine parameterization groups (following the approach of Pohl et al., 2011, their Fig. 16), where one particular scheme is fixed for each group. For example, the KF ensemble consists of the average of the nine simulations that utilize the KF cumulus scheme, and so forth.

The rainband of ENS shown in Fig. 4.4(a) is mostly too narrow with excessive precipitation in its core zone and in Central Africa in comparison to TRMM. A persistent dry bias in the eastern part of the Gulf of Guinea is introduced, which stretches into the continent (Fig. 4.4b). This might be caused by too low SST estimations in this area.

The intensities of the rainbands in Fig. 4.4(c) cover the entire range from dry conditions (ACM2, WSM3) to wet conditions (TH, KF). None of the groups is able to capture the exceptional northward extension of the rainband in 1999, especially visible over Mali, which leads to a dry bias in the northern Sahel. Since this dry bias is also found for ERA-I, one might assume that the bias of the WRF simulations is caused by the bias of the driving data. However, in ERA-I the reason for the dry bias is a shift of the relatively broad rainband to the south, while in WRF it is the small North-South extent of the rainband. For GF and MYJ, the rainband is especially narrow with a daily precipitation of only 1-2 mm at the coast. ACM2 and WSM3 show very low precipitation intensities and induce an overall dry bias. BMJ shows closest rainfall amounts to TRMM, outperforming ENS with more precipitation at the coast and less overprediction in the Sudano-Sahel.
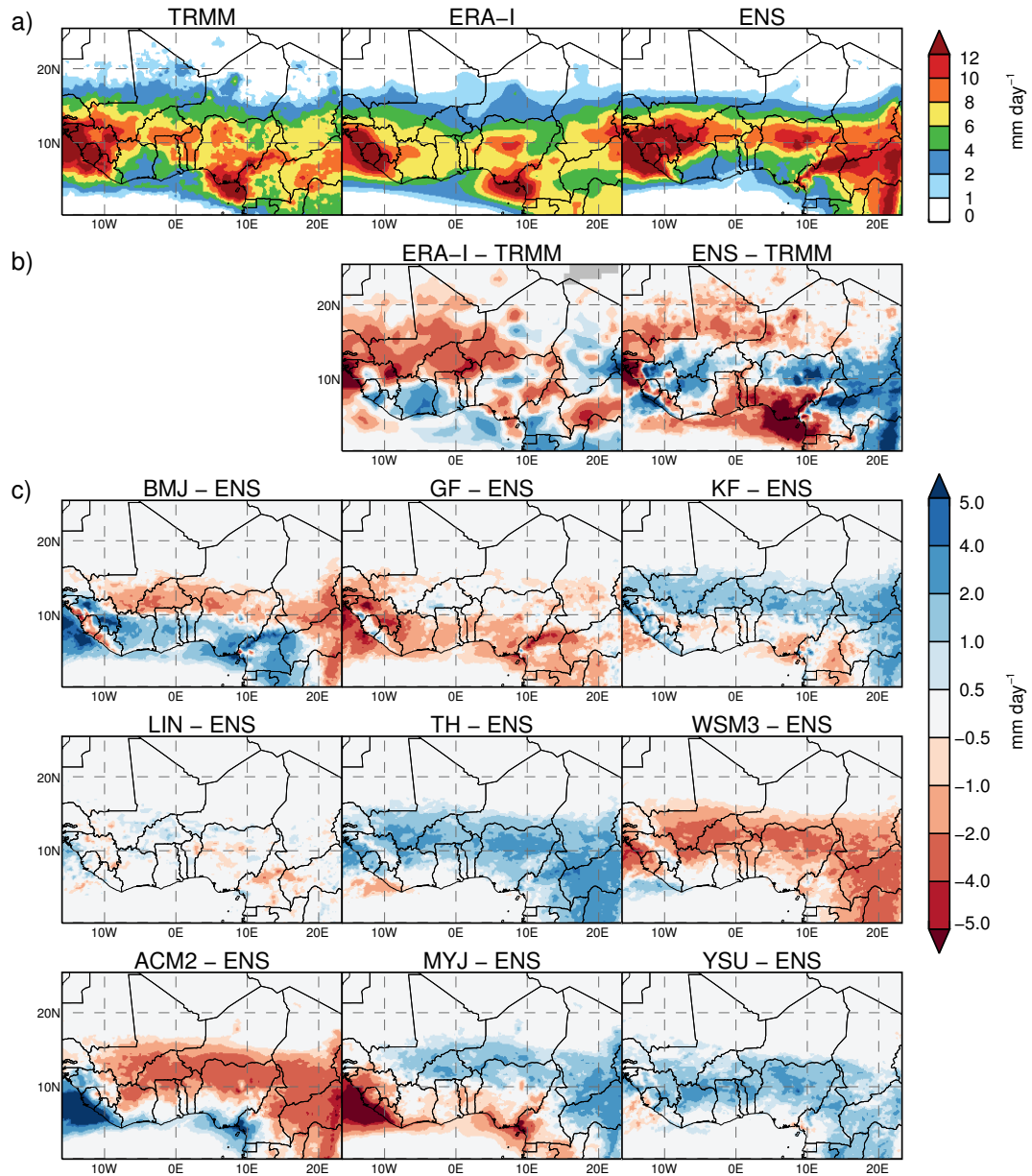
Figure 4.4: JAS 1999 average precipitation **(a)** for TRMM, ERA-I, the ensemble mean (ENS), **(b)** the bias of ERA-I and ENS against TRMM and **(c)** the bias against ENS of each of the nine parameterization groups. Each group consists of nine members using the respective scheme Central

4.2.2 Parameterization influences on rainband intensitiy and position

In the following, the contribution of the three parameterization groups (CU, MP, PBL) to the above-mentioned differences in spatial rainfall distribution is analysed. Figure 4.5 shows boxplots of the parameterization groups, compared to the ensemble mean for the whole rainy season. The spread of the boxes indicates the tendency of a scheme towards a dry or a wet regime. Small boxes imply that the scheme is the dominating factor, since the resulting regime is hardly changed by different configuration partners.
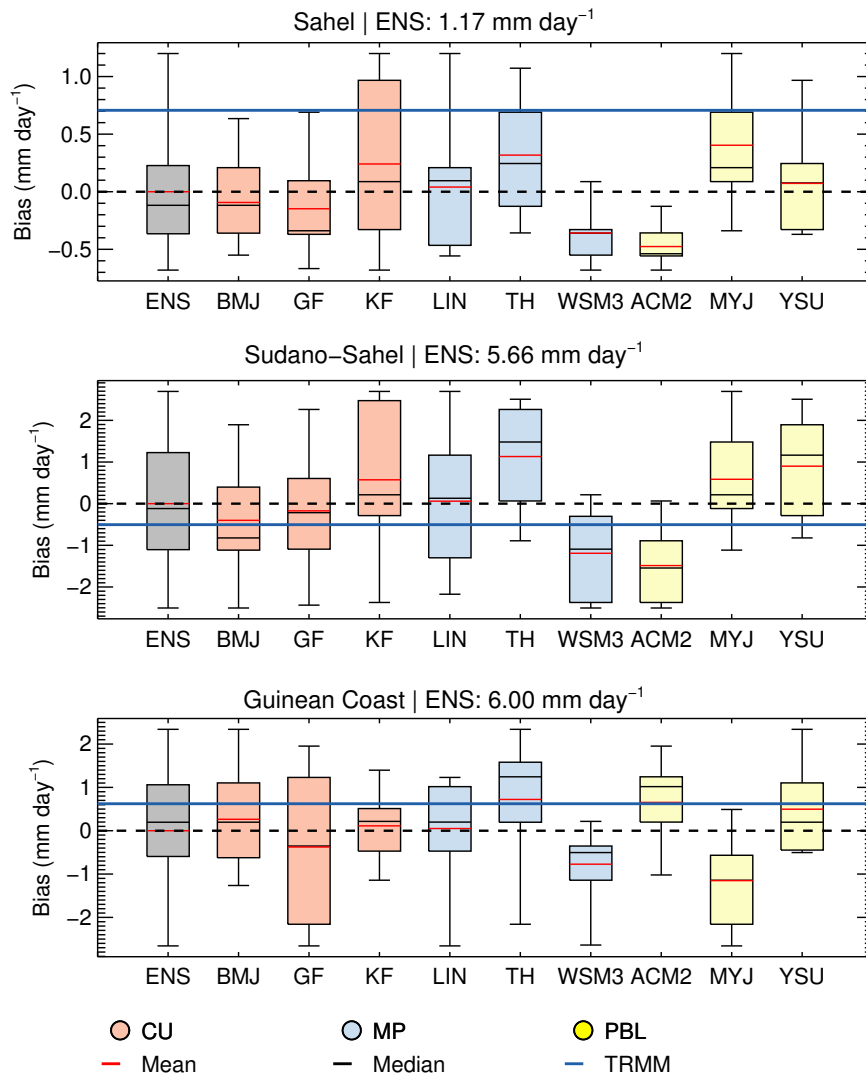
Figure 4.5: Boxplots of the bias in average precipitation from April-September 1999 with respect to the ensemble mean in the Sahel (*top*), the Soudano-Sahel (*middle*) and at the Guinea Coast (*bottom*). The parameterization groups are defined as in Fig. 4.4. The boxes indicate the interquartile range and the whiskers stretch to minimum and maximum values of each group. Blue lines depict the TRMM average precipitation

Differentiated regions are (i) the Guinea Coast, where peak precipitation occurs during the continental phase before monsoon onset, (ii) the Sudano-Sahel, where the center of the rainbelt and thus the precipitation maximum are found after monsoon onset is found, and (iii) the Sahel, where precipitation depends on the northernmost extent of the rainband (Fig. 4.1). With respect to the blue line that indicates the TRMM mean, ENS underestimates precipitation both, at the Guinea Coast and in the Sahel. However, except for the dry parameterization groups WSM3 and ACM2, there is an overestimation in the Sudano-Sahel. The largest bias reaches from -3.5 to 1.7 mm day^{-1} at the Guinea Coast, -2.1 to 3.2 mm day^{-1} in the Sudano-Sahel, and -1.4 to 0.5 mm day^{-1} in the Sahel, indicated by the whisker difference of ENS to TRMM.

The MP schemes show the same overall tendencies for the three regions, with a clear order (TH being the wettest and WSM3 being the driest). The mean precipitation difference between WSM3 and TH is 1.5 mm day^{-1} at the Guinea Coast, 2.4 mm day^{-1} in the Sudano-Sahel and 0.7 mm day^{-1} in the Sahel. Thus, the average intra-ensemble spread induced by the MP schemes is close to the magnitude of the bias to TRMM, which underlines the considerable impact of the MP schemes. Looking at the PBL schemes, the picture is more diverse for the different regions: While MYJ is dry at the Guinea Coast and wet in the Sahel, ACM2 behaves the opposite way. This indicates a shift of the monsoon rainband, dependent on the choice of the PBL scheme. YSU shows an almost as strong northward shift as MYJ, but with much wetter conditions at the Guinea Coast due to a generally wider rainband as can be seen from Fig. 4.4. In terms of northward shift of the monsoon rainband, the order of the PBL schemes is ACM2 < YSU < MYJ. The interquartile ranges of the ACM2 and MYJ parameterization groups do not intersect for any of the three regions, which underlines the opposing impact they have on the position of the rainband. However, the strongest northward shift does not necessarily coincide with largest precipitation amounts: YSU instead of MYJ shows largest values in the Sudano-Sahel, where the core of the rainband is situated.

The CU schemes show the largest interquartile-spreads and on average only weak dry/wet tendencies with respect to ENS. They also show the smallest mean difference in precipitation of only 0.6 mm day^{-1} at the Guinea Coast, 0.9 mm day^{-1} in the Sudano-Sahel and 0.4 mm day^{-1} in the Sahel. This suggests an inferior role for the generation of precipitation in the model. However, this depends on the region: In the Sahel, KF (GF) shows a neutral (restrictive) behaviour, but a restrictive (neutral) behaviour at the Guinea Coast. BMJ dampens the effect of other schemes in both regions, indicated by the consistently smaller inter-quartile spread.

4.2.3 Convective and non-convective precipitation

The ability of an atmospheric model to simulate convective processes is crucial and at the same time a limiting factor for the quality of model precipitation in the tropics and sub-tropics. In the WRF model, precipitation from unresolved deep convection is generated by the CU scheme, while the MP scheme produces grid-scale precipitation in case the air is still super-saturated after the instabilities are released. Thus, the convective fraction of the model is artificial and related to the model resolution. Nevertheless, the partitioning into convective and non-convective precipitation helps to identify the impact of either scheme on the representation of convection.

The amount of non-convective precipitation (Fig. 4.6a) follows the same order found earlier for the MP schemes ($WSM3 < LIN < TH$), with a total spread of 93 mm month^{-1} exceeding the spread of convective precipitation (68 mm month^{-1}). There is no clear correlation between the CU schemes and the amount of convective precipitation. Model configurations with KF or BMJ generate convective precipitation from 40 mm month^{-1} to 110 mm month^{-1}, depending on the choice of MP and PBL scheme, while GF generates less convective precipitation and never exceeds 80 mm month^{-1}. In particular, ACM2 leads to small amounts of convective precipitation for all CU schemes and results in a very dry regime. The impact of a particular CU scheme depends on the chosen PBL scheme and vice versa: for the MYJ PBL scheme, maximum convective precipitation is achieved in combination with KF, while for the YSU and ACM2 PBL schemes, BMJ produces almost consistently the largest amounts of convective precipitation. The mean convective fraction over the whole domain of the individual ensemble members varies between 24-63%, with consistently lower values for ACM2 and higher values for BMJ and YSU configurations.

Figure 4.6(b) illustrates more clearly the sensitivity of precipitation amounts with respect to each parameterization type. Each box consists of the nine precipitation spreads between ensemble members for which only the indicated parameterization type is rotated. For example, one of the nine spreads for CU is computed between [KF_ LIN_ YSU, GF_ LIN_ YSU, BMJ_ LIN_ YSU], another between [KF_TH_ MYJ, GF_TH_ MYJ, BMJ_TH_ MYJ] and so forth.

For non-convective precipitation, CU and PBL schemes show an average spread of about 20 mm month^{-1} compared to $\sim$60 mm month^{-1} for MP, which indicates only minor influence. The average spread in convective precipitation is larger for configurations that differ in their PBL scheme than for those that differ in their CU scheme. However, the large inter-quartile spread of both illustrates their non-linear interplay for the production of convective rainfall. Here, the MP scheme is of minor importance. The sensitivity of total precipitation amounts to the MP and PBL choice is almost equal with average spreads of 67 $\pm$ 13 mm month^{-1} and 62 $\pm$ 11 mm month^{-1}, respectively. The importance of the CU schemes is reduced and highly variable with a spread of 31 $\pm$ 21 mm month^{-1}.
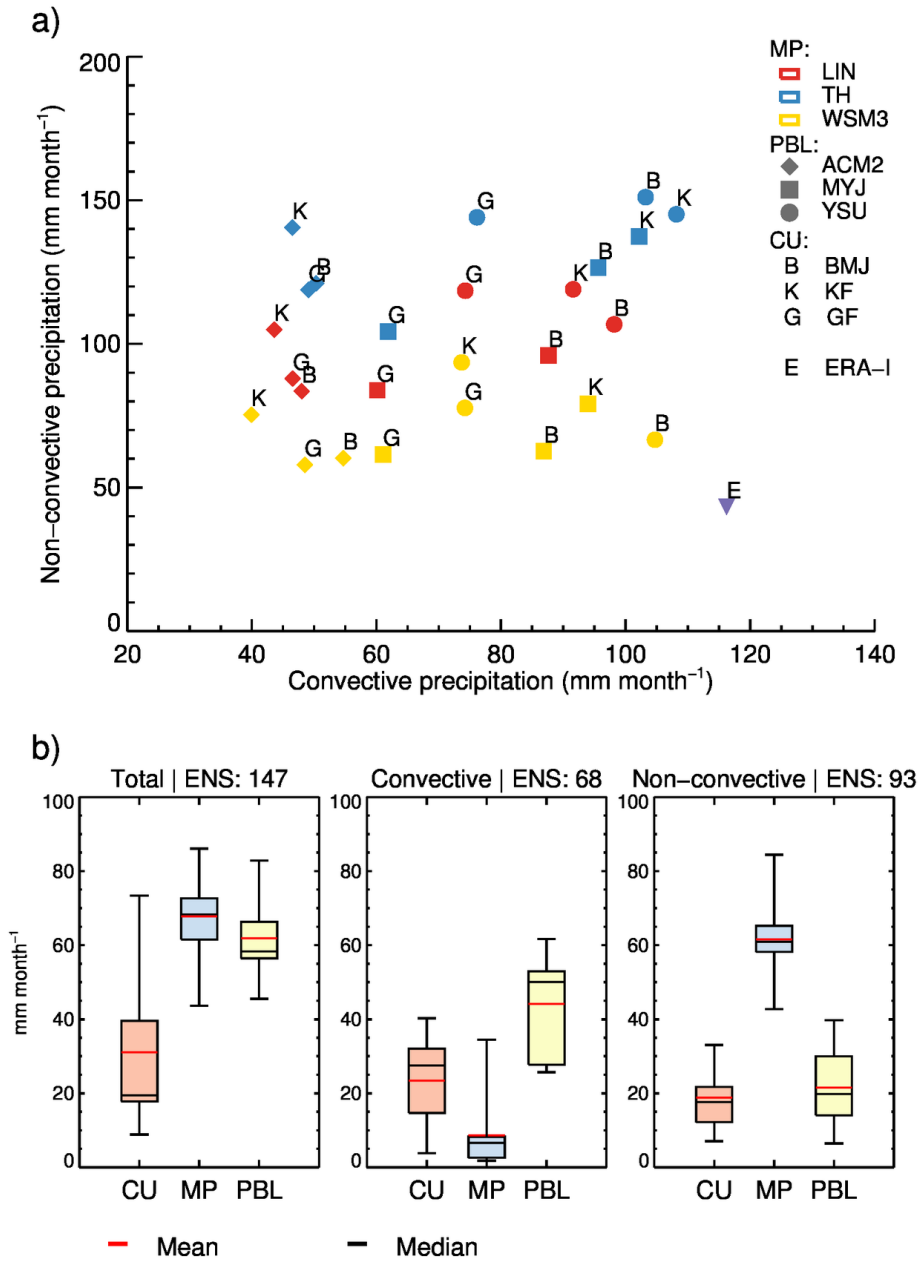
Figure 4.6: (a) Scatterplot of non-convective precipitation over convective precipitation for JAS 1999 over the whole study region for all ensemble members. **(b)** Boxplots of spreads (max-min) of each parameterization type for total precipitation (*left*), convective precipitation (*middle*) and non-convective precipitation (*right*). Each box consists of the nine spreads derived from the three members that differ in one parameterization scheme only (see text). ENS indicates the total ensemble spread for the respective precipitation fraction (mm month^{-1}).
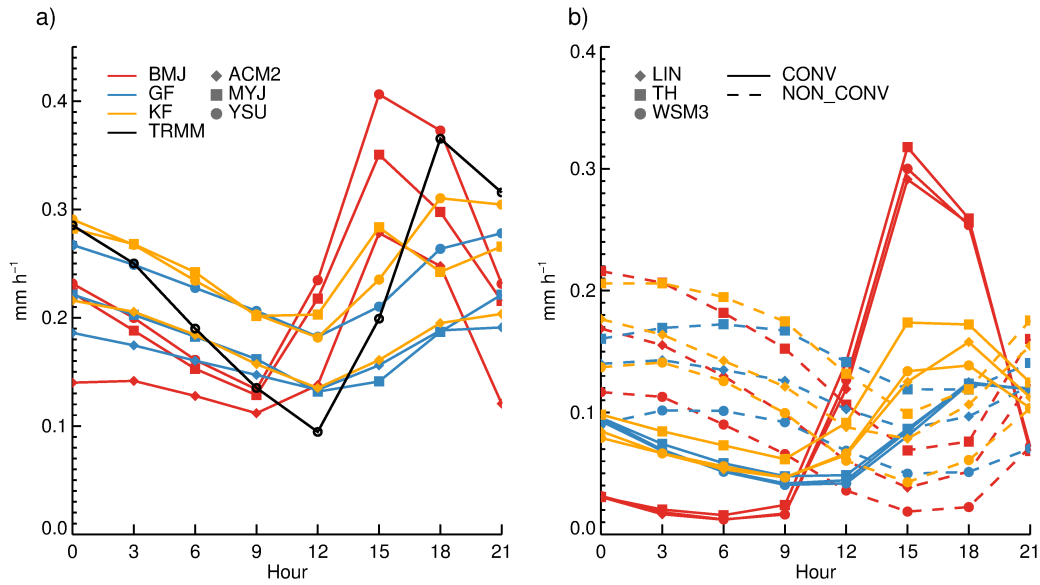
Figure 4.7: Average diurnal cycle of JAS precipitation over the whole study region for CU and PBL parameterization groups and for TRMM **(a)** for total precipitation and **(b)** for convective and non-convective precipitation. Parameterization groups comprise of configurations that differ in the MP scheme but use the same CU and PBL scheme

However, the impact of the CU schemes becomes stronger on finer temporal scales: KF and GF have difficulties to reproduce the amplitude of the diurnal cycle (Fig. 4.7a), which results in a large overestimation of precipitation in the morning hours. BMJ produces the convective peak about 3 h too early, but is close to the amplitude of TRMM, especially in combination with the YSU PBL scheme. However, the phase of the diurnal cycle is somewhat better captured by GF and KF with the convective peak at 18h for most configurations (Fig. 4.7b). Nikulin et al. (2012) report a shift of the phase of the diurnal cycle for almost all models in an ensemble of CORDEX-Africa regional climate simulations that includes the WRF model. They relate this deficiency to the formulation of the cumulus parameterizations. In line with the findings here, their WRF-KF configuration captures the phase of the diurnal cycle reasonably well, but with a stronger amplitude. Figure 4.7(b) confirms that differences in phase and amplitude mainly arise from the convective precipitation fraction. Non-convective precipitation amounts mostly show a uniform phase and the amplitude is closely related to the respective CU scheme activity. BMJ is almost inactive during night hours, as was also found by Pohl et al. (2014), leading to an underestimation of precipitation compared to TRMM. According to Marsham et al. (2013) and confirmed by the experiment presented in Chapter 5, the explicit treatment of convection greatly improves the representation of the diurnal cycle and removes the phase shift.

4.3 Parameterization influences on large-scale dynamics

The WAM precipitation is strongly tied to the characteristics of several dynamical ingredients (Section 2.1). The differences in rainfall between the parameterization groups raise the question whether these can be related to changes in the dynamics and whether these changes correspond to mechanisms known to cause interannual monsoon variability.

Figure 4.8 shows a cross section of the zonal wind for August 1999 for ERA-I, ENS and the parameterization groups. All groups show the major components of the WAM such as the mid-tropospheric AEJ (∼600 hPa), the high-level TEJ (∼200 hPa) and the near-surface south-westerly monsoon winds, but with clear differences in velocity and position.
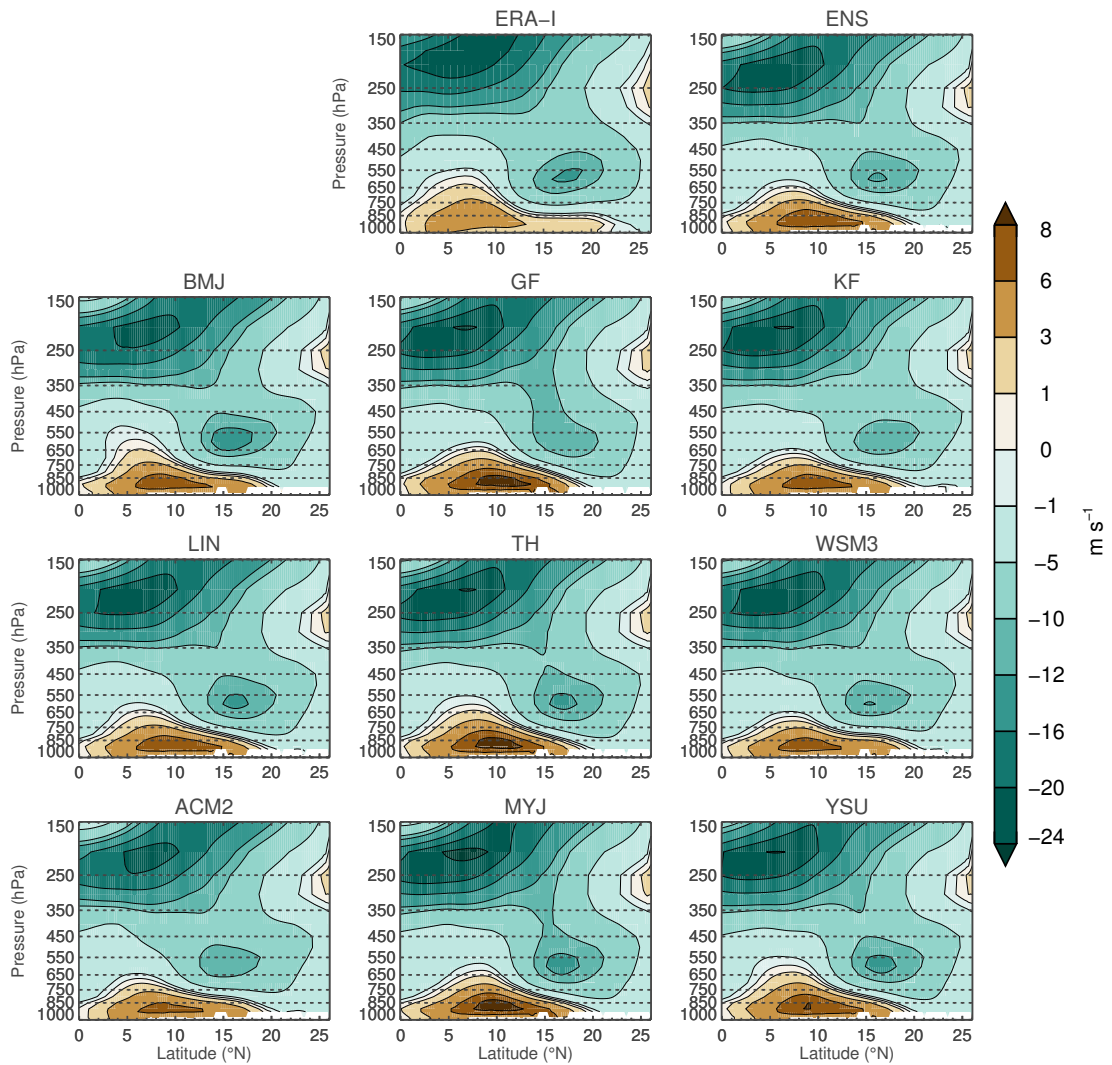
Figure 4.8: August 1999 cross section of zonal wind for ERA-I, ENS and the parameterization groups

The degree to which WRF alters these features in comparison to ERA-I illustrates how regional processes can affect large-scale features. This section concentrates on August only, since August contributes most to the interannual variability in precipitation (Dennett et al., 1985; Nicholson, 2013) and marks the maximum of the northward movement of the monsoon rainband over the continent.

4.3.1 The south-westerly monsoon wind

WRF captures the unusually thick monsoon layer that reaches up to over 750 hPa, but generally over-predicts the westerly winds with up to 6-8 m s^{-1}, compared to 3 m s^{-1} for ERA-I. The overestimation in WRF is due to a deeper SHL by approximately 2 hPa, connected to higher near-surface temperatures north of 15°N (Fig. 4.9a, b) and a resulting stronger land-sea surface pressure gradient. Figure 4.10 compares the monsoon wind velocity of the 27 ensemble members given as a function of sea level pressure (SLP) difference between the sea and two different regions on the continent. There is no correlation between the monsoon wind velocities and the land-sea SLP difference for the region north of 15°N where the SHL is positioned and where little to no rainfall occurs (Fig. 4.10a), but a clear correlation for the the moist region south of 15°N (Fig. 4.10b), r^2=0.63, p-value (P) $\leq$ 0.01). This denotes that moist processes are causing the inter-member spread in monsoon wind strength.

4.3.2 The tropical easterly jet

Configurations with stronger monsoon winds tend to have a stronger core of the TEJ. For ERA-I, the maximum winds in the core exceed 20 m s^{-1} at 200 hPa. The ensemble spread ranges from 20 m s^{-1} for configurations using ACM2 to extensive cores with maximum winds exceeding 24 m s^{-1} for MYJ (Fig. 4.8). While not yet fully understood, the intensity and interannual variability of the TEJ is usually related to non-local phenomena: the strength of the Indian summer monsoon (Flaounas et al., 2011a), the El Niño/ Southern Oscillation (Chen and van Loon, 1987), the intensity of the extratropical Southern Hemisphere westerlies (Dezfuli and Nicholson, 2013), and latitudinal temperature gradients (Nicholson, 2008). The impact of the TEJ on the WAM is mainly thought to be a causal one. The existence of the TEJ is linked to the Asian monsoon outflow and enhances the meridional Hadley-type overturning between sea and land by upper-level divergence over the West African subcontinent. This divergence promotes vertical uplift and rainfall. Figure 4.11(a) illustrates that the strength of the westerly monsoon winds and the velocity of the TEJ are indeed correlated with r^2=0.72 (P $\leq$ 0.01). Since non-local effects are prescribed by ERA-I at the domain boundary, this suggests that the intensity of the TEJ can also be modified by local processes. These processes change the monsoon flow and thus the moisture supply that feeds the TEJ via latent heating, which, in turn, can further intensify the monsoon winds.
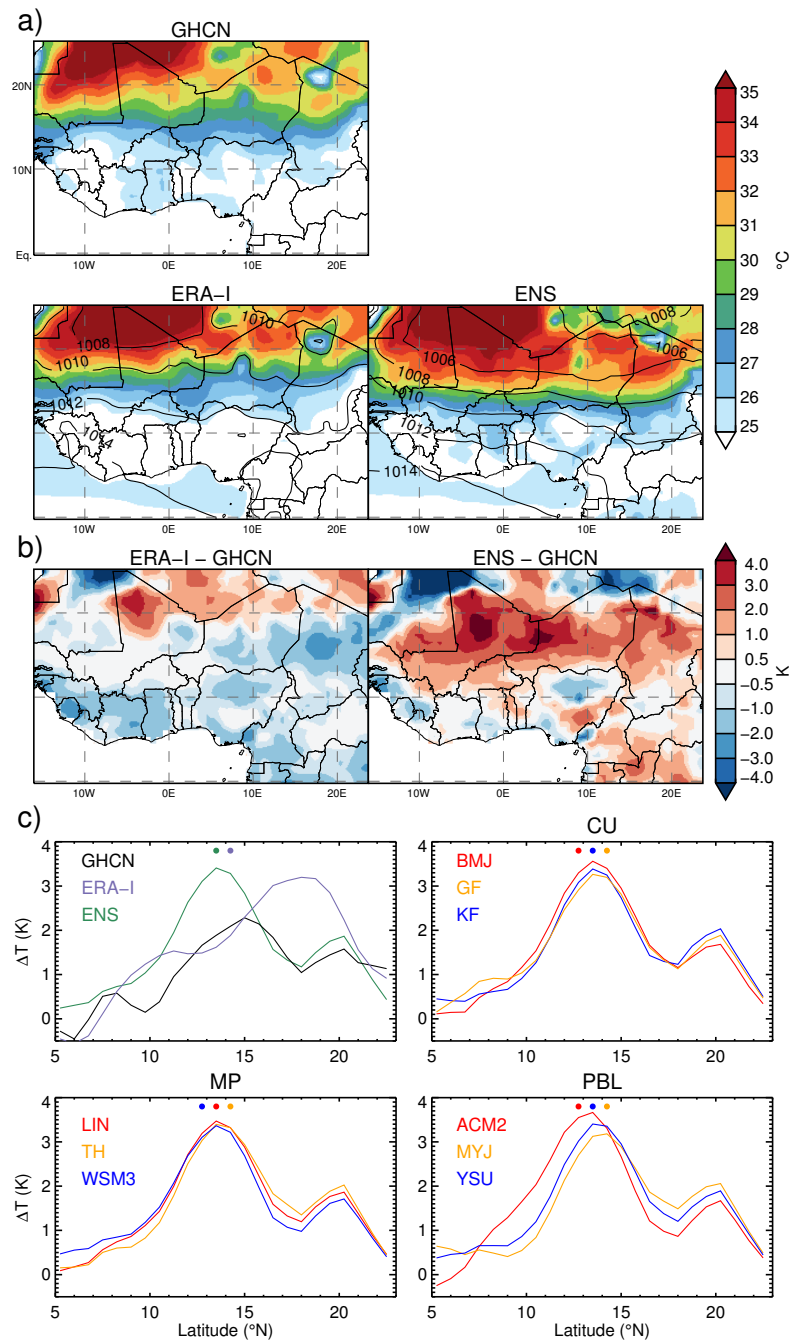
Figure 4.9: **(a)** August 1999 average near-surface temperature and superimposed mean sea level pressure (hPa) for GHCN, ERA-I, ENS, **(b)** the temperature bias of ERA-I and ENS against GHCN and **(c)** temperature gradients (ΔT) over the continent for GHCN, ERA-I, ENS and the parameterization groups. All data is interpolated on the ERA-I grid with ΔT computed over ~ 150 km (three ERA-I grid cells) 1

Figure 4.11(d) summarizes the information by parameterization group. It demonstrates that the different schemes can be classified according to the strength of the TEJ (weaker <stronger):

CU: $BMJ < KF < GF$
MP: $WSM3 < LIN < TH$
PBL: $ACM2 < YSU < MYJ$

Schemes like TH (WSM3) that favour (dampen) deep vertical motion and trigger rapid (slow) precipitation are reinforcing (weakening) the TEJ because of efficient (inefficient) moisture transport and recycling. The vertical velocities in Fig. 4.12 correspond well to this ranking. Vertical motion between the axes of the TEJ and AEJ (contours) connects the upper troposphere with the lower troposphere and completes the meridional circulation which promotes rainfall: Sahel precipitation amounts in Fig. 4.11(c) likewise show a linear relationship with the monsoon winds although it is weaker, related to a non-linear behaviour of the CU schemes in generating precipitation (Fig. 4.11f). Nevertheless, the above ranking is in good agreement with the classification of a scheme as dry or wet (cf. Fig. 4.4).

These correlations denote the strength of the moist meridional overturning as the main factor for the variability of the ensemble members in monsoon strength, and explain the governing role of the resulting SLP south of 15°N (Fig. 4.10b). This is consistent with the findings of Sultan and Janicot (2003), who suggest an increased importance of the Hadley-type meridional circulation and deep convection for the prevailing atmospheric circulation as soon as the monsoon is established.

4.3.3 The African easterly jet

The mid-level AEJ is located at about 600 hPa for ERA-I and for the WRF simulations (Fig. 4.8). GF, KF and ACM2 are not able to capture the core wind speed, which exceeds 12 m s^{-1}. This jet develops to adjust for thermal wind balance and as such moves with the position of the maximum surface temperature gradient between the monsoon rainband and the periphery of the SHL. This gradient is caused by the different thermal properties of moist/vegetated and desert land surface (Cook, 1999). According to Nicholson (2009), the position of the AEJ is typically far to the south (north) for dry (wet) years when the monsoon is weak (strong). The dry and wet ensemble members of the WRF ensemble follow the same pattern: There is a significant correlation (r^2=0.82, P $\leq$ 0.01) between the maximum strength of the monsoon winds and the position of the AEJ in Fig. 4.11(b).

The classification by scheme in Fig. 4.11(e) reveals the same order as for the velocity of the TEJ. Schemes which favour extreme southward or northward displacements of the AEJ tend to dictate the strength of the monsoon flow, independent of the configuration partners, as indicated by the standard deviation of their respective parameterization group. Moderate schemes show a larger standard deviation and can be pushed to either side.
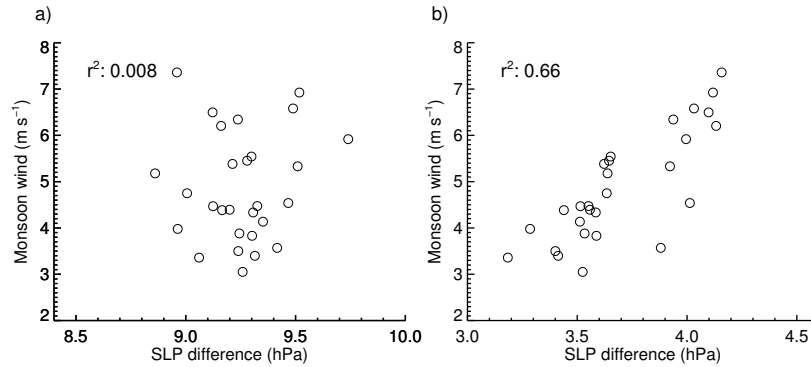
Figure 4.10: Scatterplots of August 1999 average monsoon wind velocity at 850 hPa (positive meridional wind) versus the mean sea level pressure difference (ΔSLP) between the sea (Atlantic cold tongue: 10°W-10°E; 5°S-0°N) and **(a)** the region of the SHL (10°W–10°E, 15°N-25°N), **(b)** the region of continental monsoon rainfall (10°W-10°E; 4°N-15°N).
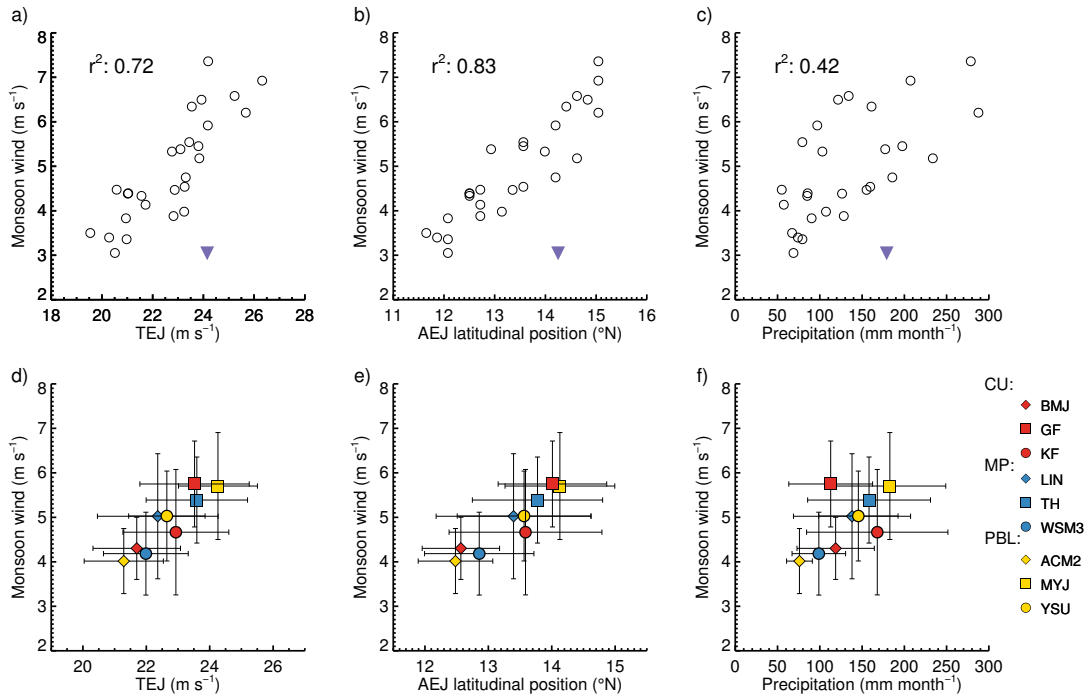
Figure 4.11: Scatterplots of August 1999 average monsoon wind velocity at 850 hPa (positive meridional wind) versus **(a)** the maximum wind velocities at 250 hPa between 4 and 15°N representing the TEJ, **(b)** the latitudinal position of the AEJ for all ensemble members, **(c)** Sahel precipitation. **(d,e,f)** Same as (a,b,c) but for each parameterization group with error bars indicating the standard deviation. The latitudinal position of the AEJ is defined as the first occurrence of the zonal wind velocity surpassing 10 m s^{-1} between 650 and 550 hPa. The purple triangle denotes corresponding variables derived from ERA-I for the wind and from GPCC for precipitation.

The impact of a parameterization scheme on the position of the AEJ comes from the displacement of the temperature gradient maximum, which is modified by the strength of the moisture advection from the ocean. The AEJ positions shown in Fig. 4.9(c) (depicted as points) correspond well to the regions of maximum temperature gradients for the member groups and ENS. The temperature gradient maximum seems to be shifted northward for ERA-I and is not in agreement with the AEJ position, which corresponds better to GHCN.

In accordance to the dry bias in the Sahel (cf. Fig. 4.4), WRF generally exhibits a southward shift of the maximum temperature gradient compared to GHCN. Furthermore, parameterizations that show a weaker monsoon flow (ACM2, WSM3, BMJ) tend to have larger temperature gradients further to the South and correspondingly show the AEJ and the monsoon rainband further to the South, too. This is especially pronounced for the PBL group with clearly shifted temperature gradient maxima in accordance to their monsoon regime. These findings are in agreement with Cornforth et al. (2009), who found moist processes contributing to the meridional extent and intensity of the temperature gradient. It can be concluded that the position of the AEJ is a result of the northernmost extent of the rainband as described by Cook (1999), who attributes the maintenance of the jet to the negative meridional soil moisture gradient and the associated hydrodynamical response of the atmosphere. In her GCM experiments, the development of the AEJ was suppressed when a uniform soil moisture, corresponding to savanna conditions, was prescribed over the whole subcontinent.

The AEJ plays a crucial role for the rainfall production by triggering AEWs. Especially along their southern track around 10°N, AEWs interact with convective processes and are amplified by them (Berry and Thorncroft, 2012). At the same time they foster convective initiation and are thus strongly associated with the formation and the life cycle of MCSs (Fink and Reiner, 2003; Sultan and Janicot, 2000). Current theory relates the formation of such atmospheric disturbances in the vicinity of the AEJ to a barotropic-baroclinic energy conversion process (Cornforth et al., 2009; Hagos and Cook, 2007). Therefore, wet years usually show a weaker AEJ, since more precipitation is related to a stronger wave activity, while dry years usually show a stronger AEJ (Grist and Nicholson, 2001).

The WRF ensemble members do not display such a relationship between the strength of the AEJ (cf. Fig. 4.8) and the AEW activity, represented by the 3-5 days bandpass filtered variance of the meridional wind vector in Fig. 4.13. For example, LIN and KF show comparable wave activity, but KF has a weaker jet. This suggests that other factors that were found to maintain the AEJ might influence the modelled AEJ such as the surface temperature gradient in the vicinity of the jet and the (parameterized) atmospheric turbulence transporting the gradient into the atmosphere (e.g. Cook, 1999). However, there is a correlation (r^2=0.69, P $\leq$ 0.01, not shown) between the wave activity and the vertical velocities in the region of strong convective activity at 10-15°N (cf. Fig. 4.12). This is in line with Hsieh and Cook (2005), who found the AEW activity to be more closely related to instabilities induced by convection in the area of vertical motion, than to shear instabilities caused by the AEJ.

ERA-I exhibits two distinct tracks of AEW at ~ 20°N and at the Guinea Coast, with a maximum in the west of West Africa. The WRF ensemble members show a different pattern: The main wave activity follows a single track and originates in the area of maximum rainfall in the eastern Sudano-Sahel. In comparison to ERA-I, the AEWs are overestimated over the Sahel and Sudano-Sahel by parameterizations that over-predict rainfall in the monsoon rainband with respect to TRMM (cf. Fig. 4.4). Sylla et al. (2013) also reported stronger AEW activity over the Sahel for several LAMs in comparison to ERA-I and attribute this to the internal representation of convection in the LAMs. Therefore, the different wave patterns visible for WRF with respect to ERA-I could be related to a minor importance of the energy transfer between AEJ and AEWs and a higher sensitivity to vertical velocities and associated convective processes.
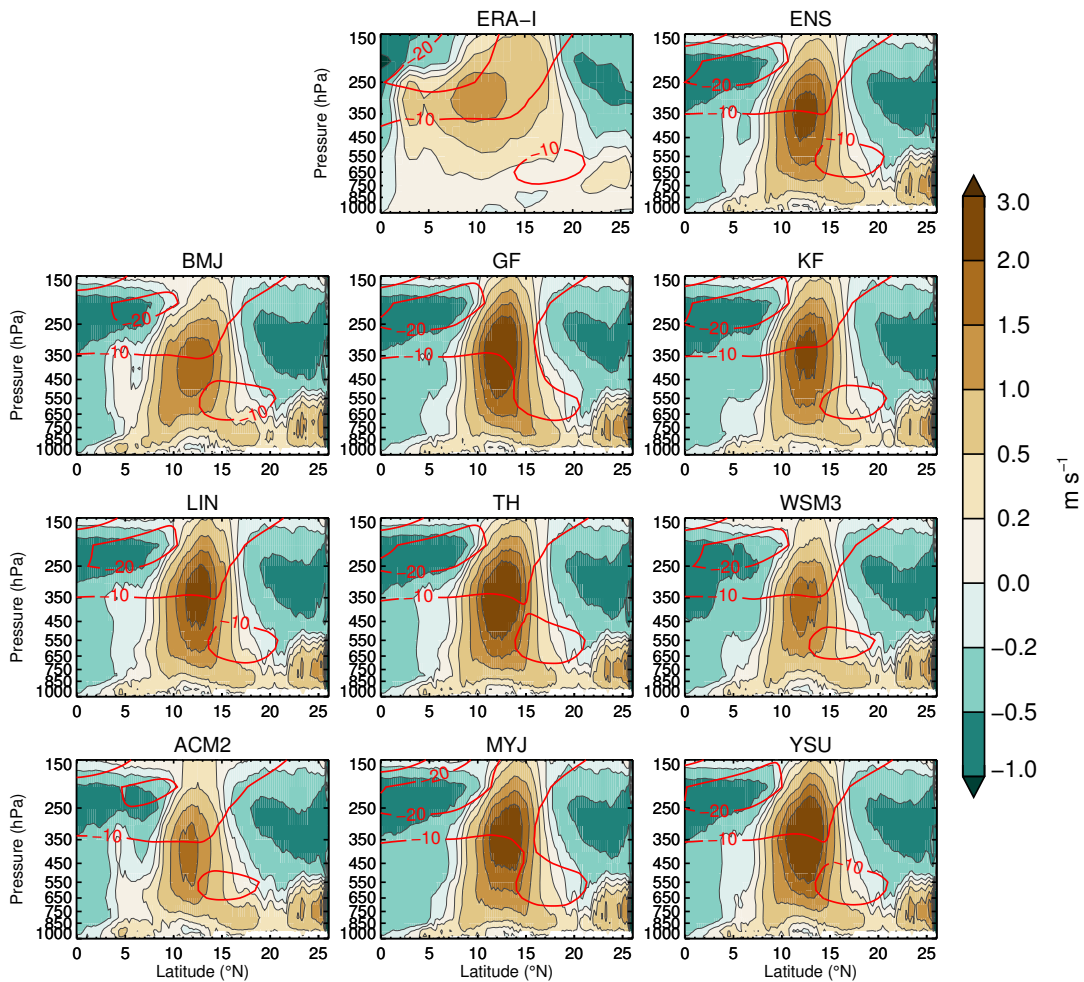
Figure 4.12: August 1999 cross section of vertical wind for ERA-I, the WRF ensemble mean (ENS) and the parameterization groups. Contours indicate u-wind (m s^{-1}) and depict the position of the AEJ and TEJ gradient
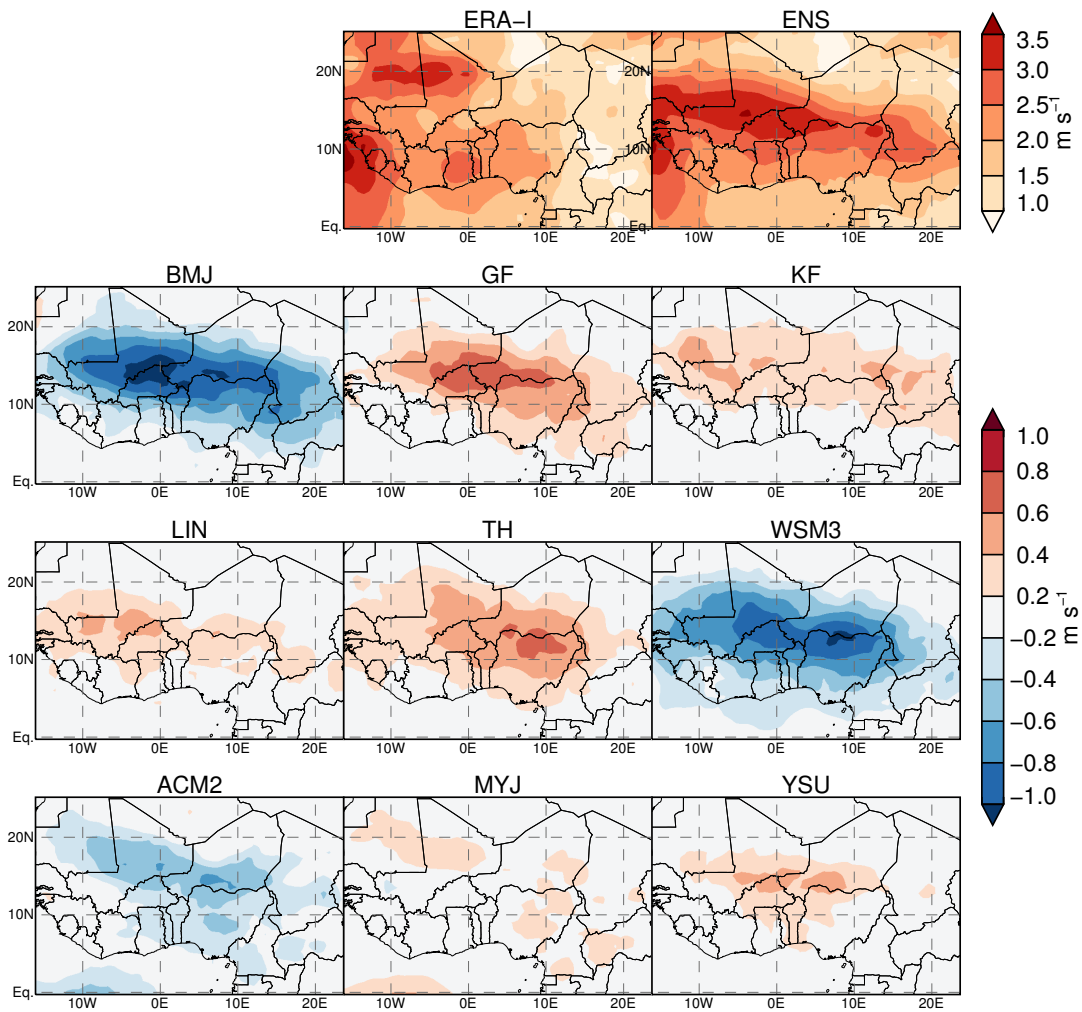
Figure 4.13: August 1999 mean standard deviation of the 3- to 5-day bandpass-filtered 600 hPa meridional wind (*top*) for ERA-I and the WRF ensemble mean (ENS) and (*bottom*) the difference between the parameterization groups and ENS

4.4 Discussion

The results show that the examined parameterizations can be classified according to their impact on the modelled WAM regime. While the quantitative skill of a certain scheme in comparison to observations might change under different conditions (e.g. time period, driving data, domain size, chosen evaluation criteria), their individual qualitative impact on monsoon dynamics is assumed to be more universal. For overlapping analyses, the model internal tendency to produce more/ less precipitation or to enhance/ weaken the dynamic features with certain parameterizations are in agreement with Flaounas et al. (2011a), which gives confidence in their robustness.

Microphysics schemes
The identified ranking for the MP schemes is in line with the findings of Hong and Lim (2006), who report that the amount of precipitation is correlated with the complexity of the microphysics scheme. While they suggested that at resolutions of about 25 km, a simple ice-scheme should be sufficient to resolve the mesoscale features, it is shown here that, even at that scale, the representation of cloud processes has a strong impact on precipitation amounts. The simple 3-class scheme WSM3 consistently leads to drier conditions in the model. During the monsoon season essentially all rainfall is associated with deep convection for which ice processes play a major role in the generation of precipitation. LIN and TH separately include cloud ice, snow and graupel, and TH additionally predicts the number concentration for cloud ice. For these two schemes, cloud particles may penetrate deeper above freezing level. According to Hong and Lim (2006), the conversion from clouds to rain is more efficient at producing precipitation than the ice phase alone in the case of WSM3. Furthermore, Hong et al. (2004) found that the interaction between ice clouds and long-wave radiation has a strong impact on the amount of precipitation because of enhanced radiative heating. In their case, precipitation was decreased with more cloud ice and vice versa.

Different from other WRF studies that evaluated microphysics schemes in other regions (e.g. Pohl et al., 2011; Crétat et al., 2012; Evans et al., 2012), the chosen MP scheme was found to be of major importance for simulated precipitation amounts. For ENS, non-convective precipitation contributes around 40 % during the pre-monsoon phase and up to 60% after the monsoon onset in July. During the WAM, MCS contribute most to the precipitation and the fraction of stratiform rainfall increases (Schumacher and Houze, 2006), which WRF is able to partly resolve explicitly. This is confirmed by Marsham et al. (2013), who compare two model simulations at 12 km horizontal resolution with explicit and parameterized convection during the WAM. Because of the large fraction of organized convection, they report a better performance of the explicit simulation and relate their findings to a better representation of the diurnal cycle and the associated monsoon dynamics. Here, the impact of different MP formulations proved to be non-negligible even at a medium horizontal resolution (24 km) and can be expected to increase with increasing horizontal model resolution.

Planetary boundary layer schemes

With respect to the PBL schemes analysed here, the results may seem to be counterintuitive. Several studies (e.g. Hu et al., 2010; Shin and Hong, 2011; Xie et al., 2012) suggest that the mixing rates and surface drag are highest for ACM2 and lowest for MYJ. Enhanced mixing and the associated improved transport of surface fluxes into the atmosphere should lead to a stronger monsoon and inversely. However, here, this is not the case since the local, weak mixing in MYJ produces the strongest monsoon winds. Figure 4.14 reveals that the strong impact of the PBL scheme is due to their influence on the incoming shortwave radiation at the surface, which is lower for ACM2 than for MYJ at the Guinea Coast and in the Sudano-Sahel.
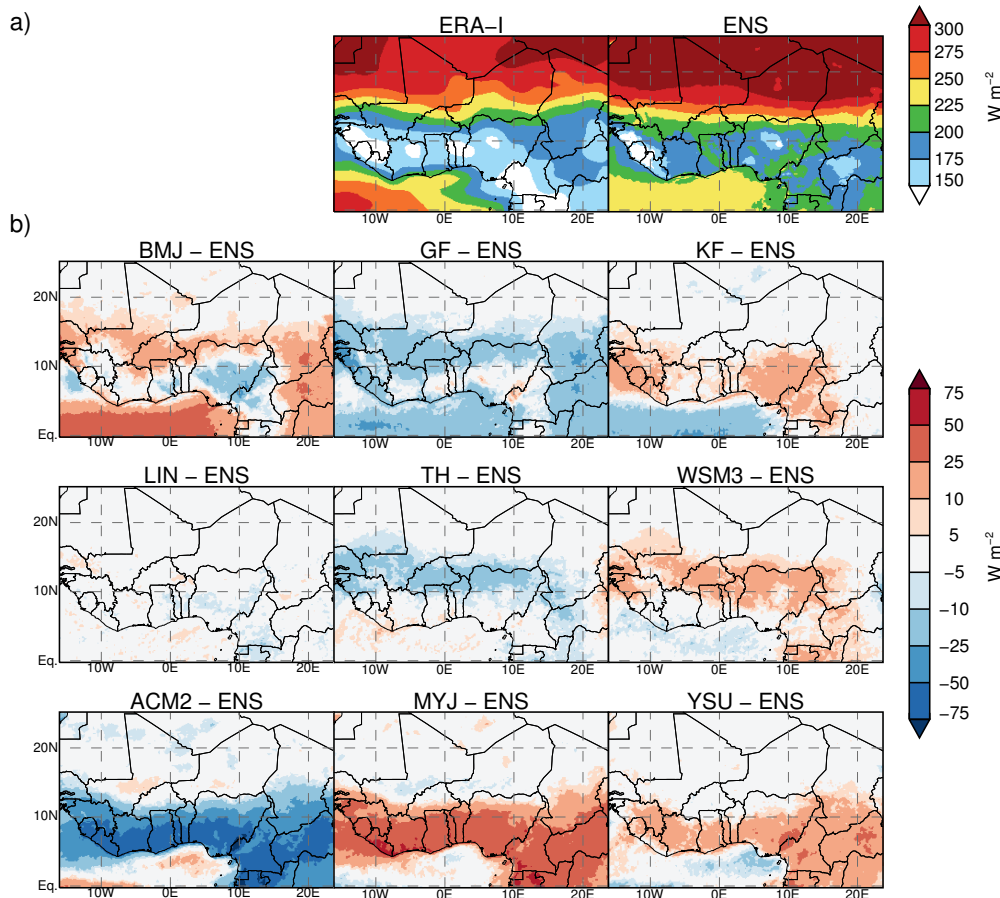
Figure 4.14: August 1999 incoming shortwave radiation at the surface **(a)** for ERA-I, the WRF ensemble mean (ENS) and **(b)** the difference between the parameterization groups and ENS

At the 700-500 hPa levels, ACM2 produces more mid-level clouds, which reflect the incident shortwave radiation (Fig. 4.15a). Meanwhile, MYJ produces less low- and mid-level clouds than ACM2 which consequently leads to larger solar irradiation and higher near-surface temperatures (cf. Fig. 4.9). The differences of the vertical moisture profiles of the three PBL schemes in Fig. 4.15(b) indeed show very dry conditions for MYJ in the lower troposphere.

The moist conditions in the mid-troposphere for ACM2 lead to a rapid saturation of the atmosphere and consequently to a build-up of clouds by the MP scheme. With MYJ and YSU, more moisture is transported into the higher levels above 400 hPa. This is presumably due to the different promotion of convective processes (CU scheme activity) by the PBL schemes, as described in Section 4.2.3. The strong mixing in ACM2 seems to generate unfavourable conditions for releasing instabilities by the CU schemes. ACM2 therefore lacks the efficient drying of the atmosphere through deep convective processes and the associated strong precipitation events, which in turn leads to an excess of moisture in the planetary boundary layer.

This ultimately attributes the largest spread in monsoon dynamics between the ensemble members to modifications of the incoming radiation, caused by the vertical moisture distribution in the PBL scheme. This is an important result, since the focus often remains on the energy transport via latent heat as main source of monsoon variability. This raises the question whether the interannual variation in cloudiness, and especially the amount and prevalence of low-level clouds, are key parameters for the surface energy budget and thus for the monsoon variability, as discussed by Knippertz et al. (2015). They also point out that the development of certain cloud types is strongly coupled to aerosol concentrations and composition that have already been considerably changed by anthropogenic emissions. They argue that air pollution from the rapidly growing cities in West Africa could be an important factor for WAM variability in the future though is often not taken into account by current climate models. Cloud-radiation interactions remain one of the least understood processes and, together with the representation of clouds, are highly difficult to parameterize in atmospheric models with potentially devastating impact on the validity of modelled monsoon dynamics.
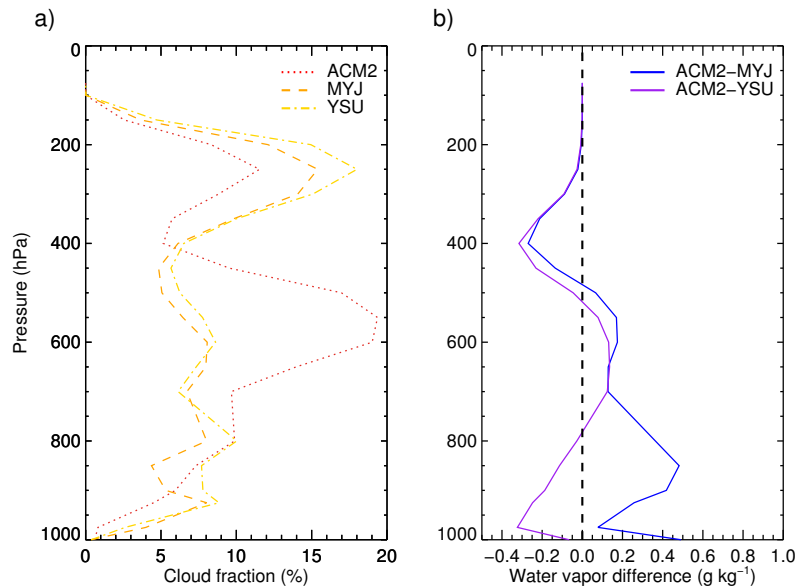
Figure 4.15: August 1999 average vertical profile for the region of monsoon rainfall ($10°$W-$10°$E, $4°$N-$15°$N) for the PBL groups of **(a)** cloud fraction, **(b)** water vapor difference.

Cumulus schemes

The effects of the cumulus parameterizations are difficult to interpret since they are the result of a complex interplay of processes as illustrated in Fig. 4.6(b). This applies especially to the ensemble approach of GF. However, the dampening effect for precipitation and monsoon dynamics of BMJ could be related to it being a sounding adjusting scheme, which will transform any atmospheric profile it starts from into a plausible, but pre-determined post-convection sounding. This might eliminate special and extreme characteristics of the vertical atmospheric structure.

Representation of monsoon dynamics

The simulations reproduce the dependency of TEJ velocity and AEJ position on the strength of moisture advection from the Atlantic Ocean (westerly monsoon winds) as reported from studies that investigate the different dynamics of wet or dry years (e.g. Sultan and Janicot, 2003; Nicholson, 2008). A drier (wetter) monsoon in the Sahel is often related to a weaker (stronger) TEJ and a southward (northward) displacement of the AEJ, reproduced here by the dry (wet) ensemble members. The identified correlations between these dynamical components are of comparable magnitude as in reanalysis studies. For example, Nicholson (2008, 2009) use NCEP reanalysis data for an analysis of the relationship between monsoon wind velocity and SLP gradient (r^2=0.84), and between the monsoon wind velocity and Sahel rainfall (r^2=0.75), respectively. Since the Sahel rainfall depends on the position of the AEJ, this also implicitly describes the relationship of the monsoon winds and the AEJ position. Table 4.2 further evaluates this picture, showing GPCC August precipitation in the Sahel of dry and wet year composites from 1979-2010, and related ERA-I dynamics in comparison to the driest and wettest WRF ensemble member. The maximum precipitation is strongly overestimated by WRF, indicating an artificial origin. Although all WRF ensemble members use the same 'wet year forcing', their spread in the AEJ position and TEJ velocity is comparable to the mean interannual range.

However, compared to ERA-I, stronger monsoon winds and thus an increased moisture supply from the ocean is necessary to reach the same TEJ velocity and AEJ position in WRF (cf. Fig. 4.11). Configurations that show comparable monsoon flows to ERA-I suffer from an equatorward displaced AEJ (maximum temperature gradient) and from overall dry conditions. The two main sources for moisture during the WAM are the south-westerly monsoon flow and local moisture recycling (Gong and Eltahir, 1996; Thorncroft et al., 2011). The latter process contributes about 30 % to the precipitation over the West African subcontinent. However, the evaporative fraction (EF) presented in Fig. 4.16 is much lower for the WRF ensemble than for ERA-I and for NCEP/ NCAR reanalysis data (Levermann et al., 2009). For both reanalysis datasets, the EF in August reaches about 70-90 % south of 15°N, where the rainband passed or still resides. For WRF, the EF only reaches about 60-80 % over a considerable smaller area. The high EF in the reanalysis data might just as well be related to model errors, but it nevertheless implies that local evaporation contributes less to the atmospheric moisture in WRF. This could partly explain the need for stronger monsoon winds as source of moisture to achieve comparable monsoon dynamics.

Table 4.2: Comparison of the observed range of a wet/dry year composite for August 1979–2010 for precipitation in the Sahel (Fig. 4.1), TEJ velocity and latitudinal AEJ position (as in Fig. 4.11) with the wet/dry WRF ensemble members in 1999. The Δ gives the observed and modelled difference between all dry and wet cases.

	GPCC/ERA-I dry	GPCC/ERA-I wet	Δ GPCC/ERA-I	WRF dry	WRF wet	Δ WRF
Precipitation	61	150	89	64	268	204
TEJ	16	22	6	20	26	6
AEJ	10.9	14.0	3.1	11.7	15.1	3.4
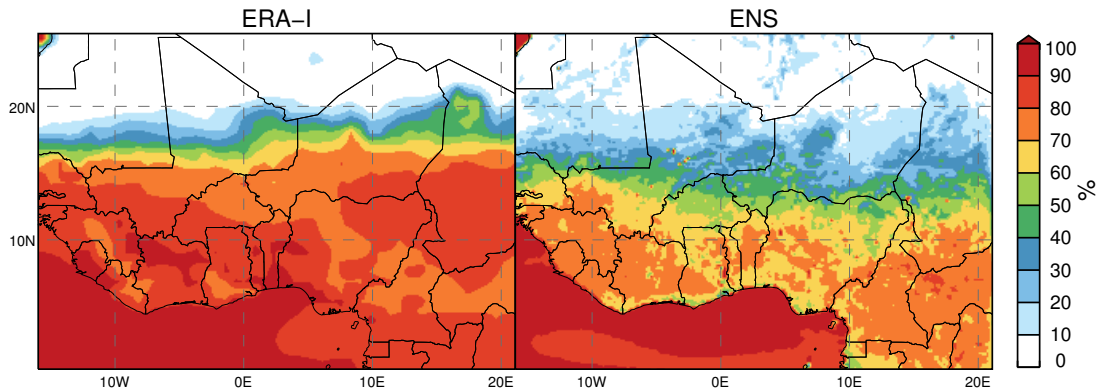
Figure 4.16: August 1999 mean evaporative fraction (EF) for ERA-I and the WRF ensemble mean (ENS). EF is the ratio of the latent heat flux to the sum of latent and sensible heat fluxes

4.5 Summary and conclusions

In this experiment, a WRF physics ensemble was employed to investigate the impact of moist process parameterizations on the WAM for the rainy season 1999 with the aim to (Section 1.2):

- evaluate the interactions of regional moist processes with the monsoon dynamics

- quantify the uncertainty in the representation of moist processes in the WRF model and to classify their process-based impact on the WAM regime in order to extract transferable guidelines to set up the model in West Africa

Three different CU, MP and PBL parameterizations were combined, resulting in an ensemble of twenty-seven members (cf. Table 4.1) whose spread was used as a quantitative measure for model uncertainty. The effects of each parameterization group on precipitation and the representation of dynamical WAM features (monsoon wind, TEJ, AEJ) were analysed and ranked accordingly. The MP and PBL schemes introduced the largest ensemble spread (147 mm month^{-1}) in total precipitation over the study region. For the ensemble mean, non-convective precipitation generated by the MP schemes contributes 50-60 % of the total rainfall during the WAM, when mesoscale convective systems prevail. Larger amounts of precipitation are associated with more complex MP schemes, which alter atmospheric dynamics by the release of latent heat.
PBL schemes have a strong influence on the movement of the WAM rainband because of their impact on the cloud fraction for which the ensemble spread ranges from 8 to 20 % at 600 hPa

during August. More (less) low- and mid-level clouds with ACM2 (MYJ) result in less (more) incoming radiation and a southward (northward) shift of the monsoon rainband.

The choice of the CU scheme has minor influences on the total amount of precipitation over the study region, but alters the spatial distribution and thus the width of the rainband and the location of intense rainfall events. Moreover, the CU schemes have a strong impact on the representation of the diurnal cycle. Ultimately, the inter-member differences in the strength of the monsoon wind and in the northward transition of the rainband could be traced back to the enhancement or weakening of the moist Hadley-type meridional circulation that connects the monsoon winds to the Tropical easterly jet. This leads to the following ranking of the parameterization schemes (weak <enhanced meridional circulation):

CU: $BMJ < KF < GF$, **MP**: $WSM3 < LIN < TH$, **PBL**: $ACM2 < YSU < MYJ$

The produced rainfall amounts are accordingly except that KF (YSU) produces slightly more total precipitation than GF (MYJ) because of respective promotion of convective precipitation, that is not always linearly related to the intensity of the dynamics.

The differences between the ensemble members illustrate that the WRF model captures the characteristic interdependencies of monsoon dynamics and rainfall that were also found for years with differing monsoon regime. The spread of the ensemble for the simulated monsoon dynamics during August 1999 is comparable to the observed interannual spread (1979-2010) in August between dry and wet years with a change of 6 m s^{-1} for TEJ velocities and a latitudinal shift of the AEJ by $\sim$3°, in spite of the same boundary forcing.

This illustrates that regional moist processes do affect the dynamical features of the WAM, for which the modification of the large-scale surface temperature gradient, shading from clouds and latent heat release were found to be major factors. With an ensemble spread in August precipitation of 204 mm month^{-1} for the Sahel, these results also underline the need for a careful selection of model parameterizations and justify the frequent ensemble applications in that region.

On basis of the above findings, the moist model physics can be combined with respect to their distinct impact on monsoon mechanisms and further schemes could be classified into this picture in the future. For subsequent experiments within this thesis, the BMJ cumulus scheme and the YSU planetary boundary layer scheme are used. Both schemes do not foster an extreme behaviour of the monsoon dynamics, lead to a preferable wider rainband and showed the diurnal cycle closest to observations. Furthermore, BMJ showed best performance in precipitation distribution and YSU supports favourable cloud development. In addition, YSU was identified to be a 'moderate' scheme that does not impose strong wet or dry tendencies which gives some confidence on its suitability for the representation of changing monsoon regimes. The MP parameterization was found to be well suited to adjust overall precipitation amounts and should be chosen according to existing biases in the particular application. Here, the moderate LIN scheme is used for further analyses since it showed the smallest precipitation bias with respect to TRMM.

The relevance of an explicit convection description for precipitation characteristics

West African monsoon precipitation is dominated by convective processes that are not explicitly resolved in LAM applications at horizontal resolutions of approximately > 10 km. Instead, they are taken into account by parameterizations. However, at even higher resolutions that are often referred to as the *convective grey scales*, convective parameterizations start to violate their assumptions. Between approximately 4-12 km (Weisman, 1997; Gerard, 2007), convective systems just start to be resolved but parametrising convection becomes less and less appropriate (Bélair and Mailhot, 2001): Processes that are implicitly taken into account by a parameterization within one grid column may spread over several grid cells, such as up- and downdrafts of an MCS, which is not supported by most of the current parameterizations. Therefore, the specific range of the grey scales and the 'degree of violation' for either approach, parameterized or explicit, also depends on the individual sizes of convective systems (Molinari and Dudek, 1992).

The correct representation of convection is crucial for modelling West African monsoon patterns and local precipitation amounts (Lafore et al., 2011). Reported shortcomings of the parameterizations of convection include a shifted diurnal cycle (e.g. Nikulin et al., 2012; Marsham et al., 2013), the incapability to capture propagating convective systems (Davis and Manning, 2003; Correia et al., 2008) or a flawed representation of land-atmosphere interactions (Hohenegger et al., 2009; Taylor et al., 2012). Further studies note an extreme sensitivity of precipitation patterns and amounts to the choice of a specific cumulus parameterization (e.g. Flaounas et al., 2011a, Chapter 4). Such shortcomings might be improved or avoided with an explicit approach, ultimately leading to a better representation of the WAM.

Since today's computer resources allow higher and higher model resolutions, high-resolution modelling gains of importance not only for numerical weather prediction but also for climatological approaches. Different regional studies for the United Kingdom (Kendon et al., 2012), the Alps (Zaengl, 2007; Hohenegger et al., 2009), the United States (Done et al., 2004; Klemp, 2006) or Asia (Oouchi et al., 2009) report that the explicit treatment of convection is able to reduce or remove mentioned major parameterization-induced shortcomings of atmospheric models. However, this is not always the case, as shown by Pohl et al. (2014), who use WRF to downscale the South African climate from 55 km down to an explicit case at 3.6 km with a nesting approach and compare it to a simulation at 18 km with parameterized convection. They find an aggravation in precipitation amounts and no improvement of the diurnal cycle for the explicit domain. However, it is not clear whether the nesting approach and therefore biases of the 55 km parent domain might have influenced these results.

During the West African monsoon, the correct representation of the diurnal cycle of rainfall and therefore of cloudiness is of special importance, since it critically affects the energy budget and the circulation of the monsoon, as was reported by Marsham et al. (2013), who were the first to apply a LAM at convection-allowing scales over whole West Africa. They used the UK Met Office Unified Model to simulate one week during the WAM at 4 km with explicit convection and at 12 km with explicit and parameterized convection within the *Cascade* project. They generally found the explicit convection being more realistic than the parameterized one. Both explicit cases improve the diurnal rainfall cycle. Using the same *Cascade* project data, Pearson et al. (2014) state that the improvement in the representation of convection between the two simulations at 12 km (parameterized) and 4 km (explicit) stems mainly from the employed parameterization rather than the increase in resolution since, in their case, the 12 km simulation outperforms the 4 km if no parameterization is used. Birch et al. (2014) finally extended the study of Marsham et al. (2013) to 40 days and report that both explicit simulations react more realistically to AEWs in terms of rainfall generation.

Except for this *Cascade* project study that was conducted with the same model and for the similar time period, all other subcontinental-scale LAM studies over West Africa use coarser horizontal resolutions with a cumulus parameterization. So far, explicit approaches are usually only used on smaller spatio-temporal scales in the form of large eddy simulations, catchment-scale simulations or 2-D models (e.g. Garcia-Carreras et al., 2011; Knoche and Kunstmann, 2013).

Therefore, there is a need to extend the few existing continental-scale studies that mainly focus on the diurnal cycle. Here, the whole rainy season 1999 is simulated at resolutions that span the typical range of LAM applications: from 24 km, as a representative for resolutions where parameterizations are generally accepted and valid, down to 4 km, which is usually thought to be the upper limit for the reasonable simulation of explicit convection. In between, a simulation at 7 km resolution with explicit convection is conducted to compare results produced in the convective grey scales to both ends of the scale. The relevance of the explicit treatment of convection is evaluated for total precipitation amounts and intense events, MCS propagation as well as the diurnal cycle of rainfall and cloud cover.

5.1 Experimental set-up and reference datasets

5.1.1 Model configuration

Four simulations are conducted with the WRF version 3.5.1 for 1999 from March to September: 24 km (WRF24) and 12 km (WRF12) horizontal resolution with cumulus parameterization and 7 km (WRF7) and 4 km (WRF4) horizontal resolution with explicit convection.

The domain set-up for all simulations is shown in Fig. 5.1. WRF4 is nested into the larger WRF12 domain since a direct downscaling from ERA-I at ~80 km to WRF4 was found to be numerically unstable for this set-up. This illustrates potential problems with resolution jumps over a too large range of scales, as was mentioned in Section3.5.1. WRF7 is of coarser resolution and can therefore be directly downscaled from ERA-I. It encompasses a larger domain than WRF4 to allow the WRF model to develop its own circulations.

The WRF physics set-up includes the Rapid Radiative Transfer Model/Dudhia long and shortwave radiation schemes (Dudhia, 1989), the LIN Microphysics scheme (Lin et al., 1983) and the YSU planetary boundary layer scheme (Hong and Lim, 2006), which is a configuration that was found to capture the WAM without showing an extreme wet or dry behaviour in Chapter 4 (Klein et al., 2015). All simulations are operated with 36 vertical levels and a model top of 20 hPa. The WRF output is written every three hours. If not indicated otherwise, all analyses are done for the grey box depicted in Fig. 5.1(b).
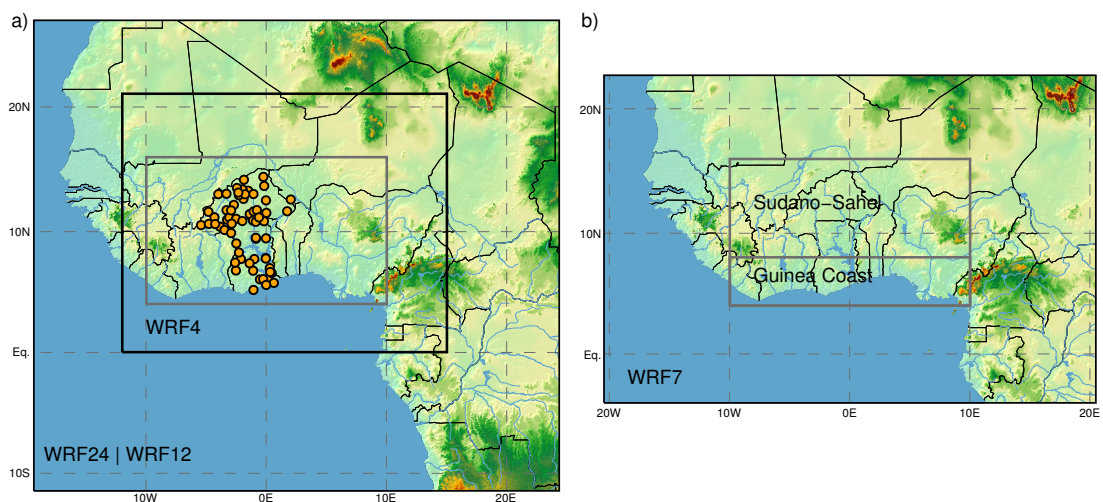
Figure 5.1: WRF domains for **(a)** WRF24, WRF12 and WRF4 with study domain (grey) and position of used weather stations. **(b)** Domain of WRF7 with study domain (-10°W-10°E; 4-16°N) and sub-regions Guinea Coast (4-8°N) and Sudano-Sahel (8-16°N).

5.1.2 Reference datasets

Precipitation Modelled precipitation is compared to TRMM 3B42V7 0.25° (3-hourly, daily) rainfall estimates (Huffman et al., 1995, 1997). Additionally, daily measurements of 62 weather stations are used, located in Burkina Faso and Ghana (cf. Appendix B), which were provided by the national meterological services.

Cloud fraction To qualitatively evaluate the modelled vertical cloud fraction over West Africa, the 2006-2012 monthly climatology of the GCM-Oriented Cloud-Aerosol Lidar and Infrared Pathfinder Satellite Observation (CALIPSO) Cloud Product (GOCCP), gridded at latitude-longitude boxes with a vertical resolution of 480 m and 40 levels, is used. It was specifically developed to facilitate the comparison of satellite-derived cloud fraction with model output by e.g. a noise reduction in the vertical layers (Chepfer et al., 2010). However, the quantitative vertical cloud fraction is highly sensitive to the actual definition of clouds and detection thresholds, which varies among different observation instruments but also in comparison to models. Differences in horizontal and vertical averaging introduce additional uncertainties in the comparison of observed and modelled clouds (Chepfer et al., 2013). Therefore, GOCCP has been designed to be fully consistent with a cloud observation simulator that can be used with GCM output, ensuring similar conditions for the resulting cloud fractions from observations and GCMs. However, this simulator is not used here, rendering a quantitative comparison of GOCCP and WRF questionable. Therefore, GOCCP is only used for a qualitative assessment of vertical cloud distribution and extent as compared to modelled cloud cover by WRF. Chepfer et al. (2013) showed that the overall picture of the GOCCP vertical cloud cover is qualitatively consistent with other CALIPSO-based cloud products derived with a different algorithm. Stein et al. (2011) assessed the four-year-average vertical cloud structure of the WAM with a combination of CALIPSO and CloudSat profiling radar data, proving the suitability of these rather new datasets to robustly evaluate the vertical cloud structure in West Africa. The CloudSat and CALIPSO satellites were co-launched in 2006 and now allow relatively robust measurements of zonal cloud fraction profiles for the first time (Chepfer et al., 2013). Since this experiment is conducted for 1999, only the GOCCP climatology can be used for an approximate estimation of the model performance in capturing the cloud cover characteristics during the WAM.

Incoming solar radiation Information on incoming shortwave radiation is taken from the Meteorological satellite (METEOSAT) Solar Surface Irradiance Dataset at ~ 3 km horizontal resolution for 1983-2005 with a regional coverage of Europe, Africa, the Atlantic Ocean and parts of South America. The product is available at monthly, daily and hourly averages. The dataset is based on the the METEOSAT Visible and Infrared Imager and is explicitly suitable for climate studies or the evaluation of global and regional models (Posselt et al., 2011). (Posselt et al., 2012) report that the dataset achieves the target accuracy for monthly and daily means in comparison to ground observations and reveals a better performance than other often used datasets, among other ERA-I. It also captures the seasonal and interannual variability of incoming shortwave radiation, making it suitable for climate monitoring and the analysis of extremes.

5.2 The average added value

In the following, it is assessed whether explicit convection improves the representation of monsoon rainfall in comparison to parameterized convection over the peak monsoon season (June-September, JAS). Figure 5.2 shows the bias of all WRF simulations with respect to TRMM revealing little impact of the resolution on the bias patterns for the simulations that share the same outer domain boundaries (WRF24, WRF12, WRF4). In the case of WRF7, the bias is comparable poleward of 10°N, but is distinctly wetter close to the coast where the other simulations exhibit a dry bias.
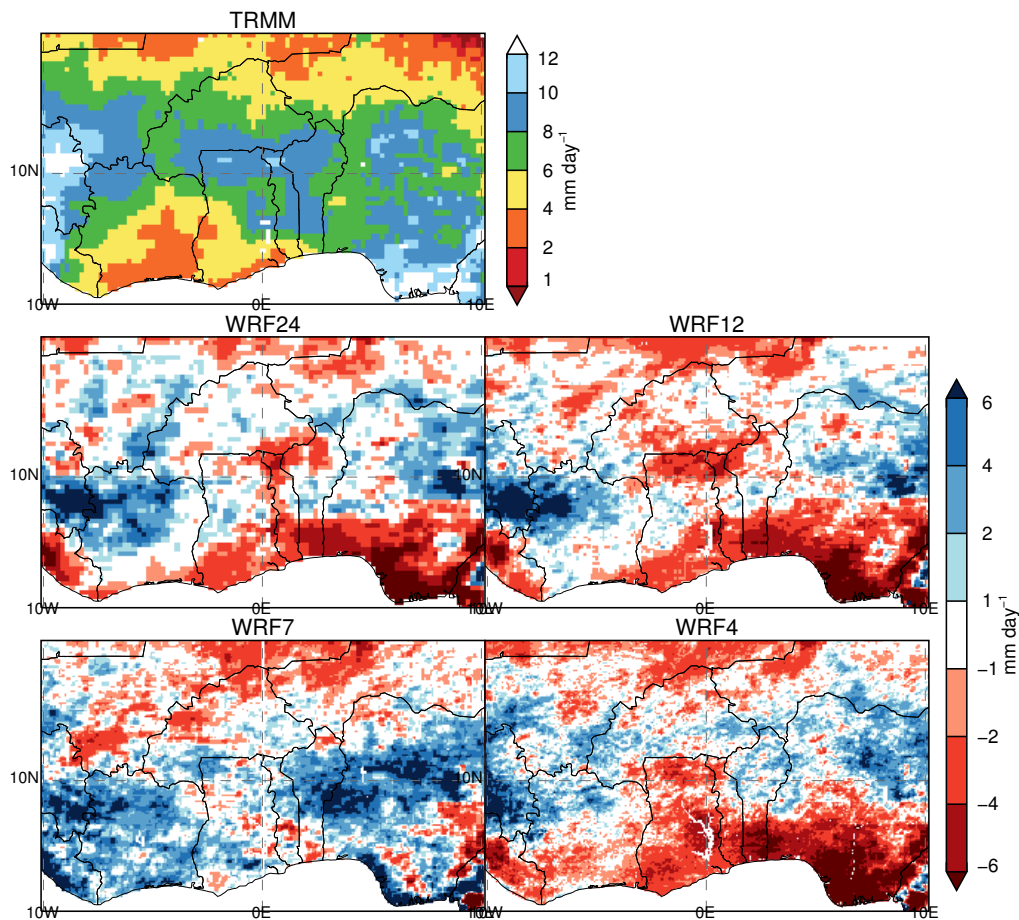
Figure 5.2: JAS 1999 average precipitation for TRMM and the bias of the four WRF simulations at their native resolution with respect to TRMM. TRMM values are bilinearly interpolated onto the corresponding WRF grid.

The fact that only WRF7 shows such a clear difference suggests that, in this case, the change of the position of the outer domain boundaries has a stronger impact on the average rainfall patterns than a change in model resolution and the choice of any or none convective parameterization (cf. WRF12 and WRF4). Browne and Sylla (2012) showed that a change of the portion of included Atlantic Ocean in the LAM domain may considerably affect the monsoon wind and

moisture transport. By just altering the model domain size, they provoked changes in modelled precipitation leading to a bias range relative to TRMM from -7.5% to +4% with the Regional Climate Model. This suggests that the northward shift of the southern domain boundary in WRF7 is the most likely cause for the different bias pattern.

In consequence, WRF7 shows an overall positive precipitation bias of about 0.9 mm day^{-1} while it is negative for the other simulations (Table 5.1). The negative bias further increases with increasing resolution from -0.14 mm day^{-1} (WRF24) to -0.63 mm day^{-1} (WRF4), implying a drying trend with higher resolution. The spatial coefficient of determination for WRF24, WF12 and WRF4 with TRMM steadily increases with increasing resolution but generally remains comparable, revealing no distinct improvement in the explicit convection case.

Interestingly, although WRF7 shows the worst results in terms of absolute precipitation amounts with the highest bias and an MAD of 2.2 mm day^{-1}, it provides the best correspondence of the monthly precipitation pattern with a coefficient of determination of 0.7 in comparison to TRMM.

In summary, the improvement of rainfall patterns by explicit convection is small for spatio-temporally averaged precipitation. Here, a shift of the lateral boundaries of the WRF domain provokes a more pronounced difference than a change from parameterized to explicit convection. Another reason why WRF4 performs worse than WRF7 might be the nesting approach, which imposes any errors introduced by the cumulus parameterization in WRF12 onto WRF4. The close correspondence between WRF12 and WRF4 shows that, on average, WRF4 is not able to diverge much from its outer parent. WRF7 on the other hand is directly forced by ERA-I which avoids the potentially negative effects of a parent domain.

Table 5.1: JAS 1999 average precipitation bias (mm day^{-1}), mean absolute deviation (MAD) and coefficient of determination (r^2) of the WRF simulations against TRMM.

Simulation	Bias	MAD	r^2
WRF24	-0.14	2.05	0.54
WRF12	-0.53	1.95	0.60
WRF7	0.91	2.20	0.70
WRF4	-0.63	1.90	0.63

5.3 Precipitation frequency and intense events

The previous section showed that simulated average rainfall patterns show only a slight improvement when using explicit instead of parameterized convection. However, the advantage of the explicit approach becomes more apparent when looking at the frequency of daily rainfall intensities (Fig. 5.3). There is a very good correspondence to station data between 1-50 mm day^{-1} for WRF4 and WRF7, while with parameterized convection, WRF12 and WRF24 overestimate (underestimate) the occurrence of precipitation rates below (above) 10 mm day^{-1}. This illustrates the lacking ability of the simulations using a cumulus parameterization to properly capture more intense precipitation events. ERA-I shows an even larger discrepancy to the observed datasets with a clear overestimation of weak precipitation events while no events above 20 mm day^{-1} can be captured at its resolution of 0.75°.
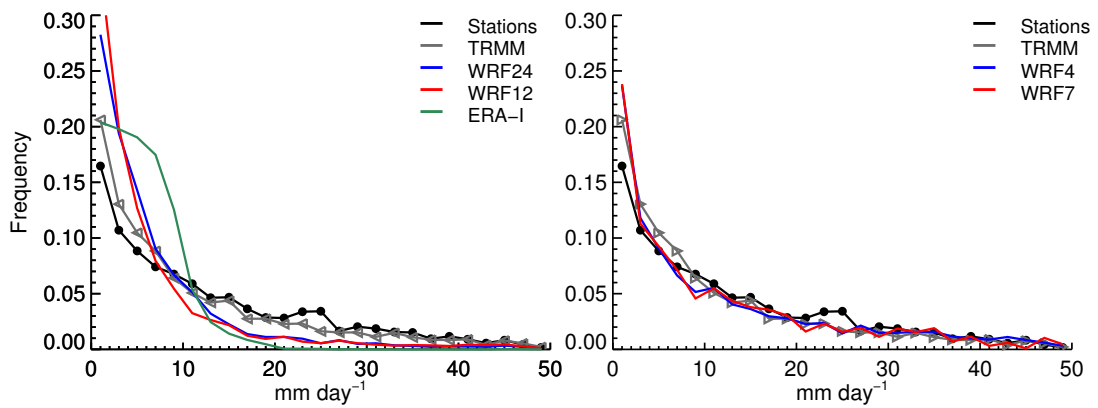
Figure 5.3: Frequencies of daily rainfall during JAS 1999 for TRMM, station data, ERA-I and WRF. The stations (cf. Fig. 5.1a) are compared to the smallest-distance grid cell values for each dataset.
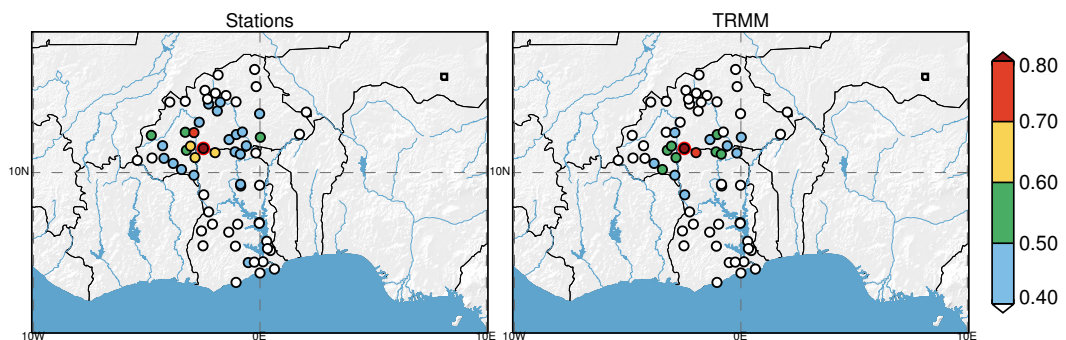
Figure 5.4: Correlation maps of JAS 1999 daily precipitation between the location of the weather station in Boura (red circled point) and the other station locations for the station dataset and TRMM (nearest grid cells). The black square in the upper right in each map indicates the size of a TRMM grid cell (0.25°x0.25°).

Interestingly, the frequency distribution of TRMM closely matches that of the stations in spite of a relatively coarse resolution of $0.25°$ (~ 27 km). This suggests that in many cases, the daily mean precipitation over 30x30=900 km^2 (approximately TRMM resolution) is representative for the daily rainfall intensity at a certain point in this area (point measurements, e.g. weather stations). An explanation might be the predominance of MCSs during the WAM since these are characterized by contiguous precipitation areas of at least 2000 km^2 (or 100 km in one direction) (Houze, 2004). To get an impression of the scale that is affected by similar rainfall events, Fig. 5.4 shows the temporal correlation of daily rainfall during JAS 1999 of the station Boura with all other station locations for station data and for TRMM. Although this is just an example for one station location, it illustrates that the daily rainfall at one location can be closely correlated with regions at a distance of 30 km and more, which could explain the good correspondence between the station data and TRMM.

To further evaluate how well regional differences in intense events are captured, Fig. 5.5 shows the number of days that are needed to reach 50% of the total precipitation during JAS for TRMM and all WRF simulations. For each pixel, the days are sorted from the highest to the lowest rainfall amount, which are then cumulated in this order until 50% of the total rainfall during the whole time period is reached. The number of days that are accumulated until the 50% value per pixel is reached is shown in the figure.

From TRMM, only 3-9 days of rainfall make up half of the total rainfall at the edges of the monsoon rainband to the North ($\sim 14°$N) and to the South ($\sim 7°$N), while in the center around 10°N the number increases to 9-15 days. WRF24 and WRF12 are not able to reproduce this meridional distribution but tend to generally overestimate the number of days that is necessary to reach the 50% threshold, which is in line with their overestimation (underestimation) of weaker (intense) precipitation events (Fig. 5.3). Similarly in line with Fig. 5.3 is the relatively good accordance of WRF4 and WRF7 to TRMM, in which WRF4 however shows a weaker performance than WRF7. This could again be related to the already mentioned nesting disadvantage of WRF4.

In summary, although the added value of convection-allowing simulations might not always be significant for spatio-temporally aggregated applications, there is a distinct improvement in the representation of daily precipitation intensities and its spatial distribution with explicitly treated convection.
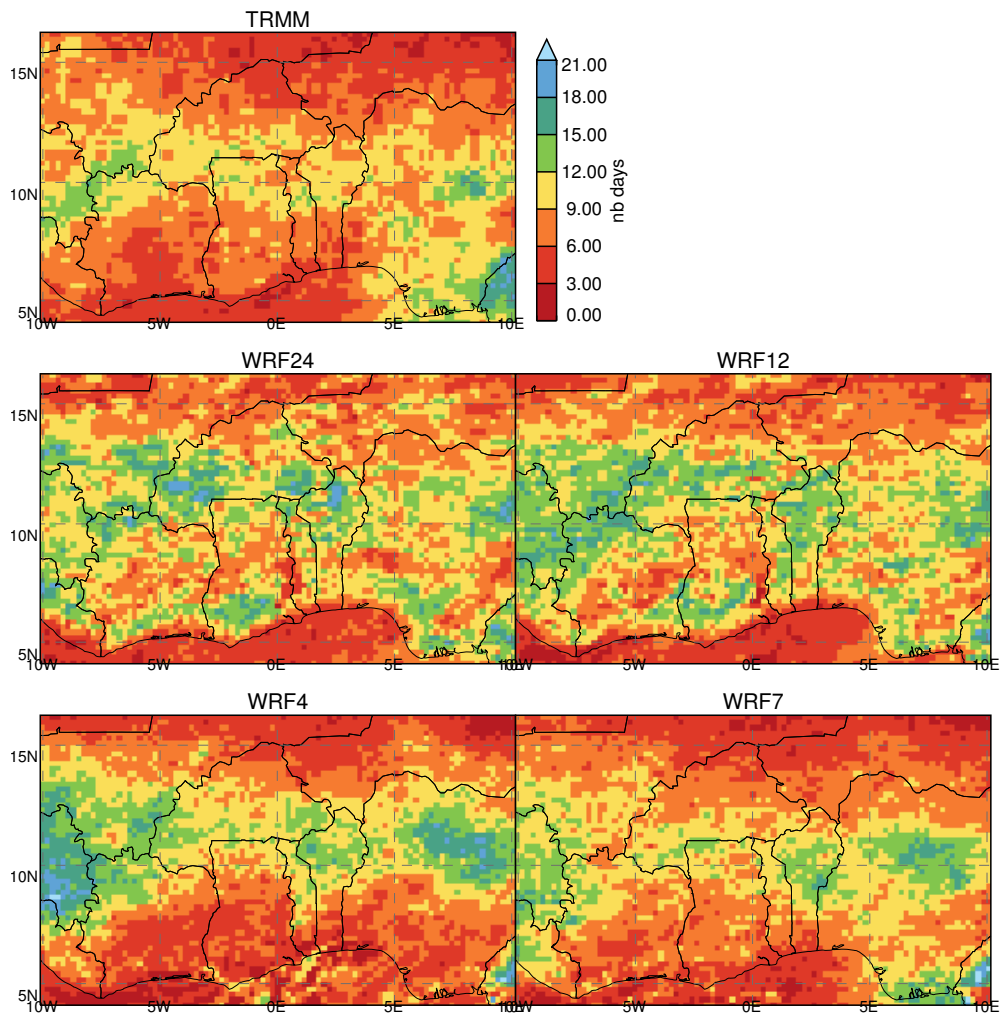
Figure 5.5: Number of days needed to reach 50% of the total precipitation amount during JAS 1999 for TRMM and WRF.

5.4 Propagation of mesoscale convective systems

Different from single, typically short-lived convective cells, MCSs consist of several organized deep-convective cells with a shared circulation system that has a much longer lifetime than its constituent clouds. The apparent forward movement of these large convective clusters, which is often referred to as MCS propagation, is not only the result of single convective cells moving with the mean wind but is also determined by the development of new cells at the flanks of the cluster (Corfidi, 2003). The evolution of new convective cells and subsequent MCS propagation during the WAM is often coupled to large-scale forcings such as AEWs on the one hand but on the other hand it is influenced by boundary layer states, cold pools and small-scale circulations.

In spite of the fact that convective parameterizations cannot directly take into account the latter effects, Stensrud et al. (2000) point out that most of them are nevertheless able to reproduce the path of an MCS. However, this ability seems to be case-dependant: Davis and Manning (2003) note that convective parameterizations used at grid spacings > 10 km have difficulties in simulating propagating convection since they act independently in individual model columns and therefore cannot properly maintain organized convection.

The ability of WRF to reproduce rainfall propagation with parameterized (WRF24, WRF12) and explicit (WRF7, WRF4) convection is assessed by comparing the meridionally averaged daily rainfall for two example periods during August and September to TRMM in Fig. 5.6 and 5.7. Indeed, WRF24 captures three propagating MCS events between 01.-15. September visible in TRMM (Fig. 5.6). However, the performance is worse for the period from 01.-15. August, where a lot of slight drizzle is produced and the rainfall track is barely visible. For comparison, the same time periods are given for WRF7, by which the storm propagations are quite well captured during both months.

The fact that both, WRF24 and WRF7, are able to capture the approximate point in time when MCSs occur, though sometimes with a positive/ negative lag of one day depending on the simulated propagation speed, implies that these systems are mainly dynamically driven via the ERA-I boundary forcing. The meridional averaging visualizes the propagation of convective activity rather than the propagation of a certain MCS, which is ultimately related to AEWs passing through the domain. However, the resulting convection seems to be better captured by WRF7. In comparison to WRF4, WRF7 shows slightly higher rainfall intensities (Fig. 5.7), which might be related to the attempt of the model to create convective circulations at 7 km resolution: Weisman (1997) found that convective circulations are too slow and their size and mass transport are spatially overestimated in low resolution simulations (8-12 km) when compared to convective up- and downdrafts at realistic length-scales. This overestimation of convective updrafts, and therefore of transported latent heat, can ultimately lead to an MCS intensification and increased rain rates. Nevertheless, they point out that their 8-12 km simulations are able to qualitatively capture the grid-scale circulations and propagation of the investigated MCSs, as is also found here.

A higher resolution can also help to better capture the storm propagation when a convective parameterization is used, as shown by WRF12 outperforming WRF24 (cf. Fig. 5.7 and 5.7). WRF12 captures all four rainfall tracks in September but the event that travelled through the domain from 12.08-15.08 was not simulated at all. In the case of the nested WRF4, certain propagation features are better resolved than in WRF12 (e.g. 10.-15.08), proving that the child can improve the representation of convective systems even if driven by an imperfect parent.

As already mentioned, the analysis of MCS propagation by meridionally averaging rainfall over a box does not identify single MCSs. Although the propagating rainfall is a good indicator for a convective activity continuously moving forward, the approach gives no information on the consistent simulation of an MCS (the averaged rainfall actually consists of disconnected 'splotchy' MCS) and therefore masks the real number of MCSs and potential problems of the convective parameterization to simulate them.
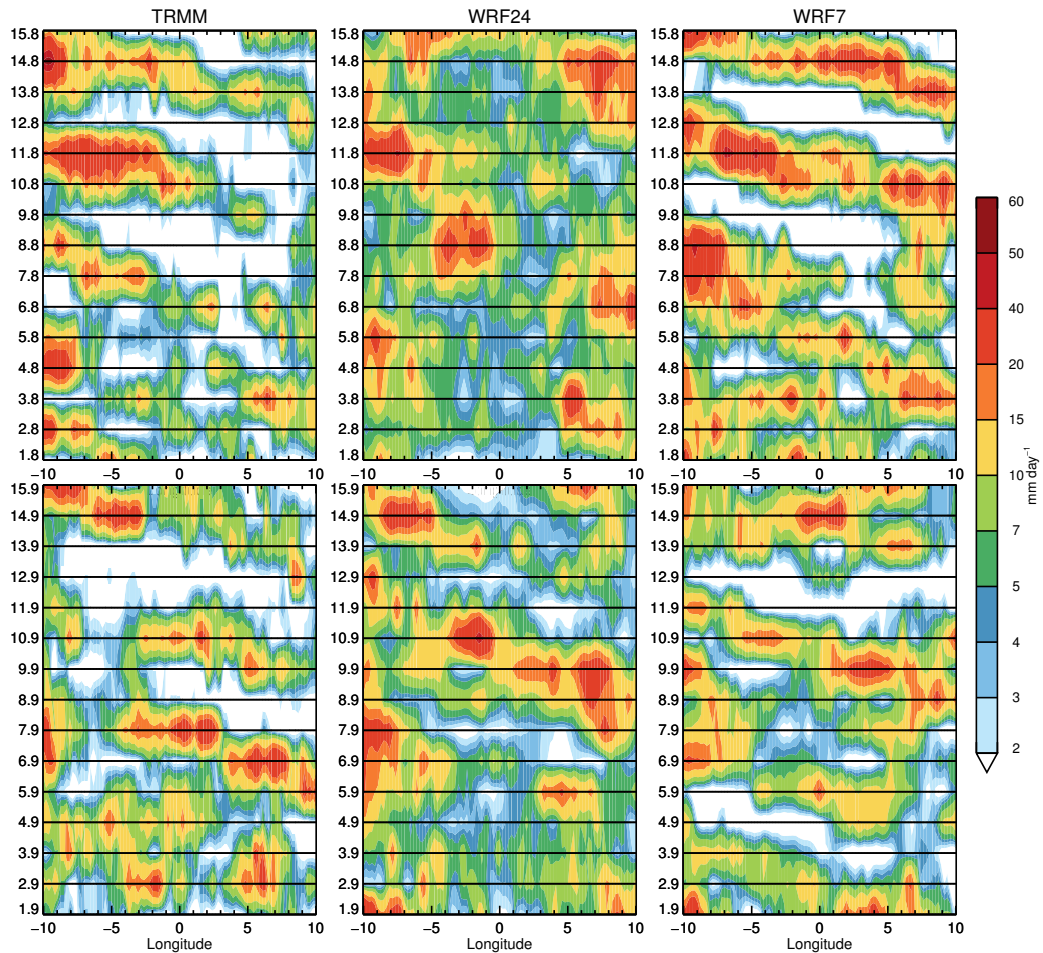
Figure 5.6: Longitude-time diagrams of meridionally averaged daily rainfall between 7-16°N for TRMM, WRF24 and WRF7 (mm day^{-1}) for the time periods 1.-15. August and 1.-15. September 1999.
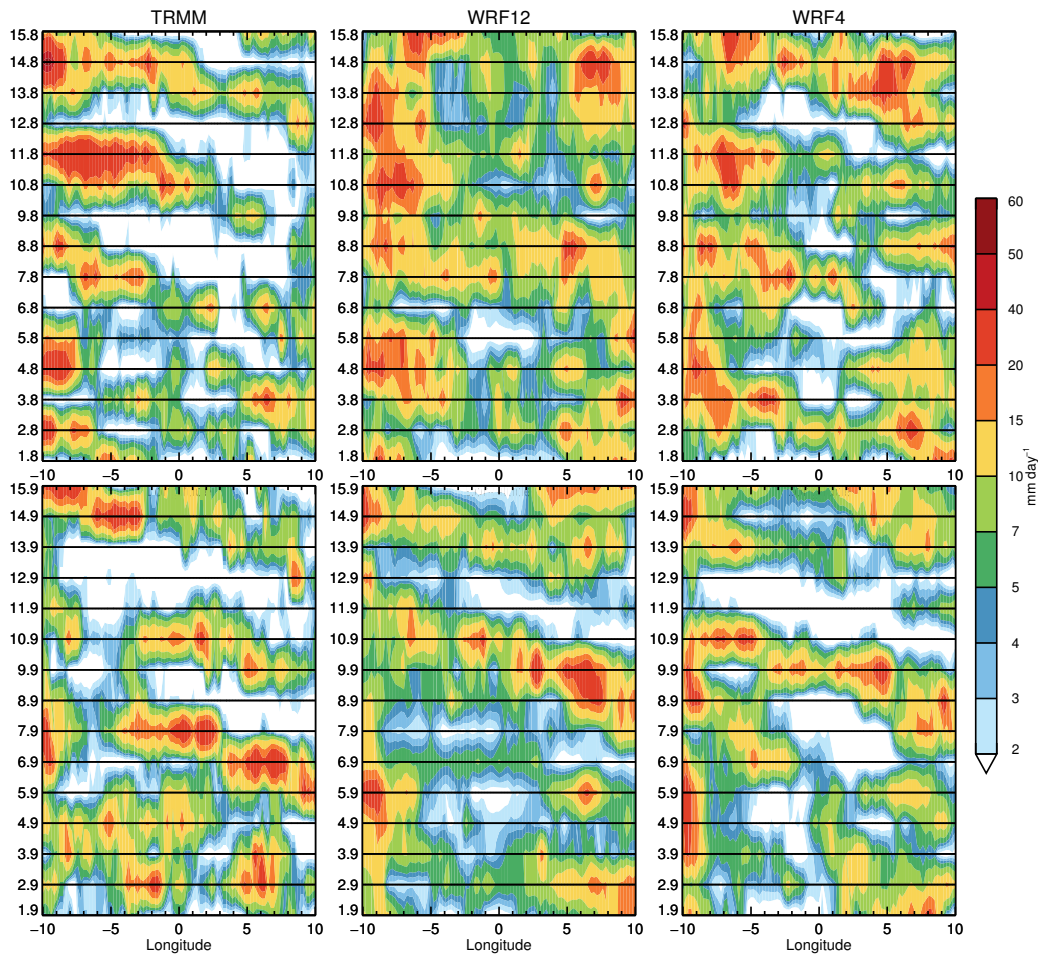
Figure 5.7: Same as Fig. 5.6 but for the nested pair WRF12 and WRF4.

An alternative to averaging over a region is to indeed track the particular convective system, as is shown exemplarily for two weeks in August in Fig. 5.8 for TRMM and WRF24. At 3-hourly time steps and averaged onto the TRMM grid, all continuous regions with rainfall of more than 1 mm h^{-1} are defined as a single system and are followed along as long as the rainfall overlaps for the following time step. If a system splits up (overlaps with two following systems), the tracker takes into account the larger system only. If a system merges, the smaller system from the previous time step is considered to have dissipated. Only systems that reach an extent of at least 10.000 km^2 and a lifetime of 6 hours are kept. The minimum area is larger than the usual definition for an MCS ($\sim 4000 \text{ km}^{-2}$) to take into account that, as the system moves forward within one time step, the 3-hourly average gives a stretched area of rainfall instead of the size of an instantaneous system. Figure 5.8 indicates the identified center point of the particular MCS at a certain point in time.
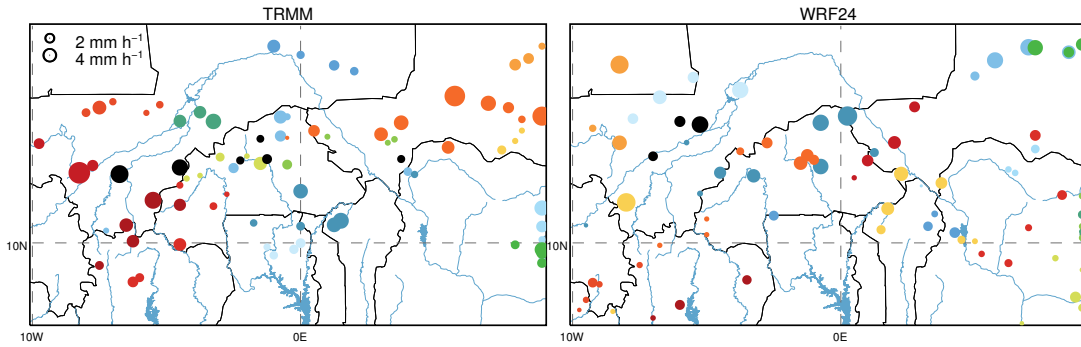
Figure 5.8: MCS tracks for TRMM and WRF24 from 1.-15. August 1999. Different colors indicate different systems. The circle size gives an impression of the average rainfall intensity (mm h^{-1}).

Table 5.2: August-September 1999 MCS number, lifetime (hours) and intensity (mm hour^{-1}) for TRMM and all WRF simulations.

	Number	Lifetime	Intensity
Simulation			
WRF24	255	9.7	2.2
WRF12	262	9.5	2.1
WRF7	219	10.9	2.6
WRF4	225	11.3	2.8
TRMM	196	11.1	3.2

With this method, WRF24 and WRF12 exhibit a comparable number of MCS during August and September but more than the explicit cases (Table 5.2). At the same time, the average MCS lifetime is about 1.5 hours shorter than for WRF4 and WRF7. The fact that both, system number and lifetime, corresponds better to TRMM for the explicit than for the parameterized cases suggests that the mechanisms that lead to a continuous, propagating system are indeed better captured with explicit convection. If the parameterization fails to trigger convection in the adjacent grid cells, a convective system might dissipate too early or might be triggered again at some distance where the tracker is not able to attribute the precipitation to the previous MCS. This would ultimately lead to higher tracked MCS numbers but shorter lifetimes.

5.5 Clouds and incoming solar radiation

It was demonstrated in Section 4.4 that turbulence parameterizations modify the evolution of clouds and related incoming solar radiation, which can significantly influence the modelled WAM state. The question remains whether the model resolution and the utilization of a convective parameterization also affect the modelled distribution of clouds.

The comparison of the meridional cross sections of the cloud fraction for the WRF simulations in Fig. 5.9 shows that there are distinct differences between the cases with and without convective parameterization. Since there exists no observational dataset for cloud fraction in 1999, the GOCCP cloud fraction climatology from 2006-2012 is used as an indicator for the average characteristics of vertical cloud distribution. The overall patterns are reasonably captured in all simulations, although WRF24 and WRF12 exhibit a second cloud fraction maximum at 650 hPa. This is visible neither in GOCCP nor in the two explicit WRF simulations. On contrary, the layer around 650 hPa constitutes a minimum in cloud cover for GOCCP. This is also in line with (Stein et al., 2011, their Fig. 6), who combined CloudSat and CALIPSO data and analysed the cloud fraction climatology from 2006-2009 over West Africa, suggesting that the 650 hPa maximum in WRF24 and WRF12 is a parameterization artefact. There is however a second maximum in GOCCP in the low-levels situated at 5-7°N above the coast, indicating increased cloud cover from frictional uplift when the monsoon winds hit the continent. Such a maximum is also visible in WRF7 and WRF4, although it is weaker and shifted northward further inland.

Generally, the cloud cover for WRF7 and WRF4 is spatially extended above 550 hPa in comparison to WRF24 and WRF12. The maximum average cloud cover of 20-25% coincides for all simulations between 250-150 hPa, but likewise covers a larger area for the simulations with explicit convection. Different from WRF4, the higher values of cloud fraction reach into the mid-levels at about 500 hPa for WRF7. This could again be related to the resolution-dependent underestimation of the velocity of convective updrafts, as discussed in the previous section. For example, Bélair and Mailhot (2001) conducted simulations at 6 km resolution with the Mesoscale Compressible Community model and also find overestimated condensation in the mid-levels.

However, both, WRF4 and WRF7 improve the northward extent of cloud cover with respect to GOCCP. Although the WRF simulations cannot be directly compared to the GOCCP climatology, the modelled northward extent of clouds should display a maximum positive anomaly since the WAM was extraordinarily strong in 1999.

Additionally, an elongated region of increased cloud cover north of 17°N is simulated between 450-550 hPa in WRF4, comparable to GOCCP. Ansmann et al. (2008) identify these clouds as a layer of altocumulus that form at the top of the SAL, especially under high dust concentrations. Since WRF does not take into account any effects of Saharan dust this might be a reason why the cloud fraction is underestimated over this region. The reason why only WRF4 captures these altocumulus clouds more clearly might be that it better resolves the shallow convection over the Sahara region (cf. Fig. 2.3).
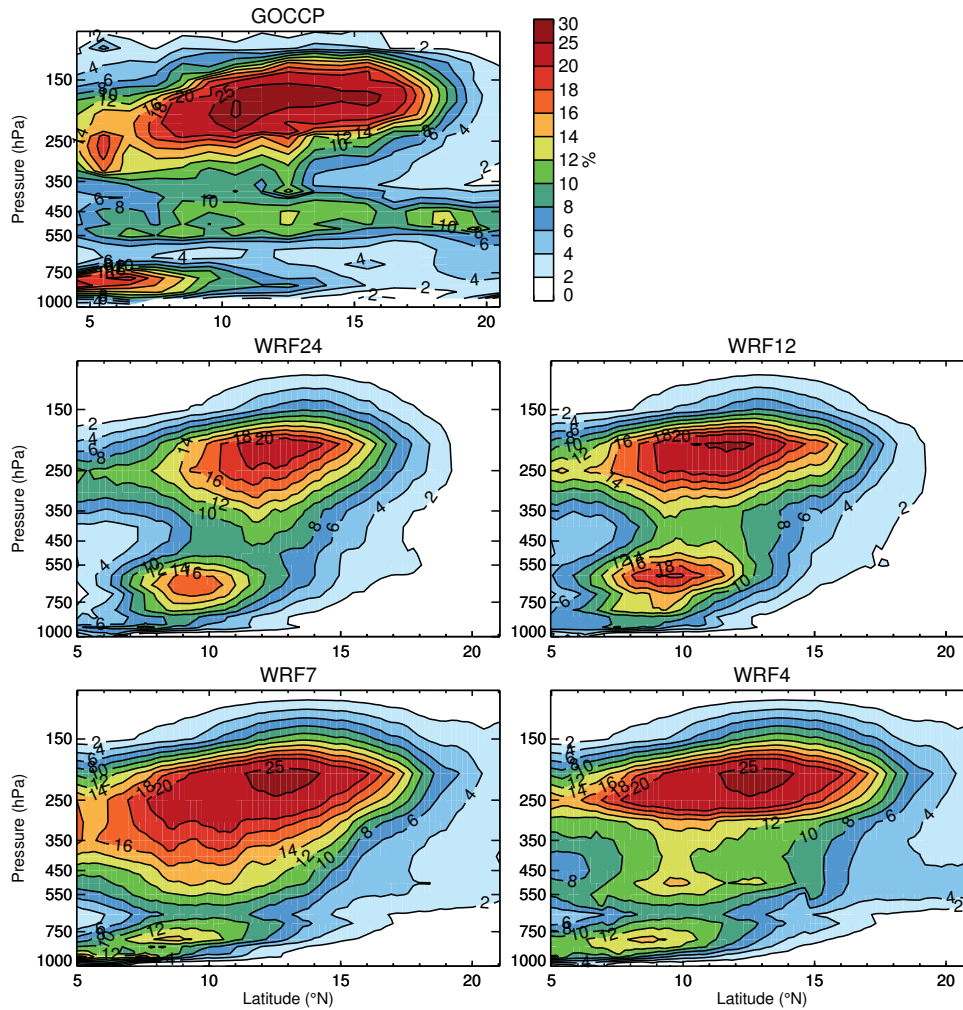
Figure 5.9: Meridional cross sections of the zonal averaged cloud fraction over 10°W-10°E for the JAS 2006-2012 GOCCP climatology and for all WRF simulations in JAS 1999.

Stein et al. (2011) point out that the Saharan cloud cover is a critical factor for climate models, since they usually have difficulties to simulate any attenuation of solar radiation in that region, which negatively affects the radiation budget at the surface. A look at the simulated shortwave incoming radiation for WRF24 and WRF12 in comparison to METEOSAT in Fig. 5.10 confirms a positive bias of mostly 25-50 W m^{-2} in the Saharan region, which might negatively affect the simulated monsoon circulation (Marsham et al., 2013). To the South, for which the incoming radiation was already adjusted and validated in Section 3.5.5, the bias remains either small or is negative in mountainous regions. The positive bias north of 15°N is significantly reduced in many regions for WRF7 and even more so for WRF4, underlining the importance of cloud representation in that region and the positive impact of an explicit treatment of convection.
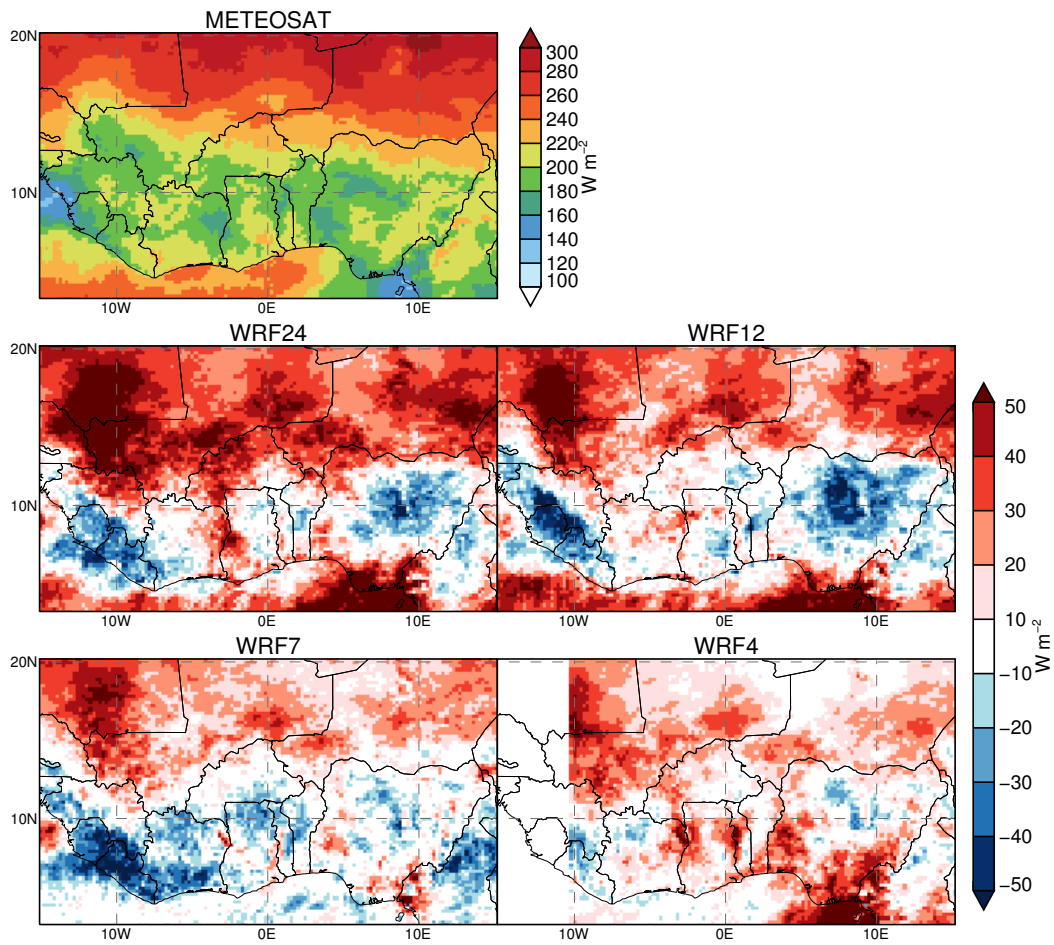
Figure 5.10: JAS incoming shortwave radiation for Meteosat and the biases for all WRF simulations (W m^{-2}). The white area for WRF4 indicates the end of the WRF4 domain.

5.6 Representation of the diurnal cycle

A typical problem of convective parameterizations is their inability to correctly capture the diurnal cycle of rainfall (e.g. Nikulin et al., 2012). For WRF24, it was already shown in Fig. 4.7 that all three tested cumulus parameterizations in Chapter 4 either showed the convective peak too early during the day or were generally underestimating the diurnal cycle.

Since only BMJ is used for this analysis, WRF24 and WRF12 exhibit the already identified shift of the convective minimum and maximum of 9h and 15h, as opposed to 12h and 18h for TRMM (Fig. 5.11). In the Sudano-Sahel however, the rainfall amount remains constant after 15h, while at the Guinean coast, rainfall amounts drop, inducing a considerable bias compared to TRMM. The overall diurnal cycle is similar for WRF24 and WRF12 with somewhat less precipitation in the case of WRF12.

Here, both explicit simulations remove the phase shift in rainfall in the Sudano-Sahel and capture the distribution of rainfall amounts during the day similarly well (Fig. 5.11). At the Guinean Coast, only WRF7 is able to reproduce the diurnal cycle with an average overprediction of 0.04 mm h^{-1}, while precipitation in WRF4 remains weak with almost no diurnal cycle. This is most likely linked to the distinct coastal dry bias in WRF24, WRF12 and WRF4 (cf. Fig.5.2) and correspondingly to the wet bias for WRF7.
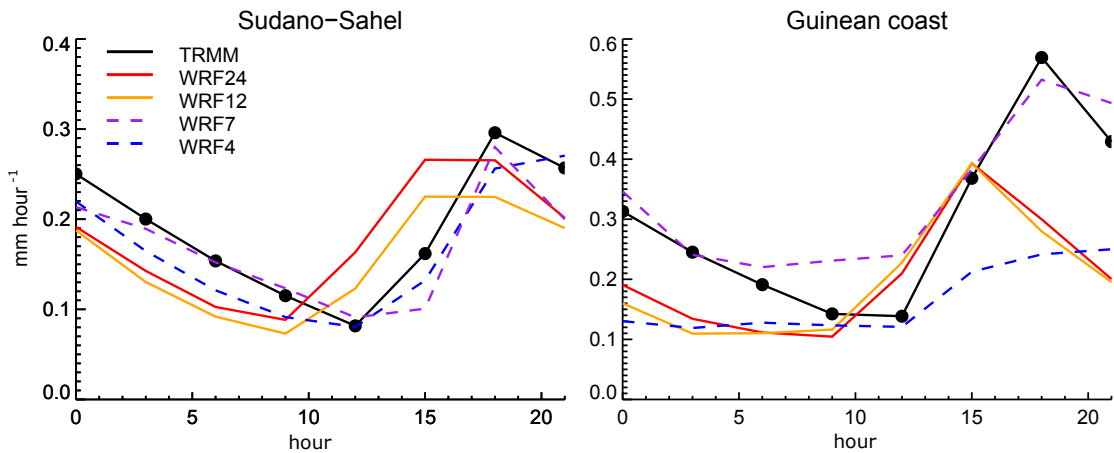
Figure 5.11: JAS 1999 average diurnal cycle of precipitation (mm hour^{-1}) in the Sudano-Sahel and at the Guinean coast (cf. Fig. 5.1) for TRMM and the WRF simulations with parameterized (solid lines) and explicit (dashed lines) convection.

5.7 Discussion and conclusions

This experiment investigated the representation of rainfall, clouds and related incoming solar radiation in the WRF model with parameterized and explicit convection during the WAM 1999 with the aim to (Section 1.2):

- assess the deficiencies of parameterized convection as compared to physically explicit convection and arising consequences for the simulated WAM and rainfall characteristics

- test the validity of simulation results with explicit convection in the convective grey scales above 4 km resolution

Two simulations at 24 and 12 km horizontal resolution (WRF24, WRF12) with parameterized convection were compared to two simulations at 7 and 4 km horizontal resolution (WRF7, WRF4) with explicit convection, all driven by ERA-I. WRF4 is nested into WRF12 while WRF7 is directly driven by the reanalysis data.

Since the study of Weisman (1997), 4 km is considered to be the minimum horizontal resolution at which convective structures can be sufficiently resolved while conserving a reasonable transport of momentum and heat for large convective systems. They investigated the development of a squall line in a three-dimensional nonhydrostatic numerical cloud model with horizontal resolutions from 1 to 12 km. In their simulations, the net state of the system was well captured at 1-4 km but they point out that these resolutions are sufficient only for the representation of mesoscale structures of the squall line and not for the analysis of cellular-scale structures. At 8 and 12 km, they found overall aspects of the circulation still reasonably well represented but report a slower convective evolution with an overestimated heat transport and rainfall rates as opposed to the finer resolutions.

The findings here generally agree to those of Weisman (1997): compared to WRF4, WRF7 seems to produce unrealistically slow convective circulations that lead to increased cloud formation in the mid-levels of the troposphere and ultimately produces increased rainfall amounts.

Nevertheless, WRF7 performs surprisingly well given that the representation of rainfall patterns, intense precipitation events, the diurnal cycle and the propagation of MCSs is similar and sometimes superior to that of WRF4. In addition, both explicit simulations improve the representation of cloud cover, partly correcting a strong positive bias of incoming solar radiation that is found for the simulations that use a convective parameterization (WRF24, WRF12). At the coarser scales with a convective parameterization, the WRF simulations are not capable to correctly represent the distribution of clouds, the diurnal cycle of rainfall or to capture observed rainfall intensities, which is in line with Marsham et al. (2013). They emphasized the importance of the diurnal cycle of cloudiness and rainfall for the correct representation of the monsoon circulation. The explicit approach corrects the diurnal cycle by shifting the rainfall peak to later times during the day, as was found here. In their explicit simulations, this leads to more incoming

solar radiation and higher temperatures that strengthens the monsoon circulation during the day, while cold pools from convective systems during the night weaken the circulation. Opposed to that, their parameterized simulation exhibits a weakened monsoon during the day due to a too early rainfall peak and a too strong meridional circulation during the night.

Here, it was also found that the used convective parameterization, the BMJ scheme, seems to have problems with continuously simulating the propagation of MCSs, since WRF24 and WRF12 exhibit shorter MCS lifetimes than WRF4, WRF7 and the observational dataset. However, for a more robust tracking analysis, observed and modelled data should at least be available at time steps of one hour and in the best case exhibit a higher spatio-temporal resolution than the observational data used in this analysis (27 km, 3-hourly). Absolute numbers for any MCS characteristic (e.g. number of MCSs, size, lifetime) have proven to be very sensitive to the spatio-temporal resolution of the data, such that here, the method could just be used for comparative purposes but not for identifying de-facto MCS lifetimes, for example. In addition, rainfall instead of cloud cover or outgoing longwave radiation were used for tracking, such that the method is also sensitive to (dis-)continuous rainfall fields and therefore gives only a vague impression on correspondences / differences between the simulations.

A further factor that encourages the use of at least convection-allowing model set-ups, although not evaluated here, is the lacking ability of convective parameterizations to correctly represent interactions between the surface and the atmosphere. Hohenegger et al. (2009) analysed the simulated soil moisture-precipitation feedback of the Consortium for Small-Scale Modeling Model in Climate Mode at 25 and 2.2 km with and without convective parameterization, respectively, for one month over the Alps. They found a positive feedback for the 25 km case while it was negative for the explicit 2.2 km. They attribute the positive feedback to a missing sensitivity of the parameterization to stable air layers and a too strong dependence on moisture, while strong thermals over dry soils than can foster convection are underestimated. Taylor et al. (2012) likewise found a generally positive soil moisture-precipitation feedback during daytime for three evaluated GCMs with convective parameterizations during the WAM, while observational data suggested the opposite. This suggests that land-atmosphere interaction studies should generally avoid parameterized convection.

In summary, although WRF7 shows limitations in cloud formation and rainfall amounts, it seems nevertheless to be able to capture the mesoscale structures of the convective systems and considerably outperforms the parameterized approaches. The 7 km resolution allows a direct downscaling from ERA-I for a relatively large WRF domain. This avoids potential errors introduced by a parent domain in which parameterized convection is active. At the same time, the strong coastal dry bias visible in WRF24, WRF12 and WRF4 does not exist in WRF7. WRF7 therefore seems to be a reasonable compromise between a truly convection-resolving simulation that also allows land-atmosphere interaction studies and a computationally feasible set-up that can be directly driven by reanalysis data. It will thus be used for the following experiment as new WRF baseline set-up.

The effect of vegetation-atmosphere feedbacks on precipitation

Current research on land-atmosphere interactions in West Africa often focuses on the impact of soil moisture on precipitation due to changed surface fluxes, imposed surface heterogeneities or the pure amount of evaporated water increasing the atmospheric moisture.

Eltahir (1998) suggests that vegetation cover and soil moisture content might play the same role in the concept of land-atmosphere interactions. The important difference is that soil moisture anomaly patterns may only last for several days to weeks. Vegetation on the other hand is able to mobilize root zone soil moisture that would otherwise not be in contact with the atmosphere. Its anomaly patterns can last over weeks to months. It therefore imposes a lower boundary condition on the atmosphere that is effective over much longer time scales and furthermore reacts much slower to single precipitation events than surface soil moisture. Taylor (2008) hypothesizes that such slow intra-seasonal modulations could be especially important in the densely vegetated southern regions of West Africa as opposed to the barren Sahel, where the main response in latent heat fluxes is within a few days.

Several studies report a distinct sensitivity of WAM rainfall on vegetation changes at climatological time scales, where a positive vegetation-precipitation feedback dominates and results in an increased natural rainfall variability compared to cases without dynamic vegetation (e.g. Alo and Wang, 2010; Kucharski et al., 2012; Zheng and Eltahir, 1998). Besides natural land cover changes, anthropogenic vegetation perturbations are another important factor that can lead to considerable vegetation changes over a few years. Taylor et al. (2002) used a land use model to generate land use change scenarios for the Sahel between 1960 and 2015 that were implemented in a GCM to quantify the impact of land use change. The predicted increase of cropland by

9% and the loss of forest cover by 28% lead to a rainfall decrease of 8.7%. Hagos et al. (2014) fed an estimation of the land degradation in the Sahel between 1950 and 2010 to WRF and likewise found a rainfall reduction. They attribute the decrease to a southward shift of the AEJ associated with a modification of the meridional moisture and temperature gradients by the land use changes.

The often identified importance of vegetation variability on longer time scales rises the question whether this holds true for the interannual and seasonal scales, for which the quantitative vegetation changes are usually relatively small. Other than for soil moisture, the mechanisms by which vegetation patterns might directly affect the atmosphere and precipitation distribution are little discussed although such studies could profit from satellite-derived information on vegetation changes nowadays available at very high spatial resolution (e.g. Camacho and Cernicharo, 2015).

Li et al. (2007) used satellite-derived data at a rather coarse resolution of 1° to investigate the influence of LAI and green vegetation fraction (VF) on the annual and interannual modulation of the WAM between 1987 and 1988 with a GCM at ~ 300 km horizontal resolution. In accordance with mentioned climatological studies, they find a northward shift of the AEJ related to a modulation of the meridional temperature gradient. However, the coarse resolution in their study does not allow an investigation of vegetation impacts below the spatial scales of monsoon dynamics.

This experiment uses a new set of satellite-derived data for VF, albedo (ALB) and LAI at high spatial resolution to address the question how interannual changes of vegetation patterns may affect surface variables, atmospheric circulations and ultimately rainfall patterns at a local to regional scale. This surface data set has been recently generated specifically for the West African region including a novel high-resolution land use map.

The surface information is provided to the WRF model version 3.61 for the years 2009 and 2010 during the WAM. A control simulation with a fixed climatological annual cycle for VF, ALB and LAI during both years is used to remove the large-scale signal from the interannual changes of surface and atmospheric variables.

6.1 Experimental set-up and datasets

6.1.1 Analysis strategy

Two WRF ensemble experiments are conducted with (i) the observed state of surface variables (ALB, VF, LAI), that was derived from remote-sensing (DYN) and (ii) default climatological datasets with a fixed annual cycle (CLIM) for the rainy seasons April-September 2009 and 2010, including one month of spin-up. These two consecutive years show a negative and positive VF anomaly of $\sim$4% in the Sahel (cf. Fig. 6.3), making them a good test case for the impact of vegetation changes on the WAM. The two rainy seasons were simulated separately instead of conducting a continuous simulation in order to have the same integration time after the first soil moisture initialization for both years and to receive eight independent simulations per ensemble.

The two ensemble groups DYN and CLIM each consist of four members per year, for which the initial starting date is shifted by -0, -1, -2 and -3 days. This approach is taken to account for the fact that a surface-driven atmospheric signal is not straightforward to extract. Given the chaotic character of convection, feedbacks on rainfall might or might not occur in response to a surface change. Therefore, if not indicated otherwise, all analyses use the average of the perturbed DYN and CLIM four-member ensembles in order to reduce the noise from internal model variability and thus to get a more robust signal of the mean changes related to the new dynamical surface dataset. The analysis focusses on the representation of the interannual difference 2010-2009 (ΔY) for the dynamical DYN (ΔY_{Dyn}) and the static CLIM (ΔY_{Clim}) surface case. The difference between the two ensembles then gives the impact of the dynamical land surface (Srfc):

$$\Delta Y_{\mathrm{Srfc}} = \Delta Y_{\mathrm{Dyn}} - \Delta Y_{\mathrm{Clim}}. \tag{6.1}$$

ΔY_{Srfc} represents a 'vegetation-induced modulation of the large-scale driven changes' between 2009 and 2010. For example, a temperature change from 25 to 30°C in CLIM and a change from 25 to 26°C in DYN equals to -4°C for the vegetation signal ΔY_{Srfc}, which means that ΔY_{Srfc} can be negative although DYN exhibits an effective net warming.

The significance of ΔY_{Srfc} is given when the means of ΔY_{Clim} and ΔY_{Dyn} are significantly different from each other as estimated with a Student's t-test. The CLIM and DYN sample populations consist of 16 members each that arise from the 2010-2009 differences of all possible member combinations (the cartesian product of a 2010 and a 2009 vector). Note that the ΔY_{Srfc} for the surface variables ALB, LAI and VF correspond to ΔY_{Dyn} since ΔY_{Clim} is zero.

6.1.2 Model set-up

The model domain encompasses the whole WAM region as can be seen in Fig. 6.1. If not indicated otherwise, all analyses are carried out for the domain (9°W-9°E, $7 - 16$°N), focussing on the Sudanian zone and the Sahel to reduce effects from the ocean and the coastline.

Different model configurations and their impact on the representation of the WAM dynamics were already investigated by Klein et al. (2015) (Chapter 4). On this basis, the WRF model is run with the RRTM/Dudhia Long and Shortwave Radiation schemes (Dudhia, 1989), the LIN MP scheme (Lin et al., 1983) and the YSU PBL scheme (Hong and Lim, 2006). This configuration reproduces the WAM without showing an extreme wet or dry behaviour. The horizontal resolution is 7 km without using a CU scheme to explicitly capture the diurnal cycle of cloudiness and rainfall, which showed better results than simulations with CU schemes in Chapter 5. In addition, the explicit treatment of convection is crucial for the available energy at the surface (Marsham et al., 2013) as well as to represent certain processes impacting the land-atmosphere feedback, which are not taken into account by current CU parameterizations (Hohenegger et al., 2009).

6.1.3 The coupled land surface model

The choice of the LSM is a critical point in assessing land-atmosphere interactions since it solves the surface energy balance, whose partitioning strongly depends on the prevailing surface conditions:

$$R_{net} = SW_{in}(1 - ALB) + LW_{in} - \epsilon\sigma\, TS^4 = LH + SH + G, \qquad (6.2)$$

where SW_{in} and LW_{in} are the incoming shortwave (Wm^{-2}) and longwave radiation (Wm^{-2}) and ϵ, σ and TS are the surface emissivity, the Stefan-Boltzmann constant and the surface temperature (K), respectively. The left-hand side of this equation represents the budget of incoming and outgoing solar radiation and gives the available net radiation R_{net} (Wm^{-2}) at the ground. The net radiation is balanced by outgoing fluxes of latent heat (LH, Wm^{-2}), sensible heat (SH, Wm^{-2}) and the ground heat flux (G, Wm^{-2}).

Hagos et al. (2014) investigated the uncertainty in modelled changes of surface flux partitioning and precipitation changes due to land use change in West Africa for three different LSMs that are available in the WRF model. They found that an LSM that favoured a drier or wetter monsoon regime showed a lower sensitivity to land use changes in comparison to the intermediate case, since the evaporation from soils that are close to saturation or close to the wilting point does not vary significantly, even under land use change conditions. In their simulations, the Noah LSM showed an intermediate behaviour and the best performance with respect to observations for the modelled precipitation amounts and the meridional gradient of the evaporative fraction. Therefore, the WRF configuration used here still employs the Noah LSM.

The atmospheric part of the WRF model forces the Noah LSM with atmospheric variables such as incoming long- and shortwave radiation, near surface temperature, pressure, humidity and precipitation. The Noah LSM then calculates the outgoing radiation with respect to ALB and TS of the previous time step and thus provides the radiative forcing R_{net} at the ground (cf. Eq. 6.2). Altogether, four variables are fed back to the atmosphere: (i) LH (evapotranspiration), (ii) SH , (iii) outgoing longwave radiation (via calculation of TS) and (iv) upward shortwave radiation (reflected portion given by surface albedo).

To derive LH, the Penman potential evaporation E_p (kg m^{-2}s^{-1}, evaporation from an open water surface) is computed and adjusted according to the bare and vegetated portion of a model grid cell, which is determined by the green vegetation fraction VF. The actual evapotranspiration is the sum of the partial fluxes for direct evaporation E_{dir} (kg m^{-2}s^{-1}) from soil and the total plant transpiration E_t (kg m^{-2}s^{-1}) (evaporation from canopy and snow sublimation are neglected in this example) that are defined as

$$E_{dir} = (1 - VF)\beta E_p \tag{6.3}$$

and

$$E_t = VF\ E_p P_c (1 - (\frac{W_c}{S})^{0.5}), \tag{6.4}$$

where W_c is the amount of water intercepted by the canopy and S is the maximum water capacity of the canopy (set to 0.5 mm). In these equations, β and P_c represent resistance factors that act to reduce E_p. Both take into account the soil hydraulic properties and corresponding soil moisture availability but the plant coefficient P_c additionally includes plant type and root depth, the influence of heat stress, the water vapour deficit and incoming solar radiation and therefore incorporates the canopy resistance. In this framework, LAI is used to upscale the parameters incorporated in P_c that represent leaf stress (due to solar radiation, humidity, soil moisture, air temperature) to the entire canopy, where a higher LAI results in a lower canopy resistance (see Chen and Dudhia, 2001 for a detailed description). Consequently, E_t depends on all available moisture within the root zone while for bare soil, E_{dir} is simply a function of relative soil moisture availability in the first soil layer. The new surface temperature TS is computed iteratively in a linear approach and arises from the surface energy balance equation in the form of

$$SH = R_{net} - LH - G \tag{6.5}$$

with

$$SH = \rho C_p C_h U(TS - \Theta_{air}) \tag{6.6}$$

with the air density ρ (kg m^{-3}), the heat capacity of dry air C_p (Jm^{-3}K^{-1}), the surface exchange coefficient C_h, the wind speed U (m s^{-1}) and the potential temperature Θ_{air} (K).

Substituting SH in Eq. 6.5 with Eq. 6.6 and solving for TS then gives

$$\mathrm{TS} = \frac{\mathrm{R_{net}} - \mathrm{LH} - \mathrm{G}}{\rho \mathrm{C_p} \mathrm{C_h} \mathrm{U}} + \Theta_{\mathrm{air}}.$$ (6.7)

This summary of variable dependencies describes how state variables and surface fluxes directly react on changes in ALB, VF or LAI: ALB has a direct effect on $\mathrm{R_{net}}$ and therefore impacts the available energy for the turbulent surface fluxes. VF is the key parameter for the partitioning between bare soil evaporation and plant transpiration. The efficiency of the latter, and therefore the actual difference between bare soil evaporation and plant transpiration, is modified by the canopy resistance and thus by LAI. However, here, the objective is not to disentangle the separate effects of these intrinsically connected surface parameters, but to investigate whether their 'bulk effect' leaves an imprint on the atmosphere. As an approximation, the presented feedback analyses therefore use VF changes as a proxy for associated changes of all three variables.

6.1.4 Reference datasets

The model simulations are compared to different satellite, observational and reanalysis data to evaluate their capability to capture the monsoon regime and interannual differences between 2009 and 2010.

Precipitation   Reference datasets comprise TRMM 0.25° resolution 3B42V7 and 3B43V7 (monthly) rainfall estimates (Huffman et al., 1997), the African Rainfall Estimate version 2 (RFE) (NOAA CPC, 2013) 0.1° resolution product and the 0.25° resolution global Climate Prediction Center Morphing technique (CMORPH, Joyce et al., 2004) dataset. All three are comparably high-resolution datasets and available at daily resolution. RFE is a combined satellite-gauge data product, operationally provided by the Climate Prediction Center (CPC). It is available for the African continent starting in 2001. RFE rainfall is merged from three satellite datasets and afterwards fitted to gauge measurements. It is used for operational hazard warnings with a focus on daily rainfall development where it however tends to show a consistent dry bias compared to other precipitation datasets (Novella and Thiaw, 2013). Different from the other datasets, the CMOPRH 'morphing technique' is not an algorithm for precipitation estimation. It describes a technique to combine motion vectors derived from geostationary satellite infrared imagery with precipitation estimates from passive microwave data such as the TRMM sensor (Joyce et al., 2004). It is therefore especially reliable in capturing the position and the track of precipitation systems while the absolute amounts are rather overestimated in West Africa (Wolters and Roebeling, 2011). It is available starting from 2003 on a near real-time basis.

Surface temperature   Model surface temperatures are again compared to the GHCN 5° gridded temperature product Version 3 (Lawrimore et al., 2011). In addition, the University of Delaware (UDEL) 0.5° station-analysis product (Legates and Willmott, 1990) and the station-data based Climatic Research Unit (CRU) time series 3.21 0.5° product (Harris et al., 2013) are used.

All three datasets are available at only monthly resolution starting in 1900 and being continued at an irregular basis. The CRU dataset is based on more than 4000 meteorological stations, which are converted to anomalies with respect to 1961-1990, before being gridded to 5° resolution. After interpolation, the temperatures are adjusted to actual values by adding on the climatological normals. Interpolation is performed by considering the correlation decay distance. UDEL is primarily based on station observations from GHCN. It is produced through interpolation of station anomalies, which are then combined with an equivalent gridded climatology to produce estimates of the monthly temperature. All three temperature datasets rely entirely on station data, making them relatively unreliable in West Africa, especially at smaller scales. There is also a considerable dependance between the datasets due to the small number of stations, attributing differences mainly to differing interpolation techniques (Vose et al., 2012). Therefore, the datasets are only used for analyses of the subcontinental-scale averages here.

Turbulent surface fluxes   Due to the small amount of available flux tower data in West Africa, the information on surface fluxes is probably the most uncertain. One of the few gridded products for latent and sensible heat fluxes is the FLUXNET Multi-Tree Ensemble (MTE) at 0.5° (Jung et al., 2011). MTE is a machine learning technique that is trained to predict turbulent fluxes based on remote sensing indices, land use information and meteorological data. The resulting flux fields are available from 1982 to 2008 and were validated in cross-validation procedure with EC measurements. However, since there are only eight active flux towers in whole West Africa contributing to FLUXNET (DAAC, 2013), the MTE results primarily rely on the machine learning algorithm interpreting other available informations. Hence, the quality of this dataset in West Africa is highly uncertain. Therefore, the reanalysis-based products ERA-Interim/LAND (Balsamo et al., 2015), available from 1979-2010, and MERRA-Land (Reichle et al., 2011), starting in 1979, are additionally used for comparison. Both are land-only reanalysis products from offline simulations with updated land surface models and a new precipitation forcing from gauge data, especially created for land surface and flux studies. Both datasets are relatively new and were not specifically validated in West Africa yet. Lorenz and Kunstmann (2014) note a consistent overestimation of LH for MERRA-Land in different regions of the world but did not include West Africa.

Soil moisture   Soil moisture estimates are taken from the 0.5° gridded CPC soil moisture (V2) dataset (Van Den Dool et al., 2003). This dataset is calculated at real time starting in 1984 by a one-layer bucket water balance model using independent precipitation and temperature datasets that are not used here. The model results compare well to the limited number of in-situ measurements in the United States, China, India, Mongolia and Russia, capturing the annual cycle and interannual variability (Fan, 2004). In addition, first comparisons to the Gravity Recovery and Climate Experiment dataset reveals close similarity.

Atmospheric dynamics   The monsoon dynamics are compared to ERA-I data.

If not indicated otherwise, all data, including WRF, is transformed (averaged) onto the grid of coarsest resolution of the different datasets used for the analyses.

6.2 The dynamical land-surface parameters

In order to represent spatio-temporal land surface changes in the WRF model, new dynamical land-surface parameters for ALB, VF and LAI (DYN) are integrated to replace the default monthly climatological datasets (CLIM). The used surface datasets are summarized in Table 6.1.

6.2.1 Generation and implementation of the dynamical datasets

The LAI_{Dyn} and VF_{Dyn} time series were created by fusing LAI and VF datasets derived from data of the Spinning Enhanced Visible and Infrared Imager (SEVIRI, LSA SAF, 2013) and Satellite Pour l'Observation de la Terre-VEGETATION (SPOT_VGT, Baret and Weiss, 2010; Camacho and Cernicharo, 2015). The SPOT_VGT-based datasets provide good quality information on LAI and VF in 10-day intervals at 1 km spatial resolution, but show frequent cloud gaps during the rainy season, while the SEVIRI-based daily datasets exhibit fewer cloud gaps but at a coarser spatial resolution of 3 km (Gessner et al., 2013). Both datasets were aggregated to a spatio-temporal resolution of 1 km and 10-daily intervals. The SEVIRI datasets were matched to SPOT_VGT values based on slope and offset of three linear regressions fitted for gap unaffected areas and three seasons (Jan-Mar, Apr-Sep and Oct-Dec). Finally, the cloud gaps in the SPOT_VGT products were filled with the adapted SEVIRI-based LAI and VF values. Remaining outliers in the time series were removed and remaining gaps were filled by temporal linear interpolation.

Table 6.1: Land surface datasets for albedo (ALB), green vegetation fraction (VF) and leaf area index(LAI) used in the WRF model: dynamical datasets for the region (9°W-10°E ; 4-16°N) (DYN), dynamical global datasets (GLOB) and the global default WRF climatology datasets (CLIM).

Name	Time step	Resolution	Time period	Source	Reference
DYN					
ALB_{Dyn}	monthly	$\sim$ 1km	2000-2014	MCD43B3	LP DAAC (2014)
VF_{Dyn}	10-daily	$\sim$ 1km	2007-2012	SEVIRI/ SPOT_VGT	Camacho and Cernicharo (2015), Gessner et al. (2013)
LAI_{Dyn}	10-daily	$\sim$ 1km	2007-2012	SEVIRI/ SPOT_VGT	Camacho and Cernicharo (2015), Gessner et al. (2013)
GLOB					
ALB_{Glob}	10-daily	$\sim$ 1km	1999-2015	SPOT_VGT	Camacho and Sánchez (2015)
VF_{Glob}	10-daily	$\sim$ 1km	1999-2015	SPOT_VGT	Camacho and Cernicharo (2015)
LAI_{Glob}	10-daily	$\sim$ 1km	1999-2015	SPOT_VGT	Camacho and Cernicharo (2015)
CLIM					
ALB_{Clim}	monthly	$\sim$ 17km	1985-1991	AVHRR	Csiszar and Gutman (1999)
VF_{Clim}	monthly	$\sim$ 17km	1985-1991	AVHRR	Gutman and Ignatov (1998)
LAI_{Clim}	monthly	$\sim$ 3km	2001-2010	MODIS	Kumar et al. (2014)
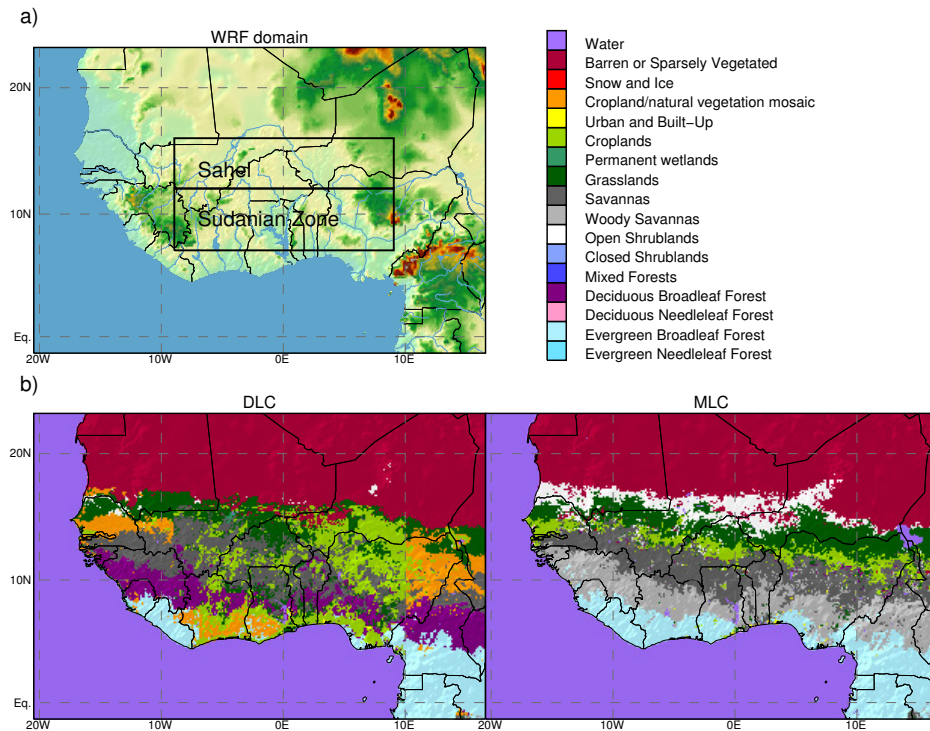
Figure 6.1: (**a**) WRF domain with indicated study region and sub-regions in the box ($9°W - 9°E, 7 - 16°N$), (**b**) *left:* regionally optimized land use classification (DLC) for the simulations with dynamical surface parameters (DYN), *right:* MODIS land use classes (MLC) for the WRF default case (CLIM).

The ALB$_{Dyn}$ time series is based on the bi-hemispherical reflectance (white-sky albedo) for the shortwave spectral range of the MODIS MCD43B3 product (LP DAAC, 2014). The MCD43B3 is a composite product based on 16-day intervals at 1 km spatial resolution. Like for LAI and VF, the product features gaps, especially during the wet season. To generate a gap free input, the product was aggregated to monthly composites by calculating the mean of corresponding months. The remaining data gaps were filled with long-term monthly mean values (15 years: 2000-2014). Finally, the time series underwent temporal smoothing using the Savitzky-Golay filter (William et al., 1992).

The DYN datasets for ALB, VF and LAI only span the focus study region $9°W$-$9°E$, $4 - 16°N$. In the rest of the WRF domain, global datasets (GLOB, Table 6.1) for broadband white-sky ALB, VF and LAI from SPOT_VGT are used to provide dynamical surface information. These datasets were found to correspond well to the DYN datasets. Sporadic remaining gaps due to cloud cover in GLOB are filled with the GLOB long-term mean value for the respective pixel and month.

All datasets shown in Table 6.1 are linearly interpolated to 6-hourly timesteps to act as boundary input for the WRF model. Spatially, the datasets are interpolated (coarser datasets) or regridded and averaged (finer datasets) to the model grid at 7 km resolution.

Other necessary land surface parameters (e.g. surface roughness, root zone depth) rely on table values that are associated with a certain land use classification. Therefore, a regionally optimized land use classification (DLC, Table A.2) map at 250 m spatial resolution, based on the year 2006 (Gessner et al., 2015), is additionally implemented in the model in order to ensure consistency of the assigned table values with the new DYN datasets. Figure 6.1(b) shows the 7 km upscaled maps of DLC and the WRF default 1 km MODIS land classification map based on 2002 (MLC, Table A.1, Friedl et al., 2010). The 7 km upscaled DLC and MLC consider the dominating land class only.

6.2.2 Comparison of dynamical and climatological datasets

There is a considerable albedo offset between DYN and CLIM, illustrated in Fig. 6.2, with a mean deviation of 2.4% in the Sahel and 1.9% in the Sudanian zone which arises because ALB_{Dyn} is based on MODIS shortwave broadband white-sky albedo, while ALB_{Clim} represents Advanced Very High Resolution Radiometer (AVHRR) broadband black-sky albedo.
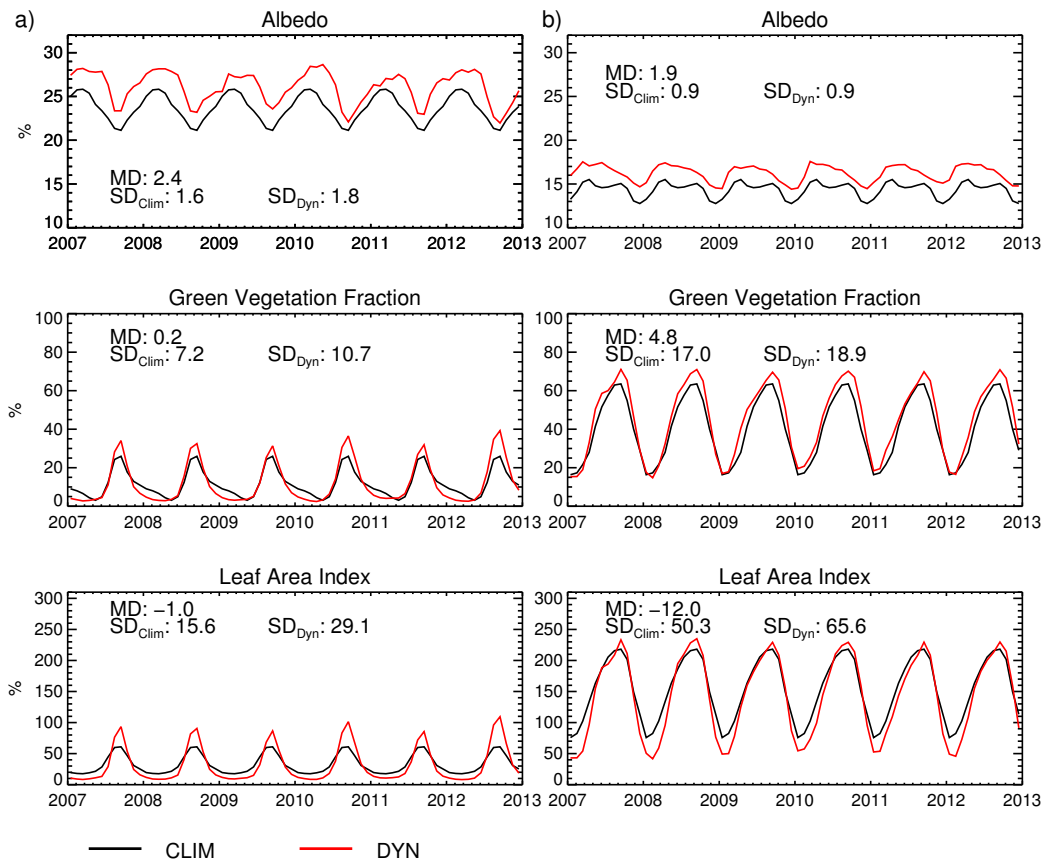
Figure 6.2: Annual cycles of the dynamical datasets (DYN) in comparison to WRF default climatologies (CLIM) in (**a**) the Sahel and (**b**) the Sudanian zone for the available time period of the DYN datasets. Additionally, the mean deviation between CLIM and DYN (MD) and the standard deviation (SD) for each dataset are given.

While the black-sky albedo represents the directional surface reflectance at local solar noon under clear sky conditions (100% directional light source), the white-sky albedo is the reflectance for diffuse conditions (100% diffuse light source). The actual albedo emerging from a mixture of directional and diffuse light (blue-sky albedo) would be the fractional sum of the two, depending on the fraction of incoming diffuse light during the examined time period.

Here, only white-sky albedo was available for DYN. The emerging offset between the black- and white-sky albedos and their physical effects hinders a direct comparison of the DYN and CLIM simulations. Instead, the interannual change of the respective simulation case (cf. Section 6.1.1) is compared, assuming that for the interannual difference ΔY, the effect of this offset is negligible.

Differences between VF_{Dyn}, LAI_{Dyn} and the climatological dataset are smaller, but show pronounced higher maxima during the rainy season. As expected, the standard deviations are generally higher for DYN datesets compared to the climatological annual cycles.

6.2.3 Consistency of the dynamical datasets

The DYN monthly anomalies for the Sahel in Fig. 6.3 show good agreement with each other as well as with observed precipitation (PCP) and soil moisture estimates (SM), giving confidence in their quality. In the Sahel, SM and VF_{Dyn} anomalies show maximum correlations with PCP anomalies of 0.71 and 0.74 with a lag of one month (Fig. 6.4). Even after two months, the correlations do not drop below 0.55.

In the moister and more densely vegetated Sudanian zone, VF reacts with a smaller temporal lag to PCP anomalies shown by similar correlations for a lag of 0 and 1 month. However, corresponding to Camberlin et al. (2007), vegetation changes are less sensitive to PCP anomalies in this region ($r \sim 0.47$) since water availability is a weaker constraint than in the Sahel.

Nevertheless, this illustrates that vegetation may retain a long-term memory of preceding rainfall anomalies over the whole region. Here, it is hypothesized that surface patterns that were induced by precipitation in the early months of the rainy season may affect the patterns of rainfall in the late rainy season. The focus lies therefore on the period from August to September (Aug-Sep), when vegetation anomalies reach their maximum (cf. Fig. 6.3).

The years 2009 and 2010 show a transition from a negative (-4.6 %) to a positive (4 %) VF anomaly in the Sahel and are therefore suitable to assess the potential contribution of the changing land surface to this transition as compared to a climatological case. The regional patterns of ΔY_{Dyn} in Fig. 6.5 show that differences in VF locally reach over 10 % with more vegetation in the Sahel but lower values in the eastern parts of the Sudanian zone. In the Sahel, which is especially prone to interannual PCP variations and where the bare sand is considerably brighter than vegetation, the albedo locally decreases by more than 3 %. The Aug-Sep spatial correlation of $\Delta Y(VF)_{Dyn}$ with the observed $\Delta Y(PCP)$ from June is still about 0.3 and confirms the local lagged co-variation of rainfall and vegetation.
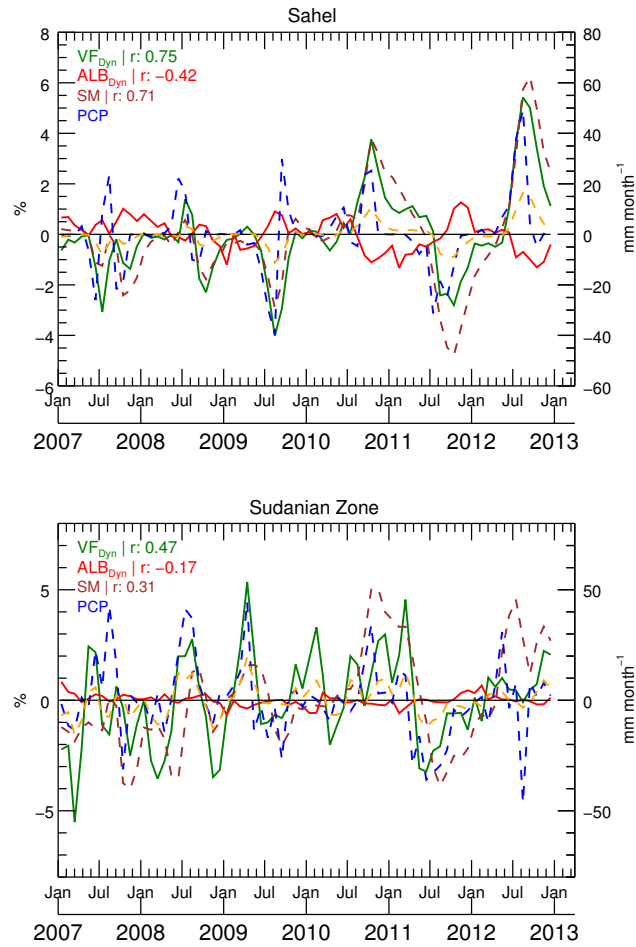
Figure 6.3: Monthly anomalies of dynamical albedo (ALB_{Dyn}), dynamical green vegetation fraction (VF_{Dyn}), CPC soil moisture (SM) and TRMM precipitation (PCP) with respect to the average annual cycle for 2007-2012. Correlations (r) represent +1 month time-lagged correlations with PCP.
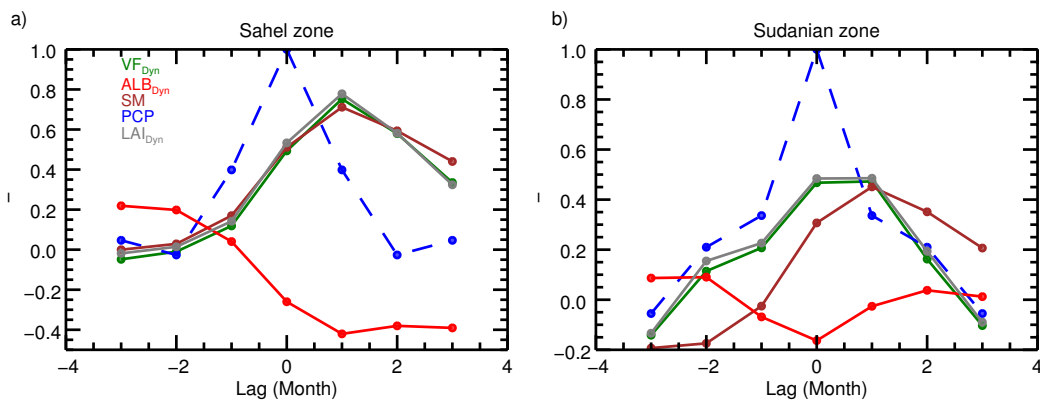
Figure 6.4: Monthly time-lagged anomaly correlations with PCP for dynamical albedo (ALB_{Dyn}), dynamical leaf area index (LAI_{Dyn}), dynamical green vegetation fraction (VF_{Dyn}), soil moisture (SM) and precipitation (PCP) in (**a**) the Sahel and (**b**) the Sudanian zone with respect to the 2007-2012 average annual cycle.
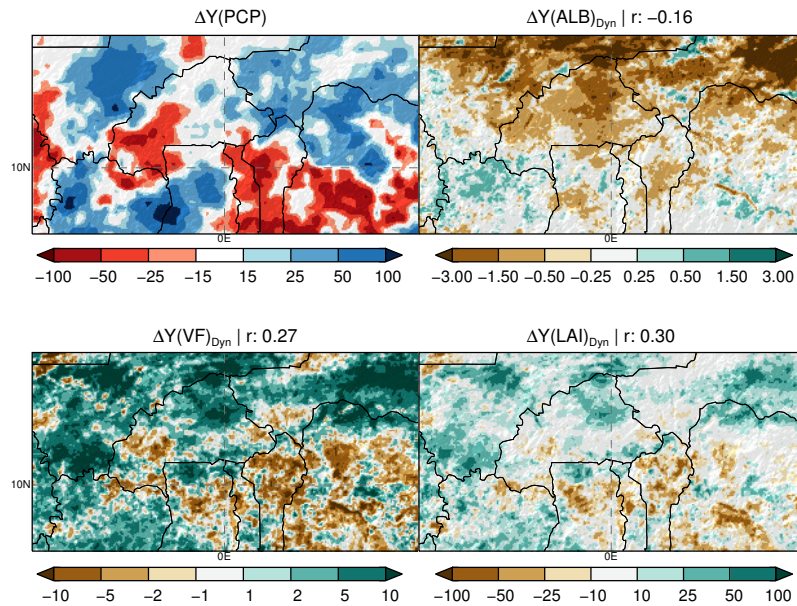
Figure 6.5: Average interannual differences 2010-2009 (ΔY) for June-July precipitation (PRCP, average of TRMM, RFE and CMORPH, mm month^{-1}) and August-September dynamical albedo (ALB$_{\mathrm{Dyn}}$, %), vegetation fraction (VF$_{\mathrm{Dyn}}$, %) and leaf area index (LAI$_{\mathrm{Dyn}}$, %). Spatial correlations (r) are with respect to ΔY(PCP).

6.3 Large-scale impact of interannual vegetation changes

6.3.1 Domain averages

The following section investigates the plausibility of the modelled effect of year-to-year vegetation changes for Aug-Sep domain-wide averages with respect to observations. As presented in Table 6.2, WRF correctly captures more PCP in 2010 than in 2009 in both the DYN and CLIM case. This illustrates that the general monsoon regime is already determined by remote drivers that are fed to the WRF model via the domain boundaries from ERA-I.

DYN shows higher LH because of higher maxima in VF$_{\mathrm{Dyn}}$ (cf. Fig. 6.2) which reduces the bias for both surface fluxes with respect to the reference data and indicates a more realistic flux partitioning. For both years, the ratio of evapotranspiration to precipitation is 6% higher than for CLIM and also 2 % higher than for the reference datasets. SH generally remains too high.

DYN also decreases the precipitation bias because of less absolute rainfall of about 12 mm month^{-1} for both years. This distinct change is most likely due to the higher values of ALB$_{\mathrm{Dyn}}$ (+1.8 % on average) in comparison to ALB$_{\mathrm{Clim}}$ (cf. Fig. 6.2) leading to more reflected solar energy (countering the bias in incoming shortwave radiation), overall lower TS of about -0.6 K and smaller SH of 6 W m^{-2}. However, these improvements are related to technical differences in the albedo dataset instead of realistic surface changes and are thus purely artificial (cf. 6.2.2).

Table 6.2: Area-averaged total values for DYN and CLIM and their bias with respect to the mean values obtained from the reference datasets (REF) for precipitation (PCP, mm month^{-1}: TRMM, RFE, CMORPH), surface temperature (TS, °C: GHCN, UDEL, CRU) and latent (LH) and sensible heat flux (SH) (W m^{-2}: MTE, ERA Interim/LAND, MERRA-Land) for the box (9°W-9°E ; 7-16°N). ΔY is the respective interannual difference (2010-2009).

	PCP			TS			LH			SH		
	REF	DYN	CLIM	REF	DYN	CLIM	REF	DYN	CLIM	REF	DYN	CLIM
Total												
2009	174.8	170.1	183.2	27.1	27.0	27.5	81.8	81.8	78.0	37.0	59.3	65.2
2010	192.4	188.7	200.5	26.7	26.5	27.1	83.2	84.0	77.9	34.5	52.0	58.0
ΔY	17.6	18.6	17.3	-0.4	-0.5	-0.4	1.4	2.2	-0.1	-2.5	-7.3	-7.2
Bias												
2009	174.8	-4.7	8.4	27.1	-0.1	0.4	81.8	0	-3.7	37.0	22.3	28.2
2010	192.4	-3.7	8.1	26.7	-0.2	0.4	83.2	0.8	-5.2	34.5	17.5	23.5
ΔY	17.6	1	-0.3	-0.4	-0.1	0	1.4	0.8	-1.5	-2.5	-4.8	-4.7

To exclude the effect of such artificial offsets, it is helpful to compare the change in ΔY, the modelled interannual difference for any variable, instead of comparing the change for a specific year. The absolute ΔY in Table 2 is generally larger for DYN than for CLIM, as could be expected under the influence of the two opposing vegetation anomalies during 2009 and 2010.

To get an impression on the significance of the difference between ΔY_{Dyn} and ΔY_{Clim} (=ΔY_{Srfc}, cf. Eq. 6.1), ΔY_{Srfc} is compared to the spread of ΔY per ensemble in Fig. 6.6. Interestingly, the spread of ΔY for the corresponding reference datasets (blue) is always smaller than the spread of the WRF ensembles, in this case attributing larger uncertainty to the model's internal variability than to the choice of a certain reference dataset.

For PCP and SH, the WRF ensemble spreads for ΔY strongly overlap. This means that, for the study region average, instead of changing the surface information, the initial conditions of the WRF model could have been changed to produce differences of the same or an even larger margin for these two variables, rendering ΔY_{Srfc} insignificant. The spread in PCP increases by 83% from 12 mm month^{-1} for ΔY_{Clim} to 22.3 mm month^{-1} for ΔY_{Dyn}, suggesting that the dynamical surface considerably increases the internal variability of precipitation generation in the model.

Other than for PCP, the ΔY_{Srfc} cooling signal of -0.1 K for TS and the related LH (+3.3 Wm^{-2}) is significant (P $\leq$ 0.01), estimated by a two-tailed t-test. In accordance to the observations, DYN shows a positive ΔY(LH), although overestimates. CLIM does not produce a clear difference in LH between the two years suggesting that the dynamical vegetation improves the models ability to represent the interannual difference of LH in this case. Associated with LH, the decrease in TS is too strong for DYN, indicating a too large sensitivity of surface fluxes on changing vegetation conditions in the WRF model that leads to a larger ΔY than observed.
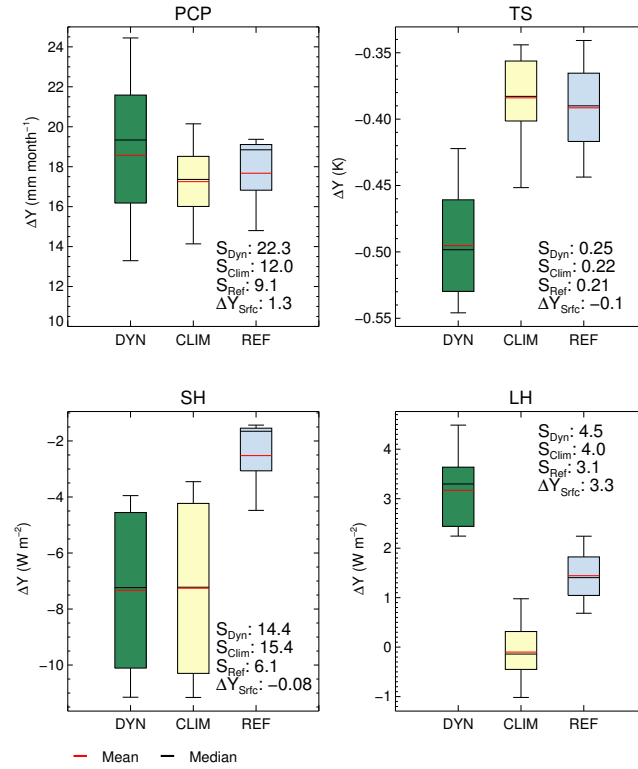
Figure 6.6: Aug-Sep ΔY boxplots for precipitation (PCP), surface temperature (TS), sensible (SH) and latent (LH) heat flux that span the spread (S) in ΔY of the WRF ensembles (DYN, CLIM) and for the reference datasets over the study area. The whiskers indicate minimum and maximum ΔY. For the WRF ensembles, the spread of ΔY is computed via the cartesian product of the four 2009/2010 pairs. Therefore, each box consists of 16 ΔY. For the observations, the box spread consists of three ΔY values of three single reference datasets. ΔY_{Srfc} is the difference of the mean values (red lines: $\Delta Y_{Dyn} - \Delta Y_{Clim}$).

6.3.2 Meridional distributions

The clear impact of vegetation changes on TS raises the question whether the monsoon dynamics, such as the AEJ, could also be affected. Being a thermal wind, the AEJ follows the largest temperature gradient over the continent that can be modulated by vegetation patterns. Disturbances of the AEJ may trigger or support MCSs in its proximity and a shift of the jet may therefore change the meridional distribution of precipitation (Cook, 1999).

The normalized meridional cross-sections in Fig. 6.7(a) reveal a broadened but weaker maximum of the Sahelian temperature gradient between 11-15°N in 2010 compared to CLIM. The resulting northward shift of the AEJ leads to a better representation of the difference between the 2010/2009 AEJ positions with respect to ERA-I. Accordingly, the precipitation peak in the Sahel for ΔY_{Dyn} is broadened to the north (Fig. 6.7b) and directly coincides with the largest ΔY_{Dyn} for VF and LH (cf. Fig. 6.7c). This PCP increase is however not visible in the reference datasets. Instead, WRF generally overestimates ΔY in the Sahel and DYN further increases this positive bias via a positive feedback between LH and PCP.
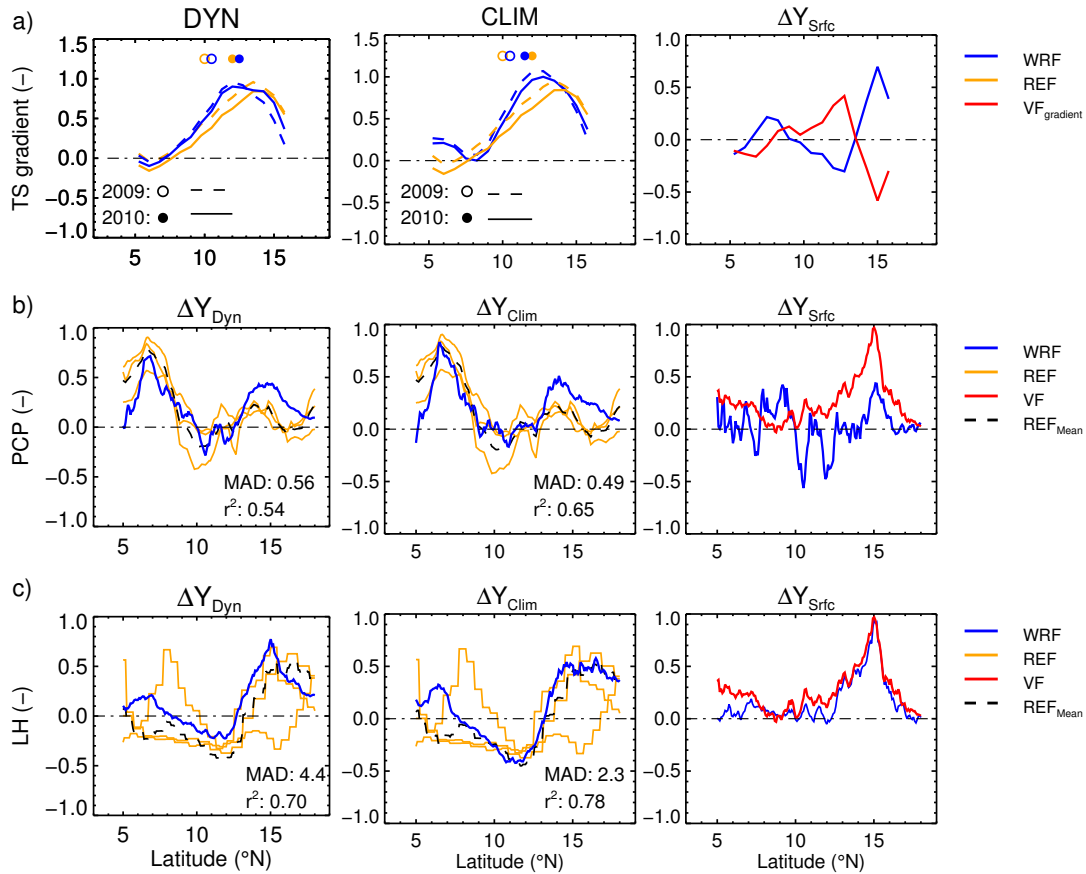
Figure 6.7: **(a)** The Aug-Sep meridional gradient of surface temperature (TS) for DYN/ CLIM (WRF) in 2009 and 2010 compared to GHCN (REF) and the resulting ΔY_{Srfc}. The TS gradient is computed between zonal averages of 50 km zonal slices. Additionally, the position of the AEJ (circles) is shown for each year. The latitudinal position of the AEJ is defined as the first occurrence of the zonal wind velocity surpassing 10 m s^{-1} between 650 and 550 hPa. **(b,c)** Aug-Sep meridional cross-sections of ΔY and ΔY_{Srfc} for the zonal average of precipitation (PCP) and latent heat flux (LH) for DYN/ CLIM (WRF) compared to the PCP reference datasets (REF: TRMM, RFE, CMORPH) and the LH reference datasets (REF: MTE, ERA Interim/LAND, MERRA-Land). Additionally, ΔY_{Srfc} for the vegetation fraction (VF) or the VF gradient (VF$_{gradient}$) are given for comparison. All variables are normalized with respect to their value range (max-min) and are therefore dimensionless. The mean absolute deviation (MAD, PCP:mm day^{-1}, LH:W m^{-2}) and r^2 are with respect to REF$_{Mean}$.

The vegetation-induced change in $\Delta Y(LH)$ is proportional to $\Delta Y(VF)$, as the overlapping curves for ΔY_{Srfc} in Fig. 6.7(c) illustrate. However, such a simple relationship does not exist for $\Delta Y(PCP)_{Srfc}$: Although $\Delta Y(VF)_{Srfc}$ is generally positive, there is a negative effect on PCP between 10-12°N (Fig. 6.7b, ΔY_{Srfc}) that is only shown by CMORPH amongst the observations. An examination of ΔY_{Srfc} in Fig. 6.7(a) reveals that in this region, the temperature (and pressure) gradient is weakened by the stronger VF gradient, suggesting a relatively lower near-surface moisture convergence that leads to reduced rainfall. Correspondingly, areas with a positive feedback on PCP are marked by a stronger temperature (pressure) gradient (positive ΔY_{Srfc}).

This confirms that large-scale differential heating due to vegetation heterogeneities can affect the dynamics and related precipitation even on continental scale. However, in this case, DYN reduces the correspondence of modelled LH and PCP with the average of the observational datasets, shown by higher MADs and lower r^2. Again, the change in LH with vegetation and the resulting lower surface temperatures seem to be overestimated, especially in the Sahel, leading to an exaggerated effect on the meridional gradients.

In summary, CLIM is able to capture the domain wide interannual differences of variable averages and meridional gradients as good or better than DYN. While the dynamical vegetation even exerts a clear influence on the modelled monsoon dynamics, the magnitude seems to be overestimated. It is therefore concluded that large-scale drivers dominate the observed interannual changes and that a dynamical surface description does not add clear value at this spatio-temporal scale within the uncertainty range of observations. It remains to be answered whether the vegetation patterns exhibit a regional or local effect that cannot be captured by CLIM.

6.4 Regional and local effects of vegetation patterns

In the previous section it was shown that, even on a larger scale, vegetation can lead to significant changes of LH and TS. Changes in both should be even more pronounced on regional and local scales and might, under favourable atmospheric conditions, affect PCP.

To get an impression of regional vegetation-induced changes of TS, LH and the evaporative fraction (EF), Fig. 6.8 shows their ΔY_{Srfc} and their spatial correlation with $\Delta Y(VF)_{Srfc}$. Locally, TS decreases (increases) by over 1 K with increasing (decreasing) VF. The changes in LH mostly range between -10 and +20 Wm^{-2}. A distinct increase of EF of more than 9% is only visible in the Sahel and at the southern border of the domain. The difference patterns match those of VF with correlations of -0.74 for TS, 0.72 for LH and 0.7 for EF.

However, the slopes of the zonal linear fit between the variables and VF in the right panels in Fig. 6.8 reveal latitudinal differences in the strength of the response per unit of VF change. Especially around 10°N, where the monsoon precipitation peaks for both years (cf. meridional precipitation distribution, Fig. 6.8 a), the effect of vegetation on the moist surface variables is smaller than at the northern or southern borders of the study domain.

6.4.1 Surface response and the evaporative regime

The meridional differences in the surface response to vegetation changes are an expected result if two factors are considered that modify the impact of vegetation on spatial LH variability: (i) the evaporative regime and thus the variable that limits evapotranspiration, (ii) the actual difference between transpiration and bare soil evaporation.

Regarding the first factor (i), Seneviratne et al. (2010) distinguish between moisture-limited regimes, where soil moisture (SM) changes have a maximum effect on the turbulent surface fluxes, and energy-limited regimes where SM is plenty and these fluxes are limited by incoming solar radiation. Only in the moisture-limited regime, vegetation (root zone soil moisture) can act as a first-order constraint for LH changes, analogous to moist bare soil.

In the moist region of the monsoon rainband however, the frequent cloud cover limits the available energy for evapotranspiration and LH patterns are therefore predominantly controlled (limited) by incoming shortwave radiation, reducing the secondary effect of spatial variations in vegetation. For the investigated time period, the transition zone of the two regimes lies approximately between 12-14°N, as depicted in Fig. 6.9(a). In the Sahel, positive daily correlations between $\Delta Y(LH)_{Srfc}$ and $\Delta Y(SM)_{Srfc}$ illustrate the moisture-limited region, while throughout the Sudanian Zone, $\Delta Y(LH)_{Srfc}$ variability is controlled by incoming shortwave radiation.
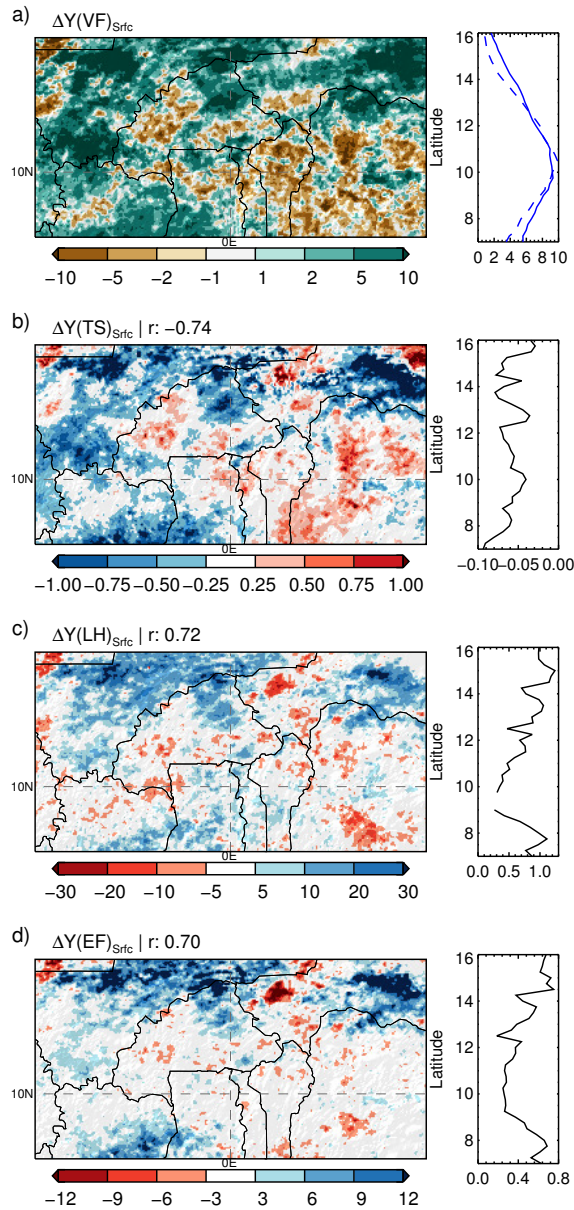
Figure 6.8: *Left*: Aug-Sep maps of ΔY_{Srfc} for **(a)** vegetation fraction (VF, %), **(b)** surface temperature (TS, K), **(c)** latent heat flux (LH, W m^{-2}) and **(d)** evaporative fraction (EF, %). EF is defined as the ratio of latent heat flux to the sum of latent and sensible heat fluxes. Only significant ΔY_{Srfc} are shown (P $\geq$ 0.01) and taken into account to compute the spatial correlation r. *Right*: **(a)** the meridional average precipitation (mm day^{-1}, 2010: solid, 2009: dashed) and **(b,c,d)** the coefficients a (the slope) of the zonal slices linear fit ($ax+b$) between $\Delta Y(VF)_{Srfc}$ and $\Delta Y(TS)_{Srfc}$, $\Delta Y(LH)_{Srfc}$ and $\Delta Y(EF)_{Srfc}$, respectively. Missing values indicate no correlation for the zonal slice.

The second factor (ii) that affects the ratio of LH and VF changes is related to the fact that vegetation exhibits an evaporative advantage compared to bare soil. The advantage exists because the volume of water in the soil that is available for vegetation transpiration is larger than for soil evaporation. This is especially important in the Sahel, where the surface soil layer dries out quickly and where vegetation provides a profound longer-lasting moisture supply to the atmosphere, resulting in a higher ratio of LH and VF changes. This effect is less important in the Sudanian zone, where surface soil moisture is replenished more frequently.

Nevertheless, an increased sensitivity to vegetation changes can be identified at the southern border of the domain in Fig. 6.8, where there is an LH increase of 1 W m^{-2} (0.04 mm day^{-1}) per unit VF, comparable to the moisture-limited Sahel. This is because the evaporative advantage also increases when vegetation density increases due to a larger evaporative surface as compared to the bare ground. The canopy is much more dense in the Sudanian zone as illustrated in Fig. 6.2 with a more than two times higher LAI than in the Sahel. Consequently, a high amount of available root zone soil moisture in dry regimes as well as a high canopy density in wet regimes contribute to a stronger increase of LH per increase of unit VF.

Interestingly, $\Delta Y(TS)_{\mathrm{Srfc}}$ does not reproduce the behaviour of LH in the Sahel (Fig. 6.8 b). While the decrease in TS per unit VF is indeed somewhat stronger (-0.09 K) in the southern Sudanian zone, the relationship varies around -0.05 K in the rest of the domain. One reason for this is that on smaller time-steps, a net-warming in the
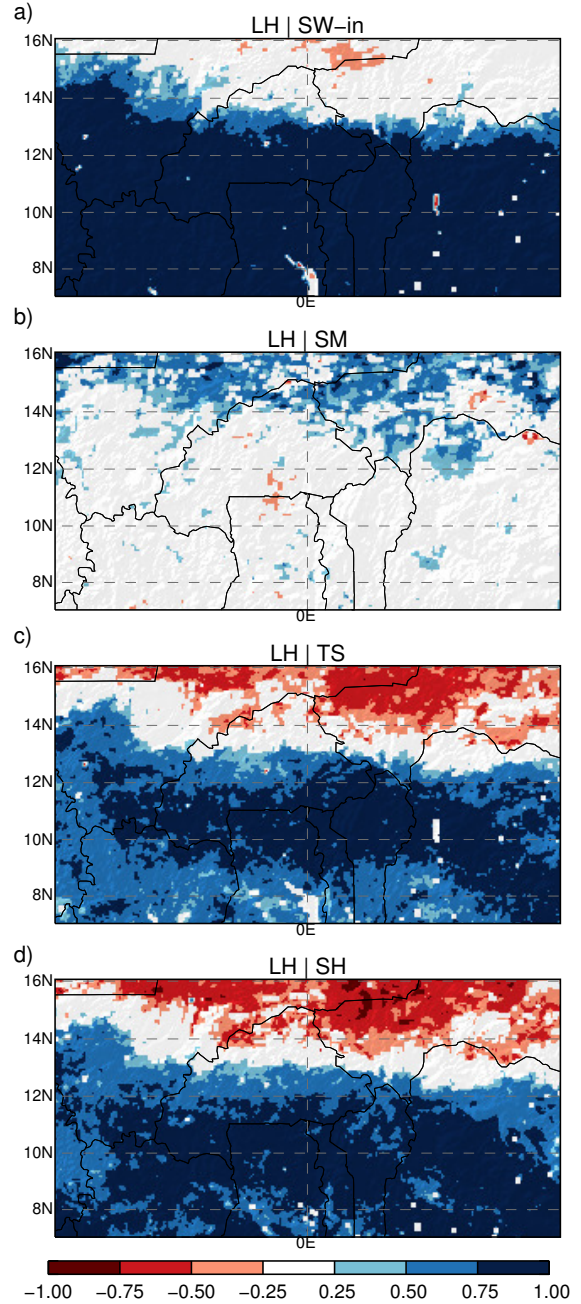
Figure 6.9: Maps of Aug-Sep temporal correlations of daily ΔY_{Srfc} between the latent heat flux (LH) and **(a)** incoming shortwave radiation (SW-in), **(b)** soil moisture (SM), **(c)** surface temperature (TS) and **(d)** sensible heat flux (SH). Only significant correlations (P $\leq$ 0.01) are shown.

vegetated areas may occur when soil moisture is not sufficient to supply transpiration. In these cases, the heating effect of lower vegetation albedo takes over and consequently weakens the time averaged overall cooling by increased VF.

In agreement with LH, the temporal variability of TS is affected by the predominant evaporative regime. Figure 6.9(c,d) reveals that only north of the transition zone at about 12°N, changes in temperature and turbulent heat flux partitioning are dominantly controlled by LH (negatively correlated).

Opposed to that, the positive correlation between $\Delta Y(LH)_{Srfc}$ and $\Delta Y(TS)_{Srfc}$ in the energy-limited Sudanian zone is a spurious correlation that is actually linked to the dependence of both variables on solar radiation which also applies to the relationship of LH and SH (Fig. 6.9d). Surface temperatures and both turbulent fluxes increase simultaneously (positive LH/ SH correlation) with higher incoming solar radiation, explaining the weaker response of EF to VF changes in Fig. 6.8(d).

These two different process pathways of dominant temperature control via soil-moisture anomalies (terrestial control) or via radiation anomalies (atmospheric control) were also identified by Berg et al. (2015) in a comparison of a set of climate simulations with and without interactive soil moisture. They conclude that land-atmosphere feedbacks in energy-limited regions can only play a minor role, since solar radiation determines temporal surface temperature variability. This drives latent heat flux variability which then drives soil moisture variability. This finding is supported by Dirmeyer (2011), who points out that the identification of strong surface-atmosphere coupling (e.g. a high correlation of the surface state and the atmospheric response) is only valid if there is surface (e.g. soil moisture) variability in time.

However, this purely temporal definition of land-atmosphere coupling does not take into account that persistent spatial surface characteristics might also have a considerable effect on the atmosphere. In the case of vegetation, Fig. 6.8 shows that, although solar radiation controls the temporal changes of the surface variables in the Sudanian zone, the long-lasting vegetation patterns lead to aggregated spatial characteristics of TS and LH. Here, it is assumed that such persistent surface gradients may force the atmosphere to reoccurring states just like, for example, a cold lake surface may impose frequent subsidence on the overlying air masses such that precipitation is suppressed. In the following, the land-atmosphere feedback is therefore defined as the spatial correlation of atmospheric characteristics with the surface over an aggregated time period as opposed to the temporal correlation approach.

6.4.2 The modelled atmospheric footprint

This section investigates whether the vegetation-driven patterns of the surface variables have a local effect on the atmosphere. Since these patterns are relatively static with respect to atmospheric time scales, a land-atmosphere feedback should manifest itself in a spatial accumulation of certain atmospheric states if the vegetation anomaly is strong enough to force the atmosphere.

The significant spatial correlations between $\Delta Y(\mathrm{VF})_{\mathrm{Srfc}}$ and the ΔY_{Srfc} of the different atmospheric variables (ranging from 0.46 to -0.76, $P \leq 0.01$) in Fig. 6.10 (a-d) indeed show that the surface characteristics modify the conditions in the PBL. The correlation coefficients are generally lower than for the surface variables, not only because the atmospheric sensitivity is ultimately determined by large-scale conditions, but also because this method can only capture pixelwise coinciding interactions between VF and the atmosphere. Therefore, it is not possible to relate any downstream changes in the atmosphere to their origin at the surface, for example.

Another factor for lower spatial correlations is the small-scale spatial heterogeneity of VF as compared to the well-mixed PBL conditions. To remedy this scale discrepancy, VF was upscaled to a length scale of 15 km, which is supposedly at the lower end at which PBL anomalies might persist and impact convection (Clark and Taylor, 2004).

In accordance to surface temperatures, the height of the PBL is anti-correlated with VF, which is most pronounced in regions where $\Delta Y(\mathrm{VF})_{\mathrm{Srfc}}$ surpasses 10% (cf. Fig. 6.8 a). More vegetated areas with lower PBL heights show an increase of daytime hours in which the lifted condensation level (LCL) lies within the PBL (Fig. 6.10 b). This is because more moisture (higher LH) trapped in a lower PBL increases the relative humidity which ultimately lowers the LCL and leads to cloud formation. Note that this cloud formation process via PBL moistening is less frequent in the Sahel (local increases of 20-40 hours), where the air is usually far from saturated due to less moisture advection (see also Findell and Eltahir, 2003 for a description of the surface-driven mechanisms of cloud formation via moistening or warming of the PBL).

Although there is a tendency to more frequent cloud cover over regions with more vegetation during the day, this does not necessarily imply an increase in precipitation. For example, in the South of Mali, $\Delta Y(\mathrm{VF})_{\mathrm{Srfc}}$ is strongly positive and locally causes over +60 hours in which the LCL lies within the PBL. This could indicate more favourable conditions for deep convection. However, a look at the convective available potential energy (CAPE) in Fig. 6.10 a reveals that there is no increased growth potential for the clouds in this region: CAPE is a measure for the buoyant energy of an air parcel close to the surface (here: lowest model level). It is computed as the integral of the difference between the potential virtual temperature of the rising air parcel and its environment between the level of free convection (the first level where the parcel is warmer than its environment) and the equilibrium level (the level where the air parcel reaches the environmental temperature and loses its buoyancy). In Fig. 6.10 a, there is no significant increase of CAPE for ΔY_{Srfc}, suggesting that there is no additional destabilization of the atmosphere that would imply a higher probability for strong updrafts and deep convection.
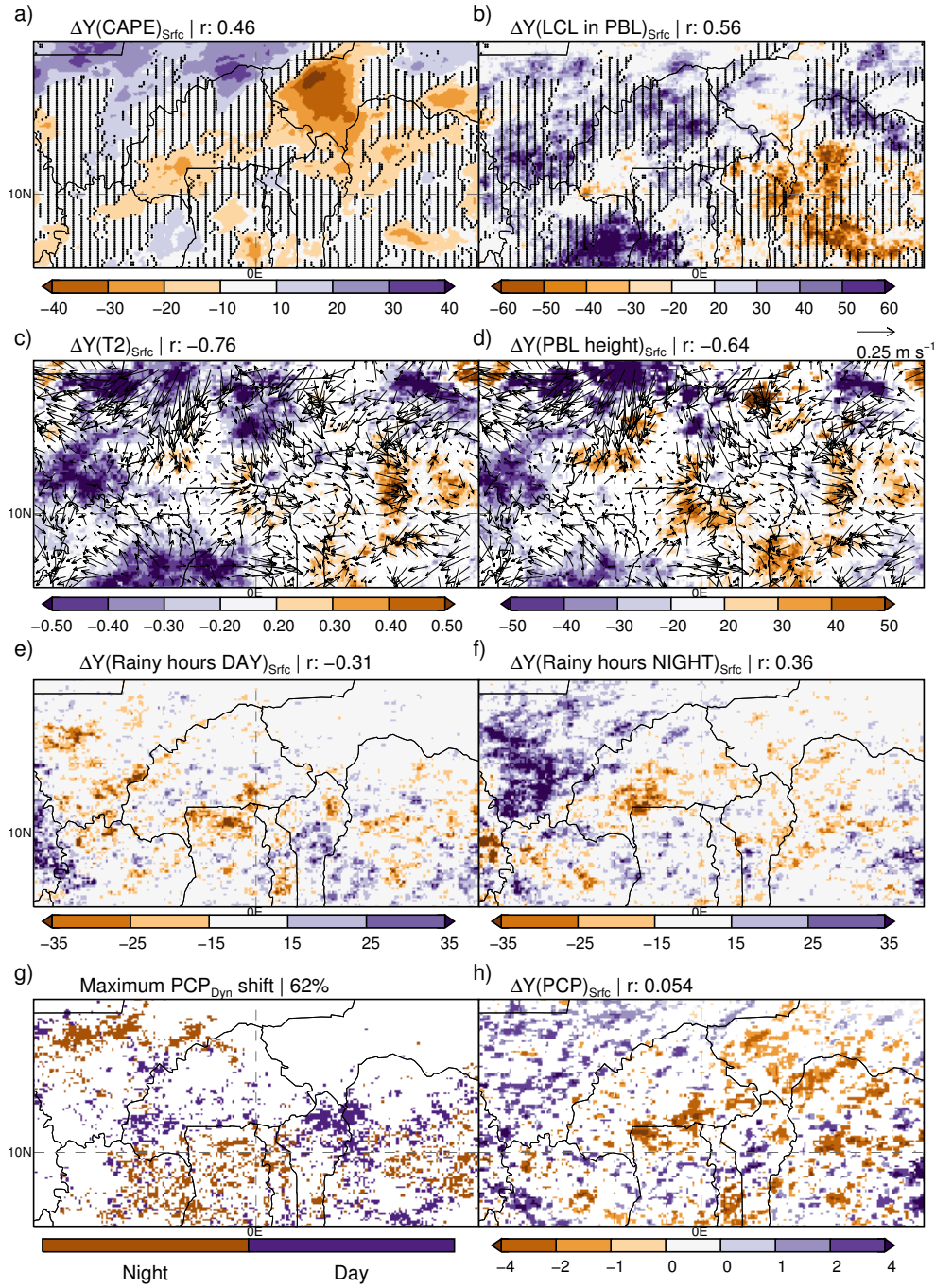
Figure 6.10: Maps for Aug-Sep: **(a)** $\Delta Y(CAPE)_{Srfc}$ (J kg^{-1}), **(b)** ΔY_{Srfc} for the number of daytime hours in which the PBL height reaches the lifted condensation level (LCL). Stripes in (a) and (b) mark insignificant changes of CAPE. **(c,d)** ΔY_{Srfc} for 2m temperature (T2, K), PBL height (m) and 10 m wind vectors (m s^{-1}). **(e,f)** ΔY_{Srfc} of rainy hours during the day (0700-1800 UTC)/ night (≥ 1 mm h^{-1}), **(g)** pixels showing a shift of the precipitation maximum from night to day ("Day") or vice-versa ("Night") between 2009 and 2010 in DYN. No shift or a shift corresponding to CLIM are ignored. The percentage is the portion of pixels where a shift to "Day" ("Night") falls together with a negative (positive) change in vegetation fraction (VF) **(h)** ΔY_{Srfc} precipitation (PCP, mm day^{-1}). Only significant ΔY_{Srfc} are shown. Spatial correlations (r) are with respect to $\Delta Y(VF)_{Srfc}$ (cf. Fig. 6.8 a) and are significant ($P \geq 0.01$) except for (h).

On the contrary, the number of daytime rainy hours is decreased over this region (Fig. 6.10 e), indicating that higher VF fosters the formation of shallow clouds but decreases the potential for initiation of deep convection in the afternoon. Hohenegger et al. (2009) suggest that the development of shallow clouds is an important ingredient for the negative vegetation-precipitation feedback due to higher stability of the air above the PBL related to the longwave radiative cooling at the cloud tops. Garcia-Carreras et al. (2011) analysed convective cloud distributions over crop land and forests with large eddy simulations and attribute the suppressed initiation of convection over forests to a stabilizing capping layer of warm air due to subsidence above the mixed layer. They found this subsidence to be part of mesoscale flows initiated by temperature gradients between the two vegetation classes.

Such mesoscale horizontal flows are also visible in our simulations between cooler and warmer surface patches in Fig. 6.10(c, d), where cooler near surface temperatures and shallower mixing layers correspond to a ΔY_{Srfc} signal of diverging winds that induce a negative VF-PCP feedback. The converging wind vectors over warmer regions indicate a moisture convergence from the surroundings that favours the initiation of convection and ultimately increases the number of rainy hours during the day (Fig. 6.10e).

During the night however, there is a distinct increase of rainy hours over the positive $\Delta Y(VF)_{\text{Srfc}}$ in southern Mali (Fig. 6.10f). This signal is weaker in the rest of the domain but the correlation coefficients in Fig. 6.10(e, f) indeed indicate a dominating negative VF-PCP feedback during the day and a positive feedback during the night. Overall, for 62% of the pixels (n=3990) that show a shift of the diurnal maximum PCP from night (day) to day (night) between 2009 and 2010, this shift coincides with negative (positive) $\Delta Y(VF)_{\text{Srfc}}$, which is 12% more likely than what would be expected by chance (Fig. 6.10g). The absolute ΔY_{Srfc} of rainy hours (positive and negative) in the Sahel is 10% higher during the night than during the day, indicating a slightly stronger effect of the positive VF-PCP feedback on nocturnal rainfall. In the Sudanian zone, the absolute ΔY_{Srfc} of rainy hours are similar for night and day.

Our findings are in line with Taylor et al. (2010), who analysed a MCS that was observed during the African Monsoon Multidisciplinary Analysis (AMMA) special observing period (Redelsperger et al., 2006) and report deepest convection over wet surface patches during its mature stage during the night (2130 UTC) while all areas of new convection emerged over drier soils. While the afternoon initiation of new convective cells is favoured over drier soil patches where thermals are more vicious, nighttime PCP mostly falls from already existing convective systems that are enhanced by moist surfaces (Gantner and Kalthoff, 2010). Wet soils have a stronger effect on the lifetime and strength of the MCS in the Sahel where moisture is limited, which might explain the enhanced positive feedback of vegetation in that region.

Due to the existence of these positive and negative VF-PCP feedbacks, especially in the Sudanian Zone, there is no correlation for $\Delta Y(PCP)_{\text{Srfc}}$ in Fig. 6.10(h). On average, the significant local changes reach ± 2.2 mm day^{-1}, for which the sign largely depends on whether the daytime or the nighttime VF-PCP feedback dominates.

6.4.3 Observed and modelled feedback on precipitation

The previous section showed that an atmospheric signal that is related to the interannual vegetation changes can be extracted not only for variables that characterize the state of the PBL, but also for rainfall. The question remains whether the simulated vegetation-driven adjustments are realistic and if so, whether the signal is detectable in the observations for which the dominating large-scale signal cannot be removed i.e. it is not possible to determine a ΔY_{Srfc}.

Nevertheless, the daily PCP statistics in Fig. 6.11 for 2009 and 2010 show a small but consistent increase of the Heidke skill score (HSS) for DYN for thresholds below 40 mm day^{-1} during both years. The HSS measures the improvement of the forecast skill over a random forecast and is computed for different thresholds over the whole study domain for every grid cell and every day. The HSS for both WRF cases is relatively low, but it should be kept in mind that WRF is only forced at the domain boundaries and is otherwise allowed to create its own weather. Reasons why these free running simulations can perform better in capturing precipitating systems in space and time than a random process (HSS >0) must therefore be related to strong atmospheric boundary conditions (e.g. atmospheric waves travelling through the model domain) or, to a lesser extent and only in the case of DYN, by the introduced land surface information. Since there is no substantial difference between DYN and CLIM in the frequency distribution or in the ability to capture daily mean PCP, the slightly higher HSS for DYN most likely stems from a surface-driven improvement in the spatio-temporal localisation of precipitating systems.

To test the impact of changes in VF, Fig. 6.12 shows the strength of the relationship between $\Delta Y(VF)_{Dyn}$ and the $\Delta Y(PCP)$ of DYN, CLIM and the reference datasets. Only pixels where $\Delta Y(PCP)_{Srfc}$ is significant are included (cf. Fig. 6.10h) presuming that these regions have the potential for considerable land-atmosphere feedbacks (sufficient surface change) and to therefore strengthen the surface signal.

The difficulty here is to extract a vegetation-precipitation feedback from the obvious precipitation-vegetation forcing. The idea is to consider the correlation between $\Delta Y(PCP)_{Clim}$ and $\Delta Y(VF)_{Dyn}$ as the baseline relationship between large-scale driven PCP changes and resulting VF patterns. Any correlation surplus (strengthened relationship) for DYN or the reference datasets in comparison to CLIM should be an indicator for an effect of the surface on the PCP patterns.

This approach works well in the Sahel (Fig. 6.12a), which shows a $\Delta Y(VF)_{Dyn}$-$\Delta Y(PCP)_{Dyn}$ correlation of 0.23 corresponding to correlations between 0.16 and 0.23 for the reference datasets. This relationship cannot be explained by large-scale interannual variability alone as illustrated by a very small correlation of 0.08 for $\Delta Y(PCP)_{Clim}$, which confirms an improved spatial PCP distribution for DYN.

The correlations of the reference datasets range from 0.16 to 0.23 in the Sahel, meaning that $\Delta Y(VF)_{Dyn}$ explains at most 5% spatial variance ($r^2 = 0.23^2 = 0.05$ for RFE) of the average PCP changes between Aug-Sep 2009 and 2010. Note that this is valid only for the regions where a potentially strong feedback was detected.
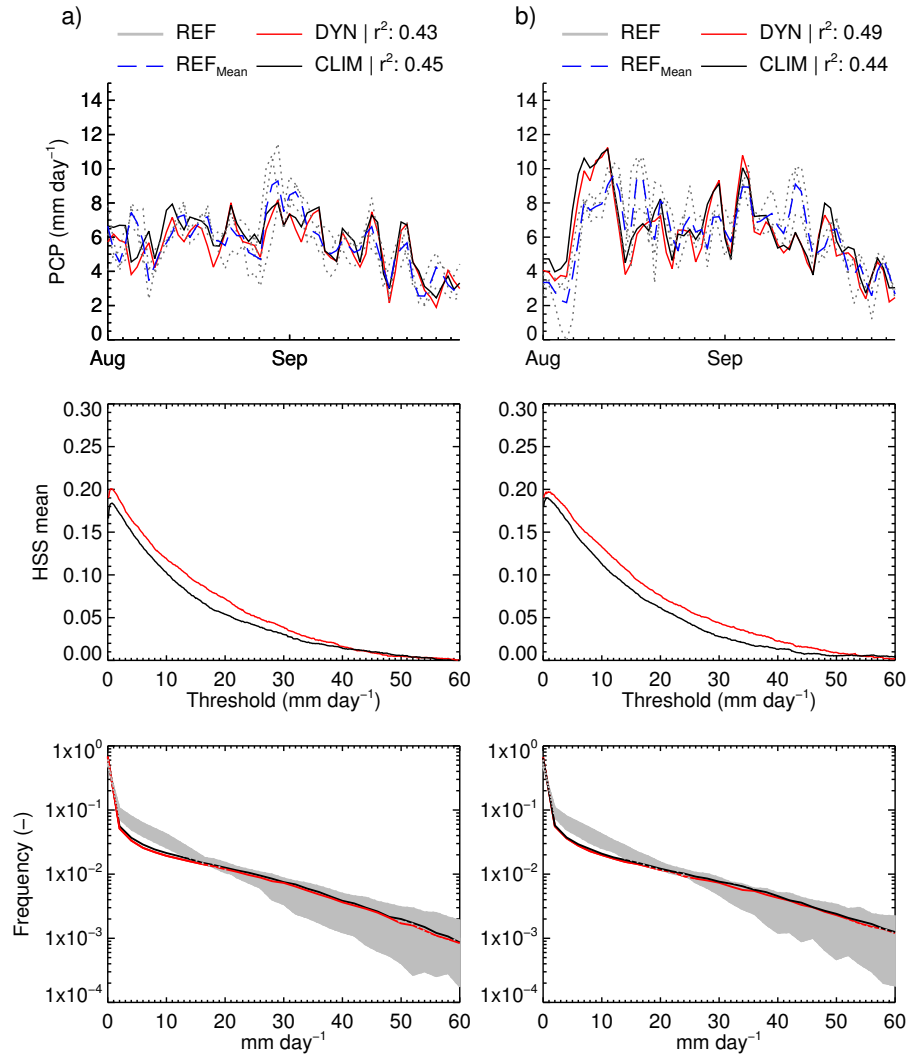
Figure 6.11: Aug-Sep precipitation **(top)** time series, **(middle)** Heidke skill score (HSS) and **(bottom)** precipitation frequency for daily values in **(a)** 2009 and **(b)** 2010 for DYN and CLIM with respect to the reference datasets (REF) TRMM, RFE and CMORPH over the study domain. HSS is computed as the average HSS_{Mean} per threshold from the complete spatio-temporal array with respect to all three references. r^2 is with respect to the reference dataset average REF_{Mean}. The grey area indicates the spread of the reference datasets.
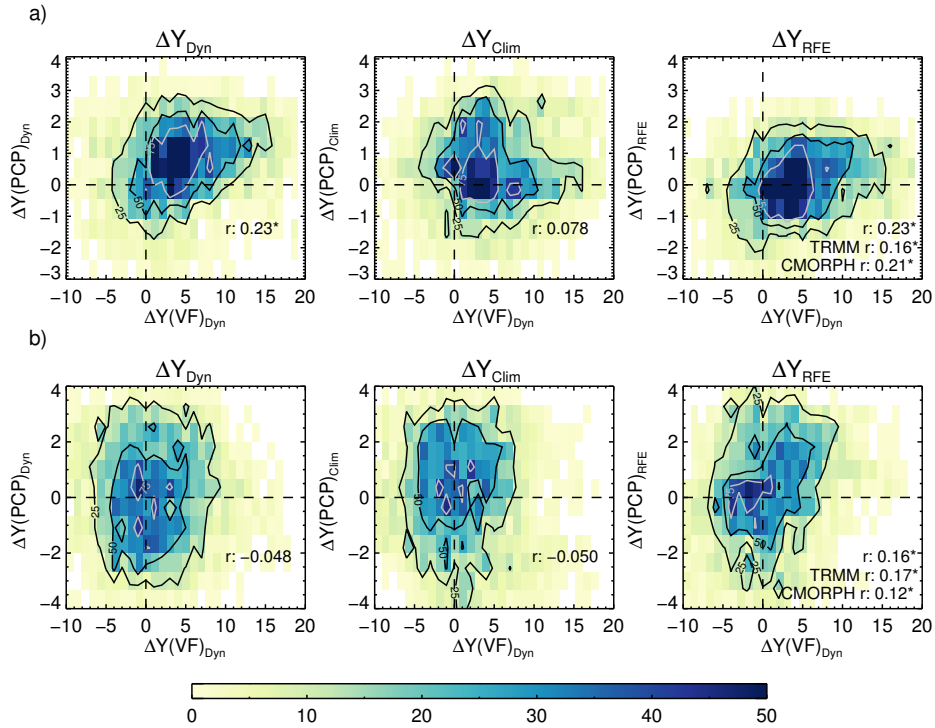
Figure 6.12: Aug-Sep density scatterplots between the ΔY for the dynamical vegetation fraction (VF_{Dyn}) and average precipitation (PCP) for DYN, CLIM and the reference dataset RFE **(a)** in the Sahel, **(b)** in the Sudanian zone. Only regions where ΔY_{Srfc} precipitation is significant (cf. Fig. 6.10 h) are included in the spatial correlation (r). Significant r are marked with a star and are also displayed for TRMM and CMORPH for comparison. Contours indicate the 75th, 50th and 25th percentile of the maximum density. The binsize is 0.75 mm day^{-1} for PCP and 1 % for VF.

In the Sudanian zone, there is no correlation for the WRF simulations but small positive correlations for the reference datasets most likely due to the precipitation-vegetation forcing (Fig. 6.12 b). WRF has difficulties to capture the observed patterns of large-scale driven PCP differences in that region, which might explain the complete lack of a correlation with $\Delta Y(VF)_{Dyn}$. Ultimately, the strong predominance of the large-scale monsoon dynamics in determining interannual precipitation differences in the Sudanian zone seems to inhibit any signal detection directly from ΔY.

6.4.4 Discussion and conclusions

This experiment examined the feedback of land surface and atmospheric variables in response to year-to-year vegetation changes between two consecutive years (2009, 2010) during the WAM in August and September with the aim to (Section 1.2):

- identify the processes by which interannual vegetation changes have an effect (if any) on the atmosphere during the WAM

- investigate whether the implementation of satellite-derived surface parameters improves the representation of surface variables and rainfall in WRF

Satellite-derived dynamical information for albedo, LAI and vegetation fraction were implemented into the WRF model. A control case used default surface parameters that follow a climatological annual cycle during both years and therefore represents the large-scale driven changes. The dynamical surface data exhibits a peak correlation of vegetation with rainfall with a lag of about one month in both, the Sahel and the Sudanian zone. The vegetation patterns during August-September still show a correlation with pre-monsoon rainfall patterns in June of ∼0.3, illustrating a long-term memory that might affect subsequent monsoon rainfall via land-atmosphere feedbacks with potential implications for seasonal predictions (Dirmeyer, 2006).

However, the impact on precipitation was found to be scale-dependant since, at the continental scale, total precipitation amounts are insensitive to vegetation changes, which is in line with previous feedback studies that focused on realistic surface changes (e.g. Lauwaet et al., 2009; Taylor et al., 2002).

The importance of vegetation changes increases at regional scale, shown by a significant response of surface temperatures and turbulent surface fluxes to vegetation patterns that is especially pronounced at the outskirts of the monsoon rainband. Related to lower surface temperatures and higher latent heat fluxes, shallower and moister PBLs reside over positive vegetation anomalies. In these regions, the PBL reaches the lifted condensation level more frequently but the number of daytime rainy hours is decreased in comparison to PBLs over less vegetated areas. The initiation of mesoscale horizontal circulations between cooler and warmer surfaces decreases the potential for initiation of deep convection in the afternoon, which Garcia-Carreras et al. (2011) attribute to the formation of a stabilizing capping layer above the PBL. Over the warmer (less vegetated) areas, on the other hand, moist air converges and stronger thermals may more easily break through the stable layer, which ultimately favours deep convection.

Comparable mechanisms were also suggested in observational studies on the development of convective clouds elsewhere, e.g. USA and Amazonia (Rabin et al., 1990; Chagnon et al., 2004). Wang et al. (2009) identify mesoscale circulations in the Amazon from forested to deforested patches as an important lifting mechanism that leads to frequent initiation of convection over deforested regions while there was no deep convection over uniform forest in spite of sufficient CAPE.

The results showed an opposite signal for nighttime precipitation, with rain falling more often over areas with more vegetation. This positive feedback is presumably related to a strengthening of mature propagating MCSs that are triggered upstream in the afternoon (Mathon and Laurent, 2001) and that feed on the moist boundary layer as was proposed by Gantner and Kalthoff (2010). Using the LAM of the Consortium for Small-scale Modelling, they conducted a MCS case-study over West Africa and found dry surfaces embedded in moist surroundings favouring the initiation of convection, while mature systems were weakened over these surfaces. A global study by Taylor et al. (2012) based on remote sensing data likewise showed that daytime (afternoon) precipitation falls preferentially over drier soils, while during the night, the picture is reversed with precipitation being more likely over wetter soils.

Correspondingly, the probability for maximum precipitation to be shifted to nighttime over increased VF and to daytime over decreased VF between the two years was found to be 12% higher than by chance. These findings suggest that vegetation patterns essentially foster the same atmospheric processes like soil moisture. They also confirm the often emphasized complexity of vegetation-rainfall interaction due to the existence of positive as well as negative feedbacks (e.g. Kunstmann and Jung, 2007; Findell and Eltahir, 2003; Hohenegger et al., 2009; Taylor et al., 2012; Gantner and Kalthoff, 2010), which was found here to be directly connected to the time of day and to the typical lifecycle of mesoscale convective systems (initiation during the afternoon versus westward propagation during the night).

Interestingly, a feedback could be detected in the Sudanian zone where soil moisture is plentiful and the monsoon dynamics are strong, which is thought to disfavour land-atmosphere interactions. This feedback might be related to the long-lasting nature of vegetation anomalies (as opposed to frequently changing soil moisture patterns) that could be more important for land-atmosphere interactions in the more densely vegetated Sudanian zone as opposed to the Sahel (Taylor et al., 2010): Firstly, the atmosphere may adapt to vegetation patterns whenever the atmospheric conditions are favourable. Secondly, the signal is spatially relatively stable such that the spatial accumulation of a certain atmospheric state can actually be detected with our approach.
Kohler et al. (2010) correspondingly found that during the mature monsoon stage July-August, vegetation instead of soil moisture becomes the dominating factor for surface processes impacting the boundary layer. This implies that land-atmosphere coupling can be identified based on a covariance of surface and atmospheric variables at temporal scale (e.g. soil moisture variance at a point, Dirmeyer, 2011) or at spatial scale (e.g. persistent vegetation patterns). Here, the latter definition suggests a feedback even under conditions where soil moisture is not limited.

However, for observed rainfall, the feedback was only traceable in the Sahel where a shift of a convective system can be a matter of 'any or none' precipitation for that location. Since it is impossible to remove the large-scale signal from observational data, the vegetation-rainfall feedback must be a considerable contribution to the large-scale driven precipitation patterns in order to be detectable, which is not given in the core of the monsoon rainband. Hence, the validity of the modelled feedback in this region remains uncertain.

In conclusion, on interannual time scales, the implementation of satellite-derived dynamical vegetation into an atmospheric model predominantly improves the simulations at the edges of the monsoon rainband. Future studies should concentrate on the dry and pre-monsoon season, when the synoptic forcing and moisture advection are weaker and the impact of prevailing vegetation patterns could quantitatively be more important. Furthermore, it should be mentioned that there is an imbalance of observational studies addressing the impact of soil moisture and vegetation patterns in West Africa, with the latter receiving much less attention. The development of methods to extract signals of vegetation-atmosphere feedbacks from measurements or satellite data will greatly help to validate modelled feedbacks.

Conclusions and outlook

The overarching aim of this thesis was

(i) to investigate by which mechanisms and to which extent moist processes, convection and interannual vegetation changes may modify precipitation characteristics during the WAM in spite of the dominating role of the large-scale forcing.

(ii) to evaluate whether a regional adjustment of these processes in the WRF model improves our ability to correctly model WAM characteristics.

(i) It was shown that the WAM is a system where interactions across scales generally take place in both directions - from large to small scales and vice versa. Imposed large-scale information can regionally be transformed from wet year to dry year characteristics if the regional moisture distribution changes. This clearly proves that regional processes forming the WAM are not only driven by the large scales but strongly interact with them. It was found that any significant change in precipitation is linked to modified monsoon dynamics: an approximately linearly coupled change of the strength of the near-surface monsoon wind and of the tropical easterly jet as well as of the African easterly jet position. The fact that the complete range of dry to wet monsoon states with corresponding dynamical features can be reproduced by changing the representation of moist processes in WRF suggests that any change in the monsoon regime can theoretically be triggered by a change in the water cycle. In particular, the connection between water and energy cycle via the effect of clouds on the surface energy balance turned out to play a key role for strengthening or weakening the meridional monsoon circulation.

The moist processes experiment revealed that clouds can ultimately have two opposing effects on the meridional temperature gradient and therefore on the monsoon circulation: a strengthening due to deep convection and high clouds most likely linked to latent heat release and a positive or neutral cloud albedo effect (warming tendency) or a weakening linked to a decrease in incoming

shortwave radiation and a negative cloud albedo effect for shallow convection and thus mid-level clouds (cooling tendency).

Compared to atmospheric moist processes, interannual vegetation changes only play a secondary role for determining the monsoon regime but nevertheless leave a distinct imprint on the atmosphere that gains of importance at the local scale.

Vegetation influences the local wind field determining regions of convergence over warmer and divergence over cooler surfaces leading to either higher probabilities of maximum rainfall during the day or during the night, respectively. Natural year-to-year vegetation changes may shift such regions of convergence or divergence and therefore alter local rainfall likelihood. It was shown for the first time that such natural interannual vegetation changes are a significant driver for interannual changes of precipitation patterns in the Sahel where a net positive (nighttime) vegetation-rainfall feedback dominates. Rainfall events during the early monsoon season initiate the seasonal plant growth in this arid region and therefore predetermine vegetated regions that can reinforce subsequent rainfall suggesting that vegetation may lock certain precipitation patterns throughout a season.

Different from the impact of moist processes, vegetation heterogeneities mainly have the potential to modify the spatial distribution of rainfall events rather than total rainfall amounts. However, an overestimation of the modelled latent heat fluxes in the Sahel provoked a slight northward shift of the African easterly jet. This suggests that vegetation changes at a scale of hundreds of kilometres that are large enough to affect the meridional temperature gradient and therefore the monsoon dynamics could lead to significant large-scale precipitation changes.

(ii) Different compartments of the WRF model were adjusted to potentially improve the representation of the WAM. A typical but cumbersome first step in the model adjustment is to choose a favourable set of model parameterizations that is however often not transferable to other applications. Here, a process-based classification of the analysed parameterizations with respect to their effect on the monsoon dynamics and the related monsoon regime was proposed. It was found that microphysics, planetary boundary layer and cumulus parameterizations mostly influence the total precipitation amounts, the rainband position and the diurnal cycle of precipitation, respectively, for which causal mechanisms were suggested. With this kind of classification, weak model behaviour can more easily be traced back to a certain parameterization choice and provides a systematic guideline to set-up changes in order to improve the WAM representation in the WRF model. This process-oriented approach greatly simplifies the identification of favourable WRF set-ups for new applications over West Africa. Here, it provided a robustly well-behaving set-up for different years in the subsequently presented experiments. In addition, the approach was already successfully used for a systematic adjustment of WRF for long-term climate simulations and projections conducted within WASCAL.

It was also shown that WRF is able to relate variations in the monsoon dynamics to the corresponding dry or wet monsoon states comparably to what is observed. This gives confidence

in the model's capability to capture the whole range of WAM variability. However, since this whole range of monsoon states was modelled by just changing moist process parameterizations, this also illustrates the high uncertainty in the description of these processes. It underlines the great potential for a model improvement with a regionally adjusted set of parameterizations but also justifies the frequent ensemble applications in West Africa. Of all processes, the representation of radiation was identified to be the most sensitive factor for model performance. Therefore, the capability of the model to correctly capture cloud cover and the overall radiation budget should be a focus of any thorough performance assessment.

In this context, the explicit treatment of convection revealed an improvement in modelled cloud cover and of incoming shortwave radiation compared to parameterized convection. This illustrates the potential of avoiding cumulus parameterization shortcomings with the explicit approach. In addition, the cases with explicit convection also improved the rainfall characteristics and frequencies, even in the convective grey zone. The large size of convective systems during the WAM allows reasonable model results with explicit approaches at resolutions coarser than 4 km. For land-atmosphere interaction studies, the explicit approach is the only possibility to reduce the artificial links between surface fluxes and convection to the PBL parameterization only. This should be preferred in view of remaining uncertainties with the PBL parameterization, the choice of an LSM and prescribed surface conditions.

The reduction of uncertainty in surface conditions by implementing satellite-derived surface parameters into WRF realised a limited model improvement: In the Sahel, precipitation patterns were enhanced but total amounts were overestimated. This was partly related to WRF exaggerating the modelled latent heat flux associated with a vegetation increase. The experiment illustrated that the implementation of observed surface conditions does not necessarily lead to a significant model improvement although realistic processes governing land-atmosphere interactions were simulated. This might be on one hand related to the Noah LSM being tuned to work reasonably well with the default climatological surface data, which provokes biases with new datasets even if these are more realistic. On the other hand, the land surface is not of considerable importance under all circumstances. Under strong dynamical forcing, simulations using climatological surface data corresponded similarly well to observations, rendering the implementation of satellite data for 'model improvement' unnecessary. Nevertheless, this implementation allowed to better define the processes that are driven by natural vegetation changes.

In conclusion, it is not possible to find a 'one-for-all' WRF set-up. Depending on the application and study aims, requirements regarding the represented processes, horizontal resolution or model performance change - and so does the 'ideal model set-up'. However, it proved helpful to be aware of the process interactions at the surface and in the atmosphere that affect the WAM variability. This knowledge gives the capability to approximately predict the model behaviour when a certain screw is turned in one or the other direction, which greatly facilitates the process of model adjustment.

Outlook

From the atmospheric perspective, future WRF model set-ups should consider parameterizations that allow the implementation of aerosol concentrations for different regions. This will help to improve the representation of incoming solar radiation as well as of rainfall generation. Furthermore, the sensitivity of the WAM system to clouds is an especially critical point in view of changing aerosol concentrations caused by spreading urban areas in West Africa. This calls for studies evaluating the potential impact of current and future aerosol concentrations on cloud cover in this region.

The explicit treatment of convection at only convection-allowing scales should be considered an intermediate solution for cases where high-resolving simulations below 4 km are not feasible. Scale-aware cumulus schemes (e.g. Grell and Freitas, 2014) could be tested in the convective grey zone to avoid the shortcomings of explicit convection that only captures mesoscale circulations.

For the evaluation of the impact of vegetation changes on the atmosphere, the already presented object tracking method might be a useful tool: besides rainfall, other subjacent variables in the atmosphere could be tracked. This would give the opportunity to evaluate typical atmospheric states before, during and after rainfall events and to identify up- or downstream effects of surface changes.

Regarding the implementation of satellite data into WRF, the introduced uncertainty by in-consistencies between prescribed surface parameters and interactive soil moisture (e.g. high vegetation fraction but dry soil) is an open question. Simulations additionally prescribing soil moisture could be conducted to assess related errors in the representation of the land-atmosphere feedback.

In the future, the evaluation of land-atmosphere interactions could also be extended from vegetation patterns to actual land use changes that are extensively taking place in West Africa. This was not possible here because reliable land use information was available only for a single year. MODIS land use maps are available[1] from 2001 to 2012 but would need a quality control before being used to evaluate land use changes over longer time periods. Connected to this, the performance of grid cell tiling in the LSM could be considered in order to take into account sub-grid heterogeneities of the surface instead of the dominant land class only. Subsequently, land use scenarios could be developed to assess the impact of future land use changes under climate change.

However, for a robust quantitative analysis of the effect of vegetation or land use changes on the WAM, especially for climate projections, it will be necessary to use an LSM ensemble. The LSM translates a new surface forcing into a response in form of turbulent fluxes, which can considerably vary between different LSMs. The proceedings of the AMMA Land Surface Model Intercomparison Project (Boone et al., 2009) give a good impression on these differences. For retrospective land-atmosphere interaction studies, it could be checked whether the coupling of

---

[1]http://glcf.umd.edu/data/lc/

WRF to NASA's Land Information System[1] might provide a more flexible framework for using LSM ensembles and for implementing different observational surface data than WRF standalone.

An alternative to an LSM ensemble would be to extensively test and tune one specific LSM in comparison to observations. However, this would have to be done for all important land surface classifications and all major climate zones in West Africa to make sure that the model is able to transfer its performance from one surface state to another and to different climate conditions. The lack of spatio-temporally sufficient flux measurements to properly validate the LSM strongly limits the single model approach to small scale applications where measurements are available and questions its applicability to climate change studies with land use scenarios.

Generally, new approaches for regional modelling across scales using Voronoi meshes could help to overcome some of the identified shortcomings of a dynamical downscaling with common LAMs like WRF. For example, the Model for Prediction Across Scales is an Earth System modelling package that allows global simulations while further refining chosen regions with a finer mesh without nesting. A pilot study by Heinzeller et al. (2016) already showed that this model is able to reproduce the WAM dynamics and the rainband movement. Since the model does not depend on boundary conditions and allows a seamless transition between scales including a scale-aware cumulus scheme, it does not suffer from inconsistencies or scale jump limitations at the boundaries of nested domains as was shown for WRF. Furthermore, such a model allows to assess the impact of regional characteristics (e.g. land use changes) at the global scale, which is not possible with a LAM that is constrained by lateral boundary conditions.

---

[1]https://modelingguru.nasa.gov/community/atmospheric/lis

Appendix

Land use classification tables

The MODIS Land Cover

Table A.1: MODIS land cover classification and corresponding numbers in WRF. The land classification and description is based on the International Geosphere Biosphere Program (IGBP) DISCover Data Set Land Cover Classification System (Belward, 1996)

MODIS land cover classes	WRF number	Description
Evergreen Needleleaf Forest	1	Needleleaf trees covering > 60% and height > 2m. Almost all trees remain green all year.
Evergreen Broadleaf Forest	2	Same as 1 but with broadleaf trees
Deciduous Needleleaf Forest	3	Needleleaf trees covering > 60% and height > 2m. Consits of seasonal needle leaf tree communities with an annual cycle of leaf-on and leaf-off periods.
Deciduous Broadleaf Forest	4	Same as 3 but with broadleaf trees
Mixed Forests	5	Trees covering > 60% and height exceeding 2m. Consists of tree communities and mixtures or mosaics of the other four forest types. None of the forest types exceeds 60% of landscape
Closed Shrublands	6	Woody vegetation less than 2m tall with shrub canopy cover > 60%. The shrub foliage can be either evergreen or deciduous
Open Shrublands	7	Same as 6 but with shrub canopy cover between 10-60%.
Woody Savannas	8	Herbaceous/understory systems and with forest canopy cover between 30-60%. The forest cover height exceeds 2m.
Savannas	9	Same as 8 but with forest canopy cover between 10-30%.
Grasslands	10	Herbaceous types of cover. Tree and shrub cover < 10%.
Permanent Wetlands	11	Mixture of water and herbaceous or woody vegetation. The vegetation can be present in either salt, brackish or fresh water
Croplands	12	Covered with temporary crops followed by harvest and a bare soil period. Perennial woody crops will be classified as the appropriate forest or shrub land cover type.
Urban and Built-up	13	Land covered by buildings and other man made structures.
crop/natural veg. mosaic	14	Mosaic of croplands, forests, shrubland and grasslands i which no one component coprises more than 60% of the landscape
Snow and Ice	15	lands under snow/ice cover throughout the year.
Barren/sparsely vegetated	16	Exposed soil, sand rocks or snow and never has more than 10% vegetated cover during any time of the year
Water	17	Oceans, seas, (lakes) and rivers). Fresh or salt-water bodies.
Woody Tundra	18	Lands with herbaceous/understory systems with forest canopy cover between 30-60%. The forest cover height exceeds 2 m.
Mixed Tundra	19	Mixture of Tundra occurrences where any type occupies less than two-thirds of area.
Barren Tundra	20	Less than one third vegetated. Considerable areas of exposed rock, sand, or gravel and low herbaceous and shrubby plants.
Lakes	21	In-land water bodies

The West African Land Cover (WALC)

Creator: Ursula Gessner, German Aerospace Center (DLR)

Data basis: MODIS, ASAR, TerraSAR-X

Table A.2: Translation table for WALC and MODIS (WRF) classification. The MODIS translation is a DLR suggestion on basis of classification descriptions. The finally *used* translations in WRF partly differ due to individually specified reasons (see footnotes).

WALC classes	Number	Description	MODIS translation	Used
Evergreen forest	1	Broadleaved trees with a cover > 80%. Almost all trees remain green all year.	2	2
Evergreen woodland	2	Broadleaved trees with a cover of 10-80%. Almost all trees remain green all year. Usually agriculturally used	14	14
Deciduous forest	3	Broadleaved trees with a percent cover > 60%. Seasonal tree communities with an annual cycle of leaf-on and leaf-off periods	4	4
Open woodland, deciduous	8	Land with herbaceous/understory systems and with tree canopy cover between 10-60%	8 / 9	9[1]
Closed to open shrubland	6	Shrub vegetation with a woody canopy cover > 10%. Can be evergreen or deciduous	6 / 7	9[2]
Grassland	9	Dominated by herbaceous types of cover. Tree and shrub cover is < 10%	10	10
Cropland	11	Temporary crops followed by harvest and a bare soil period	12	12
Sparse vegetation	14	Land with vegetation cover of 1-10%	16	10[3]
Bare areas	23	Land with vegetation cover < 1%	16	16
Dry season vegetation	24	Land with vegetation during dry season where moisture is available in the absence of sufficient rainfall. Comprises irrigated agriculture and wetlands	11 / 12	11[4]
Permanent water bodies	15	Water covers the surface > 9 months per year	17	17
Seasonal water bodies	16	Water covers the surface < 9-4 months per year	17	17
Medium-/High-density urban area	25	Buildings and other man-made structures cover 50-100%	13	13
Low-density urban area	26	Buildings and other man-made structures cover 30-49%	13	13

1: Savannas (9) instead of woody savannas (8) since the MODIS table values for woody savannas produce unrealistically low latent heat fluxes.

2: Savannas (9) instead of shrub land classes (6/7) to be more consistent with the MODIS land classification map, which does not attribute 'closed shrublands' to any region in West Africa and 'open shrublands' are considered almost barren (cf. Fig. 6.1(b)).

3: Grassland (10) instead of barren (16) since these areas show sometimes more than 10% vegetation cover during the year. An 'appropriate' sparse vegetation classification is missing in MODIS classification. Without code change, WRF handles 'barren' as zero vegetation.

4: Wetlands (11) instead of crop lands (12) to ensure moisture supply during dry season ('irrigation' not implemented in WRF)

Weather stations

Table B.1: Used automatic weather stations and eddy covariance stations in Burkina Faso and Ghana.

	Name	Lon	Lat	Source
0	Sumbrungu	-0.917	10.847	WASCAL EC-station
1	Kayoro	-1.321	10.918	WASCAL EC-station
2	Nazinga	-1.586	11.152	WASCAL EC-station
3	Tamale	-0.850	9.417	Burkina Faso Meteorological Service
4	Bam Tourcoing	-1.500	13.333	Burkina Faso Meteorological Service
5	Bousse	-1.883	12.667	Burkina Faso Meteorological Service
6	Diebougou	-3.250	10.968	Burkina Faso Meteorological Service
7	Kete-Krachi	-0.033	7.819	Burkina Faso Meteorological Service
8	Kpandu-Prisons	0.300	7.000	Ghana Meteorological Service
9	Abidome	-0.517	6.067	Ghana Meteorological Service
10	Agogo	-1.083	6.786	Ghana Meteorological Service
11	Akuse	0.134	6.101	Ghana Meteorological Service
12	Atebubu	-0.983	7.750	Ghana Meteorological Service
13	Baraboule	-1.850	14.217	Ghana Meteorological Service
14	Gorom-Gorum	-0.233	14.450	Ghana Meteorological Service
15	Bomborokuy	-3.984	13.051	Ghana Meteorological Service
16	Kassoum	-3.300	13.083	Ghana Meteorological Service
17	Seguenega	-1.967	13.434	Ghana Meteorological Service
18	Bani	-0.167	13.717	Ghana Meteorological Service
19	Tiogo	-2.683	12.183	Ghana Meteorological Service
20	Yako	-2.267	12.967	Ghana Meteorological Service
21	Bilanga	-0.017	12.550	Ghana Meteorological Service
22	Kourouma	-4.800	11.617	Ghana Meteorological Service
23	Bobo-Dioulasso	-4.300	11.168	Ghana Meteorological Service
24	Bagassi	-3.300	11.750	Ghana Meteorological Service
25	Dano	-3.067	11.151	Ghana Meteorological Service
26	Boromo	-2.917	11.734	Ghana Meteorological Service
27	Boura	-2.500	11.050	Ghana Meteorological Service
28	Betare	-1.367	11.433	Ghana Meteorological Service
29	Ouargaye	0.017	11.533	Ghana Meteorological Service
30	Mahagada	1.747	11.663	Ghana Meteorological Service
31	Baguera	-5.417	10.533	Ghana Meteorological Service
32	Banfora Agri	-4.767	10.633	Ghana Meteorological Service
33	Ouo	-3.833	10.400	Ghana Meteorological Service
34	Kampit	-3.467	10.134	Ghana Meteorological Service
35	Botou	2.046	12.621	Ghana Meteorological Service
36	Garu	-0.180	10.850	Ghana Meteorological Service
37	Goaso	-2.516	6.803	Ghana Meteorological Service
38	Ho	0.460	6.594	Ghana Meteorological Service
39	Koforidua	-0.250	6.086	Ghana Meteorological Service
40	Lawra	-2.866	10.652	Ghana Meteorological Service
41	Navrongo	-1.100	10.902	Ghana Meteorological Service
42	Tumu	-1.983	10.867	Ghana Meteorological Service
43	Wenchi	-2.100	7.750	Ghana Meteorological Service
44	Yendi	-0.017	9.450	Ghana Meteorological Service
45	Bui	-2.266	8.286	Ghana Meteorological Service
46	Berekum	-2.583	7.453	Ghana Meteorological Service
47	Bolgatanga	-0.867	10.800	Ghana Meteorological Service
48	Bole	-2.483	9.033	Ghana Meteorological Service
49	Batié	-2.917	9.884	Ghana Meteorological Service
50	Kpeve	0.333	6.679	Ghana Meteorological Service
51	Ada	0.640	5.781	Ghana Meteorological Service
53	Saltpond	-1.056	5.194	Ghana Meteorological Service
54	Tamale	-0.860	9.491	Ghana Meteorological Service
55	Tema	0.001	5.609	Ghana Meteorological Service
56	Kaya	-1.058	13.062	Ghana Meteorological Service
57	Manga	-1.046	11.652	Ghana Meteorological Service
58	Niaogho	-0.777	11.760	Ghana Meteorological Service
59	Ouahigouya	-2.428	13.554	Ghana Meteorological Service
60	Sideradougou	-4.240	10.620	Ghana Meteorological Service
61	Tema2	-1.755	13.045	Ghana Meteorological Service
62	Zabre	-0.603	11.164	Ghana Meteorological Service
63	Gourcy	-2.316	13.179	Ghana Meteorological Service
64	Ejura	-1.379	7.400	Ghana Meteorological Service

List of Figures

List of Tables

Bibliography

Alo, C. A. and Wang, G.: Role of dynamic vegetation in regional climate predictions over western Africa, Climate Dynamics, 35, 907–922, doi:10.1007/s00382-010-0744-z, 2010.

Ansmann, a., Tesche, M., Althausen, D., Müller, D., Seifert, P., Freudenthaler, V., Heese, B., Wiegner, M., Pisani, G., Knippertz, P., et al.: Influence of Saharan dust on cloud glaciation in southern Morocco during the Saharan Mineral Dust Experiment, Journal of Geophysical Research, 113, D04 210, doi:10.1029/2007JD008785, 2008.

Anthes, R. A.: Enhancement of Convective Precipitation by Mesoscale Variations in Vegetative Covering in Semiarid Regions, Journal of Climate and Applied Meteorology, 23, 541–554, 1984.

Balsamo, G., Albergel, C., Beljaars, A., Boussetta, S., Brun, E., Cloke, H., Dee, D., Dutra, E., Muñoz Sabater, J., Pappenberger, F., de Rosnay, P., Stockdale, T., et al.: ERA-Interim/Land: a global land surface reanalysis data set, Hydrology and Earth System Sciences, 19, 389–407, doi:10.5194/hess-19-389-2015, 2015.

Barbe, L. E., Lebel, T., and Tapsoba, D.: Rainfall Variability in West Africa during the Years 1950–90, Journal of Climate, 15, 187–202, 2002.

Baret, F. and Weiss, M.: Towards an Operational GMES Land Monitoring Core Service—BioPar Methods Compendium-LAI, FAPAR, F COVER NDVI, Geoland2, 2010.

Bélair, S. and Mailhot, J.: Impact of horizontal resolution on the numerical simulation of a midlatitude squall line: Implicit versus explicit condensation, Monthly weather review, 129, 2362–2376, 2001.

Belward, A.: The IGBP-DIS global 1 km land cover data set ”DISCover” - Proposal and implementation plans. Report of the Land Cover Working Group of the IGBP-DIS., 1996.

Bengtsson, L.: Can climate trends be calculated from reanalysis data?, Journal of Geophysical Research, 109, D11 111, 2004.

Berg, A., Lintner, B. R., Findell, K., Seneviratne, S. I., van den Hurk, B., Ducharne, A., Chéruy, F., Hagemann, S., Lawrence, D. M., Malyshev, S., Meier, A., et al.: Interannual Coupling between Summertime Surface Temperature and Precipitation over Land: Processes and Implications for Climate Change*, Journal of Climate, 28, 1308–1328, doi:10.1175/JCLI-D-14-00324.1, 2015.

Berry, G. and Thorncroft, C. D.: African Easterly Wave Dynamics in a Mesoscale Numerical Model: The Upscale Role of Convection, Journal of the Atmospheric Sciences, 69, 1267–1283, doi:10.1175/JAS-D-11-099.1, 2012.

Bharati, L., Rodgers, C., Erdenberger, T., Plotnikova, M., Shumilov, S., Vlek, P., and Martin, N.: Integration of economic and hydrologic models: Exploring conjunctive irrigation water use strategies in the Volta Basin, Agricultural Water Management, 95, 925–936, doi:10.1016/j.agwat.2008.03.009, 2008.

Birch, C., Parker, M., Marsham, J., Copsey, D., and Garcia-carreras, L.: A seamless assessment of the role of convection in the water cycle of the West African Monsoon, Journal of Geophysical Research: Atmospheres, 119, 2890–2912, doi:10.1002/2013JD020887, 2014.

Bliefernicht, J., Kunstmann, H., Hingerl, L., Rummler, T., Andresen, S., Mauder, M., Quensah, E., Awotuse, A., Neidl, F., and Barry, B.: Field- and simulation experiments for investigating regional land-atmosphere interactions in West Africa : experimental setup and first results, Climate and Land Surface Changes in Hydrology, IAHS Publ., 1–7, 2013.

Boone, A., Decharme, B., Guichard, F., de Rosnay, P., Balsamo, G., Beljaars, A., Chopin, F., Orgeval, T., Polcher, J., Delire, C., Ducharne, A., Gascoin, S., Grippa, M., et al.: The AMMA Land Surface Model Intercomparison Project (ALMIP), Bulletin of the American Meteorological Society, 90, 1865–1880, doi:10.1175/2009BAMS2786.1, 2009.

Box, G. and Draper, N.: Empirical Model-Building and Response Surfaces, John Wiley & Sons, Ltd., 1987.

Brovkin, V., Boysen, L., Raddatz, T., Gayler, V., Loew, A., and Claussen, M.: Evaluation of vegetation cover and land-surface albedo in MPI-ESM CMIP5 simulations, Journal of Advances in Modeling Earth Systems, 5, 48–57, 2013.

Browne, N. a. K. and Sylla, M. B.: Regional Climate Model Sensitivity to Domain Size for the Simulation of the West African Summer Monsoon Rainfall, International Journal of Geophysics, 2012, 1–17, doi:10.1155/2012/625831, 2012.

Camacho, F. and Cernicharo, J.: Gio Global Land Component - Lot I "Operation of the Global Land Component", Tech. rep., 2015.

Camacho, F. and Sánchez, J.: Gio Global Land Component - Lot I "Operation of the Global Land Component", Tech. rep., 2015.

Camberlin, P., Janicot, S., and Poccard, I.: Seasonality and atmospheric dynamics of the teleconnection between African rainfall and tropical sea-surface temperature: Atlantic vs. ENSO, International Journal of . . . , 1005, 973–1005, 2001.

Camberlin, P., Martiny, N., Philippon, N., and Richard, Y.: Determinants of the interannual relationships between remote sensed photosynthetic activity and rainfall in tropical Africa, Remote Sensing of Environment, 106, 199–216, doi:10.1016/j.rse.2006.08.009, 2007.

Chagnon, F. J. F., Bras, R. L., and Wang, J.: Climatic shift in patterns of shallow clouds over the Amazon, Geophysical Research Letters, 31, doi:10.1029/2004GL021188, 2004.

Chen, F. and Dudhia, J.: Coupling an advanced land surface-hydrology model with the Penn State-NCAR MM5 modeling system. Part I: Model implementation and sensitivity, Monthly Weather Review, 129, 569–585, 2001.

Chepfer, H., Bony, S., Winker, D., Cesana, G., Dufresne, J. L., Minnis, P., Stubenrauch, C. J., and Zeng, S.: The GCM-Oriented CALIPSO Cloud Product (CALIPSO-GOCCP), Journal of Geophysical Research, 115, D00H16, doi:10.1029/2009JD012251, 2010.

Chepfer, H., Cesana, G., Winker, D., Getzewich, B., Vaughan, M., and Liu, Z.: Comparison of Two Different Cloud Climatologies Derived from CALIOP-Attenuated Backscattered Measurements (Level 1): The CALIPSO-ST and the CALIPSO-GOCCP, Journal Of Atmospheric And Oceanic Technology, 30, 725–744, 2013.

Chiao, S. and Jenkins, G. S.: Numerical Investigations on the Formation of Tropical Storm Debby during NAMMA-06, Weather and Forecasting, 25, 866–884, doi:10.1175/2010WAF2222313.1, 2010.

Clark, D. and Taylor, C. M.: Feedback between the Land Surface and Rainfall at Convective Length Scales, Journal of Hydrometeorology, 5, 625–639, 2004.

Cook, K. H.: Generation of the African Easterly Jet and Its Role in Determining West African Precipitation, Journal of Climate, 12, 1165–1184, 1999.

Cook, K. H. and Vizy, E. K.: The Congo Basin Walker circulation: dynamics and connections to precipitation, Climate Dynamics, doi:10.1007/s00382-015-2864-y, 2015.

Corfidi, S.: Cold pools and MCS propagation: Forecasting the motion of downwind-developing MCSs, Weather and forecasting, pp. 997–1017, 2003.

Cornforth, R. J.: West African Monsoon 2012 *, Weather, 68, 256–263, doi:10.1002/wea.2161, 2013.

Cornforth, R. J., Hoskins, B. J., and Thorncroft, C. D.: The impact of moist processes on the African Easterly Jet–African Easterly Wave system, Quarterly Journal Of The Royal Meteorological Society, 135, 894–913, doi:10.1002/qj, 2009.

Correia, J., Arritt, R. W., and Anderson, C. J.: Idealized Mesoscale Convective System Structure and Propagation Using Convective Parameterization, Monthly Weather Review, 136, 2422–2442, doi:10.1175/2007MWR2229.1, 2008.

Crétat, J., Pohl, B., Richard, Y., and Drobinski, P.: Uncertainties in simulating regional climate of Southern Africa: sensitivity to physical parameterizations using WRF, Climate dynamics, pp. 613–634, doi:10.1007/s00382-011-1055-8, 2012.

Csiszar, I. and Gutman, G.: Mapping global land surface albedo from NOAA AVHRR, Journal of Geophysical Research, 104, 6215–6228, 1999.

DAAC, O.: Fluxnet World Map, Tech. rep., Oak Ridge National Laboratory Distributed Active Archive Center, Oak Ridge, Tennessee, USA, URL `http://fluxnet.ornl.gov/maps-graphics`, 2013.

Davis, C. and Manning, K.: Coherence of warm-season continental rainfall in numerical weather prediction models, Monthly weather . . . , 131, 2667–2679, 2003.

Decker, M., Brunke, M. a., Wang, Z., Sakaguchi, K., Zeng, X., and Bosilovich, M. G.: Evaluation of the Reanalysis Products from GSFC, NCEP, and ECMWF Using Flux Tower Observations, Journal of Climate, 25, 1916–1944, doi:10.1175/JCLI-D-11-00004.1, 2012.

Dee, D. P., Uppala, S. M., Simmons, a. J., Berrisford, P., Poli, P., Kobayashi, S., Andrae, U., Balmaseda, M. a., Balsamo, G., Bauer, P., Bechtold, P., et al.: The ERA-Interim reanalysis: configuration and performance of the data assimilation system, Quarterly Journal of the Royal Meteorological Society, 137, 553–597, doi:10.1002/qj.828, 2011.

Denis, B., Laprise, R., and Caya, D.: Sensitivity of a regional climate model to the resolution of the lateral boundary conditions, Climate Dynamics, 20, 107–126, doi:10.1007/s00382-002-0264-6, 2003.

Dennett, M., Elston, J., and Rodgers, J.: A reappraisal of rainfall trends in the Sahel, International Journal Of Climatology, 5, 353–361, doi:10.1002/joc.3370050402, 1985.

Dezfuli, A. and Nicholson, S.: The Relationship of Rainfall Variability in Western Equatorial Africa to the Tropical Oceans and Atmospheric Circulation. Part II: The Boreal Autumn, Journal of Climate, 26, 66–84, doi:http://dx.doi.org/10.1175/JCLI-D-11-00686.1, 2013.

Dirmeyer, P.: The hydrologic feedback pathway for land-climate coupling, Journal of Hydrometeorology, pp. 857–867, 2006.

Dirmeyer, P. a.: The terrestrial segment of soil moisture-climate coupling, Geophysical Research Letters, 38, n/a–n/a, doi:10.1029/2011GL048268, 2011.

Done, J., Davis, C. a., and Weisman, M.: The next generation of NWP: explicit forecasts of convection using the weather research and forecasting (WRF) model, Atmospheric Science Letters, 5, 110–117, doi:10.1002/asl.72, 2004.

Douville, H., Conil, S., Tyteca, S., and Voldoire, A.: Soil moisture memory and West African monsoon predictability: artefact or reality ?, Climate Dynamics, 28, 723–742, 2007.

Druyan, L. M., Fulakeza, M., Lonergan, P., and Noble, E.: Regional climate model simulation of the AMMA Special Observing Period # 3 and the pre-Helene easterly wave, Meteorology and Atmospheric Physics, 105, 191–210, doi:10.1007/s00703-009-0044-5, 2009.

Dudhia, J.: Numerical study of convection observed during the winter monsoon experiment using a mesoscale two-dimensional model, Journal Of The Atmospheric Sciences, 46, 3077–3107, 1989.

Eltahir, E.: A soil moisture-rainfall feedback mechanism 1. Theory and observations, Water Resources Research, 34, 765–776, 1998.

Emori, S.: The interaction of cumulus convection with soil moisture distribution: An idealized simulation, Journal of Geophysical Research, 103, 8873–8884, 1998.

Evans, J. P., Ekstro, M., and Ji, F.: Evaluating the performance of a WRF physics ensemble over South-East Australia, Climate Dynamics, 39, 1241–1258, doi:10.1007/s00382-011-1244-5, 2012.

Fan, Y.: Climate Prediction Center global monthly soil moisture data set at 0.5 ° resolution for 1948 to present, Journal of Geophysical Research, 109, 1–8, doi:10.1029/2003JD004345, 2004.

Ferguson, C. R. and Wood, E. F.: Observed Land–Atmosphere Coupling from Satellite Remote Sensing and Reanalysis, Journal of Hydrometeorology, 12, 1221–1254, doi:10.1175/2011JHM1380.1, 2011.

Fersch, B. and Kunstmann, H.: Atmospheric and terrestrial water budgets: sensitivity and performance of configurations and global driving data for long term continental scale WRF simulations, Climate Dynamics, doi:10.1007/s00382-013-1915-5, 2013.

Feser, F., Rockel, B., von Storch, H., Winterfeldt, J., and Zahn, M.: Regional climate models add value to global model data, Bulletin Of The American Meteorological Society, pp. 1181–1192, doi:10.1175/2011BAMS3061.1, 2011.

Findell, K. and Eltahir, E.: Atmospheric controls on soil moisture-boundary layer interactions. Part I: Framework development, Journal of Hydrometeorology, pp. 552–569, 2003.

Fink, A. H. and Reiner, A.: Spatiotemporal variability of the relation between African Easterly Waves and West African Squall Lines in 1998 and 1999, Journal of Geophysical Research, 108, 4332, doi:10.1029/2002JD002816, 2003.

Flaounas, E., Bastin, S., and Janicot, S.: Regional climate modelling of the 2006 West African monsoon: sensitivity to convection and planetary boundary layer parameterisation using WRF, Climate Dynamics, 36, 1083–1105, doi:10.1007/s00382-010-0785-3, 2011a.

Flaounas, E., Janicot, S., Bastin, S., Roca, R., and Mohino, E.: The role of the Indian monsoon onset in the West African monsoon onset: observations and AGCM nudged simulations, Climate Dynamics, 38, 965–983, doi:10.1007/s00382-011-1045-x, 2011b.

Freitas, C. J.: The issue of numerical uncertainty, Applied Mathematical Modelling, 26, 237–248, 2002.

Friedl, M. a., Sulla-Menashe, D., Tan, B., Schneider, A., Ramankutty, N., Sibley, A., and Huang, X.: MODIS Collection 5 global land cover: Algorithm refinements and characterization of new datasets, Remote Sensing of Environment, 114, 168–182, doi:10.1016/j.rse.2009.08.016, 2010.

Gantner, L. and Kalthoff, N.: Sensitivity of a modelled life cycle of a mesoscale convective system to soil conditions over West Africa, Quarterly Journal of the Royal Meteorological Society, 136, 471–482, doi:10.1002/qj.425, 2010.

Garcia-Carreras, L., Parker, D. J., and Marsham, J. H.: What is the Mechanism for the Modification of Convective Cloud Distributions by Land Surface–Induced Flows?, Journal of the Atmospheric Sciences, 68, 619–634, doi:10.1175/2010JAS3604.1, 2011.

Gerard, L.: An integrated package for subgrid convection, clouds and precipitation compatible with meso-gamma scales, Quarterly Journal of the Royal Meteorological Society, 730, 711–730, doi:10.1002/qj, 2007.

Gessner, U., Niklaus, M., Kuenzer, C., and Dech, S.: Intercomparison of Leaf Area Index Products for a Gradient of Sub-Humid to Arid Environments in West Africa, Remote Sensing, 5, 1235–1257, 2013.

Gessner, U., Machwitz, M., Esch, T., Tillack, A., Naeimi, V., Kuenzer, C., and Dech, S.: Multi-sensor mapping of West African land cover using MODIS, ASAR and TanDEM-X/TerraSAR-X data, Remote Sensing of Environment, 164, 282–297, doi:10.1016/j.rse.2015.03.029, 2015.

Giannini, A., Saravanan, R., and Chang, P.: Dynamics of the boreal summer African monsoon in the NSIPP1 atmospheric model, Climate Dynamics, 25, 517–535, 2005.

Giorgi, F. and Bi, X.: A study of internal variability of a regional climate model, Journal of Geophysical Research, 105, 503–521, 2000.

Giorgi, F., Jones, C., and Asrar, G.: Addressing climate information needs at the regional level: the CORDEX framework, WMO Bull, 58, 175–183, 2009.

Gong, C. and Eltahir, E.: Sources of moisture for rainfall in West Africa, Water Resources Research, 32, 3115–3121, doi:10.1029/96WR01940, 1996.

Goosse, H.: Climate System Dynamics and Modelling, Cambridge University Press, 2015.

Grell, G., Dudhia, J., and Stauffer, D.: A description of the fifth generation Penn State/NCAR mesoscale model (MM5), Technical Report, National Centre for Atmospheric Research, Boulder, Colorado, USA, NCAR/TN-39, 1994.

Grell, G. a. and Freitas, S. R.: A scale and aerosol aware stochastic convective parameterization for weather and air quality modeling, Atmospheric Chemistry and Physics, 14, 5233–5250, doi:10.5194/acp-14-5233-2014, 2014.

Grist, J. P. and Nicholson, S. E.: A Study of the Dynamic Factors Influencing the Rainfall Variability in the West African Sahel, Journal of Climate, 14, 1337–1359, doi:10.1175/1520-0442(2001)014⟨1337:ASOTDF⟩2.0.CO;2, 2001.

Gutman, G. and Ignatov, A.: The derivation of the green vegetation fraction from NOAA / AVHRR data for use in numerical weather prediction models, International Journal of Remote Sensing, 19, 1533–1543, 1998.

Hagos, S., Leung, L. R., Xue, Y., Boone, A., de Sales, F., Neupane, N., Huang, M., and Yoon, J.-H.: Assessment of uncertainties in the response of the African monsoon precipitation to land use change simulated by a regional model, Climate Dynamics, 43, 2765–2775, doi:10.1007/s00382-014-2092-x, 2014.

Hagos, S. M. and Cook, K. H.: Dynamics of the West African Monsoon Jump, Journal of Climate, 20, 5264–5284, doi:10.1175/2007JCLI1533.1, 2007.

Harris, I., Jones, P., Osborn, T., and Lister, D.: Updated high-resolution grids of monthly climatic observations, International Journal Of Climatology, doi:10.1002/joc.3711, 2013.

Heinzeller, D., Duda, M. G., and Kunstmann, H.: Towards convection-resolving, global atmospheric simulations with the Model for Prediction Across Scales (MPAS) v3.1: an extreme scaling experiment, Geoscientific Model Development, 9, 77–110, doi:10.5194/gmd-9-77-2016, 2016.

Hertig, E., Beck, C., Wanner, H., and Jacobeit, J.: A review of non-stationarities in climate variability of the last century with focus on the North Atlantic-European sector, Earth Science Reviews, 147, 1–17, doi:10.1016/j.earscirev.2015.04.009, URL http://dx.doi.org/10.1016/j.earscirev.2015.04.009, 2015.

Hoerling, M., Hurrell, J., Eischeid, J., and Phillips, A.: Detection and Attribution of Twentieth-Century Northern and Southern African Rainfall Change, Journal of Climate, 19, 3989–4008, 2006.

Hohenegger, C., Brockhaus, P., Bretherton, C. S., and Schär, C.: The Soil Moisture–Precipitation Feedback in Simulations with Explicit and Parameterized Convection, Journal of Climate, 22, 5003–5020, doi:10.1175/2009JCLI2604.1, 2009.

Hong, S., Dudhia, J., and Chen, S.: A revised approach to ice microphysical processes for the bulk parameterization of clouds and precipitation, Monthly Weather Review, 132, 103–120, 2004.

Hong, S.-Y. and Lim, J.-o. J.: The WRF Single-Moment 6-Class Microphysics Scheme (WSM6), The Korean Meteorological Society, 42, 129–151, 2006.

Hong, S.-Y., Koo, M.-S., and Jang, J.: An Evaluation of the Software System Dependency of a Global Atmospheric Model, Monthly Weather Review, 141, 4165–4172, doi:10.1175/MWR-D-12-00352.1, 2013.

Houze, R.: Mesoscale convective systems, Reviews Of Geophysics, 42, 1–43, 2004.

Hsieh, J.-S. and Cook, K. H.: Generation of African Easterly Wave Disturbances: Relationship to the African Easterly Jet, American Meteorological Society, 133, 1311–1327, 2005.

Hu, X.-M., Nielsen-Gammon, J. W., and Zhang, F.: Evaluation of Three Planetary Boundary Layer Schemes in the WRF Model, Journal of Applied Meteorology and Climatology, 49, 1831–1844, doi:10.1175/2010JAMC2432.1, 2010.

Huffman, G., Adler, R., Rudolf, B., Schneider, U., and Keehn, P.: Global precipitation estimates based on a technique for combining satellite-based estimates, rain gauge analysis, and NWP model precipitation information, Journal of Climate, 8, 1284–1295, 1995.

Huffman, G., Adler, R., Arkin, P., Chang, A., Ferraro, R., Gruber, A., and Janowiak J, McNab A, Rudolph B, S. U.: The global precipitation climatology project (GPCP) combined precipitation dataset, Bulletin of the American Meteorological Society, 78, 5–20, 1997.

Hutchinson, T. A.: An Adaptive Time-Step for Increased Model Efficiency, Tech. rep., Weather Services International, Andover, Massachusetts, 2007.

IPCC: Africa, Tech. rep., URL https://www.ipcc.ch/pdf/assessment-report/ar5/wg2/WGIIAR5-Chap22_FINAL.pdf, 2014.

Janicot, S., Trzaska, S., and Poccard, I.: Summer Sahel-ENSO teleconnection and decadal time scale SST variations, Climate Dynamics, 18, 303–320, 2001.

Janicot, S., Thorncroft, C. D., Ali, A., Asencio, N., Berry, G., Bock, O., Bourles, B., Caniaux, G., Chauvin, F., Deme, A., et al.: Large-scale overview of the summer monsoon over West Africa during the AMMA field experiment in 2006, Annales Geophysicae, 26, 2569–2595, 2008.

Janjic, Z. I.: The Step-Mountain Eta Coordinate Model: Further Developments of the Convection, Viscous Sublayer, and Turbulence Closure Schemes, American Meteorological Society, 1994.

Janjic, Z. I.: Comments on "development and evaluation of a convection scheme for use in climate models", Journal of the Atmospheric Sciences, 57, 3686, 2000.

Joly, M., Voldoire, A., Douville, H., Terray, P., and Royer, J.-F.: African monsoon teleconnections with tropical SSTs: validation and evolution in a set of IPCC4 simulations, Climate Dynamics, 29, 1–20, doi:10.1007/s00382-006-0215-8, 2007.

Joyce, R., Janowiak, E., Arkin, P., and Xie, P.: CMORPH: A method that produces global precipitation estimates from passive microwave and infrared data at high spatial and temporal resolution, Journal Of Hydrometeorology, 5, 487–503, 2004.

Jung, G. and Kunstmann, H.: High-resolution regional climate modeling for the Volta region of West Africa, Journal of Geophysical Research, 112, D23108, doi:10.1029/2006JD007951, 2007.

Jung, M., Reichstein, M., Margolis, H. a., Cescatti, A., Richardson, A. D., Arain, M. A., Arneth, A., Bernhofer, C., and Bonal, D.: Global patterns of land-atmosphere fluxes of carbon dioxide, latent heat, and sensible heat derived from eddy covariance, satellite, and meteorological observations, Journal of Geophysical Research, 116, G00J07, doi:10.1029/2010JG001566, 2011.

Kain, J.: The Kain–Fritsch Convective Parameterization: An Update, Journal Of Applied Meteorology, 43, 170–181, 2004.

Kendon, E. J., Roberts, N. M., Senior, C. a., and Roberts, M. J.: Realism of Rainfall in a Very High-Resolution Regional Climate Model, Journal of Climate, 25, 5791–5806, doi:10.1175/JCLI-D-11-00562.1, 2012.

Klein, C., Heinzeller, D., Bliefernicht, J., and Kunstmann, H.: Variability of West African monsoon patterns generated by a WRF multi-physics ensemble, Climate Dynamics, doi:10.1007/s00382-015-2505-5, 2015.

Klemp, J. B.: Advances in Geosciences Advances in the WRF model for convection-resolving forecasting, Advances in Geosciences, 7, 25–29, 2006.

Knippertz, P., Evans, M. J., Field, P. R., Fink, A. H., Liousse, C., and Marsham, J. H.: The possible role of local air pollution in climate change in West Africa, Nature Climate Change, 5, 815–822, doi:10.1038/nclimate2727, 2015.

Knoche, H. R. and Kunstmann, H.: Tracking atmospheric water pathways by direct evaporation tagging: A case study for West Africa, Journal of Geophysical Research: Atmospheres, 118, 12,345–12,358, doi:10.1002/2013JD019976, 2013.

Knutti, R. and Hegerl, G.: The equilibrium sensitivity of the Earth's temperature to radiation changes, Nature Geoscience, 1, 735–743, 2008.

Kohler, M., Kalthoff, N., and Kottmeier, C.: The impact of soil moisture modifications on CBL characteristics in West Africa: A case-study from the AMMA campaign, Quarterly Journal of the Royal Meteorological Society, 136, 442–455, doi:10.1002/qj.430, 2010.

Koster, R., Dirmeyer, P., Guo, Z., and Bonan, G.: Regions of strong coupling between soil moisture and precipitation, Science, 2004.

Kucharski, F., Zeng, N., and Kalnay, E.: A further assessment of vegetation feedback on decadal Sahel rainfall variability, Climate Dynamics, 40, 1453–1466, doi:10.1007/s00382-012-1397-x, 2012.

Kumar, A., Chen, F., Barlage, M., Ek, M. B., and Niyogi, D.: Assessing Impacts of Integrating MODIS Vegetation Data in the Weather Research and Forecasting (WRF) Model Coupled to Two Different Canopy-Resistance Approaches, Journal of Applied Meteorology and Climatology, 53, 1362–1380, doi:http://dx.doi.org/10.1175/JAMC-D-13-0247.1, 2014.

Kunstmann, H. and Jung, G.: Influence of soil-moisture and land use change on precipitation in the Volta Basin of West Africa, International Journal of River Basin Management, 5, 1–8, 2007.

Lafore, J.-P., Flamant, C., Guichard, F., Parker, D. J., Bouniol, D., Fink, A. H., and Giraud, V.: Progress in understanding of weather systems in West Africa, Atmospheric Science Letters, 12, 7–12, doi:10.1002/asl.335, 2011.

Lauwaet, D., van Lipzig, N. P. M., and De Ridder, K.: The effect of vegetation changes on precipitation and Mesoscale Convective Systems in the Sahel, Climate Dynamics, 33, 521–534, doi:10.1007/s00382-009-0539-2, 2009.

Laux, P., Jäckel, G., Tingem, R. M., and Kunstmann, H.: Impact of climate change on agricultural productivity under rainfed conditions in Cameroon—A method to improve attainable crop yields by planting date adaptations, Agricultural and Forest Meteorology, 150, 1258–1271, doi:10.1016/j.agrformet.2010.05.008, 2010.

Lawrimore, J., Menne, M., Gleason, B., Williams, C., Wuertz, D., Vose, R., and Rennie, J.: An overview of the global historical climatology network monthly mean temperature data set, version 3, Geophysical Research Letters, 116, D19 121, doi:10.1029/2011JD016187, 2011.

Legates, D. R. and Willmott, C. J.: Mean seasonal and spatial variability in global surface air temperature, Theoretical and Applied Climatology, 41, 11–21, doi:10.1007/BF00866198, 1990.

Levermann, A., Schewe, J., Petoukhov, V., and Held, H.: Basic mechanism for abrupt monsoon transitions., Proceedings of the National Academy of Sciences of the United States of America, 106, 20 572–7, doi:10.1073/pnas.0901414106, 2009.

L'Hôte, Y., Mahé, G., Somé, B., and Triboulet, J. P.: Analysis of a Sahelian annual rainfall index from 1896 to 2000; the drought continues, Hydrological Sciences Journal, 47, 563–572, doi:10.1080/02626660209492960, 2002.

Li, R., Jin, J., Wang, S.-Y., and Gillies, R. R.: Significant impacts of radiation physics in the Weather Research and Forecasting model on the precipitation and dynamics of the West African Monsoon, Climate Dynamics, doi:10.1007/s00382-014-2294-2, 2014.

Li, W., Xue, Y., and Poccard-Leclercq, I.: Numerical Investigation of the Impact of Vegetation Indices on the Variability of West African Summer Monsoon, Journal Of The Meteorological Society Of Japan, 85A, 363–383, 2007.

Lin, Y., Farley, R., and Orville, H.: Bulk parameterization of the snow field in a cloud model, Journal of Applied Meteorology, 22, 1065–1092, 1983.

Linden, v. d. P. and Mitchell, J.: ENSEMBLES: Climate Change and its Impacts: Summary of Research and Results from the ENSEMBLES Project, Tech. rep., Met Office Hadley Center, Exeter, 2009.

Lorenz, C. and Kunstmann, H.: The Hydrological Cycle in Three State-of-the-Art Reanalyses: Intercomparison and Performance Analysis, Journal of Hydrometeorology, 13, 1397–1420, doi:10.1175/JHM-D-11-088.1, 2012.

Lorenz, C. and Kunstmann, H.: Large-Scale Runoff from Landmasses: A Global Assessment of the Closure of the Hydrological and Atmospheric Water Balances, Journal of Hydrometeorology, 15, 2111–2139, doi:10.1175/JHM-D-13-0157.1, 2014.

Lorenz, E.: Deterministic Nonperiodic Flow, Journal Of The Atmospheric Sciences, 20, 130–141, 1963.

Lorenz, P. and Jacob, D.: Influence of regional scale information on the global circulation: A two-way nesting climate simulation, Geophysical Research Letters, 32, 4–7, doi:10.1029/2005GL023351, 2005.

Losada, T., Rodríguez-Fonseca, B., Janicot, S., Gervois, S., Chauvin, F., and Ruti, P.: A multi-model approach to the Atlantic Equatorial mode: impact on the West African monsoon, Climate Dynamics, 35, 29–43, doi:10.1007/s00382-009-0625-5, 2010.

Losada, T., Mohino, E., Bader, J., Janicot, S., and Mechoso, C. R.: Tropical SST and Sahel rainfall: A non-stationary relationship, Geophysical Research Letters, 39, 1–7, doi:10.1029/2012GL052423, 2012.

LP DAAC: Modis product MCD43B3, Tech. rep., NASA EOSDIS Land Processes Distributed Active Archive Center, , USGS/Earth Resources Observation and Science (EROS) Center, Sioux Falls, South Dakota, 2014.

LSA SAF: Product User Manual Vegetation Parameters (VEGA), Tech. rep., The EUMETSAT Satellite Application Facility on Land Surface Analysis, 2013.

Lutz, K., Jacobeit, J., and Rathmann, J.: Atlantic warm and cold water events and impact on African west coast precipitation, International Journal of Climatology, 35, 128–141, doi:10.1002/joc.3969, 2015.

Ma, L.-M. and Tan, Z.-M.: Improving the behavior of the cumulus parameterization for tropical cyclone prediction: Convection trigger, Atmospheric Research, 92, 190–211, doi:10.1016/j.atmosres.2008.09.022, 2009.

Mantua, N. and Hare, S.: The Pacific Decadal Oscillation, Journal of Oceanography, 58, 35–44, 2002.

Marsham, J. H., Dixon, N. S., Garcia-carreras, L., Lister, G. M. S., Parker, D. J., Knippertz, P., and Birch, C. E.: The role of moist convection in the West African monsoon system : Insights from continental-scale convection-permitting simulations, Geophysical Research Letters, 40, 1843–1849, doi:10.1002/grl.50347, 2013.

Mathon, V. and Laurent, H.: Life cycle of Sahelian mesoscale convective cloud systems, Quarterly Journal of the Royal Meteorological Society, 127, 377–406, 2001.

Mesinger, F. and Arakawa, A.: Numerical methods used in atmospheric models, volume 1, Global Atmospheric Research Program World Meteorological Organization, Geneva (Switzerland), 1976.

Meynadier, R., Bock, O., Gervois, S., Guichard, F., Redelsperger, J.-L., Agustí-Panareda, A., and Beljaars, A.: West African Monsoon water cycle: 2. Assessment of numerical weather prediction water budgets, Journal of Geophysical Research, 115, D19 107, doi:10.1029/2010JD013919, 2010.

Mlawer, E., Taubman, S., Brown, P., Iacono, M., and Clough, S.: Radiative transfer for inhomogeneous atmosphere: RRTM, a validated correlated-k model for the long-wave, Journal of Geophysical Research, 102, 16 663–16 682, 1997.

Moeng, C.-H., Dudhia, J., Klemp, J., and Sullivan, P.: Examining Two-Way Grid Nesting for Large Eddy Simulation of the PBL Using the WRF Model, Monthly Weather Review, 135, 2295–2311, doi:10.1175/MWR3406.1, URL `http://journals.ametsoc.org/doi/abs/10.1175/MWR3406.1`, 2007.

Mohino, E., Rodríguez-Fonseca, B., Mechoso, C. R., Gervois, S., Ruti, P., and Chauvin, F.: Impacts of the Tropical Pacific/Indian Oceans on the Seasonal Cycle of the West African Monsoon, Journal of Climate, 24, 3878–3891, doi:10.1175/2011JCLI3988.1, 2011.

Mohr, K. I. and Thorncroft, C. D.: Intense convective systems in West Africa and their relationship to the African easterly jet, Quarterly Journal of the Royal Meteorological Society, 132, 163–176, doi:10.1256/qj.05.55, 2006.

Molinari, J. and Dudek, M.: Parameterization of Convective Precipitation in Mesoscale Numerical Models: A Critical Review, Monthly Weather Review, 120, 326–344, 1992.

Morris, M., Binswanger, H., Byerlee, D., and Staatz, J.: A Breadbasket for Africa: Farming in the Guinea Savannah Zone http://www.thesolutionsjournal.com/print/1080, Solutions, 3, 44–49, 2012.

Murphy, J. M., Sexton, D., Barnett, D., Jones, G., Webb, M., Collins, M., and Stainforth, D.: Quantification of modelling uncertainties in a large ensemble of climate change simulations, Nature, 430, 768–772, doi:10.1038/nature02770.1., 2004.

NCAR: WRF Version 3 Modeling System User's Guide July 2015, Tech. Rep. July, National Center for Atmospheric Research, 2015.

Nicholson, S. E.: The intensity , location and structure of the tropical rainbelt over west Africa as factors in interannual variability, International Journal Of Climatology, 1785, 1775–1785, doi:10.1002/joc, 2008.

Nicholson, S. E.: On the factors modulating the intensity of the tropical rainbelt over West Africa, International Journal Of Climatology, 689, 673–689, doi:10.1002/joc, 2009.

Nicholson, S. E.: The West African Sahel: A Review of Recent Studies on the Rainfall Regime and Its Interannual Variability, ISRN Meteorology, 2013, 1–32, doi:10.1155/2013/453521, 2013.

Nicholson, S. E., Some, B., McCollum, E., Nelkin, E. J., Klotter, D., Berte, Y., Diallo, B., Gaye, I., Kpabeba, G., Ndiaye, O., Noukpozounkou, J., Tanu, M., Thiam, A., Toure, A., et al.: Validation of TRMM and Other Rainfall Estimates with a High-Density Gauge Dataset for West Africa . Part I : Validation of GPCC Rainfall Product and Pre-TRMM Satellite and Blended Products, Journal Of Applied Meteorology, 42, 2003a.

Nicholson, S. E., Some, B., McCollum, E., Nelkin, E. J., Klotter, D., Berte, Y., Diallo, B., Gaye, I., Kpabeba, G., Ndiaye, O., Noukpozounkou, J., Tanu, M., Thiam, A., Toure, A., et al.: Validation of TRMM and Other Rainfall Estimates with a High-Density Gauge Dataset for West Africa . Part II : Validation of TRMM Rainfall Products, American Meteorological Society, 42, 1355–1368, 2003b.

Nikulin, G., Jones, C., Giorgi, F., Asrar, G., Büchner, M., Cerezo-Mota, R., Christensen, O. B. s., Déqué, M., Fernandez, J., and Hänsler, A.: Precipitation Climatology in an Ensemble of CORDEX-Africa Regional Climate Simulations, Journal of Climate, 25, 6057–6078, doi:10.1175/JCLI-D-11-00375.1, 2012.

NOAA CPC: NOAA CPC African rainfall estimates, URL `http://iridl.ldeo.columbia.edu/SOURCES/.NOAA/.NCEP/.CPC/.FEWS/`, 2013.

Noble, E., Druyan, L. M., and Fulakeza, M.: The Sensitivity of WRF Daily Summertime Simulations over West Africa to Alternative Parameterizations. Part I: African Wave Circulation, Monthly Weather Review, 142, 1588–1608, doi:10.1175/MWR-D-13-00194.1, 2014.

Notaro, M., Chen, G., and Liu, Z.: Vegetation Feedbacks to Climate in the Global Monsoon Regions*, Journal of Climate, 24, 5740–5756, doi:10.1175/2011JCLI4237.1, 2011.

Novella, N. S. and Thiaw, W. M.: African Rainfall Climatology Version 2 for Famine Early Warning Systems, Journal of Applied Meteorology and Climatology, 52, 588–606, doi:10.1175/JAMC-D-11-0238.1, URL `http://journals.ametsoc.org/doi/abs/10.1175/JAMC-D-11-0238.1`, 2013.

Oouchi, K., Noda, A. T., Satoh, M., Wang, B., Xie, S.-P., Takahashi, H. G., and Yasunari, T.: Asian summer monsoon simulated by a global cloud-system-resolving model: Diurnal to intraseasonal variability, Geophysical Research Letters, 36, L11 815, doi:10.1029/2009GL038271, 2009.

Ozer, P., Erpicum, M., Demarée, G., and Vandiepenbeeck, M.: The Sahelian drought may have ended during the 1990s, Hydrological Sciences Journal, 48, 489–492, doi:10.1623/hysj.48.3.489.45285, 2003.

Paeth, H. and Friederichs, P.: Seasonality and time scales in the relationship between global SST and African rainfall, Climate Dynamics, 23, 815–837, doi:10.1007/s00382-004-0466-1, 2004.

Paeth, H., Hall, N. M., Gaertner, M. A., Alonso, M. D., Moumouni, S., Polcher, J., Ruti, P. M., Fink, A. H., Gosset, M., and Lebel, T.: Progress in regional downscaling of west African precipitation, Atmospheric Science Letters, 12, 75–82, doi:10.1002/asl.306, 2011.

Parker, B. D. J., Thorncroft, C. D., and Burton, R. R.: Analysis of the African easterly jet , using aircraft observations from the JET2000 experiment, Quarterly Journal Of The Royal Meteorological Society, 131, 1461–1482, doi:10.1256/qj.03.189, 2005a.

Parker, D., Burton, R. R., Ellis, R. J., Felton, M., Taylor, C. M., Thorncroft, C. D., Bessemoulin, P., and Tompkins, A. M.: The diurnal cycle of the West African monsoon circulation, Quarterly Journal Of The Royal Meteorological Society, 131, 2839–2860, doi:10.1256/qj.04.52, 2005b.

Pearson, K. J., Lister, G. M. S., Birch, C. E., Allan, R. P., Hogan, R. J., and Woolnough, S. J.: Modelling the diurnal cycle of tropical convection across the 'grey zone', Quarterly Journal of the Royal Meteorological Society, 140, 491–499, doi:10.1002/qj.2145, 2014.

Pleim, J.: A combined local and non-local closure model for the atmospheric boundary layer. Part 1: model description and testing, Journal Of Applied Meteorology and Climatology2, 46, 1383–1395, 2007.

Pohl, B., Crétat, J., and Camberlin, P.: Testing WRF capability in simulating the atmospheric water cycle over Equatorial East Africa, Climate Dynamics, 37, 1357–1379, doi:10.1007/s00382-011-1024-2, 2011.

Pohl, B., Rouault, M., and Roy, S. S.: Simulation of the annual and diurnal cycles of rainfall over South Africa by a regional climate model, Climate Dynamics, 43, 2207–2226, doi:10.1007/s00382-013-2046-8, 2014.

Posselt, R., Müller, R., Stöckli, R., and Trentmann, J.: CM SAF Surface Radiation MVIRI Data Set 1.0 - Monthly Means / Daily Means / Hourly Means., Tech. rep., Satellite Application Facility on Climate Monitoring., doi:DOI:10.5676/EUM_SAF_CM/RAD_MVIRI/V001, 2011.

Posselt, R., Mueller, R. W., Stöckli, R., and Trentmann, J.: Remote sensing of solar surface radiation for climate monitoring — the CM-SAF retrieval in international comparison, Remote Sensing of Environment, 118, 186–198, doi:10.1016/j.rse.2011.11.016, URL http://dx.doi.org/10.1016/j.rse.2011.11.016, 2012.

Rabin, R., Stadler, S., Wetzel, P., Stensrud, D., and Gregory, M.: Observed Effects of Landscape Variability on Convective Clouds, Bulletin of the American Meteorological Society, 71, 272–280, 1990.

Redelsperger, J.-L., Thorncroft, C. D., Diedhiou, A., Lebel, T., Parker, D. J., and Polcher, J.: African monsoon multidisciplinary analysis, Bulletin of the American Meteorological Society, pp. 1739–1746, doi:10.1175/BAMS-87-12-1739, 2006.

Reichle, R., Koster, R. D., de Lannoy, G., Forman, B., Liu, Q., Mahanama, S., and Touré, A.: Assessment and Enhancement of MERRA Land Surface Hydrology Estimates, Journal of Climate, 24, 6322–6338, doi:10.1175/JCLI-D-10-05033.1, 2011.

Rienecker, M., Suarez, M. J., Gelaro, R., Todling, R., Bacmeister, J., Liu, E., Bosilovich, M. G., and Al., E.: MERRA: NASA's Modern-Era Retrospective Analysis for Research and Applications, Journal of Climate, 24, 3624–3648, doi:10.1175/JCLI-D-11-00015.1, 2011.

Rockel, B., Castro, C. L., Pielke, R. A., von Storch, H., and Leoncini, G.: Dynamical downscaling: Assessment of model system dependent retained and added variability for two different regional climate models, Journal Of Geophysical Research-Atmospheres, 113, D21 107, doi: 10.1029/2007JD009461, 2008.

Rodríguez-Fonseca, B., Janicot, S., Mohino, E., Losada, T., Bader, J., Caminade, C., Chauvin, F., Fontaine, B., García-Serrano, J., Gervois, S., Joly, M., et al.: Interannual and decadal SST-forced responses of the West African monsoon, Atmospheric Science Letters, 12, 67–74, doi:10.1002/asl.308, 2011.

Rodríguez-Fonseca, B., Mohino, E., Mechoso, C. R., Caminade, C., Biasutti, M., Gaetani, M., Garcia-Serrano, J., Vizy, E. K., Cook, K., Xue, Y., et al.: Variability and Predictability of West African Droughts: A Review on the Role of Sea Surface Temperature Anomalies, Journal of Climate, 28, 4034–4060, doi:10.1175/JCLI-D-14-00130.1, 2015.

Rowell, D.: The Impact of Mediterranean SSTs on the Sahelian Rainfall Season, Journal of Climate, 16, 849–862, 2003.

Saha, S., Moorthi, S., Pan, H.-L., Wu, X., Wang, J. J., Nadiga, S., Tripp, P., Kistler, R., Woollen, J., and Behringer, D.: The Ncep Climate Forecast System Reanalysis, Bulletin of the American Meteorological Society, 91, 1015–1057, doi:10.1175/2010BAMS3001.1, 2010.

Salack, S., Sarr, B., Sangare, S., Ly, M., Sanda, I., and Kunstmann, H.: Crop-climate ensemble scenarios to improve risk assessment and resilience in the semi-arid regions of West Africa, Climate Research, 65, 107–121, doi:10.3354/cr01282, 2015.

Schneider, U., Becker, A., Finger, P., Meyer-Christoffer, A., Rudolf, B., and Ziese, M.: GPCC full data reanalysis version 6.0 at 0.5: monthly land-surface precipitation from rain-gauges built on GTS-based and historic data, Tech. rep., Global Precipitation Climatology Centre, doi:10.5676/DWD_GPCC/FD_M_V6_050, 2011.

Schumacher, C. and Houze, R. a.: Stratiform precipitation production over sub-Saharan Africa and the tropical East Atlantic as observed by TRMM, Quarterly Journal of the Royal Meteorological Society, 132, 2235–2255, doi:10.1256/qj.05.121, 2006.

Senatore, A., Mendicino, G., Knoche, H. R., and Kunstmann, H.: Sensitivity of Modeled Precipitation to Sea Surface Temperature in Regions with Complex Topography and Coastlines: A Case Study for the Mediterranean, Journal Of Hydrometeorology, 15, 2370–2397, doi: 10.1175/JHM-D-13-089.1, 2014.

Seneviratne, S. I., Corti, T., Davin, E. L., Hirschi, M., Jaeger, E. B., Lehner, I., Orlowsky, B., and Teuling, A. J.: Investigating soil moisture–climate interactions in a changing climate: A review, Earth-Science Reviews, 99, 125–161, doi:10.1016/j.earscirev.2010.02.004, 2010.

Shin, H. H. and Hong, S.-Y.: Intercomparison of Planetary Boundary-Layer Parametrizations in the WRF Model for a Single Day from CASES-99, Boundary-Layer Meteorology, 139, 261–281, doi:10.1007/s10546-010-9583-z, 2011.

Shukla, J.: Predictability in the Midst of Chaos: A Scientific Basis for Climate Forecasting, Science, 282, 728–731, doi:10.1126/science.282.5389.728, 1998.

Siam, M. S., Demory, M.-E., and Eltahir, E. a. B.: Hydrological Cycles over the Congo and Upper Blue Nile Basins: Evaluation of General Circulation Model Simulations and Reanalysis Products, Journal of Climate, 26, 8881–8894, doi:10.1175/JCLI-D-12-00404.1, 2013.

Siegmund, J., Bliefernicht, J., Laux, P., and Kunstmann, H.: Toward a seasonal precipitation prediction system for West Africa: Performance of CFSv2 and high-resolution dynamical downscaling, Journal of Geophysical Research: Atmospheres, 120, 7316–7339, doi:10.1002/2014JD022692.Received, 2015.

Sijikumar, S., Roucou, P., and Fontaine, B.: Monsoon onset over Sudan-Sahel: Simulation by the regional scale model MM5, Geophysical Research Letters, 33, L03 814, doi:10.1029/2005GL024819, 2006.

Skamarock, W. C., Klemp, J. B., Dudhia, J., Gill, D. O., Barker, D. M., Duda, M. G., Huang, X.-y., Wang, W., Powers, J. G., and Division, M. M.: A Description of the Advanced Research WRF Version 3, Tech. rep., NCAR, Boulder, Colorado, USA, 2008.

Stein, T. H. M., Parker, D. J., Dixon, N. S., Hogan, R. J., Maidment, R. I., and Marsham, J. H.: The vertical cloud structure of the West African monsoon: A four-year climatology using CloudSat and CALIPSO, Journal of Geophysical Research, 116, 2156–2202, 2011.

Stensrud, D.: Parameterization Schemes: Keys to Understanding Numerical Weather Prediction Models, Cambridge University Press, Oklahoma, 2009.

Stensrud, D., Bao, J.-W., and Warner, T. T.: Using Initial Condition and Model Physics Perturbations in Short-Range Ensemble Simulations of Mesoscale Convective Systems, Monthly Weather Review, 128, 2077–2107, 2000.

Sultan, B. and Janicot, S.: Abrupt shift of the ITCZ over West Africa and intra-seasonal variability, Geophysical Research Letters, 27, 3353–3356, 2000.

Sultan, B. and Janicot, S.: The West African Monsoon Dynamics . Part I : Documentation of Intraseasonal Variability, Journal of Climate, 16, 3389–3406, 2003.

Sylla, M., Diallo, I., and Pal, J.: West African monsoon in state-of-the-science regional climate models, Climate Variability - Regional and Thematic Patterns, pp. 3–36, doi:http://dx.doi.org/10.5772/55140, 2013.

Sylla, M. B., Giorgi, F., Ruti, P. M., Calmanti, S., and Dell'Aquila, A.: The impact of deep convection on the West African summer monsoon climate: a regional climate model sensitivity study, Quarterly Journal of the Royal Meteorological Society, 137, 1417–1430, doi:10.1002/qj.853, 2011.

Taylor, C., Harris, P., and Parker, D.: Impact of soil moisture on the development of a Sahelian mesoscale convective system: a case-study from the AMMA Special Observing Period, Quarterly Journal of the Royal Meteorological Society, 136, 456–470, doi:10.1002/qj.465, 2010.

Taylor, C. M.: Intraseasonal Land–Atmosphere Coupling in the West African Monsoon, Journal of Climate, 21, 6636–6648, doi:10.1175/2008JCLI2475.1, 2008.

Taylor, C. M., Lambin, E. F., Stephenne, N., Harding, R. J., and Essery, R. L. H.: The Influence of Land Use Change on Climate in the Sahel, Journal of Climate, 15, 3615–3629, 2002.

Taylor, C. M., Gounou, A., Guichard, F., Harris, P. P., Ellis, R. J., Couvreux, F., and Kauwe, M. D.: Frequency of Sahelian storm initiation enhanced over mesoscale soil-moisture patterns, Nature Geoscience, 4, 430–433, doi:10.1038/ngeo1173, 2011a.

Taylor, C. M., Parker, D. J., Kalthoff, N., Gaertner, M. A., Philippon, N., Bastin, S., Harris, P. P., Boone, A., Guichard, F., and Agusti-Panareda, A.: New perspectives on land-atmosphere feedbacks from the African Monsoon Multidisciplinary Analysis, Atmospheric Science Letters, 12, 38–44, doi:10.1002/asl.336, 2011b.

Taylor, C. M., de Jeu, R. a. M., Guichard, F., Harris, P. P., and Dorigo, W. a.: Afternoon rain more likely over drier soils., Nature, 489, 423–6, doi:10.1038/nature11377, 2012.

Tebaldi, C. and Knutti, R.: The use of the multi-model ensemble in probabilistic climate projections., Philosophical transactions. Series A, Mathematical, physical, and engineering sciences, 365, 2053–75, doi:10.1098/rsta.2007.2076, 2007.

Teutschbein, C. and Seibert, J.: Regional Climate Models for Hydrological Impact Studies at the Catchment Scale: A Review of Recent Modeling Strategies, Georaphy Compass, 7, 834–860, 2010.

Thompson, G., Field, P., Rasmussen, R., and Hall, W.: Explicit forecasts of winter precipitation using an improved bulk microphysics scheme. part II: implementation of a new snow parameterization, Monthly Weather Review, 136, 5095–5115, doi:10.1175/2008MWR2387.1, 2008.

Thorncroft, C. D., Nguyen, H., Zhang, C., and Peyrillé, P.: Annual cycle of the West African monsoon: regional circulations and associated water vapour transport, Quarterly Journal of the Royal Meteorological Society, 137, 129–147, doi:10.1002/qj.728, 2011.

Thunis, P. and Bornstein, R.: Hierarchy of Mesoscale Flow Assumptions and Equations, Journal of the Atmospheric Sciences, 53, 380–397, 1996.

Trenberth, K. E., Stepaniak, D. P., Hurrell, J. W., and Fiorino, M.: Quality of Reanalyses in the Tropics, Journal of Climate, 14, 1499–1510, 2001.

Trenberth, K. E., Koike, T., and Onogi, K.: Progress and Prospects for Reanalysis for Weather and Climate, Eos, Transactions American Geophysical Union, 89, 234–235, 2008.

Van Den Dool, H., Huang, J., and Fan, Y.: Performance and Analysis of the constructed analogue method applied to US soil moisture applied over 1981-2001, Journal of Geophysical Research, 108, 1–16, 2003.

Vigaud, N., Roucou, P., Fontaine, B., Sijikumar, S., and Tyteca, S.: WRF/Arpege-Climat simulated climate trends over West Africa, Climate Dynamics, 36, 925–944, 2011.

Vizy, E. K. and Cook, K. H.: Development and application of a mesoscale climate model for the tropics : Influence of sea surface temperature anomalies on the West African monsoon, Journal of Geophysical Research, 107, 4023, doi:10.1029/2001JD000686, 2002.

Vizy, E. K. and Cook, K. H.: Tropical Storm Development from African Easterly Waves in the Eastern Atlantic: A Comparison of Two Successive Waves Using a Regional Model as Part of NASA AMMA 2006, Journal Of The Atmospheric Sciences, 66, 3313–3334, doi:10.1175/2009JAS3064.1, 2009.

Vose, R., Arndt, D., Banzon, V., Easterling, D., Gleason, B., Huang, B., Kearns, E., Lawrimore, J., Menne, M., Peterson, T., Reynolds, R., et al.: NOAA's merged land–ocean surface temperature analysis, Bulletin of the American Meteorological Society, pp. 1677–1685, doi:10.1175/BAMS-D-11-00241.1, 2012.

Wang, G. and Eltahir, E. a. B.: Biosphere-atmosphere interactions over West Africa. I: Development and validation of a coupled dynamic model, Quarterly Journal of the Royal Meteorological Society, 126, 1239–1260, 2000.

Wang, J., Chagnon, F., Williams, E. R., Betts, A. K., Renno, N. O., Machado, L. A. T., Bisht, G., Knox, R., and Bras, R. L.: Impact of deforestation in the Amazon basin on cloud climatology, Proceedings of the National Academy of Sciences of the USA, doi:10.1073/pnas.0810156106, 2009.

Waongo, M., Laux, P., Traoré, S. B., Sanon, M., and Kunstmann, H.: A Crop Model and Fuzzy Rule Based Approach for Optimizing Maize Planting Dates in Burkina Faso, West Africa, Journal of Applied Meteorology and Climatology, 53, 598–613, doi:10.1175/JAMC-D-13-0116.1, 2014.

Weisman, M.: The resolution dependence of explicitly modeled convective systems, Monthly Weather Review, 125, 527–548, 1997.

William, H., Flannery, B., Teukolsky, S., and Vetterling, W.: 14.8 Savitzky-Golay Smoothing Filters, in: Numerical Recipes in C: The Art of Scientific Computing, pp. 650–655, Cambridge University Press, 2 edn., 1992.

Wolters, E. L. A. and Roebeling, R. A.: Evaluation of rainfall retrievals from SEVIRI reflectances over West Africa using TRMM-PR and CMORPH, Hydrology and Earth System Sciences, 15, 437–451, doi:10.5194/hess-15-437-2011, 2011.

Xie, B., Fung, J. C. H., Chan, A., and Lau, A.: Evaluation of nonlocal and local planetary boundary layer schemes in the WRF model, Journal of Geophysical Research: Atmospheres, 117, D12 103, doi:10.1029/2011JD017080, 2012.

Zaengl, G.: To what extent does increased model resolution improve simulated precipitation fields? A case study of two north-Alpine heavy-rainfall events, Meteorologische Zeitschrift, 16, 571–580, doi:10.1127/0941-2948/2007/0237, 2007.

Zheng, X. and Eltahir, E. a. B.: The Role of Vegetation in the Dynamics of West African Monsoons, Journal of Climate, 11, 2078–2096, doi:10.1175/1520-0442-11.8.2078, 1998.

Acknowledgements